Far Infrared Conductivity of Charge Density Wave Materials and the Oxygen Isotope effect in High-T_c Superconductors

By

William Nance Creager

B.A. (Rice University) 1983

DISSERTATION

Submitted in partial satisfaction of the requirements for the degree of

DOCTOR OF PHILOSOPHY

in

PHYSICS

in the

GRADUATE DIVISION

of the

UNIVERSITY OF CALIFORNIA at BERKELEY

Approved:

Chair: ..... Date

.....

.....

* * * * * * * * * * * * * * * * * * * *

FAR-INFRARED CONDUCTIVITY OF CHARGE DENSITY WAVE MATERIALS AND THE OXYGEN ISOTOPE EFFECT IN HIGH-T_c SUPERCONDUCTORS

William Nance Creager

FAR-INFRARED CONDUCTIVITY OF CHARGE DENSITY WAVE MATERIALS AND THE OXYGEN ISOTOPE EFFECT IN HIGH-T_c SUPERCONDUCTORS

by

William Nance Creager

Department of Physics
University of California, Berkeley

ABSTRACT

(to be completed)

for my parents,

Nance and Barbara Creager,

and for my wife,

Angela Nelle

Table of contents

List of Figures

Figure

Figure

List of Tables

Acknowledgements

to be completed

Vita

March 24, 1961:	Born in Roswell, New Mexico
May, 1983:	B.A. in Physics, Rice University
June, 1983 to July, 1985:	Taught high school science as a Peace Corps Volunteer in Banjul, The Gambia, West Africa
September, 1985 to June, 1986:	Teaching Assistant, Department of Physics, Harvard University
September, 1986 to August, 1991:	Teaching and Research Assistant, Department of Physics, University of California at Berkeley

Publications

1. L.C. Bourne, Marvin L. Cohen, William N. Creager, Michael F. Crommie, Angelica M. Stacy, and A. Zettl, "Onset of Superconductivity in Y-Ba-Cu-O at 100K", Phys. Lett. **A 120**, 494 (1987).

2. L.C. Bourne, Marvin L. Cohen, W.N. Creager, M.F. Crommie, and A. Zettl, "Compositionally Dependent Superconducting Transition Temperature of Y-Ba-Cu Oxides", Phys. Lett. **A 123**, 34 (1987).

3. L.C. Bourne, S. Hoen, M.F. Crommie, W.N. Creager, A. Zettl, Marvin L. Cohen, Luis Bernardez, John Kinney, and Donald E. Morris, "Magnetic and Resistive Determination of the Oxygen Isotope Effect in $La_{1.85}Sr_{0.15}CuO_4$", Solid State Comm. **67**, 707 (1988).

4. A. Zettl, L.C. Bourne, W.N. Creager, M.F. Crommie, S. Hoen, "Electron-phonon Interactions in High-temperature Oxide Superconductors: Isotope Effects and Elasticity Studies", Syn. Met. **29**, F723 (1988).

5. M.F. Crommie, Amy Y. Liu, A. Zettl, Marvin L. Cohen, P. Parilla, M.F. Hundley, W.N. Creager, S. Hoen, and M.S. Sherwin, "c-axis Stress Dependence of Normal and Superconducting State Properties of $YBa_2Cu_3O_7$", Phys. Rev. B **39**, 4231 (1989).

6. S. Hoen, W.N. Creager, L.C. Bourne, M.F. Crommie, T.W. Barbee III, Marvin L. Cohen, A. Zettl, Luis Bernardez, and John Kinney, "Oxygen Isotope Study of $YBa_2Cu_3O_7$", Phys. Rev. B **39**, 2269 (1989).

7. I.D. Parker, A.L. Chen, W.N. Creager, A. Zettl, and P.Y. Yu, "Pressure and Magnetic Field Effects on Transport in $NbSe_3$", Syn. Met. **41-43**, 3859 (1990).

8. S. Hoen, I.D. Parker, W.N. Creager, and A. Zettl, "Magneto-elastic properties of $NbSe_3$", Syn. Met. **41-43**, 3863 (1990).

9. P. Parilla, A. Behrooz, W.N. Creager, and A. Zettl, "Asymmetry in the Static and Dynamic Charge Density Wave States of $NbSe_3$: Heat and Electrical Current Flow", Syn. Met. **41-43**, 3855 (1990).

10. P. Parilla, M.F. Hundley, A. Behrooz, W.N. Creager, and A. Zettl, "Temperature-gradient-induced Subdomain Scaling in $NbSe_3$", Syn. Met. **41-43**, 3871 (1990).

11. P. Parilla, M.F. Hundley, W.N. Creager, and A. Zettl, "Model of Dynamic Charge Density Wave Break-up in an Applied Temperature Gradient", Syn. Met. **41-43**, 3851 (1990).

12. W.N. Creager, P.L. Richards, and A. Zettl, "Far Infrared Reflectance and Conductivity of TaS_3: Completion of the AC Response Spectrum", Syn. Met. **41-43**, 3867 (1990).

13. W.N. Creager, P.L. Richards, and A. Zettl, "Far Infrared Conductivity of TaS_3: Identification of the Intrinsic Charge Density Wave Excitation Modes", Phys. Rev. **B** (in press).

Part I: Far Infrared Conductivity of Charge Density Wave Materials

Chapter 1

Overview of the Dissertation

Charge density waves and superconductors are linked historically and conceptually. In an early and erroneous speculation about the origin of superconductivity, Fröhlich suggested that freely sliding charge density waves might account for at least the zero-resistivity aspect of superconductivity.[1] The Bardeen-Cooper-Schrieffer[2, 3] (BCS) theory laid to rest such simple connections between the two phenomena, and in the intervening thirty years the similarities and distinctions between charge density wave conductors and superconductors have become clear. Both phenomena are manifestations of strongly correlated electron systems. In charge density wave (CDW) conductors, electrons and holes on opposite sides of the Fermi surface correlate below the Peierls transition temperature T_P. They form a modulation of the electronic density that opens a gap in the excitation spectra at the Fermi surface. In superconductors below T_c, the correlation is between electrons with opposite spin and momentum.

This dissertation addresses the dynamics of electrons in charge density waves and the coupling mechanism between electrons in the recently discovered rare earth oxide superconductors.[4] It is organized in two sections. The first part is an investigation of the dynamics of charge density waves at far infrared (FIR) frequencies. The ac conductivity of CDW materials is dominated by a microwave and a large infrared mode. The former is the well-known pinning resonance, or acoustic phason mode. It corresponds to the oscillatory response of the entire charge density wave constrained by interactions with impurities. Under certain conditions, the acoustic phason mode may shift to dc and carry large amounts of current with zero differential

resistivity. The origin of the infrared mode is not well known. In fact, the observation of the giant infrared mode in $(TaSe_4)_2I$ and was a big surprise in a relatively settled field.[5] Many theories have been proposed as explanations of the FIR mode. Some suggest that the infrared mode should be a universal feature of charge density wave conductors. The theories appeal to various excitations of the CDW condensate, to the interactions of the charge density wave with impurities, and to subtle structural aspects of these complicated materials. The first part of the thesis is a systematic exploration of the giant far infrared mode and its interactions with pinned and sliding charge density waves in a variety of materials at different temperatures and impurity concentrations. Our results rule out several theories of the infrared mode and place tight constraints on the remaining ones.

Chapter 2 gives an overview of the conventional understanding of CDW conductivity. It explains the formation of charge density waves in quasi-one-dimensional conductors and reviews the widely-accepted models for the microwave resonance and various midgap states. It presents the evidence for the giant FIR mode and closes with a discussion of the structures of the materials. Chapter 3 discusses far infrared measurement techniques. It describes the interferometer, filters, detectors, and reflectance/transmittance apparatus used in our experiments. Chapter 4 reports the measurement of the far infrared conductivity of TaS_3. This material has a simpler structure than $(TaSe_4)_2I$ and according to some theories should not have an infrared mode at all. We find that TaS_3 does have a small mode near $10cm^{-1}$ and that the size and frequency of the resonance give important information about the origin of the giant infrared mode. Chapter 5 is an investigation of the giant infrared mode in $(Ta_{1-x}Nb_xSe_4)_2I$ alloys. The main pinning resonance of the charge density wave shifts to far infrared frequencies when niobium

impurities replace tantalum atoms in the crystals. The interaction of the shifted pinning resonance with the giant infrared mode places constraints on the theories that assume that impurities are the origin of the latter mode. Chapter 6 presents models and measurements of the transmittance of $K_{0.3}MoO_3$ when the material carries a sliding CDW. It is the first measurement of the shift in oscillator strength to dc when the CDW depins and enters the sliding, apparently dissipationless Fröhlich state. It also constitutes a very strict test of one theory that associates the infrared mode with the effects of impurities in the crystals.

In the second part of the dissertation, we turn to measurements of the oxygen isotope effect in high-T_c superconductors. Chapter 7 reviews the history of the isotope effect and discusses its importance in elucidating the origins of the electron pairing mechanism in superconductors. It summarizes the sometimes disparate results of previous isotope effect studies in copper-oxide superconductors and indicates the problems and unresolved difficulties inherent in those studies. Chapter 8 presents a detailed study of the oxygen isotope effect in $YBa_2Cu_3O_7$. This chapter summarizes the experimental strategies that suppressed many of the systematic errors that had plagued prior isotope effect studies. We find small but finite shifts for both bulk and filamentary superconductivity in $YBa_2Cu_3O_7$. The chapter concludes with a discussion of these results and their significance for application of the standard three-dimensional BCS theory of superconductivity to the oxide materials.

The dissertation concludes with an appendix that discusses the relation between measured optical quantities and the dielectric function of materials. The appendix includes a large library of computer code used in the far infrared optics calculations.

References

1. H. Fröhlich, Proc. R. Soc. London Ser. A **223**, 296 (1954).

2. J. Bardeen, L.N. Cooper and J.R. Schrieffer, Phys. Rev. **108**, 1175 (1957).

3. J. Bardeen, L.N. Cooper and J.R. Schrieffer, Phys. Rev. **106**, 162 (1957).

4. J.G. Bednorz and K.A. Müller, Z. Phys. B **64**, 189 (1986).

5. M.S. Sherwin, A. Zettl and P.L. Richards, Phys. Rev. B **36**, 6708 (1987).

Chapter 2

Introduction to Charge Density Wave Dynamics

Introduction

Interest in the dynamics of charge density waves preceded the synthesis of CDW materials by almost two decades, and after an additional two decades, the study of CDW dynamics continues to provide new insights into the rich behavior of this collective mode. In 1954, Fröhlich showed that a CDW in a one dimensional metal should be superconducting if the wavelength of the charge modulation is incommensurate with the atomic lattice.[1] Quasi-one dimensional conductors with many parallel metallic chains were synthesized in the early 1970's and nonlinear conductivity associated with a sliding CDW was observed soon thereafter.[2] Fröhlich superconductivity is always destroyed in real crystals due to pinning by impurities, scattering of the CDW by phonons, or crystal defects. Nonetheless, the low-frequency oscillator strength associated with the massive, highly polarizable condensate is manifest in a number of interesting effects. Charge density wave conductors typically have an enormous static dielectric constant, a strong resonance corresponding to the pinned CDW, and a threshold field for nonlinear conductivity. At low temperatures, the depinning can be extremely abrupt, and the sliding Fröhlich mode has no measurable *differential* resistivity in some materials.[3] Charge density wave conductors also display metastable effects, mode locking and chaotic behavior.

The first part of this dissertation will be primarily concerned with the conductivity $\sigma(\omega)$ of the CDW in the pinned state at far infrared frequencies, and this chapter gives the experimental and theoretical background necessary for understanding these experiments. More specifically, we will measure the

far infrared reflectance and derive the far infrared conductivity of the inorganic conductors TaS_3 and niobium-doped $(TaSe_4)_2I$ in an effort to elucidate the origin of a giant far infrared mode previously seen in pure samples of the latter material.[4] In this chapter, then, we will discuss the well understood fundamental excitation modes of the CDW condensate, including the single particle gap, the acoustic phason and its description as a rigid harmonic oscillator, the phase phonons, and dielectric relaxation. For each of these excitations we will present a model conductivity and the associated reflectance. We will then discuss the measured reflectance and conductivity of $(TaSe_4)_2I$ and show how the existence of a far infrared resonance challenges the prevailing understanding of charge density wave conduction.

Before discussing the intrinsic CDW excitations, we will begin by introducing the formation of the Peierls distortion of the ionic lattice and the electronic charge density in low-dimensional conductors. Finally, we will conclude the chapter with a discussion of the crystal structure and some electronic properties of TaS_3, $(TaSe_4)_2I$, and $K_{0.3}MoO_3$, the materials studied in this thesis.

Formation of a charge density wave: the Peierls distortion

The Lindhard electronic susceptibility $\chi(\tilde{q})$ gives the response $\delta\rho$ of the electronic charge density to the potential $V(\tilde{q})$ associated a periodic ion displacement characteristic of a phonon with wavevector $\tilde{q}$. For a metal, $\chi(\tilde{q}) = -\delta\rho/V(\tilde{q})$ is given by

$$\chi(\tilde{q}) = \sum_{\tilde{k}} \frac{f(\tilde{k}) - f(\tilde{k} + \tilde{q})}{E(\tilde{k} + \tilde{q}) - E(\tilde{k})} \qquad (2\text{-}1)$$

where $f(\tilde{k})$ is the Fermi-Dirac distribution and $E(\tilde{k})$ is the energy for an electron with wavevector $\tilde{k}$. For a one-dimensional metal, a single wavevector perfectly nests the Fermi surface at the two points $k = \pm k_F$. The energy denominator in Eq. (2-1) goes to zero and for low temperatures $\chi(q)$ gets very large at $Q = 2k_F$. At $T = 0$ the susceptibility diverges logarithmically.

The diverging susceptibility indicates that the electrons are vulnerable to a static distortion with spatial periodicity $2\pi/2k_F$. Such a distortion opens a gap 2Δ precisely at the Fermi level, and lowers the energy of the conduction electrons. The electronic distortion comes at the energy cost, though, of displacing the lattice ions through electron-phonon coupling. When the force on the ions exerted by the distorted electronic charge balances the harmonic force constraining the ions to the crystal lattice sites, the phonon frequency at $Q = 2k_F$ goes soft:

$$\omega^2(2k_F) = \omega_Q^2 - \frac{2\,g^2\chi(2k_F)}{M} \qquad (2\text{-}2)$$

where ω_Q is the phonon frequency at $2k_F$ in the absence of the static distortion, g is the dimensionless electron-phonon coupling constant, and M is the ionic mass. At the Peierls transition temperature T_P, χ is big enough so that $\omega(2k_F)$ goes to zero and the static periodic lattice distortion and electronic charge density wave are established throughout the crystal. Expressions similar to those describing BCS superconductors relate the magnitude of the electronic Peierls gap to the mean field transition temperature ($2\Delta = 3.52k_BT_C$) and the coupling constant ($\Delta = 2\varepsilon_F e^{-1/\lambda}$). In these relations, $\lambda \equiv N(\varepsilon_F)g^2/M\omega_Q^2$ and $N(\varepsilon_F)$ is the density of states at the Fermi energy. At the mean field transition temperature T_C a charge density wave begins to be established on the individual chains, but three dimensional ordering of the

CDW throughout the crystal occurs at the lower Peierls transition temperature T_P, where $T_C \approx 4T_P$. Fig. 2-1 shows the undistorted phonon dispersion relation and the softened phonon bands for $T \geq T_P$, as well as dispersion relations for several excitations that will be discussed in the following sections.

The softening of the $Q=2k_F$ phonon is known as the Kohn anomaly, and the concomitant distortions of the ionic lattice and the conduction electronic density are known as the periodic lattice distortion and the charge density wave. The size of the CDW wavevector Q is set by the details of the filling of the electronic bands. It has no intrinsic relation to the lattice spacing. We shall see in Chapter 4 that the relative location in reciprocal space of Q and the Brillouin zone edge is important for understanding the FIR excitations of the system.

Fundamental CDW excitations: the Lee-Rice-Anderson model

The opening of the Peierls gap at the Fermi surface eliminates absorption for electromagnetic radiation with frequency between dc and 2Δ. The oscillator strength within the gap is redistributed among the CDW condensate and states above the gap in a way reminiscent of BCS superconductors.[5] The ac conductivity of a charge density wave coupled to the static $Q=2k_F$ phonon was calculated in the important work of P.A. Lee, T.M. Rice, and P.W. Anderson (LRA).[6] They calculated the phonon propagator for the collective mode and found that the two lowest energy excitations have dispersion relations near the zone center given by

$$\omega_{\mp}^2 = \lambda\omega_Q^2 + \frac{4}{3}\left(\frac{m}{m^*}\right) v_F^2 q^2 \qquad (2\text{-}3)$$

Fig. 2-1 a) Dispersion relation for phonons in a linear one-dimensional crystal. The dashed line represents the Kohn anomaly, a softening of the $Q = 2k_F$ phonon as $T \rightarrow T_P$. [Figure adapted from Ref. 10.]

b) Dispersion relations for the fundamental excitations of the CDW condensate. The acoustic phason and amplitudon are described by P.A. Lee, T.M. Rice, and P.W. Anderson [Ref. 6], and M.J. Rice describes the phase and amplitude phonon modes [Ref. 7].

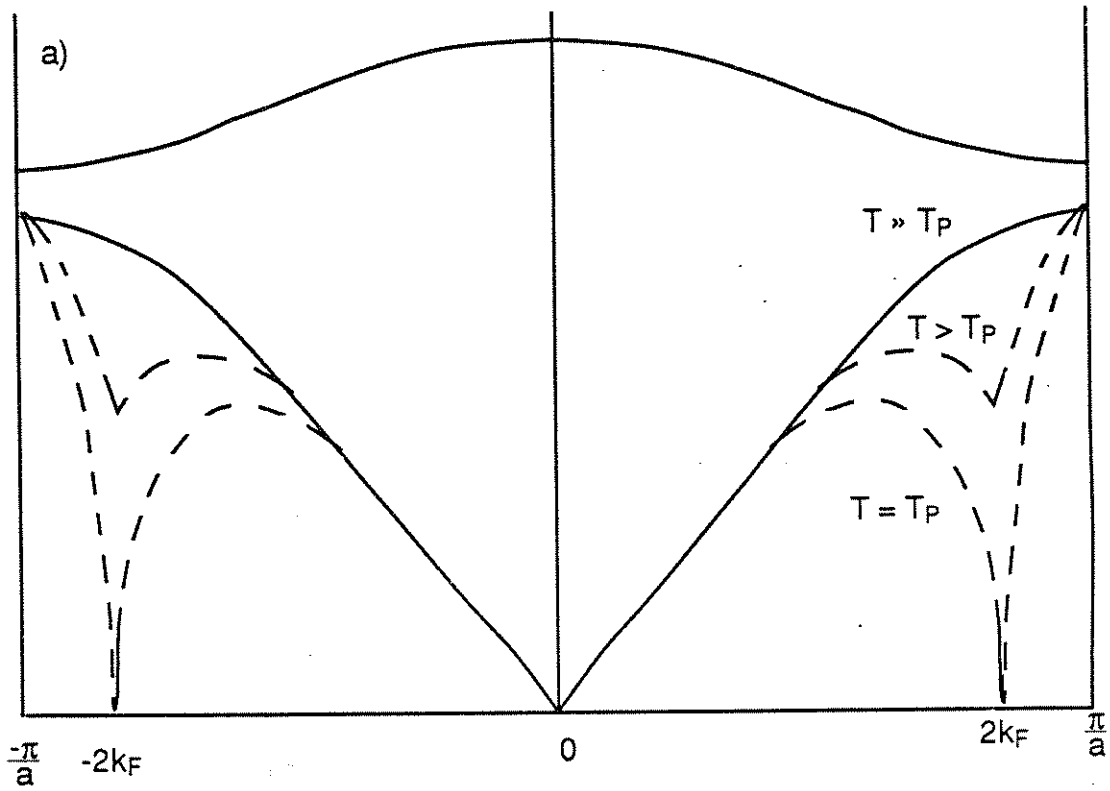
a)
T » TP
T > TP
T = TP
-π/a
-2kF
0
2kF
π/a

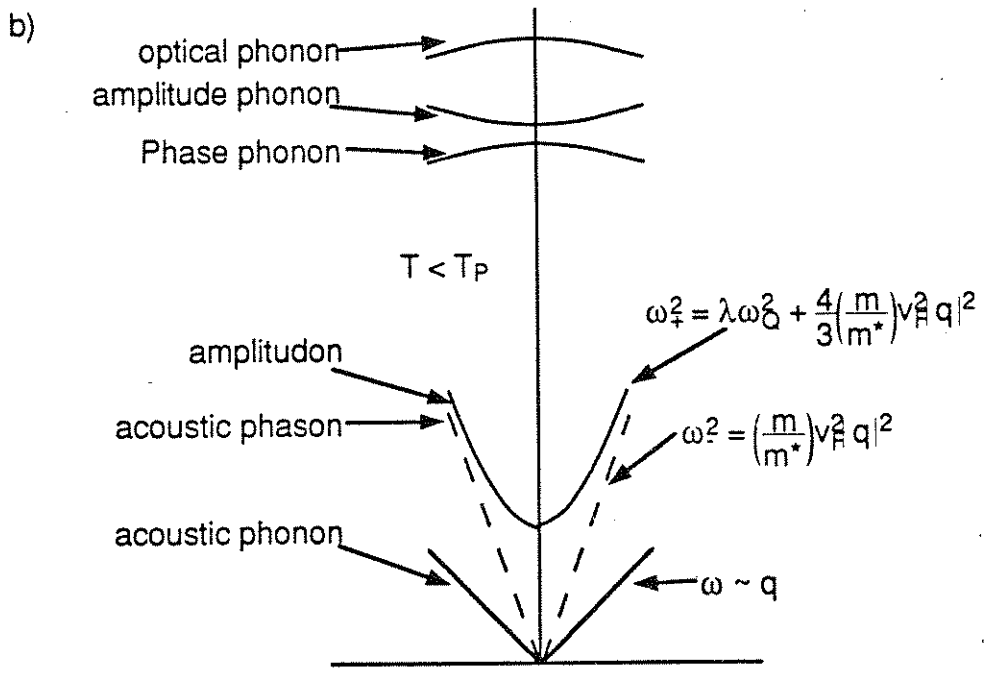
b)
optical phonon
amplitude phonon
Phase phonon
T < TP
$\omega_+^2 = \lambda\omega_Q^2 + \frac{4}{3}\left(\frac{m}{m^*}\right)v_F^2 q^2$
amplitudon
acoustic phason
$\omega_-^2 = \left(\frac{m}{m^*}\right)v_F^2 q^2$
acoustic phonon
ω ~ q

and

$$\omega_-^2 = \left(\frac{m}{m^*}\right) v_F^2 |q|^2 . \qquad (2\text{-}4)$$

The two excitations are known respectively as an amplitudon and an acoustic phason. They represent amplitude and phase fluctuations of the CDW order parameter about its equilibrium value. Fig. 2-1b shows the calculated dispersion for the two modes. The effective mass m* of the CDW (the Fröhlich mass) is a measure of the mass enhancement of the electrons over their usual band mass due to coupling to the ions. A large effective mass slows the response of the collective mode and flattens both branches of the dispersion curve.

The amplitudon is Raman active and it has a higher energy than the acoustic phason. Its excitation spectrum has a gap $\lambda\omega_Q^2$ where $\lambda = \nu g^2/\omega_Q \varepsilon_F$ is the dimensionless electron phonon coupling constant (ν is the number of conduction electrons per atom). Since ω_Q is roughly the Debye frequency (near 50K) and $\lambda \approx 1/3$, the amplitudon frequency is typically in the FIR. The acoustic phason mode corresponds to shifting charge in the CDW relative to the background lattice, so this lower frequency mode is optically active. If the wavelength of the CDW is incommensurate with the lattice spacing and no impurities or crystal defects are present, the acoustic phason mode has zero energy for q=0 translational motion. Impurities or commensurability break the translational invariance of the energy of the CDW and open a pinning gap in the acoustic phason spectrum.

The conductivity of the collective mode is given by[6]

$$\sigma(\omega) = \frac{\omega_p^2}{4\pi i\omega}\left(\frac{f(\omega)}{1 + (\lambda\omega_Q^2/4\Delta^2)f(\omega)} - f(0)\right) \qquad (2\text{-}5)$$

where

$$f(\omega) = \frac{2\Delta^2}{\omega^2 y}\left(\pi i + \ln\frac{1-y}{1+y}\right), f(0) = 1 \tag{2-6}$$

and

$$y = \left(1 - \frac{4\Delta^2}{\omega^2}\right)^{1/2}. \tag{2-7}$$

In these equations, ω_p^2 is the plasma frequency of the non-interacting electrons, and Δ is the single particle Peierls gap. In the absence of electron-phonon coupling, the denominator of the first bracketed term in Eq. (2-5) is unity, and $\sigma(\omega)$ describes an insulator with zero dc conductivity, zero conductivity in the gap $0 \leq \omega < 2\Delta$, and a square root conductivity divergence at $\omega = 2\Delta$. A finite coupling constant establishes the acoustic phason mode and enhances the dc conductivity. The coupling constant λ is related to the Fröhlich mass by

$$\frac{m^*}{m} = 1 + \frac{4\Delta^2}{\lambda\omega_Q^2}. \tag{2-8}$$

For $m^* > m$ but not infinite, a fraction m/m^* of the total oscillator strength appears as a delta function at zero frequency.

Fig. 2-2 shows the conductivity $\sigma(\omega) = \sigma_1(\omega) + i\sigma_2(\omega)$ and the reflectance signature corresponding to Eq. (2-5) for $m^*/m = 715$. In the Figure, the square root edge in σ_1 at 2Δ clearly shows the interband transitions, and the rise in σ_2 as $\omega \rightarrow 0$ is associated with the dc delta function in σ_1. The imaginary part of $\sigma(\omega)$ crosses from a large positive value at dc to negatively diverging values before the gap. The reflectance is unity for frequencies below

Fig. 2-2 a) Complex conductivity $\sigma(\omega)$ of the Lee-Rice-Anderson acoustic-phonon-stabilized CDW condensate, from Eq. (2-5). The gap (Δ) and the frequency of the unsoftened $Q = 2k_F$ phonon are labelled. The zero-crossing of the dielectric function at ω_{LO} corresponds to an infrared reflectance edge. The parameters used in the Figure are appropriate for TaS_3: $\Delta = 8.1 \times 10^{12}$Hz (390K), $m^*/m = 715$, $\omega_Q = 1 \times 10^{12}$Hz (50K), $\omega_p^2/4\pi = 1.8 \times 10^{27}$ ($\approx 1000\sigma_{max}\tau$ from microwave experiments) [Ref. 17, 20].

b) Reflectance for a semi-infinite sample with the Lee-Rice-Anderson conductivity. The experiments discussed in this dissertation span the frequency range indicated at the top of the Figure.

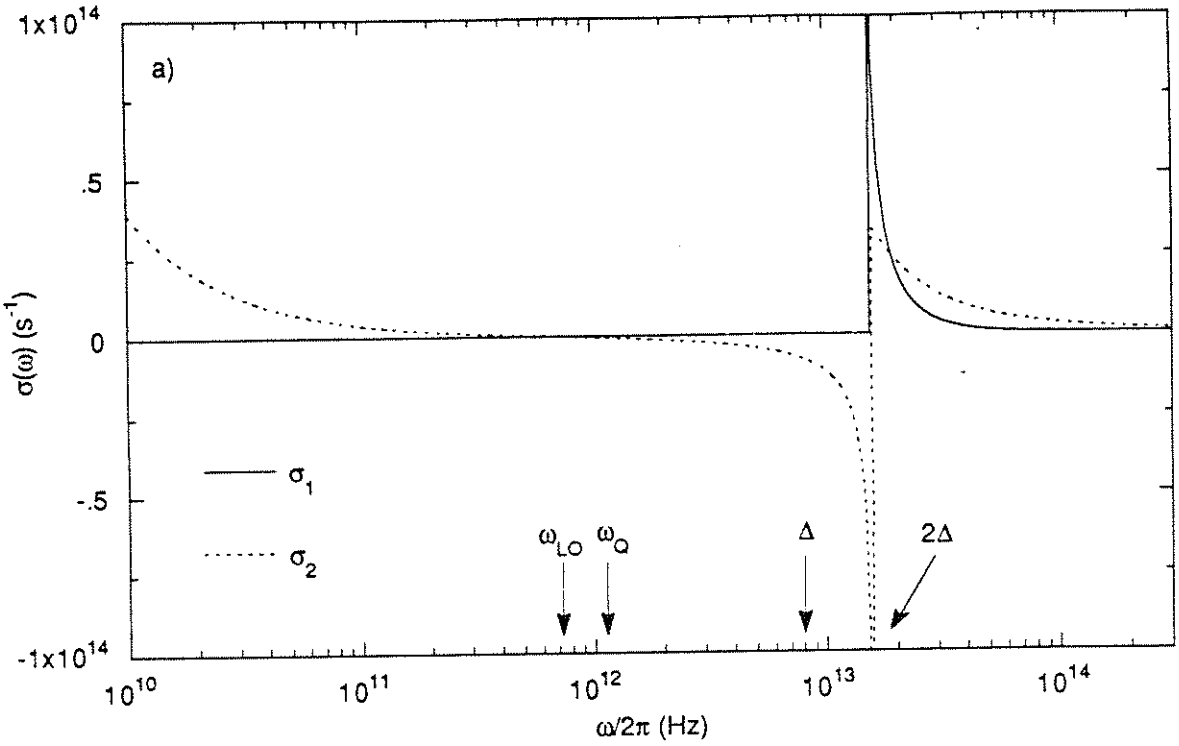
a)
1x10^14
.5
0
-.5
-1x10^14
σ(ω) (s^-1)
σ1
σ2
ωLO
ωQ
Δ
2Δ
10^10
10^11
10^12
10^13
10^14
ω/2π (Hz)

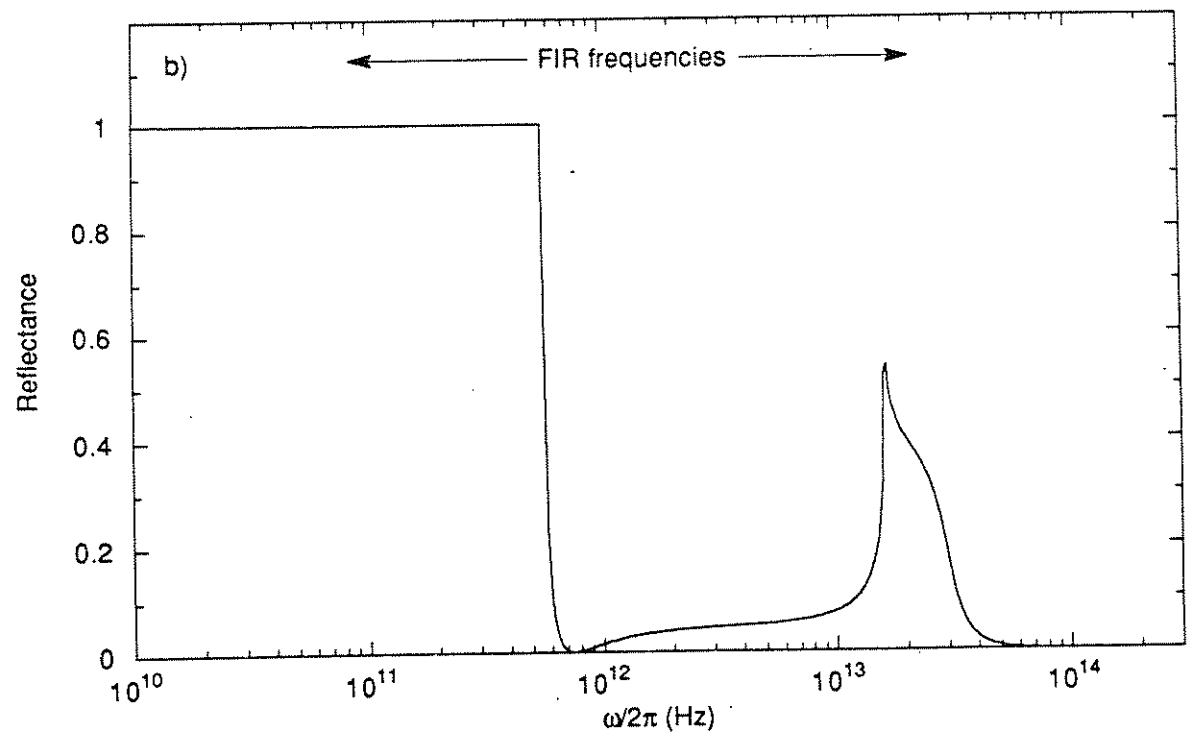
b)
FIR frequencies
1
0.8
0.6
0.4
0.2
0
Reflectance
10^10
10^11
10^12
10^13
10^14
ω/2π (Hz)

$$\omega_{LO} = (1.5\,\lambda)^{1/2}\,\omega_Q \tag{2-9}$$

when the real part of the dielectric function $\varepsilon(\omega)=1+4\pi i\sigma(\omega)/\omega$ crosses zero. The reflectance is very small through most of the FIR frequencies, but it is enhanced starting well below the gap edge due to the large negative σ_2. We note that for spin density wave systems, the Fröhlich mass is equal to the band mass. None of the spectral weight is in the pair-breaking absorption at $\omega = 2\Delta$; all the spectral weight lies in the dc delta function.

Multi-phonon stabilized CDWs: phase phonons

The LRA approach treats the collective mode of condensed electrons coupled to a single acoustic phonon. Some CDW conductors have a rich phonon structure with many optical phonon branches; this is particularly true for the organic compounds like TEA-$(TCNQ)_2$† and TTF-TCNQ††. In addition, these compounds often have a chain of donor or acceptor complexes that establish a static external potential V with the periodicity of the (commensurate) CDW. M.J. Rice calculates[7, 8] the dynamics of a system of electrons coupled not only to the static distortion with $Q=2k_F$ but also to a system of G independent phonon bands. The conductivity of such a system is

$$\sigma(\omega) = \frac{\omega_p^2}{4\pi i\omega}\left(f(\omega) - f(0) - \left(\frac{\omega}{2\Delta}\right)^2 (f(\omega))^2 \lambda\, D_\phi(\omega)\right) \tag{2-11}$$

where

$$D_\phi^{-1}(\omega) = D_0^{-1}(\omega) + 1 - \frac{V}{\Delta} + \frac{\lambda\omega^2 f(\omega)}{4\Delta^2} \tag{2-12}$$

and

---

† Triethyl ammonium tetracyanoquinodimethane

†† Tetrathiafulvalene tetracyanoquinodimethane

$$D_0(\omega) = -\sum_{n=1}^{G} \frac{\lambda_n}{\lambda}\left(\frac{\omega_{nQ}^2}{\omega_{nQ}^2 - \omega^2 - i\omega\Gamma_n}\right). \qquad (2\text{-}13)$$

In these equations, $f(\omega)$ is defined by Eq. (2-6), ω_{nQ} is the frequency of the n^{th} phonon band at $Q=2k_F$, and $1/\Gamma_n$ is the natural width of the n^{th} phonon band. V is the contribution of the external static potential to the total gap Δ. Phase fluctuations corresponding to each of the G modes also contribute to Δ, and $\Delta = V + \Sigma_n\Delta_n$. Each mode has a coupling constant λ_n, and $\lambda = \Sigma_n\lambda_n$. Peaks in the conductivity occur at the poles of $D_\phi(\omega)$. These in turn occur at frequencies slightly below the poles associated with each phonon branch in $D_0(\omega)$, and the frequency shift is due to the additional terms including V/Δ in Eq. (2-12). The factor V/Δ roughly measures the degree of stabilization of the CDW provided by the optical phonons: a small V/Δ indicates that the CDW is stabilized almost entirely by the many optical phonons. The gap can persist even in the limit of V=0, with no $Q = 2k_F$ external static distortion, and this is called many-phonon stabilization of the CDW. Typically, $V/\Delta \sim 0.1$ for organic conductors and for $K_{0.3}MoO_3$,[8, 9] and $V/\Delta = 0$ for TaS_3 and $NbSe_3$.[10]

Each phonon branch has an associated resonance due to a combined distortion of the lattice and the CDW phase about their equilibrium values. The oscillator strength of such resonances can be quite large because of the partially electronic rather than purely ionic character. Perhaps more importantly, though the phonon itself may not be optically active, the collective mode associated with the phonon *will be* optically active for light polarized along the CDW wavevector. Thus, a variety of these "phase phonons" will be present in reflectance measurements with light polarized parallel to the long axis of a sample but absent in cross-polarized measurements.

Figure 2-3 depicts the conductivity and reflectance signature for a CDW system with a phase phonon at a frequency on either side of the single-particle excitation gap. The conductivity is given by Eq. (2-11). The phase phonon for $\omega < 2\Delta$ has a lifetime limited only by the longevity of the unscreened phonon. The conductivity peak is narrow and the associated reflectance is a very sharp phonon-like resonance. In contrast, the phase phonon above the gap decays by the creation of electron-hole pairs so the associated reflectance feature is much broader. These high-frequency phase phonons cause a *dip* rather than a peak in the background conductivity due to single-particle absorption. This is a Fano interference effect.[11-14] The crossover from narrow to broad reflectance features has been used to identify the value of 2Δ in $NbSe_3$, a CDW material with an incompletely gapped Fermi surface and metallic conduction even below T_P.[10, 15]

Pinned mode: the single particle rigid oscillator model

Real CDW crystals show nonlinear conduction, but not at zero field. Similarly, the linear ac conductivity is enhanced, but not at zero frequency. The presence of pinning by impurities or commensurability or even the finite lifetime of the acoustic phonon always opens a pinning gap and the oscillator strength in the dc delta function moves to finite frequencies. The magnitude of the pinning gap (or pinning frequency ω_0) depends on the source of pinning. For nominally pure inorganic CDW conductors, ω_0 is typically about 20GHz. For $w \ll \Delta$, the dielectric function becomes[6, 7]

$$\varepsilon(\omega) = 1 + \frac{\omega_p^2}{6\Delta^2} + \left(\frac{m^*}{m}\right)\frac{\omega_p^2}{\omega_0^2 - \omega^2}. \qquad (2\text{-}14)$$

Fig. 2-3 a) Complex conductivity $\sigma(\omega)$ for a many-phonon-stabilized CDW described by M.J. Rice [Ref. 7], from Eq. (2-11). The gap, total oscillator strength and effective pinned mode mass are the same as those in Fig. 2-2, and V=0. A phonon with frequency $\omega_{pin} = 1x10^{12}$Hz simulates the pinned acoustic phason mode. It has damping frequency $\Gamma_{pin} = 1.25x10^{11}$Hz, and coupling constant $\lambda_{pin} = .31$. Two higher frequency optical phonons flank the gap, with $\omega_1 = 1.35x10^{13}$ and $\omega_2 = 2.1x10^{13}$. The latter two modes each have $\Gamma = 3x10^{10}$Hz and $\lambda = .017$.

b) Reflectance for the many-phonon-stabilized CDW. Phase phonons appearing below the gap have a linewidth limited by the bare phonon lifetime, but phase phonons above the gap are severely damped by decay into electron-hole pairs.

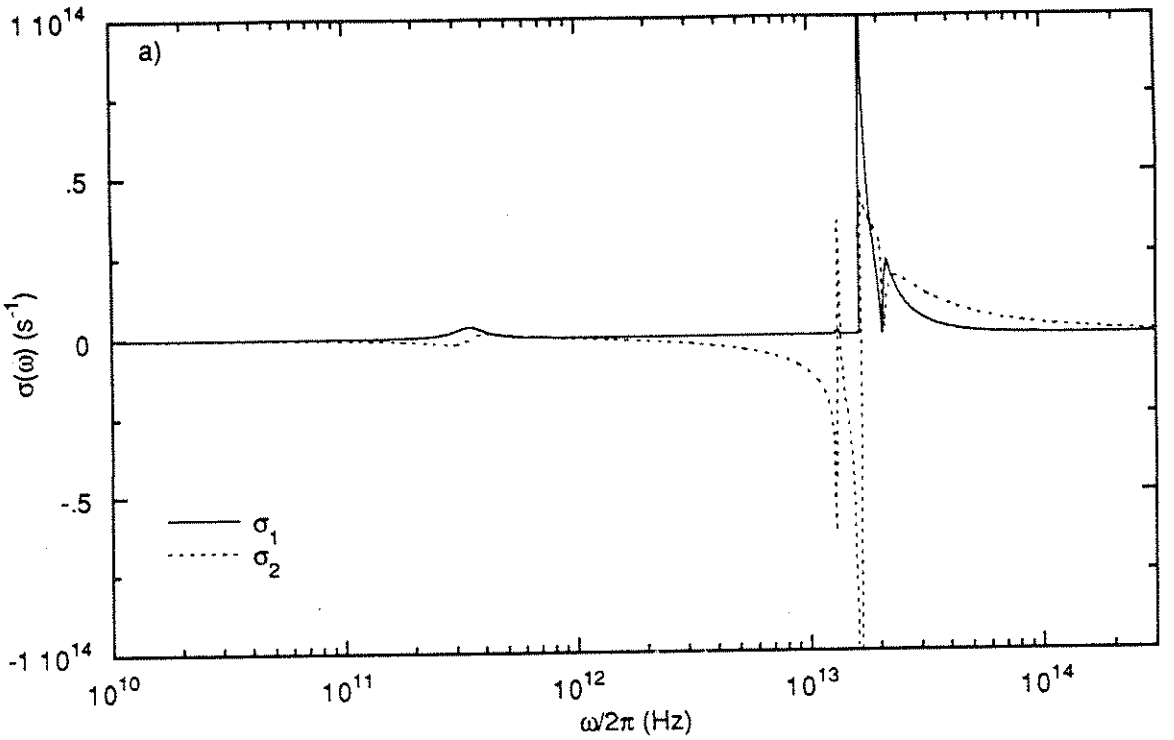
a)
1 10^14
.5
0
-.5
-1 10^14
σ(ω) (s^-1)
σ1
σ2
10^10
10^11
10^12
10^13
10^14
ω/2π (Hz)

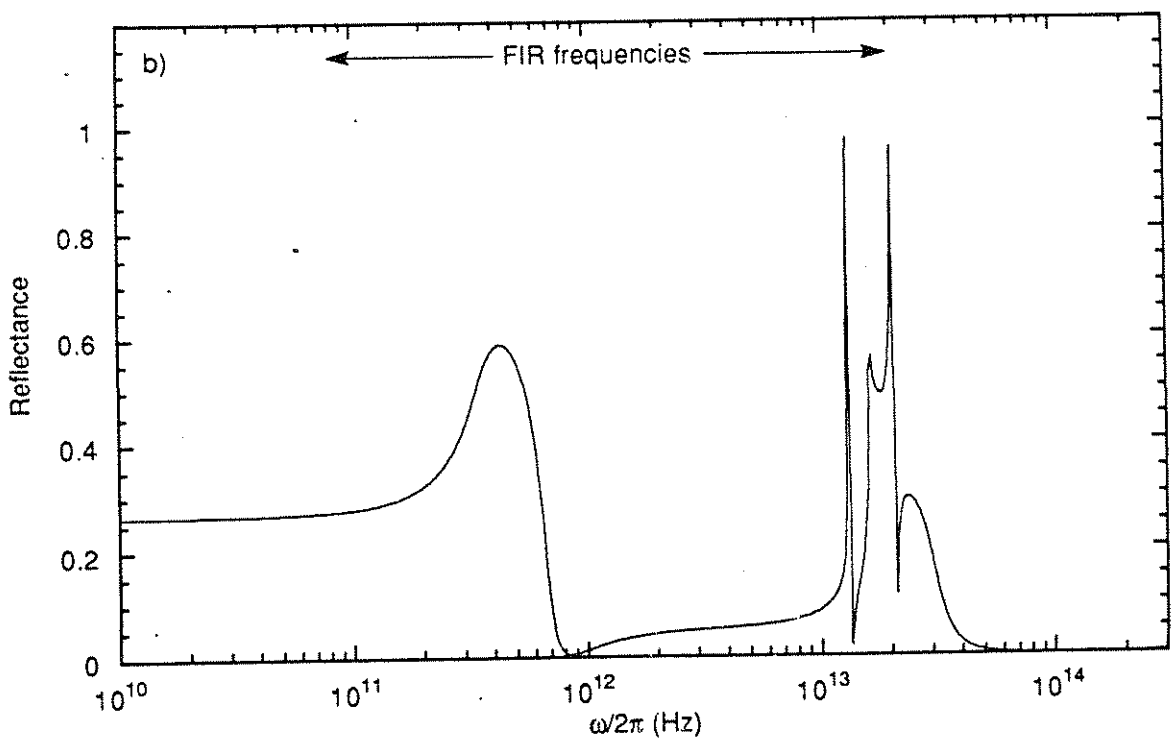
b)
FIR frequencies
1
0.8
0.6
0.4
0.2
0
Reflectance
10^10
10^11
10^12
10^13
10^14
ω/2π (Hz)

At zero frequency, the conductivity is zero but the dielectric constant is very large. The form of $\varepsilon(\omega)$ is identical to that of a polariton, and the reflectance has a *restrahl* resonance at the pinning frequency. Again, the pinned mode is the acoustic phason. It corresponds to $q = 0$ excitations of the phase of the CDW; in a simple picture, it is the sloshing of the entire CDW within a periodic pinning potential.

The simplest phenomenological model describing the dynamics of the pinned mode is the single particle classical model of Grüner *et al.*[16] The CDW is described as a single object comprised of n condensed electrons per unit volume with with no internal degrees of freedom. It has mass m^* and charge density ne. The equation of motion is

$$\frac{d^2x}{dt^2} + \frac{1}{\tau}\frac{dx}{dt} + \frac{\omega_0^2}{Q}\sin(Qx) = \frac{neE}{m^*}, \tag{2-15}$$

where x is the center of mass coordinate of the CDW relative to some origin, E is the applied electric field, and $1/\tau$ is a phenomenological damping constant. Q is the periodicity of the CDW and consequently the periodicity of the pinning potential. The pinning frequency ω_0 is related to the restoring pinning force k by $\omega_0^2 = k/m^*$. Assuming harmonic time dependence, the ac conductivity is given by

$$\sigma(\omega) = \left(\frac{ne^2\tau}{m^*}\right)\left(\frac{i\omega}{i\omega - (w_0^2 - \omega^2)\tau}\right). \tag{2-16}$$

The low and high frequency limits of this expression are

$$\sigma(\omega) = \left(\frac{ne^2\tau}{m^*}\right)\left(\frac{i\omega}{i\omega - \omega_0^2\tau}\right) \tag{2-17}$$

and

$$\sigma(\omega) = \left(\frac{ne^2\tau}{m^*}\right)\left(\frac{1}{1 - i\omega\tau}\right). \qquad (2\text{-}18)$$

Eq. (2-17) is the relaxational limit ($\omega \ll \omega_0$) and Eq. (2-18) is the inertial, or Drude limit ($\omega \gg \omega_0$). For an overdamped oscillator, $\omega_0\tau \ll 1$ and the two regimes are well separated in frequency.

In a subsequent section we will examine the measured conductivity in the relaxational frequency regime and see that the conductivity significantly exceeds that predicted by Eq. (2-17). At millimeter and microwave frequencies, though, and at temperatures not too far below the Peierls transition, Eqs. (2-16) and (2-18) fits the data quite well. Figs. 2-4a and 2-4b show the conductivity for the single particle rigid oscillator fit to measured microwave conductivity points for TaS_3 and $(TaSe_4)_2I$.[17, 18] The pinned acoustic phason in TaS_3 has an overdamped resonance and an extremely broad peak in the conductivity (the frequency scale in the Figure is logarithmic). $NbSe_3$ and $K_{0.3}MoO_3$ also have overdamped pinning resonances.[19-21] In $(TaSe_4)_2I$, the resonance is underdamped, as it is in $(NbSe_4)_2I$.[22] Figure 2-4c shows the different reflectance signatures for the two cases.

The fit of the rigid oscillator model to measurements like those shown in Fig 2-4 is important because it quantifies the important parameters m^*, ω_0, and τ that characterize the CDW condensate and its interaction with impurities and normal electrons. For most materials, the crossover frequency $\omega_{co} = \omega_0^2\tau$ can be determined from straightforward RF measurements: it is the frequency where $\sigma_1(\omega)$ reaches half its maximum value and $\sigma_2(\omega)$ has a minimum. From more difficult microwave measurements, the full shape of the $\sigma(\omega)$ curve can be determined. The imaginary part of the conductivity crosses zero at the pinning frequency ω_0. At this frequency, the conductivity

Fig. 2-4 a) Rigid oscillator model fit to the microwave conductivity for TaS_3 at 160K [Ref. 20]. The conductivity shown here is an overdamped response. The measured values stray from the model fit below $\omega_0 = 4.3$GHz.

b) Rigid oscillator model fit to the microwave conductivity of $(TaSe_4)_2I$ at 150K [Ref. 18] The response is characteristic of an underdamped oscillator.

c) Reflectance for ideal samples of TaS_3 and $(TaSe_4)_2I$, calculated from the microwave conductivity using $\varepsilon_\infty = 1$.

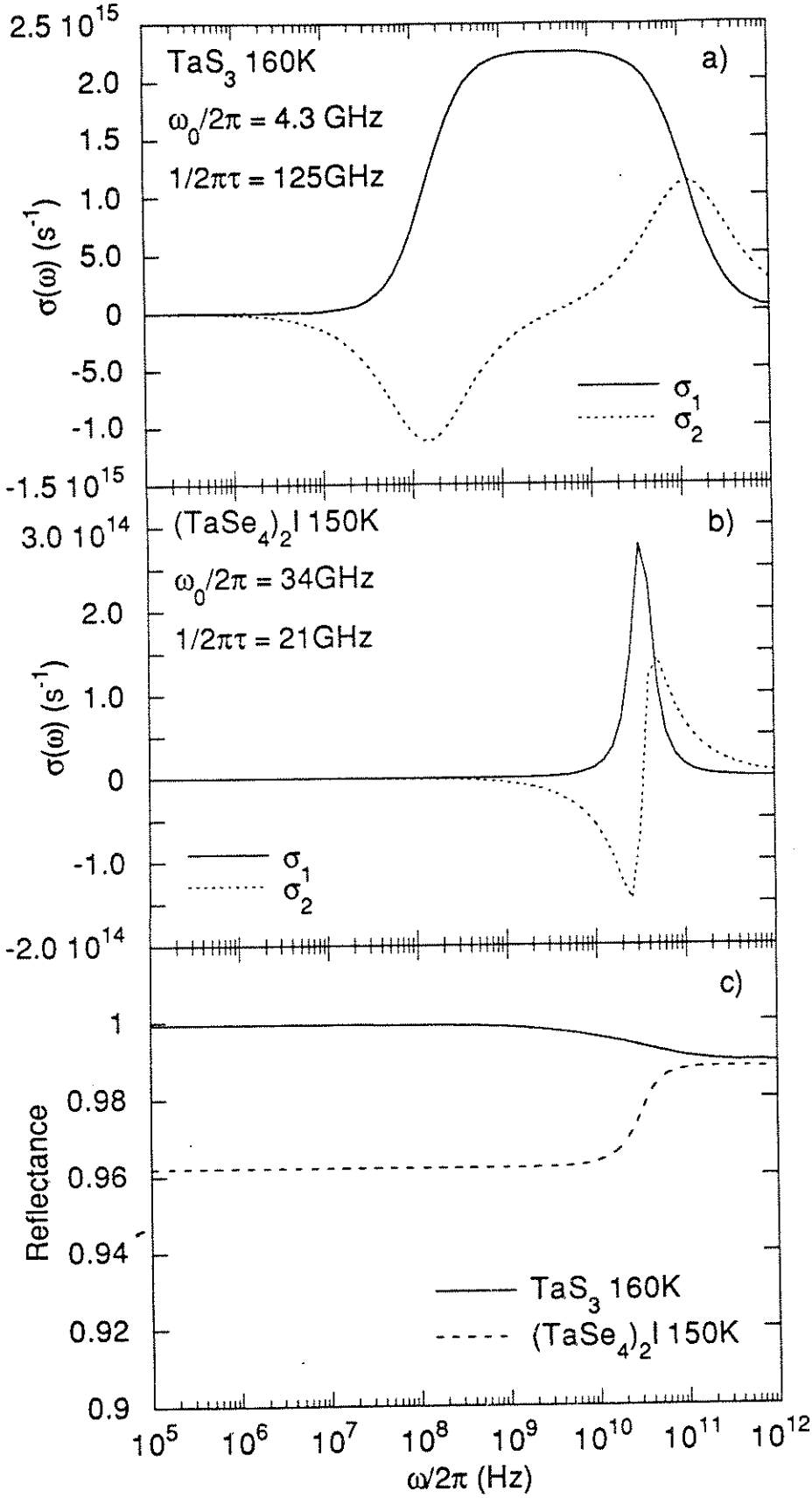
TaS3 160K
ω0/2π = 4.3 GHz
1/2πτ = 125GHz
a)
σ1
σ2
σ(ω) (s-1)
(TaSe4)2I 150K
ω0/2π = 34GHz
1/2πτ = 21GHz
b)
c)
Reflectance
TaS3 160K
(TaSe4)2I 150K
ω/2π (Hz)

has a maximum $\sigma_{max} = ne^2\tau/m^*$. With an estimate of n from a band filling argument using the measured crystal lattice size, all the parameters m^*, ω_0, and τ can then be evaluated. We will now consider each of these parameters and their significance within more detailed models of CDW conductivity.

The Fröhlich effective mass m^* is related to the parameters of the microscopic LRA theory by Eq. (2-8). Neutron scattering and dc resistance measurements determine the gap $\Delta = 1.74\ k_B T_C$ and the unsoftened phonon frequency ω_Q, and the coupling constant $\lambda = -1/\ln(\Delta/\varepsilon_F)$ can be estimated from a tight-binding model. For most materials, the estimate of m^* from these static quantities using Eq. (2-8) agrees well with the mass determined from the fit to the rigid oscillator model.[20] Moreover, both the effective mass and the number density of condensed electrons should vary as $\Delta^2(T)$, and the ac conductivity experiments show m^*/n is constant in temperature except near T_P. These results constitute an important support for the LRA theory.

The pinning frequency ω_0 is set by the interaction of the CDW with impurities, grain boundaries, a commensurate atomic lattice, electrical contacts, the sample surface, or other entities that destroy the translational invariance of the energy of the CDW. The standard Fukuyama-Lee-Rice model[23-27] of pinning describes internal variations of the phase ϕ of the CDW with a Hamiltonian

$$H = \frac{\kappa}{2}\int |\nabla\phi|^2 d^3r + V_0\rho_1\sum_i \cos[2k_F r_i + \phi(r_i)] + \frac{1}{2k_F}\int e\,\rho\,\phi\,E\,dr\,. \qquad (2\text{-}19)$$

In this equation κ is the elastic constant for deformations of the CDW, V_0 is the impurity potential, ρ_1 is the average charge density, r_i are the positions of individual impurities (with overall concentration n_i), ρ is the local charge density, and E is the applied electric field. The first term is minimized when

the CDW has only long wavelength deformations of its phase, and the second term is minimized by severely distorting the CDW phase at each impurity site to drive the cosine term to zero. This competition between elastic energy and potential energy determines the behavior of the CDW under the influence of impurities. When the ratio $\alpha = 2\pi V_0 \rho_1 / V_F n_i$ greatly exceeds unity, the CDW is strongly pinned and the pinning frequency is given by[26, 27]

$$\omega_0 = \left(\frac{m}{m^*}\right)^{1/2} V_F n_i \, . \tag{2-20}$$

In this limit, the CDW phase is firmly pinned at each impurity. When $\alpha \ll 1$, the CDW phase adjusts gradually within a phase-coherence domain of dimension $L_0 = (3\alpha/\pi)^{-2/3} n_i^{-1}$. The domain is much larger than the average distance between impurities. The CDW is said to be weakly pinned and[26, 27]

$$\omega_0 = \left(\frac{3}{\pi^2}\right)^{2/3} \left(\frac{m}{m^*}\right)^{1/2} V_F L_0^{-1} \, . \tag{2-21}$$

In either limit, the pinning frequency is predicted to increase with increasing impurity concentration, and measurements of the millimeter-wave and microwave response of TaS_3 doped with Nb impurities confirm that expectation.[28] Though the character of the pinning can in principle be determined from the measured magnitude of ω_0, the impurity concentration is not known accurately enough to distinguish between the two pinning regimes. The pinning frequency varies[28] with Nb concentration x as $\omega_0 = \omega_0(\text{pure}) + Bx$, with $B \approx 500\text{GHz/at.\%}$. This indicates that the pinning in nominally pure specimens is not due to residual substitutional impurities, but to commensurability or other effects.

The damping time τ is set by the interaction of the CDW with impurities, uncondensed normal electrons, phonons, and phasons. The fit[17,

[28] to the single oscillator model shows τ is only weakly temperature dependent, with

$$\frac{1}{2\pi\tau} = A + BT^n, n \approx 1 \tag{2-22}$$

The weak temperature dependence of τ is surprising because the phonon and uncondensed electron interactions should vary sharply with temperature and disappear as $T \rightarrow 0$. A theory of scattering of the CDW by phasons predicts[29]

$$\frac{1}{2\pi\tau} = \frac{\pi^3}{64\sqrt{2}}\left(\frac{2m_b\lambda^2}{m^*\omega_Q}\right)T^2 \tag{2-23}$$

This theory yields estimates for $1/2\pi\tau$ much smaller than the measured values, but the temperature dependence it predicts for τ may be consistent with the measured trend since the value of n in Eq. (2-22) is not firmly determined.

The rigid pinned oscillator model defined by Eq. (2-15) gives a good general picture of the high frequency ac conductivity of CDW materials, but the predicted conductivity $\sigma(\omega)$ fails to fit the measured conductivity in detail at low frequencies. The description also fails at very low temperatures, temperatures near the Peierls transition, and at high impurity concentrations. In a similar way, the model succeeds in describing the general features of nonlinear (depinned) charge density wave conductivity, including the threshold field, narrow-band noise, and harmonic mode locking. It cannot account, though, for the metastable effects seen in CDW materials, for broad band noise, or for switching phenomena. Clearly, charge density waves are not completely rigid, and their internal degrees of freedom are important in some aspects of CDW conduction. The elastic-CDW model of Fukuyama, Lee, and Rice has been discussed above (Eqs. (2-19ff)), and several other models of

CDW dynamics exist.[30-33] We will now discuss the ac conductivity at very low frequencies, where the relaxation of short wavelength internal distortions of the CDW greatly enhances the conductivity.

Dielectric relaxation

The simple rigid damped oscillator model describes $\sigma(\omega)$ fairly well for most materials at temperatures not too far below the Peierls transition and for frequencies near the pinning resonance. At audio and low RF frequencies, however, the internal degrees of freedom of the CDW become important, and the measured conductivity greatly exceeds that predicted by rigid oscillator model. This phenomenon, known as dielectric relaxation, is ubiquitous in insulating CDW conductors. Dielectric relaxation is now considered to be a collective CDW response separate from the pinned acoustic phason mode, but this distinction was not immediately recognized. The first discussion of the phenomena followed measurement[34] of a relatively small conductivity resonance near 100kHz in $K_{0.3}MoO_3$. The experiment occurred well before FIR measurements[35] showed the existence of a strong mode in the material near $3cm^{-1}$, and the audio/RF resonance was taken to be the pinned acoustic phason. The rigid single oscillator model fit the measured $\sigma(\omega)$ rather poorly though, and these results were seen as a critique of the rigid oscillator model rather than as a supplement to it. Though subsequent work by Cava *et al.*[36-38] and by Wu *et al.*[39, 40] clarified the situation, we shall see that the exact form of the lowest frequency conductivity remains controversial.

The rigid oscillator CDW conductivity given by Eqs. (2-16) is equivalent to the dielectric function derived by Debye[41] for a system with a single degree of freedom and a single characteristic relaxation time τ_0:

$$\varepsilon(\omega) = \varepsilon_{HF} + \frac{(\varepsilon_0 - \varepsilon_{HF})}{(1 - i\omega\tau_0)}, \tag{2-24}$$

where ε_0 is the dc dielectric constant and ε_{HF} is the dielectric constant for frequencies much greater than the relaxation rate $1/\tau_0$.† The relaxation time τ_0 in Eq. (2-24) is related to the damping time τ in Eq. (2-16) by $\tau_0^{-1} = \omega_{co} = \omega_0^2\tau$. For a system with a single relaxation process but a non-symmetrical distribution of relaxation times about a mean time τ_0, $\varepsilon(\omega)$ becomes

$$\varepsilon(\omega) = \varepsilon_{HF} + \frac{(\varepsilon_0 - \varepsilon_{HF})}{(1 + (-i\omega\tau_0)^{1-\alpha})^{\beta}} \tag{2-25}$$

where α and β characterize the width and skewness of the distribution. Cava *et al.*[34, 36-38] have applied this formula extensively in their analysis of the low-frequency dynamics of CDW systems; it was originally derived as a description of the dispersion in organic polymers.[42] On a Cole-Cole (ε_1 vs. ε_2) plot, the dielectric function given by Eq. (2-25) is a skewed semicircle.

Figure 2-5 shows the conductivity and reflectance signatures for the distributed relaxation process corresponding to Eq. (2-25) and for the rigid oscillator where $\alpha = 0$ and $\beta = 1$. The rigid oscillator model predicts that for $\omega \rightarrow 0$, $\mathrm{Re}\sigma \sim \omega^2$ and $\mathrm{Im}\sigma \sim \omega$. The Figure also shows the conductivity given by

$$\sigma(\omega) = \sigma_{\infty}\frac{(-i\omega\tau)^{\gamma}}{1 + (-i\omega\tau)^{\gamma}}, \gamma < 1\,. \tag{2-26}$$

---

† Cava *et al.*[29] give this formula as $\varepsilon(\omega) = \varepsilon_{HF} + \frac{(\varepsilon_0 - \varepsilon_{HF})}{(1 - i\omega\tau_0)}$ and define $\varepsilon = \varepsilon_1 - i\varepsilon_2$; other authors use a different convention.[37] Throughout this dissertation, we will use $\varepsilon = \varepsilon_1 + i\varepsilon_2$, $\sigma = \sigma_1 + i\sigma_2$, $\varepsilon(\omega) = \varepsilon 0 + 4\pi i\sigma/\omega$, and we will assume the time dependence of oscillating quantities varies as $e^{-i\omega t}$. All equations from the literature have be adapted to this convention.

Fig. 2-5 a) σ_1 and $-\sigma_2$ for the single particle rigid oscillator model and the model conductivities for dielectric relaxation proposed by *Cava et al.* [Refs. 34, 36-38] and *Wu et al.* [Refs. 39,40, and 43].

b) Reflectance in the dielectric relaxation frequency range for the various models, plotted on an extremely expanded scale. For the purpose of extrapolation of reflectance values to dc for use with Kramers-Kronig techniques, the models are equivalent.

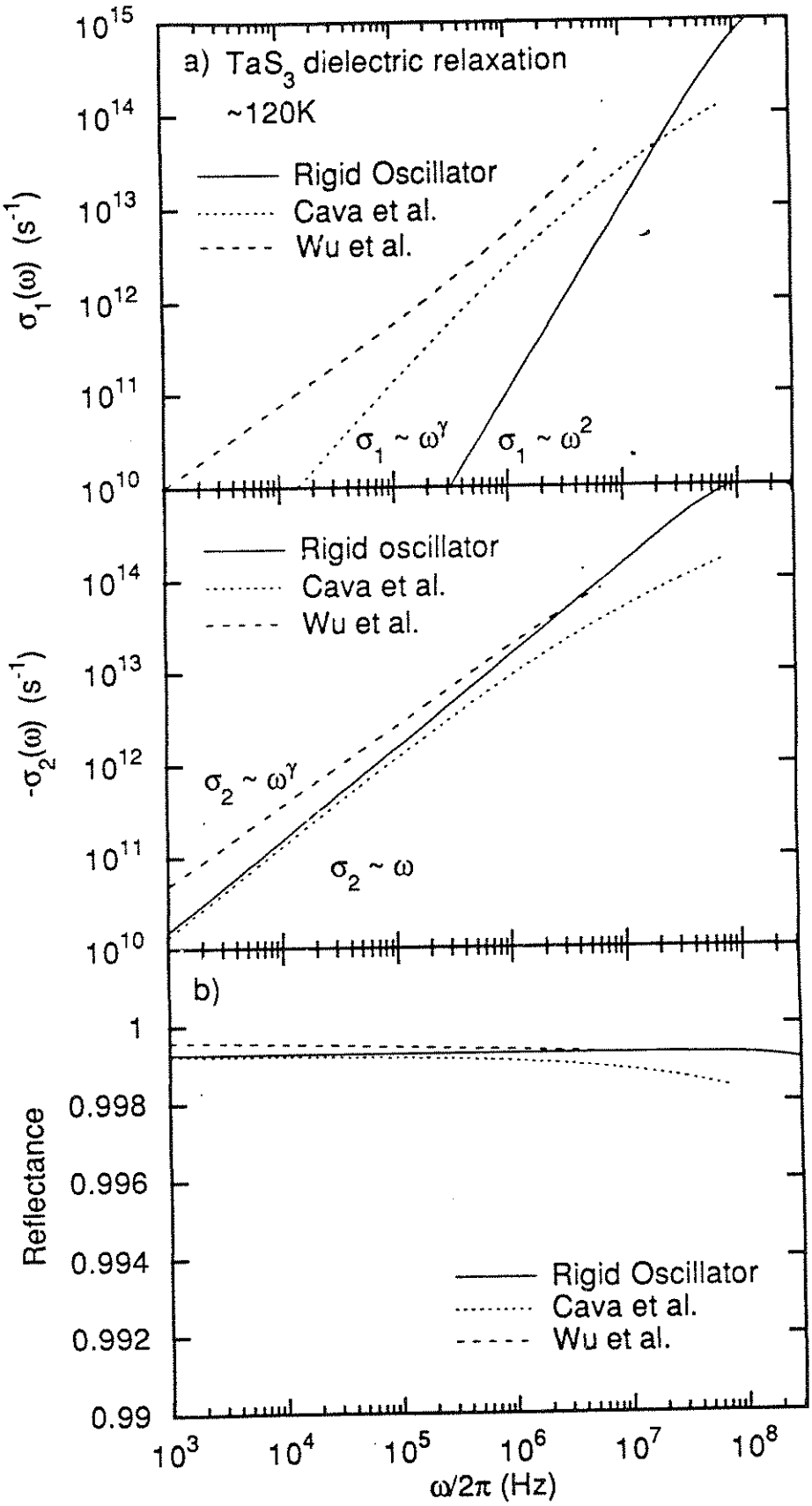
a) TaS_3 dielectric relaxation
~120K
Rigid Oscillator
Cava et al.
Wu et al.
$\sigma_1(\omega)$ (s^{-1})
$\sigma_1 \sim \omega^\gamma$
$\sigma_1 \sim \omega^2$
Rigid oscillator
Cava et al.
Wu et al.
$-\sigma_2(\omega)$ (s^{-1})
$\sigma_2 \sim \omega^\gamma$
$\sigma_2 \sim \omega$
b)
Reflectance
Rigid Oscillator
Cava et al.
Wu et al.
$\omega/2\pi$ (Hz)

Eq. (2-26) has been used by Wu *et al.*[39, 40, 43] to fit the measured conductivity of various CDW materials. Like Eq. (2-25), it is indicative of a distribution of relaxation times, though it predicts a different low frequency dependence for $\sigma(\omega)$. Fig. 2-5b shows that the choice of a model for the low frequency $\sigma(\omega)$ has almost no bearing on the reflectance and will not affect Kramers-Kronig calculations of the FIR conductivity. We will now discuss separately the parameter values obtained for various materials within these two phenomenological descriptions for distributed relaxation, and then consider explanations for the very different low frequency conductivities measured by the two groups.

The parameters α, β, ε_0, ε_{HF}, and τ_0 in Eq. (2-25) have quite different values and temperature dependences for different materials. For $K_{0.3}MoO_3$, the distribution of relaxation times (described by α) becomes broader with decreasing temperature, but the symmetry of the distribution (described by β) becomes less skewed. The high frequency dielectric constant ε_{HF} is small, and this led to the original claim that the oscillator strength for the pinned mode was contained within what is now known as the dielectric relaxation. (Higher frequency relaxation was attributed to an ionic relaxation process.)[34] Both the mean relaxation time τ_0 and the low frequency dielectric constant ε_0 have Arrhenius behavior, but with different activation energies. Neither activation energy matches the Peierls gap value as determined by dc resistance measurements.

Doping the $K_{0.3}MoO_3$ crystals with tungsten substantially decreases both τ_0 and ε_0. For increasing impurity concentration, the two parameters fall much more rapidly than the threshold field for nonlinear conductivity increases. The temperature dependence of the two parameters is quite

different: τ_0 remains activated, but with two distinct activation energies at different temperatures, and ε_0 becomes very nearly temperature independent.

In TaS_3, the most striking feature is the complete disappearance of the dielectric relaxation oscillator strength ($\varepsilon_0 - \varepsilon_{HF}$) at temperatures below 75K.[36] The value of ε_{HF} remains high at low temperature, indicating the presence of the strong pinned mode at higher frequencies. The authors speculate that the disappearance of the relaxation is associated with a possible locking of the incommensurate CDW into commensuration with the crystal lattice that may occur near 80K.[44] Within this picture, the current in the relaxation mode is carried by CDW phase discommensurations, and the density of discommensurations falls dramatically as the temperature falls.

In $(TaSe_4)_2I$, the static dielectric constant ε_0 is relatively small. The mean relaxation time τ_0 is several orders of magnitude longer than those found for the other materials, and it has an activated behavior with the same activation energy as the Peierls gap. This connection between the dynamic behavior embodied in τ_0 and the CDW order parameter may indicate that dielectric relaxation involves normal carrier conversion in the bulk of the sample.[38]

Equation (2-26) represents an alternate approach to fitting the low frequency conductivity of CDW materials.[39, 40, 43] As $\omega \rightarrow 0$, it predicts that $\sigma(\omega) \rightarrow A\,(i\omega)^{\gamma}$. In this limit, Re$\sigma$ and Imσ have the same frequency dependence; similar behavior has been seen in glassy systems. Monte Carlo simulations of the dynamics of CDW's with random pinning give a similar form for $\sigma(\omega)$, though with a smaller exponent.[45] The dielectric constant diverges as $\varepsilon(\omega) \sim \omega^{\alpha-1}$ rather than saturating at low frequencies. The parameter γ is between 0.9 and 1.0 for TaS_3, $NbSe_3$, and $(TaSe_4)_2I$, and it is only weakly temperature dependent.

The fit of the data of Wu *et al.*[39, 40, 43] to Eq. (2-26) is equally as convincing as the fit of the data of Cava *et al.*[34, 36-40] to Eq. (2-25). Both groups have suggested that that the discrepancies in the measurements may be due to the use by the opposite group of too large an ac excitation field. The response of the CDW is inherently nonlinear and in principle it must be measured with a vanishingly small probe field. In addition, it has been suggested[40] that differences in the apparatus and signal processing techniques may contribute to the different forms of $\sigma(\omega)$ found in these studies. The significance of these results, however, is not in the determination of a specific functional form for $\sigma(\omega)$: both Eqs. (2-25) and (2-26) are after all phenomenological fits with parameters unrelated to a particular microscopic theory. Rather, the results are important because they clarify that the loss mechanism at audio and rf frequencies is distinct from the pinned acoustic phason resonance at microwave or infrared frequencies. Littlewood[46] shows that the dielectric relaxation is related to normal carrier screening of internal fields in the CDW excited as longitudinal modes, and that the microwave pinned mode is a transverse mode of the CDW and is much more weakly damped.

An unexpected giant FIR mode

We have seen that the well-understood contributions of the CDW condensate to the ac conductivity are excitations of single-particles across the Peierls gap, the strong response of the pinned acoustic phason resonance (and additional phase phonon resonances for materials with optical phonon branches), and a low frequency relaxational response. A recent far infrared study[4, 47] has raised the possibility that an additional, extremely large contribution to the ac conductivity may lie in the far infrared frequency

regime. Figures 2-2 and 2-3 show that the main features predicted in the FIR by the accepted theories of CDW conduction are a reflectance edge corresponding to the zero crossing of the dielectric function from the pinned mode and a rise in reflectance below the gap. These figures should be compared to Fig. 2-6, which shows the measured FIR reflectance for the CDW conductor $(TaSe_4)_2I$ and the associated conductivity. An extremely large mode at $38cm^{-1}$ in $(TaSe_4)_2I$ dwarfs the pinned acoustic phason mode. A review[4] of previous measurements[35, 48] in $K_{0.3}MoO_3$ suggests that this material may have a giant FIR mode as well. Part I of this dissertation is a detailed investigation of the giant FIR mode in impurity doped $(TaSe_4)_2I$ (Chapter 5) and in TaS_3 (Chapter 4), a CDW material with a less complicated crystal structure. Before we proceed to the experiments and the related discussions of the source of the FIR mode, we will conclude this chapter by briefly introducing the structure and electronic properties of the specific materials to be studied.

Structure of CDW conductors

A. TaS_3

Long fibrous crystals of TaS_3 are grown by vapor transport of elemental tantalum and sulfur within sealed tubes in a gradient furnace. On a microscopic level, the material is composed of long chains of evenly spaced tantalum atoms. Each metal atom is separated from the subsequent one by a triangle of S atoms so that the unit cell along the chain direction contains a $[TaS_6]$ trigonal bipyramid. Interchain Ta-S bonds are substantially weaker than intrachain Ta-S bonds. Figure 2-7a shows the chains of trigonal pyramids. The structure is reminiscent of that in $NbSe_3$, through Ta is more electropositive than Nb, and S more electronegative than Se. This

Fig. 2-6 a) Measured reflectance for $(TaSe_4)_2I$ at 10K [Ref. 47]. The rise in reflectance at $38cm^{-1}$ and the reflectance edge near $100cm^{-1}$ are the signatures of a huge conductivity resonance.

b) Conductivity fit to the measured reflectance.

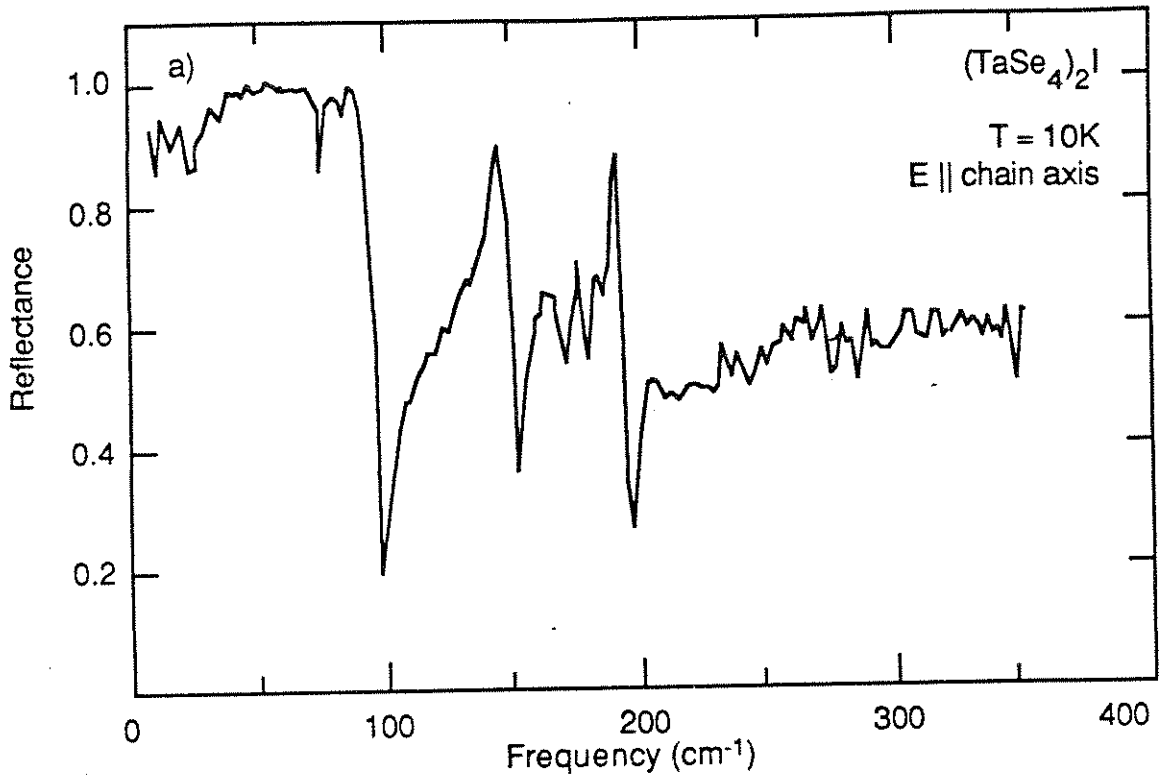
a)
$(TaSe_4)_2I$
T = 10K
E || chain axis
Reflectance
1.0
0.8
0.6
0.4
0.2
0
100
200
300
400
Frequency (cm^{-1})

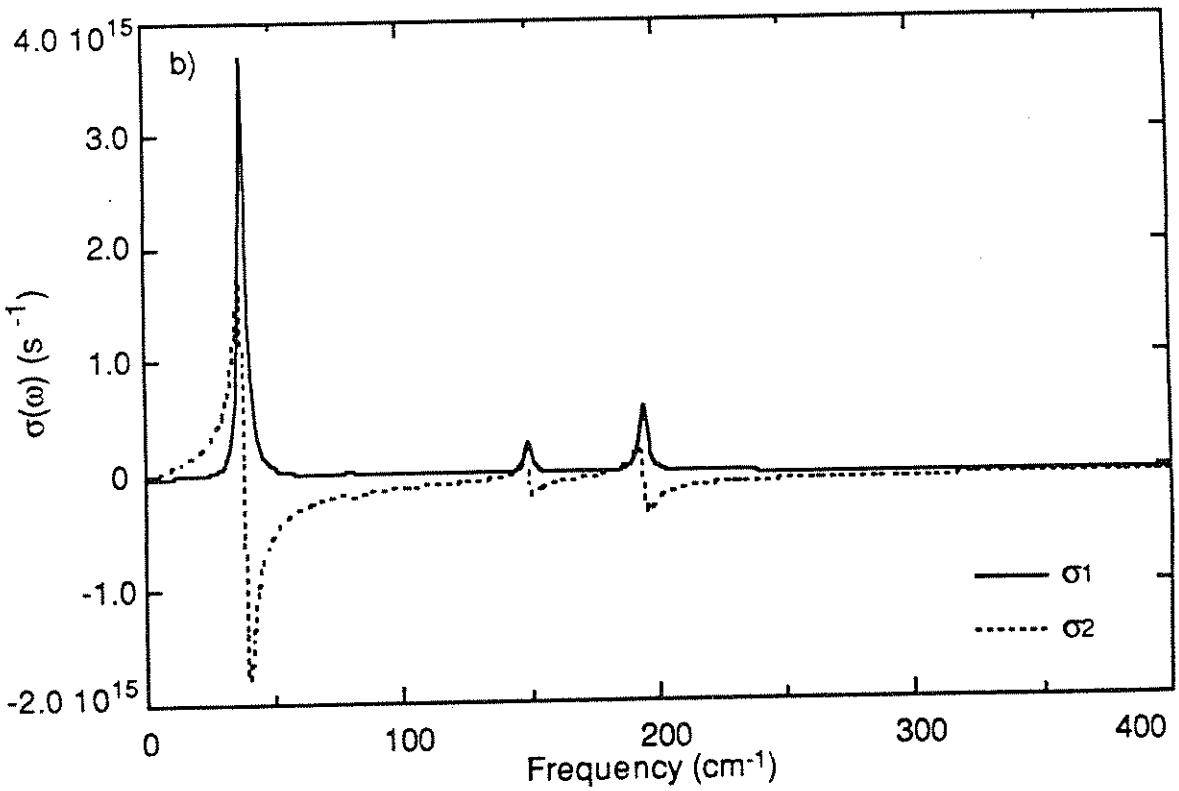
b)
$\sigma(\omega)$ (s^{-1})
4.0 10^{15}
3.0
2.0
1.0
0
-1.0
-2.0 10^{15}
σ1
σ2
0
100
200
300
400
Frequency (cm^{-1})

Fig. 2-7 a) Side view of the chain structure in TaS_3 (adapted from the illustration for $NbSe_3$ in Ref. 58).

b) Arrangement of the TaS_3 chains in extended slabs (adapted from Ref. 49). The solid and dashed outlines are the orthorhombic and monoclinic unit cells. The high conductivity axes b_{mono} and c_{ortho} are perpendicular to the plane of the Figure.

a)

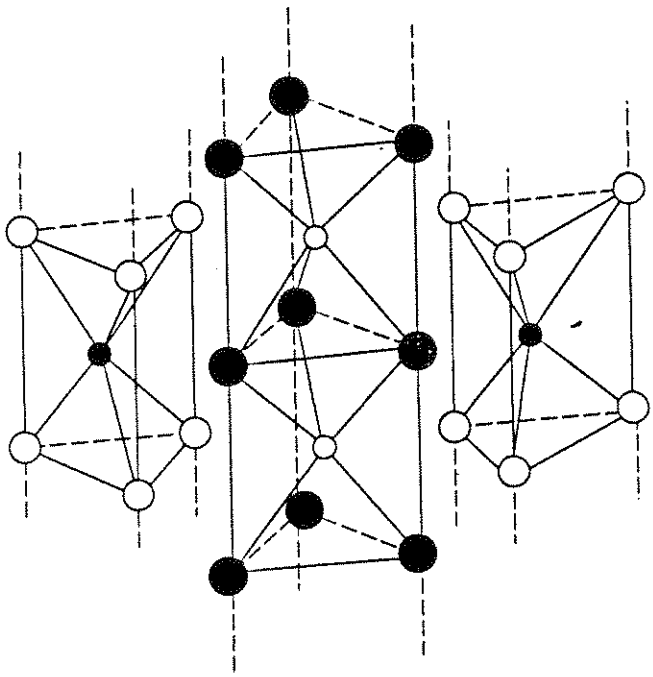

b)

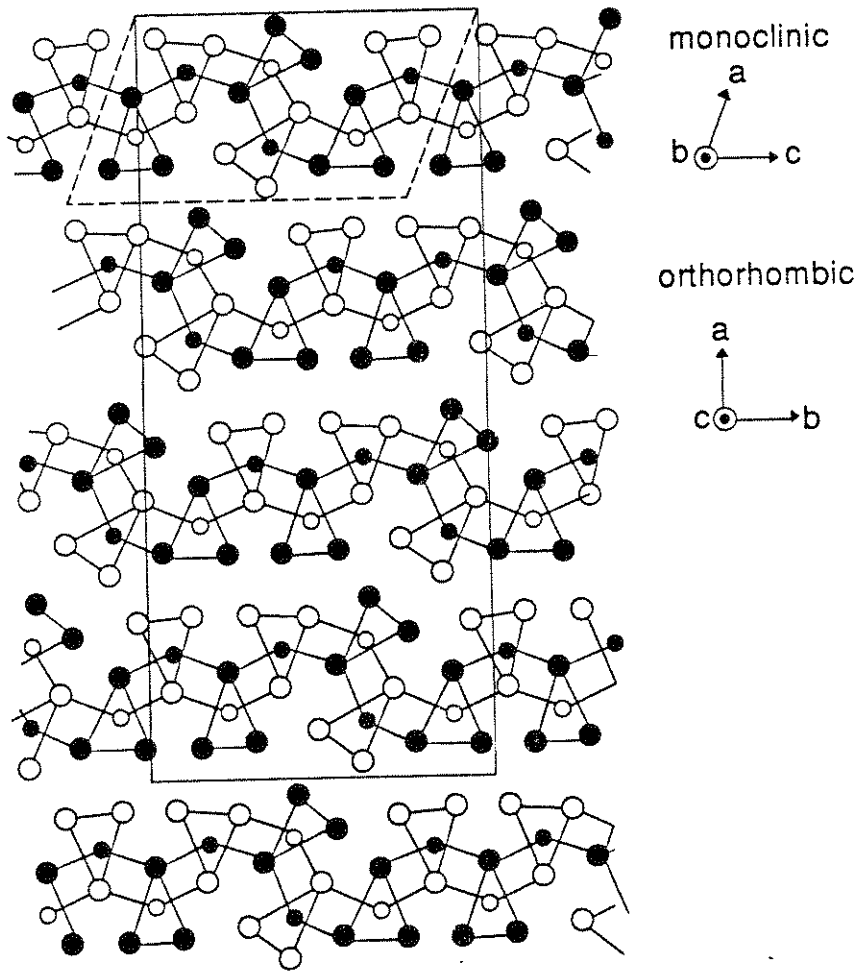

contributes to an increased 1D character in TaS_3, and the material has a higher transition temperature than $NbSe_3$.

Part b of Fig. 2-7 shows the end view of the chains and outlines the unit cell for two forms of TaS_3. The monoclinic form has three distinct types of chains with different S-S bonds lengths. Two chains of each type lie along the b axis within each unit cell. Monoclinic TaS_3 has two Peierls transitions at 240K and 160K, and precursors of the electron diffraction pattern associated with the CDW superstructure appear at room temperature.[49]

The far infrared reflectance of the second, orthorhombic form of TaS_3 is discussed in Chapter 4 of this dissertation. The unit cell of o-TaS_3 has dimensions (36.804A, 15.173A, 3.340Å) with twenty-four chains parallel to the c axis.[50] In contrast to the situation in the monoclinic polytype, all the chains in orthorhombic TaS_3 are identical. The exact structure of o-TaS3 is not known but recent studies[51] indicate the space group is likely to be Cmcm with TaS_3 chains coordinated in four slabs across the narrow dimension of the unit cell, as shown in Fig. 2-7b. The Peierls transition temperature is 210K, and the CDW wavevector is Q.= (0.5, 0.125, ≈.250). The wavevector is inside the first Brillouin zone of the material, and it becomes commensurate with the lattice at low temperatures.[44]

B. $(TaSe_4)_2I$

The halogenated tetrachalcogenide $(TaSe_4)_2I$ grows via thermal vapor transport as needle shaped crystals with cross-section 1mmx1mm or greater. Tetragonal prisms of $TaSe_4$ are arranged along the crystallographic c axis, separated by columns of iodine. Each Se_4 rectangle is made from two $(Se_2)^{2-}$ dimers. The tantalum atoms form chains with regular spacing of 3.206Å, but neighboring selenium rectangles are rotated by about 45°. The orientation of

a given selenium rectangle is repeated on the fourth subsequent rectangle, and the unit cell is consequently quite large along the c axis. The large unit cell (9.531Å, 3.206Å, 12.824Å)[52] leads to a diminutive Brillouin zone, and the CDW wavevector Q = (0, 0, 0.94)[53] lies in the second Brillouin zone.

C. $K_{0.3}MoO_3$

The blue bronze $K_{0.3}MoO_3$ is synthesized by electrocrystallization of a melt of K_2MoO_4 and MoO_3.[54] The crystals have a striking deep blue appearance, and they can be easily cleaved along the [101] direction of the unit cell. The crystal structure is shown in Figure 2-8. The monoclinic unit cell has dimensions (18.25Å, 7.56Å, 9.85Å).[55] It contains a group of ten MoO_6 octahedra of three different types. These assemblies are linked into long chains along the crystallographic b axis, with intervening potassium atoms separating the chains. Figure 2-8b shows a top view of the unit cell. Two type 2 octahedra are joined at their edges and flanked by two type 3 octahedra. A second identical layer joins the first along its octahedral edges, and two type 1 octahedra complete the ten-octahedra unit. Adjacent units join at the corners of the type 3 octahedra, forming infinite slabs along the [101] direction.

Despite the uniform appearance of its crystals, the blue bronze $K_{0.3}MoO_3$ is highly anisotropic. The room temperature dc conductivity along the chains is 80 times that along the planes, and over 1000 times the conductivity perpendicular to the planes.[56] At 180K, the material undergoes a metal to semiconductor transition associated with the formation of a charge density wave with wavevector Q = (0., 0.74, 0.5).[57] One of the more interesting electrical features of this material is its abrupt non-linear conductivity when the CDW depins at low temperatures.[3] At 4K, the sliding CDW state in $K_{0.3}MoO_3$ has near-zero differential resistivity and it may

Fig.2-8 a) Side view of the crystal structure of $K_{0.3}MoO_3$. Groups of ten MoO_6 octahedra form long chains along the b axis. Potassium ions separate the chains and contribute electrons to the conduction band (adapted from Ref. 56).

b) End view of the blue bronze structure. The dashed outline is the unit cell (adapted from Refs. 56 and 59).

a)

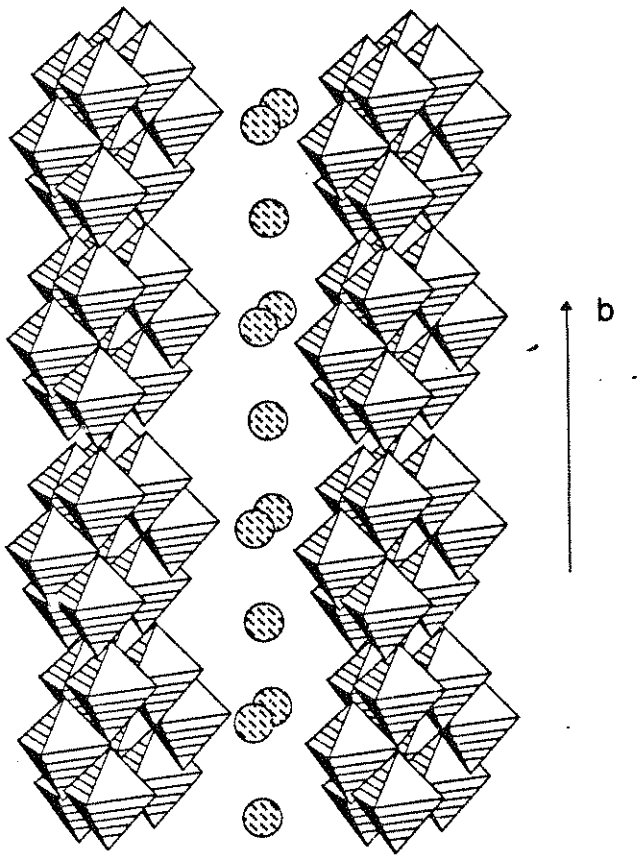

b)

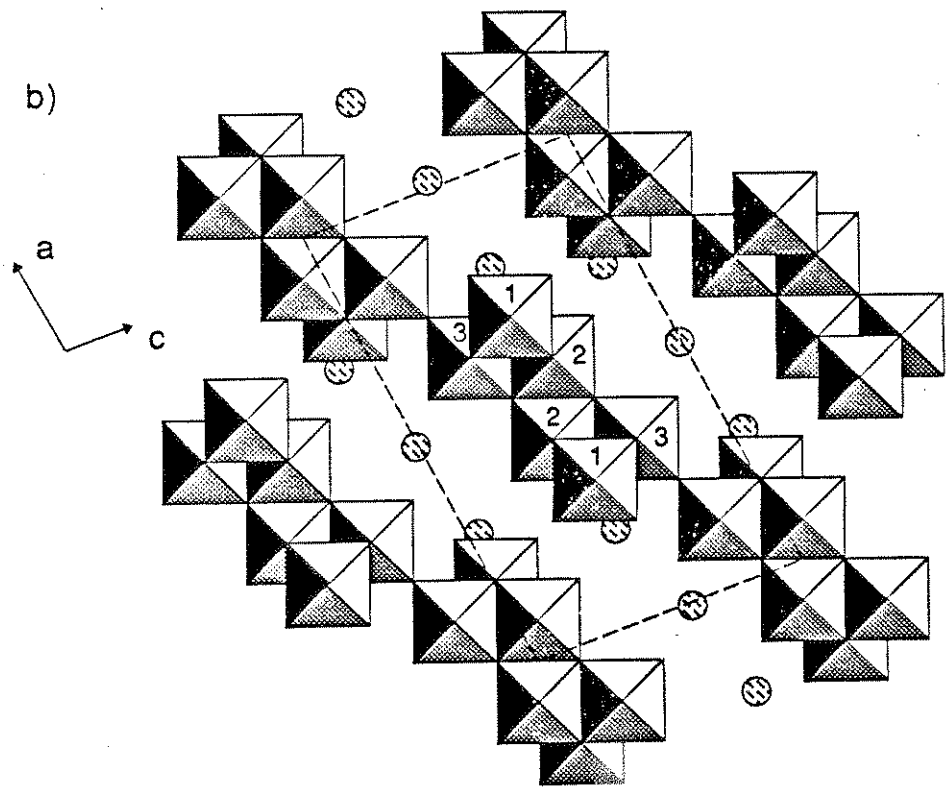

correspond to the sliding Fröhlich state. Chapter 6 is an investigation of the effect of CDW depinning at low temperatures on the dielectric function of blue bronze.

Conclusion

In this introductory chapter we have presented the background to the far infrared conductivity studies to be presented in the first part of this dissertation. We have introduced the crystal structure and some of the electronic properties of the quasi-one dimensional inorganic materials TaS_3, $(TaSe_4)_2I$, and $K_{0.3}MoO_3$. A charge density wave forms along with a periodic lattice distortion in each of these materials, and the basic notion of the Peierls transition was reviewed. The well-understood intrinsic excitation modes of CDW systems are the pinned mode, the single particle gap excitations, the phase phonons, and dielectric relaxation; each of these modes has been discussed in some detail. Finally, we have considered the giant conductivity mode recently seen in $(TaSe_4)_2I$. An elucidation of the possible origins for the giant FIR mode and a search for the mode in other CDW materials forms the bulk of the first part of this work.

References

1. H. Fröhlich, Proc. R. Soc. London Ser. A **223**, 296 (1954).
2. P. Monceau, J. Richard and M. Renard, Phys. Rev. Lett. **45**, 43 (1980).
3. G. Mihály and P. Beauchêne, Solid State Comm. **63**, 911 (1987).
4. M.S. Sherwin, A. Zettl and P.L. Richards, Phys. Rev. B **36**, 6708 (1987).
5. R.E. Glover III and M. Tinkham, Phys. Rev. **108**, 243 (1957).
6. P.A. Lee, T.M. Rice and P.W. Anderson, Solid State Comm. **14**, 703 (1974).
7. M.J. Rice, Phys. Rev. Lett. **37**, 36 (1976).
8. M.J. Rice, Solid State Comm. **25**, 1083 (1978).
9. L. Degiorgi, B. Alavi, G. Mihály and G. Grüner, (unpublished).
10. W.A. Challener IV, Ph. D. Thesis, University of California at Berkeley (1983).
11. M.V. Belousov, A.M. Vaînrub and R.M. Vlasova, Soviet Physics of the Solid State **18**, 1538 (1976).
12. U. Fano, Phys. Rev. **118**, 451 (1960).
13. U. Fano, Phys. Rev. **124**, 1866 (1961).
14. L.P. Gor'kov and E.I. Rashba, Solid State Comm. **27**, 1211 (1978).
15. W.A. Challener and P.L. Richards, Solid State Comm. **52**, 117 (1984).
16. G. Grüner, A. Zawadowski and P.M. Chaikin, Phys. Rev. Lett. **46**, 511 (1981).
17. S. Sridhar, D. Reagor and G. Grüner, Phys. Rev. B **34**, 2223 (1986).
18. D. Reagor, S. Sridhar, M. Maki and G. Grüner, Phys. Rev. B **32**, 8445 (1985).
19. D. Reagor, S. Sridhar and G. Grüner, Phys. Rev. B **34**, 2212 (1986).

20. S. Sridhar, D. Reagor and G. Grüner, Phys. Rev. Lett. **55**, 1196 (1985).

21. Tae Wan Kim, D. Reagor, G. Grüner, K. Maki and A. Virosztek, Phys. Rev. B **40**, 5372 (1989).

22. A. Philipp, W. Mayr, T.W. Kim, B. Alavi, M. Maki and G. Grüner, Phys. Rev. B **39**, 7356 (1989).

23. K.B. Efetov and A.I. Larkin, Zh. Eksp. Teor. Fiz. **72**, 2350 (1977) [Sov. Phys.--JETP **45**, 1236 (1977)].

24. H. Fukuyama, J. Phys. Soc. Jpn. **45**, (1978).

25. H. Fukuyama, J. Phys. Soc. Jpn. **41**, 513 (1976).

26. H. Fukuyama and P.A. Lee, Phys. Rev. B **17**, 535 (1987).

27. P.A. Lee and T.M. Rice, Phys. Rev. B **19**, 3970 (1979).

28. D. Reagor and G. Grüner, Phys. Rev. B **39**, 7626 (1989).

29. S. Takada, M. Wong and T. Holstein, in *Charge Density Waves in Solids*, G. Hutiray and J. Solyom ed., (Springer-Verlag, Berlin, 1985), p. 227.

30. L. Sneddon, Phys. Rev. Lett. **52**, 65 (1983).

31. L. Sneddon, M.C. Cross and D.S. Fisher, Phys. Rev. Lett. **49**, 292 (1982).

32. J. Bardeen, Phys. Rev. Lett. **45**, 1978 (1980).

33. J. Bardeen, Physica B **143**, (1986).

34. R.J. Cava, R.M. Fleming, P. Littlewood, E.A. Rietman, L.F. Schneemeyer and R.G. Dunn, Phys. Rev. B **30**, 3228 (1984).

35. H.K. Ng, G.A. Thomas and L.F. Schneemeyer, Phys. Rev. B **33**, 8755 (1986).

36. R.J. Cava, R.M. Fleming, R.G. Dunn and E.A. Rietman, Phys. Rev. B **31**, 8325 (1985).

37. R.J. Cava, L.F. Schneemeyer, R.M. Fleming, P.B. Littlewood and E.A. Rietman, Phys. Rev. B **32**, 4088 (1985).

38. R.J. Cava, P. Littlewood, R.M. Fleming, R.G. Dunn and E.A. Rietman, Phys. Rev. B **33**, 2439 (1986).

39. Wei-yu Wu, L. Mihály, George Mozurkewich and G. Grüner, Phys. Rev. Lett. **52**, 2382 (1984).

40. Wei-Yu Wu, L. Mihaly, George Mozurkewich and G. Grüner, Phys. Rev. B **33**, 2444 (1986).

41. P. Debye, *Polar Molecules* (Chemical Catalog Company, New York, 1929).

42. S. Havriliak and S. Negami, J. Polym. Sci. C **14**, 99 (1966).

43. M.K. Wu, J.R. Ashburn, C.J. Torng, P.H. Hor, R.L. Meng, L. Gao, Z.J. Huang, Y.Q. Wang and C.W. Chu, Phys. Rev. Lett. **58**, 908 (1987).

44. Z.Z. Wang, H. Salva, P. Monceau, M. Renard, C. Roucau, R. Aryoles, F. Levy, L. Guenas and A. Meerschaut, J. Phys. (Paris) Lett. **44**, L311 (1983).

45. P. Littlewood and C.M. Varma, (unpublished).

46. P.B. Littlewood, Phys. Rev. B **36**, 3108 (1987).

47. M.S. Sherwin, Doctoral Thesis, University of California at Berkeley (1988).

48. G. Travaglini and P. Wachter, Phys. Rev. B **30**, 1971 (1984).

49. C. Roucau, R. Ayroles, P. Monceau, L. Guemas, A. Meerschaut and J. Rouxel, Phys. Status Solidi A **62**, 483 (1980).

50. E. Bjerkelund and A. Kjekshus, Z. Anorg. & Allg. Chem. B **328**, 235 (1964).

51. A. Meerschaut, P. Grenouilleau and J. Rouxel, J. Solid State Chem. **61**, 90 (1986).

52. P. Gressier, L. Guemas and A. Meerschaut, Acta Crystallogr. Sect. B **38**, 2877 (1982).

53. C. Roucau, R. Ayroles, P. Gressier and A. Meerschaut, J. Phys. C. **17**, 2993 (1984).

54. A. Wold, W. Kunnmann, R.J. Arnott and A. Ferreti, Inorg. Chem. **3**, 545 (1964).

55. J. Dumas, C. Schlenker, J.Y. Veuillen, R. Chevalier, J. Marcus, R.J. Cinti and E. Al Khoury Nemeh, Synth. Met. **19**, 937 (1987).

56. C. Schlenker, in *Low Dimensional Conductors and Superconductors*, D. Jerome and L.G. Caron ed., (Plenum Press, New York, 1987), p. 477.

57. J.P. Pouget, S. Kogoshima, C. Schlenker and J. Marcus, J. Physique Lett. **44**, L113 (1983).

58. A. Meerschaut and J. Rouxel, J. Less Common Metals **39**, 167 (1975).

59. M. Ghedira, J. Chenavas, M. Marezio and J. Marcus, J. Solid State Chem. **57**, 300 (1985).

Chapter 3

Far Infrared Equipment

Introduction

Many important physical processes in condensed matter physics have characteristic energies between 100μeV and 1eV. The Peierls gap and mid-gap states in CDW conductors lie in this frequency range,[1,2] and the pinned CDW phason mode may approach 1.25meV under heavy impurity doping.[3] The gap in a conventional superconductor described by BCS theory typically has an energy near 5×10^{-4}eV.[4-6] The *restrahl* resonance in insulating alkali halide crystals occurs at about 20meV,[7] and in semiconductors the band gap absorption and the exciton absorption band lie near or above 1eV. Phonons typically have frequencies between 10^{-1}-10^{-2}eV. In more recently synthesized systems, the separation of hydrogenic levels for electrons in zero-dimensional quantum dot systems is a few meV,[8] the folded phonon dispersion relation in semiconductor superlattices has rich features starting at 8meV,[9] and second harmonic generation in epitaxially grown $Al_xGa_{1-x}As$ parabolic quantum wells has been demonstrated at 4meV.[10]

The interesting sub-eV energy range corresponds to the far and mid infrared frequencies that bridge the gap between microwave radiation (wavelengths greater than about 2 cm) and visible light (wavelengths shorter than about 8×10^{-5} cm). Far infrared (FIR) wavelengths are comparable to easily generated mechanical movements for optical components, and hence interferometric techniques have been developed that allow measurement of optical properties over a wide range of frequencies simultaneously without the necessity for either tuneable monochromatic light sources or frequency-sensitive detectors.[11] In contrast, measurements in the frequency regimes on either side of the FIR typically employ monochromatic radiation. (In the

microwave, few tunable radiation sources exist and the light propagates in waveguides built specifically for a narrow band of frequencies; at optical frequencies, the availability of lasers as intense coherent light sources makes single frequency experiments attractive. The frequency components in broad-bandwidth optical measurements are typically separated by a grating spectrometer rather than by interferometric techniques.)

Though the physical quantities of interest are conductivities and complex dielectric functions, these are measured indirectly in the FIR by determination of optical properties such as reflectance, transmittance, and absorption. This chapter will describe the equipment and methods used for optical measurements in the infrared, including the light source and bolometric detectors, interferometric techniques, and a reflectance/transmittance apparatus built for polarized optical measurements on cooled samples.

Michelson interferometer

If a beam of monochromatic light splits in two, and then recombines after the two beams travel different optical paths, the intensity of the recombined beam may be decreased from that of the original beam if the split beams negatively interfere due to a relative phase shift.[12] If the optical path difference is mechanically varied, the intensity of the recombined beam reaches a maximum each time the path difference is a multiple of the wavelength of the light. A Michelson Fourier Transform Interferometer uses this phenomena to analyze the spectral content of an infrared light source. A mercury vapor lamp produces blackbody radiation over the entire FIR frequency range. A thin piece of mylar splits the light into two beams. One beam reflects from a fixed mirror and the other from a movable mirror, and

the beams then recombine. As the position of the latter mirror is changed, the intensity of the output beam is modulated. The output beam typically contains a broad range of frequency components and its intensity can be detected by monitoring the temperature rise the light causes in a bolometric detector. A record of the output light intensity as a function of discrete mirror positions is an interferogram; the Fourier transform of the interferogram is the spectrum of the intensity of the light as a function of frequency. The resolution of the spectrum is inversely proportional to the length of the interferogram (i.e., the total distance travelled by the movable mirror).

Though Fourier Transform Infrared Spectroscopy is conceptually simple, its implementation is quite complex. The infrared light beam is chopped and the bolometer output recorded with lock-in techniques to avoid problems with low-frequency noise and background room temperature radiation. Separate cryogenic systems cool the bolometer and the sample, and each cryogenic system has an associated vacuum system. Additional vacuum spaces must be maintained in the cavity around the bolometer, in the light-pipes joining various components, and within the interferometer itself. A stepper-motor controls the mirror motion. The mirror must accurately travel to a given position, pause while data is collected, then continue on in discrete steps until the interferogram is completed. Thermal drifts in the beamsplitter and mirror alignments must be compensated, and slow changes in the sample and bolometer temperatures must also be minimized.

A major portion of the work underlying the research reported in this dissertation was the writing of computer code to automate control of the Fourier interferometer and the associated detector systems. Working from a framework of FORTRAN code provided by the group at McMaster University,[13] we wrote extensive programs to interface an existing

interferometer to an IBM PC/AT computer. These programs control the motion of the movable mirror, digitize the signal level indicated by the lock-in, and coordinate the data collection, storage, Fourier analysis, and averaging of spectra. They give the user great flexibility in the choice of apodization and other details pertinent to the Fourier transforms. The programs implement an algorithm[14] that corrects linear phase errors in asymmetric interferograms to first order. They provide for correction of various types of systematic errors that commonly appear in interferograms and can automate the collection and coadding of multiple spectra to enhance the ratio of signal to noise. In addition, I wrote a library of programs that analyze the measured reflectances and calculate dielectric functions and conductivities for the samples. This library, written in C for the Apple Macintosh computer, is included in Appendix B.

Reflectance/transmittance apparatus

We calculate the reflectance of a sample by normalizing the intensity spectrum for light reflected from the sample to that reflected from a polished brass disk of the same dimensions. The apparatus shown in Fig. 3-1 holds two samples and the brass reference disk in a copper slide attached with copper braid to a coldfinger.[15] A calibrated Lakeshore DT-471-SD diode embedded in the copper slide with Stycast 2850FT epoxy measures the sample temperature. An aluminum radiation shield surrounds the coldfinger and sample slide, and the larger aluminum chamber holding this assembly is evacuated to a pressure of about 1×10^{-5} torr nitrogen. Evacuating the chamber avoids infrared absorption by atmospheric water vapor and thermally isolates the sample. An Air Products LT 3-110 continuous flow helium cryostat cools the copper coldfinger, and a Lakeshore Cryogenics DRC-81C proportional

Fig. 3-1. Mechanical design of the reflectance/transmittance apparatus for variable temperature samples. The inset shows the details of the baffle structure and the sample mounting slide. The three sample mounting holes are each 7/16" in diameter.

a) Schematic view of apparatus

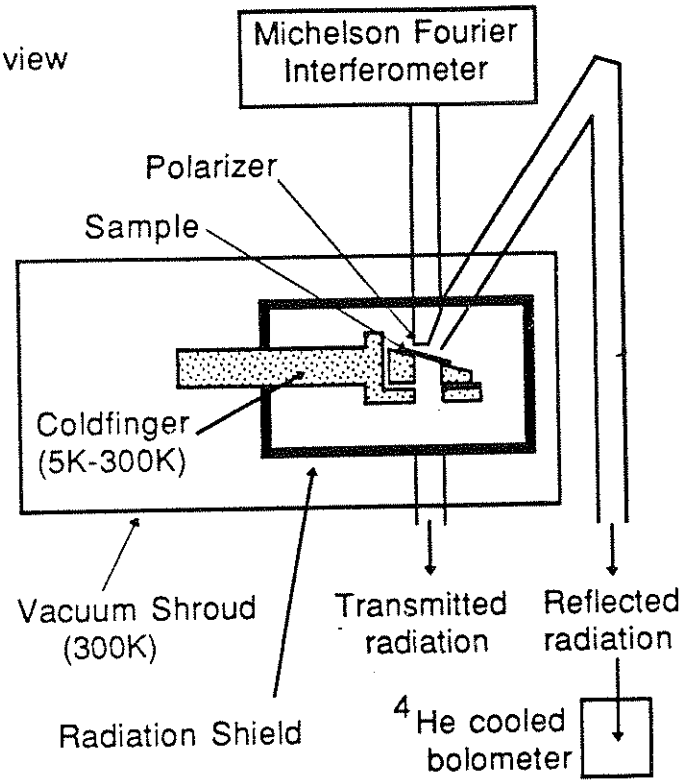

b) Sample slide detail

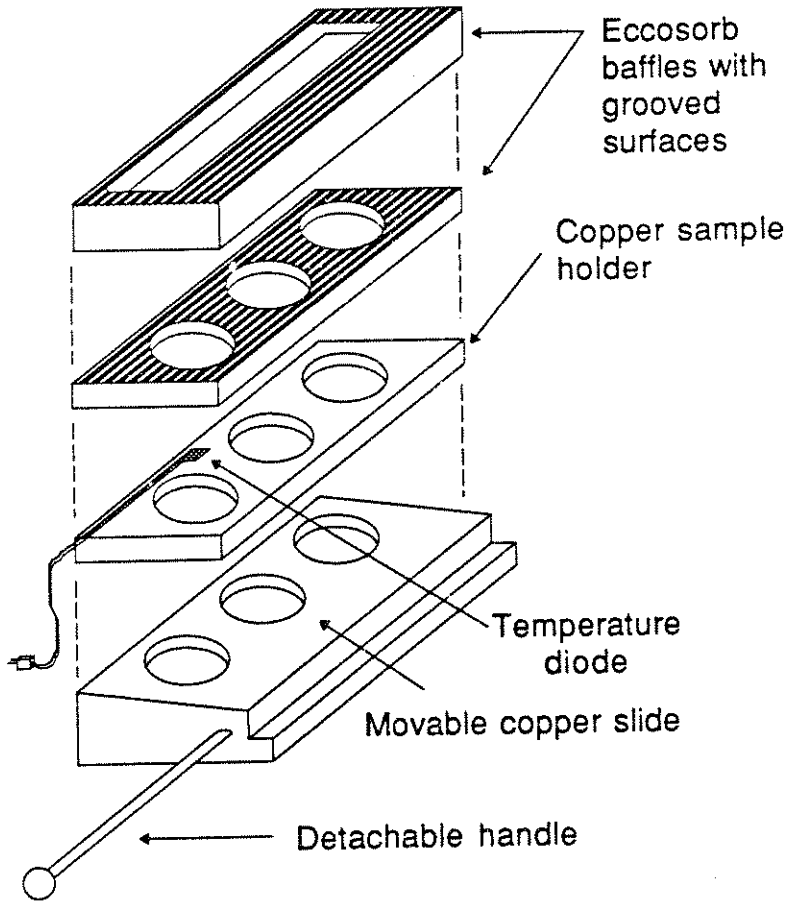

temperature controller connected to a second temperature diode and a resistance heater on the coldfinger maintains a stable temperature between 10K and 300K. Light from the interferometer enters the top of the chamber through a .001" polypropylene window. The light propogates several centimeters through a 7/16" diameter f/1.5 brass light pipe and strikes the sample after passing through a wire grid polarizer. We measured polarization exceeding 95% from 2-700cm^{-1} for similar polarizers; the polarizer is parallel copper wires deposited every 3.6 μm on a 4 μm thick clear mylar substrate by photolithographic techniques.[16]

The infrared light reflects from the sample or brass reference disk into a return light-pipe leading to the detector. The polarizer terminating the source light-pipe and the entrance to the return light-pipe lie side by side about 1/2cm above the sample. The two light-pipes merge at an 11° angle and are divided by a brass septum. The separation between the end of the source light pipe and the sample surface allows the light to diverge slightly and illuminate some of the area around the 7/16" diameter sample. To eliminate stray reflections from the copper slide around the sample, we covered it with a two piece baffle. The lower part of the baffle immediately surrounds the circular sample and covers the copper slide and temperature diode; the upper part extends to the level of the polarizer and prevents stray reflections from the radiation shield and other parts of the apparatus. The baffles are machined from Eccosorb MF 110 iron-filled epoxy. This material is a poor reflector in the infrared, and we degraded its reflectance further by machining a series of fine grooves into the upper surface of the baffles. Despite these precautions, stray reflection from the baffles remained a problem in some of the experiments: the reflectance measurements on TaS_3 described in Chapter 4 contain features at low frequencies that are Fabry-Perot

fringes due to light reflected from the baffle surrounding the sample interfering with light reflected directly from the sample. This problem was eliminated in the measurements on $(TaSe_4)_2I$ described in Chapter 5 by placing the sample faces flush with the surface of the lower Eccosorb baffle.

The apparatus in Fig. 3-1 can also be configured for transmittance experiments by replacing the Z-shaped light-pipe path with a path straight through the sample. In this configuration the polarizer terminating the source light pipe lies directly above the sample and covers the entire area of the sample. Although the final results reported in Chapters 4 and 5 are for reflectance measurements, we used tranmittance measurements in the early stages of the experiments to verify small features in the reflectance, particularly in frequency ranges where the reflectance of the sample was near unity.

Bolometric detector

After leaving the reflectance/transmittance apparatus, the infrared light travels via light-pipes through a mylar window into a double glass dewar holding superfluid liquid helium surrounded by a liquid nitrogen bath. A Winston cone at the furthest tip of the light-pipe concentrates the light onto a composite bolometer[17] in a brass vacuum can immersed in the helium. Kevlar threads suspend a .001"x4mmx4mm sapphire substrate coated with a 1000Å evaporated layer of bismuth within a brass ring.[18] Electrons in the substrate and the bismuth absorb the light and convert the optical energy into thermal motion of the atoms. The heat passes through a tiny amount of Emerson-Cummings 307 epoxy into a 227μmx248μmx248μm chip of neutron-transmutation-doped germanium.[19] Brass or copper wires

connect gold pads on the faces of the germanium chip to the brass ring, which is held at the temperature of the helium bath.

The energy of the infrared light collected by the sapphire antenna heats the germanium chip quickly. The chip then cools to near the bath temperature at a rate controlled by the thermal conductivity of the metal wires. The metal wires also serve as electrical contacts for a small (~2μA) bias current through the germanium chip. Since the resistance of the germanium chip is a sensitive function of its temperature, the voltage across the chip under constant current bias is a measurement of the incident infrared optical power. This optical loading is a combination of the light reflected from the sample and room temperature blackbody radiation from the mylar window and the light-pipes near the top of the helium dewar. To separate these contributions, the interferometer output is chopped at about 25Hz and the voltage across the bolometer detected with a PAR 124A lock-in amplifier after amplification with a home-built low-noise preamplifier and a PAR 117 differential preamplifier.

The germanium chip is heated not only by the chopped and background optical radiation coupled to it by the sapphire absorber, but also by Ohmic dissipation of the bias current. The thermal conductivity of the metal wires is a crucial parameter in the bolometer design. We chose the composition and size of the metal wires so that the thermal system has a relaxation time appropriate for the chopping rate and so that the overall temperature rise of the doped-germanium chip yields a resistance corresponding to the optimum input resistance for the preamplifiers. Typically, the bolometers have a dc temperature offset of .5K above the bath temperature of 1.2K at about 1 torr helium pressure. Their resistance is about 500kΩ. We optimized the bolometer used for reflection measurements in

Chapters 4 and 5 for a relatively high background optical and electrical loading of about 1 μW. It has .002" copper wires with thermal conductivity $G = 3.25 \times 10^{-6} W/K$.

Beamsplitters and filters

Just before the infrared light enters the vacuum can containing the composite bolometer, it passes through one or more low-pass filters. These cold filters serve two purposes. First, they attenuate the unchopped room temperature blackbody radiation from the warm parts of the apparatus. If unimpeded, this radiation can heat the bolometer chip several degrees above the bath temperature and seriously diminish its responsivity. Secondly, the cold filters attenuate radiation from the second and higher order "beamsplitter maxima" in the spectrum of the chopped light. The light from the interferometer is roughly a blackbody spectrum modulated in a series of "beamsplitter maxima" in the frequency domain by an interference pattern due to the finite thickness of the mylar beamsplitter. (The blackbody spectrum is also affected by absorption lines in water vapor, mylar beamsplitters, and clear polypropylene windows in the interferometer, and by the alignment of the mirrors.) The frequency interval between extrema in this modulation is inversely proportional to the beamsplitter thickness. Typically, only frequencies below the first beamsplitter minimum (the cutoff frequency) are used in the experiments; warm Yoshinaga filters in the interferometer and the cold filters in the superfluid helium bath attenuate light at higher frequencies. This avoids aliasing of the high frequency spectral components to lower frequencies during the Fourier transform process. The optical properties for a spectral feature at a certain frequency are usually measured using the thickest possible beamsplitter with a cutoff frequency

greater than the frequency of interest. Thick beamsplitters are easier to align. In addition, their low cutoff frequencies allow less frequent spatial sampling of the interferogram. In a given amount of time then, the experimenter can take longer interferograms and obtain finer frequency resolution in the spectrum being measured.

Table 3-I lists the characteristics of the cold and warm filters and the beamsplitters used in these experiments. Figure 3-2 is an illustration of typical raw spectra measured in different frequency ranges corresponding to various combinations of the components. The top part of the Figure gives the useable frequency ranges for the beamsplitters (typically 10-90% of the cutoff frequency) and the middle part of the Figure shows the pass bands for the filters. The bottom part of the Figure shows (to scale) representative raw spectra for light reflected from a brass reference disk at room temperature.

Several considerations set the low frequency limit of these experiments ($2cm^{-1}$): very little signal power is generated by the mercury lamp at low frequencies; the low-pass filters admit background radiation below about $30cm^{-1}$ and thus degrade the signal to noise ratio; the bolometer must be optimized to operate at very low signal levels. At high frequencies, the limiting considerations are very different. Mechanical tolerances become crucial: the accuracy of spectra above $500cm^{-1}$ critically depends on the precision of the linear motion of the mirror and on the alignment of the extremely thin beamsplitter appropriate for these high frequencies. The alignment sometimes changes appreciably during the course of an interferogram due to thermal drifts. In addition, the optical signal falls off rapidly above $500cm^{-1}$ because the mylar beamsplitters and windows have absorption bands at this frequency and again near $1000cm^{-1}$. Finally, the bolometer responsivity degrades seriously at high frequencies as the

TABLE 3-I. Beamsplitter and Filter Characteristics

a) Mylar beamsplitters

Thickness (.001")	First Interference Minimum (cm^{-1})	Useful Frequency Range (cm^{-1})
.125	1000	200 to 800
.25	500	100 to 400
.50	250	38 to 200
3	42	8 to 38
10	12.5	2 to 10

b) Room temperature filters

Type	Composition	Approximate cutoff frequency(cm^{-1})	Beam-splitter (.001")
Yoshinaga #1	Polyethylene (.84), BeO (.08), ZnO (.08)	400	.25
Yoshinaga #3	Polyethylene (.85), SrF_2 (.08), LiF (.07)	220	.50
Yoshinaga #5	Polyethylene (.53), TlI (.15), TlCl (.05), KBr (.05) BiOCl (.07), Cu_2O (.03), BaF_2 (.04), KCl (.08)	52	3
Fluorogold		30	10

c) 1.2K cold filters

Type	Approximate cutoff frequency(cm^{-1})	Beam-splitter thickness (.001")
1.0 mil black polyethylene	700	.125
Z-cut quartz (wedged)	250	.50
Perkin-Elmer 1048 (white)	100	1
Perkin-Elmer 1049 (yellow)	60	3
Glass beads embedded in black polyethlene, backed by Fluorogold	25	10

Fig. 3-2. Characteristics of the beamsplitters and filters used in this investigation. In the upper portion of the figure, each set of three bars shows the cutoff frequencies for a pair of cold and warm filters and the useful frequency range for a given beamsplitter used with the filters. The lower portion of the Figure shows to scale typical spectra measured for different frequency ranges using each beamsplitter/filter combination.

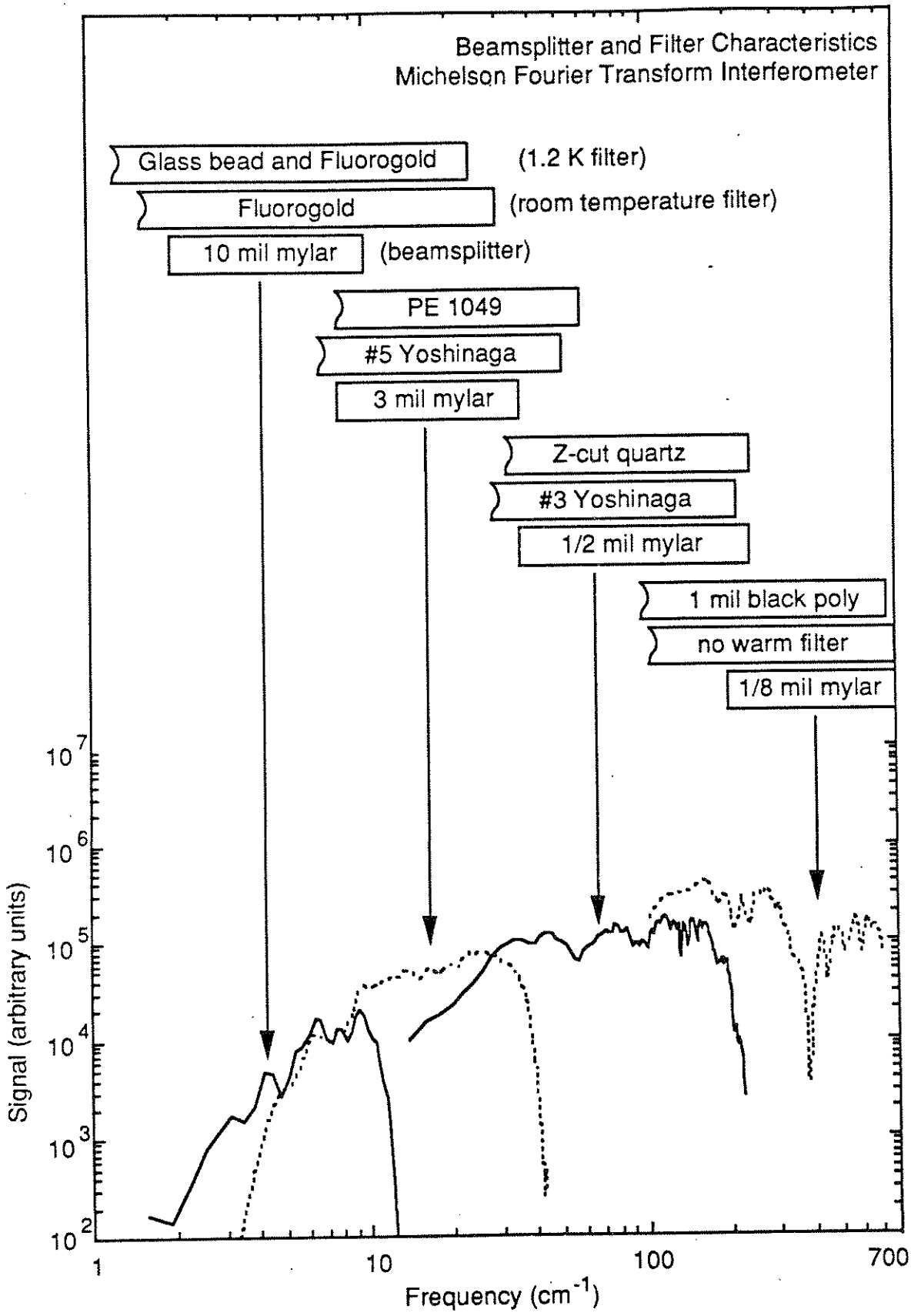
Beamsplitter and Filter Characteristics
Michelson Fourier Transform Interferometer
Glass bead and Fluorogold
(1.2 K filter)
Fluorogold
(room temperature filter)
10 mil mylar
(beamsplitter)
PE 1049
#5 Yoshinaga
3 mil mylar
Z-cut quartz
#3 Yoshinaga
1/2 mil mylar
1 mil black poly
no warm filter
1/8 mil mylar
Signal (arbitrary units)
10^7
10^6
10^5
10^4
10^3
10^2
1
10
100
700
Frequency (cm^-1)

background optical loading heats the bolometer chip well above its design operating temperature.

References

1. S.L. Herr, G. Minton and J.W. Brill, Phys. Rev. B **33**, 8851 (1986).

2. G. Minton and J.W. Brill, Solid State Comm. **65**, 1069 (1988).

3. L. Degiorgi and G. Grüner, (in press).

4. J. Bardeen, L.N. Cooper and J.R. Schrieffer, Phys. Rev. **106**, 162 (1957).

5. J. Bardeen, L.N. Cooper and J.R. Schrieffer, Phys. Rev. **108**, 1175 (1957).

6. R.E. Glover III and M. Tinkham, Phys. Rev. **108**, 243 (1957).

7. R.S. Knox and K.J. Teegarden, in *Physics of Color Centers*, W.B. Fowler ed., (Academic Press, New York, 1968), p. 625.

8. U. Merkt, Bull. Am. Phys. Soc. **36**, 511 (1991).

9. C. Colvard, R. Merlin, M.V. Klein and A.C. Gossard, Phys. Rev. Lett. **45**, 298 (1980).

10. W.W. Bewley, C.L. Felix, J.J. Plombon, M.S. Sherwin and A. Markelz, Bull. Am. Phys. Soc. **36**, 758 (1991).

11. For a general introduction see Robert John Bell, *Introductory Fourier Transform Spectroscopy* (Academic Press, New York, 1972).

12. A.A. Michelson, Phil. Mag. **34**, 280 (1892).

13. *FIRMS Spectroscopy System* provided by T. Timusk, McMaster University, Hamilton, Ontario, Canada (1988).

14. R.B. Sanderson and E.E. Bell, App. Opt. **12**, 266 (1973).

15. M.S. Sherwin, Doctoral Thesis, University of California at Berkeley (1988).

16. W.A. Challener, P.L. Richards, S.C. Zilio and H.L. Garvin, Infra. Phys. **20**, 215 (1980).

17. A.E. Lange, E. Kreysa, S.E. McBride, P.L. Richards and E.E. Haller, Int. J. IR + MM Waves **4**, 689 (1983).

18. N.S. Nishioka, P.L. Richards and D.P. Woody, App. Opt. **17**, 1562 (1978).

19. E.E. Haller, Infra. Phys. **25**, 257 (1985).

Chapter 4

Reflectance and Conductivity of TaS_3: the Intrinsic CDW Conductivity Modes

Introduction

One of the most outstanding features of relatively weakly pinned charge density wave (CDW) conductors is the unusual ac response spectrum. It is well established that there are at least three distinct and clearly-defined excitation modes: dielectric relaxation at low (audio) frequencies, the pinned acoustic phason (in the microwave region), and single particle excitations across the Peierls gap (at frequencies near 10^{13}-10^{14}Hz).[1]

A recent far infrared[2] study demonstrated that, in addition to the three established excitation modes, the CDW conductor $(TaSe_4)_2I$ has a giant conductivity mode in the FIR frequency range between the acoustic phason and the Peierls gap.[2] Reinterpretation of several previously published conductivity data sets on the blue bronze $K_{0.3}MoO_3$ shows that this CDW conductor most probably also has a distinct giant FIR mode.[2] Hence, a very prominent fourth IR-active mode exists in the two CDW materials for which the full ac response spectrum is known.[3]

It has been suggested that the giant FIR mode observed in $(TaSe_4)_2I$ and $K_{0.3}MoO_3$ may be generic to all CDW conductors and, on this basis, several general CDW conductivity models have been constructed.[2, 4] On the other hand, both $(TaSe_4)_2I$ and $K_{0.3}MoO_3$ are relatively complicated CDW systems (as discussed below), and it is possible that the giant FIR mode arises from peculiarities of these materials.

In this chapter, we report on FIR reflectivity measurements of the CDW conductor TaS_3 which, together with previous microwave[5-7] and optical[8, 9] measurements, complete the excitation spectrum for this system.

From the FIR reflectance in the CDW state, we show conclusively that in TaS_3, no FIR mode exists comparable in size to the giant mode seen in two other CDW materials. The strengths and frequencies of smaller FIR modes are determined. From these results, we rule out several models predicting a generic giant FIR mode and place constraints on any new models. The applicability of a zone-folding model is evaluated.

Crystal growth and sample preparation

High-purity crystals of TaS_3 were grown by conventional vapor transport methods in new quartz tubes with 2.4cm exterior diameter.[10] The tubes were cleaned by soaking overnight in a 20% solution of HNO_3:HF (3:1), followed by rinsing five times each with 2M KOH, distilled H_2O, electronics grade tricloroethlyene, acetone, and ethanol. Using a hydrogen-oxygen torch, we sealed one end of each 1m long tube and divided the remainder into subsections by melting constrictions every 20cm. The tubes were firepolished to remove exterior oxidation. While they were being worked with the torch, the tubes emitted a brown gas of unknown composition. We removed this gas as well as much of the water vapor and hydrogen that commonly diffuse from quartz at elevated temperatures[11] by baking the tubes under $1x10^{-6}$ torr vacuum for 2 hours at 100°C and then 24 hours at 850°C. The tube cooled to room temperature under vacuum. Using a long funnel to avoid creating crystal nucleation sites on the tube walls, we poured approximately 1gm of a stoichiometric mixture of the highest available purity Ta and S into the sealed end of the tube.[12, 13] The tube was flushed and evacuated five times with argon, and then sealed and separated at the constriction. The final argon pressure in the tube was about 300mTorr.

Ten such tubes were baked simultaneously in a large multiple-zone oven. The oven maintained a temperature gradient from 630°C to 550°C along the tubes, with the starting materials at the hot end. The temperature gradient induced circulation of the vaporized sulfur. TaS_3 nucleated and grew at numerous sites near the cold end of the tubes. After ten days, we quenched the hot end of the tubes in water to condense the remaining sulfur away from the TaS_3 crystals. We opened the tubes at room temperature by puncturing them in vacuum and gradually venting air through a hollow needle into the tubes.

In order to prepare a sample suitable for FIR reflectance studies, we aligned over a thousand single crystals by hand into an opaque mat 1cm in diameter. Only cohesive crystals with lengths greater than 1cm and wide (>50μm) single crystal faces were used; early attempts at this measurement showed that the reflectance of the sample decays over a period of months if small or fibrous TaS_3 crystals are included in the sample. The crystals in the mat were held in place by a trace amount of a plastic resin.[14] Figure 4-1 shows the optical properties of the resin at room temperature. The reflectance and transmittance shown in the Figure were measured on two samples of different thickness; the measured values do not add to unity, but this is not necessarily a sign of strong absorption in the resin. Rather, the even spacing and slowly varying amplitude of the Fabry-Perot reflectance fringes indicate that the resin has a slowly varying dielectric constant and small conductivity.[15] Though these fringes are not resolved in the Figure above $30cm^{-1}$, they persist to much higher frequencies. The resin has no strong modes in the FIR frequency range and no spectral features in common with those measured for the crystal mat.

Fig. 4-1. Room temperature reflectance and transmittance versus frequency for the plastic binding resin used to immobilize the TaS_3 samples. The samples used for the two measurements were of different thickness.

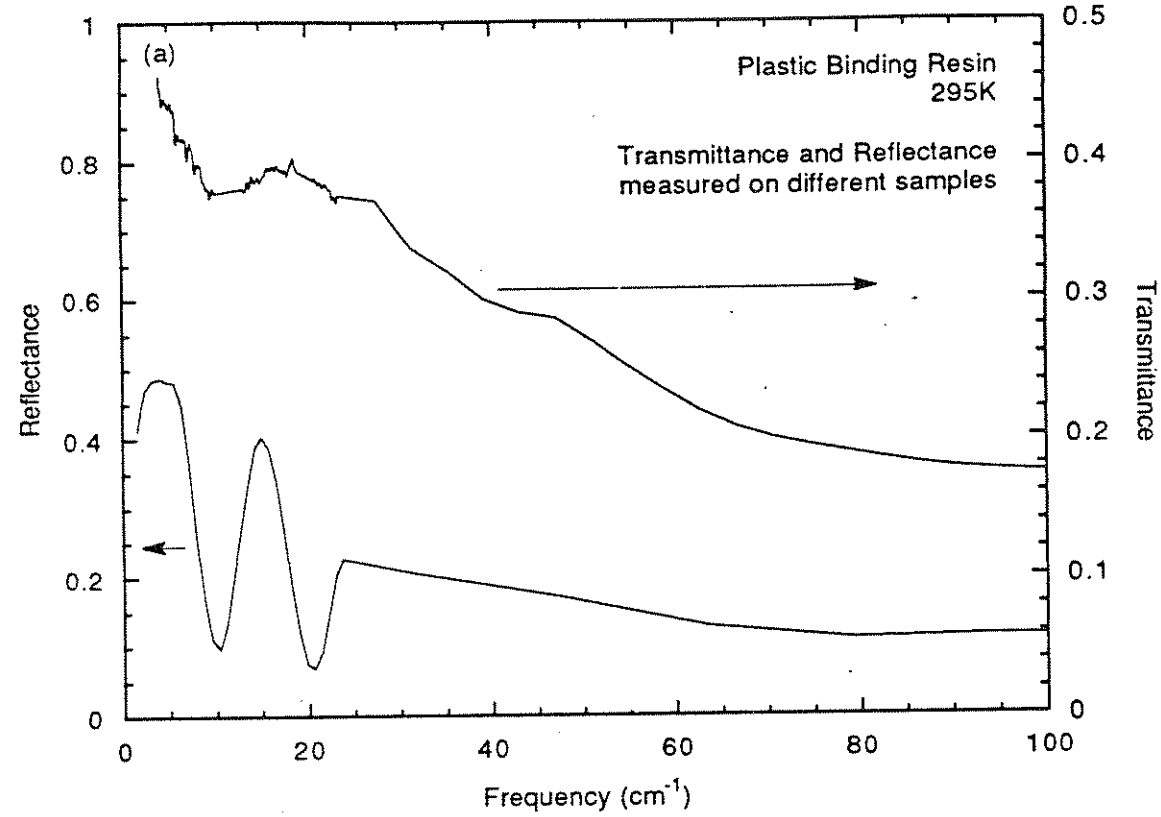
(a)
Plastic Binding Resin
295K
Transmittance and Reflectance
measured on different samples
Reflectance
Transmittance
Frequency (cm-1)
0
0.2
0.4
0.6
0.8
1
0.1
0.3
0.5
20
40
60
80
100

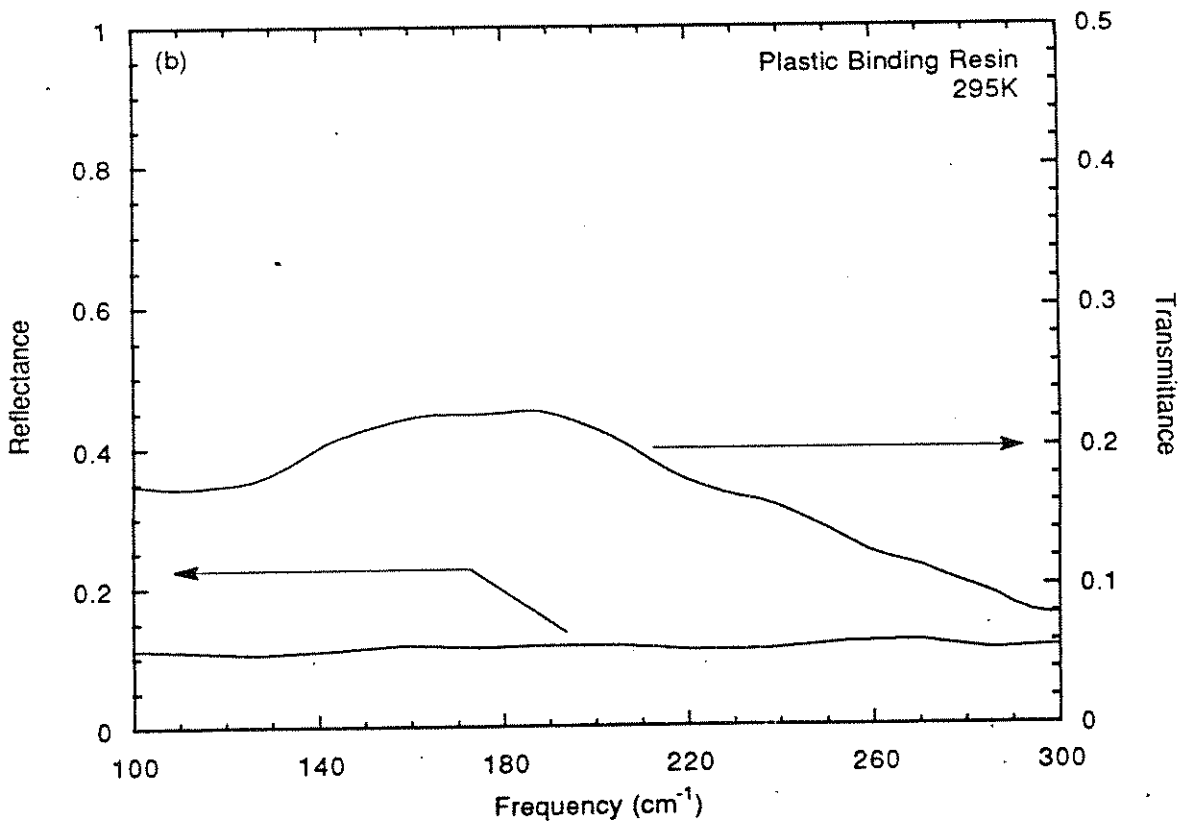
(b)
Plastic Binding Resin
295K
Reflectance
Transmittance
Frequency (cm-1)
0
0.2
0.4
0.6
0.8
1
0.1
0.3
0.5
100
140
180
220
260
300

Figure 4-2 is a depiction of the mounting technique used to align the crystals and immobilize them with the resin. Crystals were laid one by one onto a glass slide covered with an adhesive teflon tape.[16] Additional crystals were added until an area about 1cmx1cm was completely opaque; the process took many days. During pauses in the building of the sample, a second tape-covered glass slide served as a weight to prevent shifting of the crystals. When the sample was finally completely opaque, small strips of the teflon tape were applied along the long edges of both the top and bottom slides, and the two slides were clamped with spring clips. The clips bowed the glass slides enough to hold the TaS_3 crystals tightly, but the slides did not completely touch because of the TaS_3 mat and the tape strips along the edges. Additional teflon tape was then applied to seal the long edges of the two slides together. The plastic resin and its catalyst were mixed in a ratio of 20:1 (a lower ratio than that recommended for large-volume castings) and diluted about 5:1 with trichloroethylene. The thinned resin was applied with an eyedropper to the end of the slide sandwich. As the resin wicked slowly into the space between the slides, we monitored the progress of the meniscus by shining a strong light through the tape/slide assembly. After the TaS_3 crystals were completely wetted with resin, the slide assembly was baked at 80°C for twenty minutes and cooled to room temperature. The spring clips and exterior teflon tape strips were removed and the slides pried apart. At this point the sample can easily delaminate--great care is necessary. The sample was lifted from the lower slide and then baked in air an additional 45 minutes at 80°C to fully cure the resin.

Fig. 4-2 Technique for mounting and fixing TaS_3 samples in binding resin.
a) Exploded view of glass and teflon tape assembly used to support immobilize the crystals.

b) Slides and sample assembled and clamped for saturation with plastic resin.

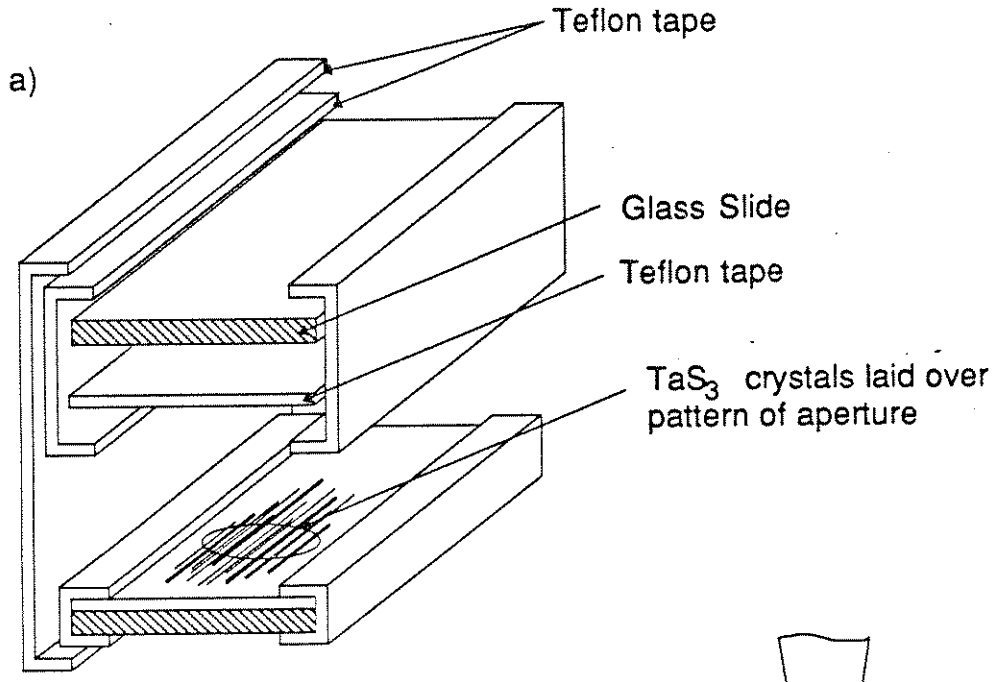
a)
Teflon tape
Glass Slide
Teflon tape
TaS_3 crystals laid over pattern of aperture

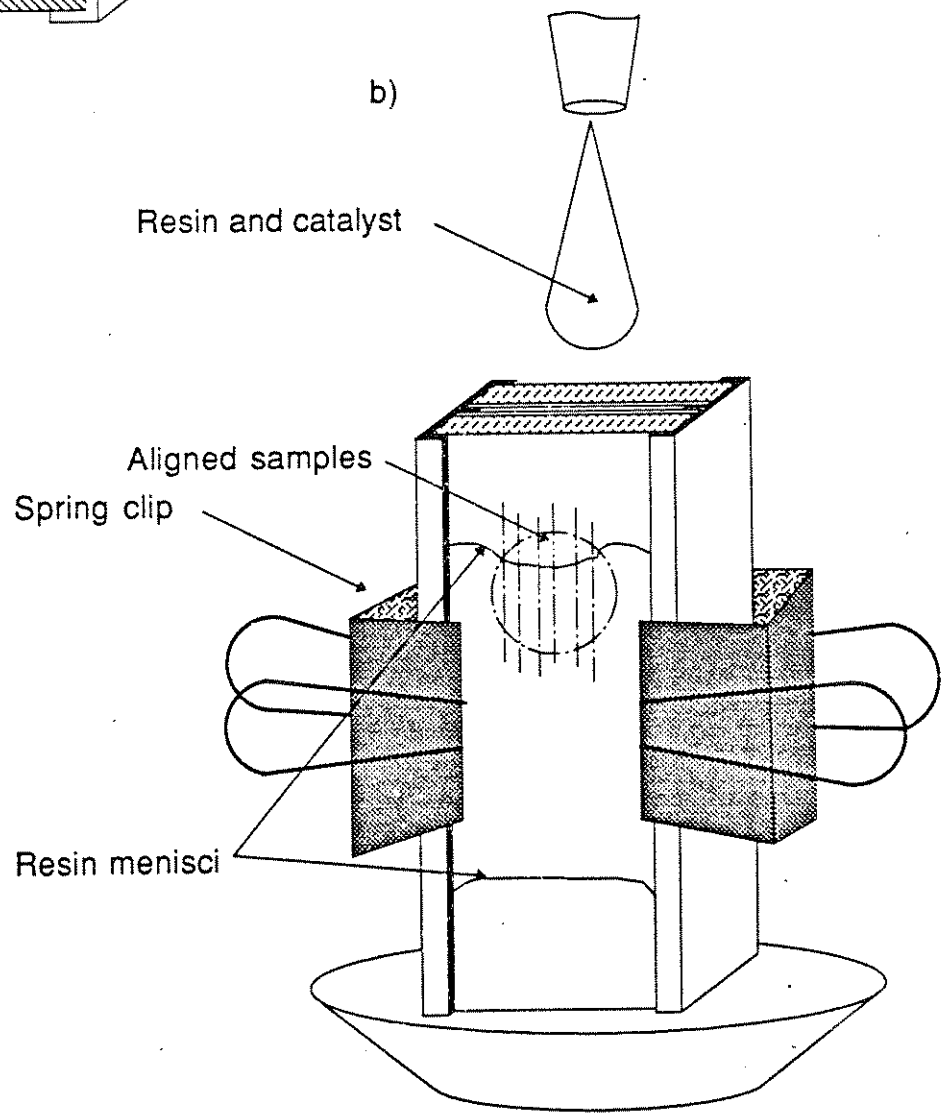
b)
Resin and catalyst
Aligned samples
Spring clip
Resin menisci

Mounting the samples

We mounted the sample in the variable temperature reflectance/transmittance apparatus described in Chapter 3. The lower Eccosorb baffle clamped the flat sample against the copper slide. This pressure mounting provided sufficient thermal contact between the sample and the cold copper slide. We saw no evidence in the reflectance measurements of drifts in sample temperature relative to the measured slide temperature. The surface of the baffle was .070" above the surface of the sample, and this contributed to spurious Fabry-Perot fringes in the measured reflectance at low frequencies. The smoothing of these fringes will be discussed below.

Temperature-dependent reflectance of TaS_3

Reflectance measurements were made at numerous temperatures both above and below the CDW transition temperature Tp=220K, with light polarized parallel and perpendicular to the chain axis. Because of the high electrical anisotropy of the material, the information about the charge density wave dynamics is contained in the measurements for parallel polarization. Before proceeding to these more important measurements, we will briefly discuss the results for light polarized perpendicular to the conducting chain axis.

A: Perpendicular polarization

Fig. 4-3 shows the reflectance of TaS_3 as a function of temperature for perpendicular polarization. The reflectance is nearly temperature independent except for the emergence of phonon features. Using techniques that will be described in detail below, we derived the conductivity from the reflectance and fit the features of the conductivity to appropriate models. Fig. 4-4a shows the dielectric function at 32K and Fig. 4-4b shows the model fit.

Fig. 4-3. Far infrared reflectance of TaS_3 for light polarized perpendicular to the long axis of the crystals. The dashed curve was measured at room temperature and the solid curve at 32K.

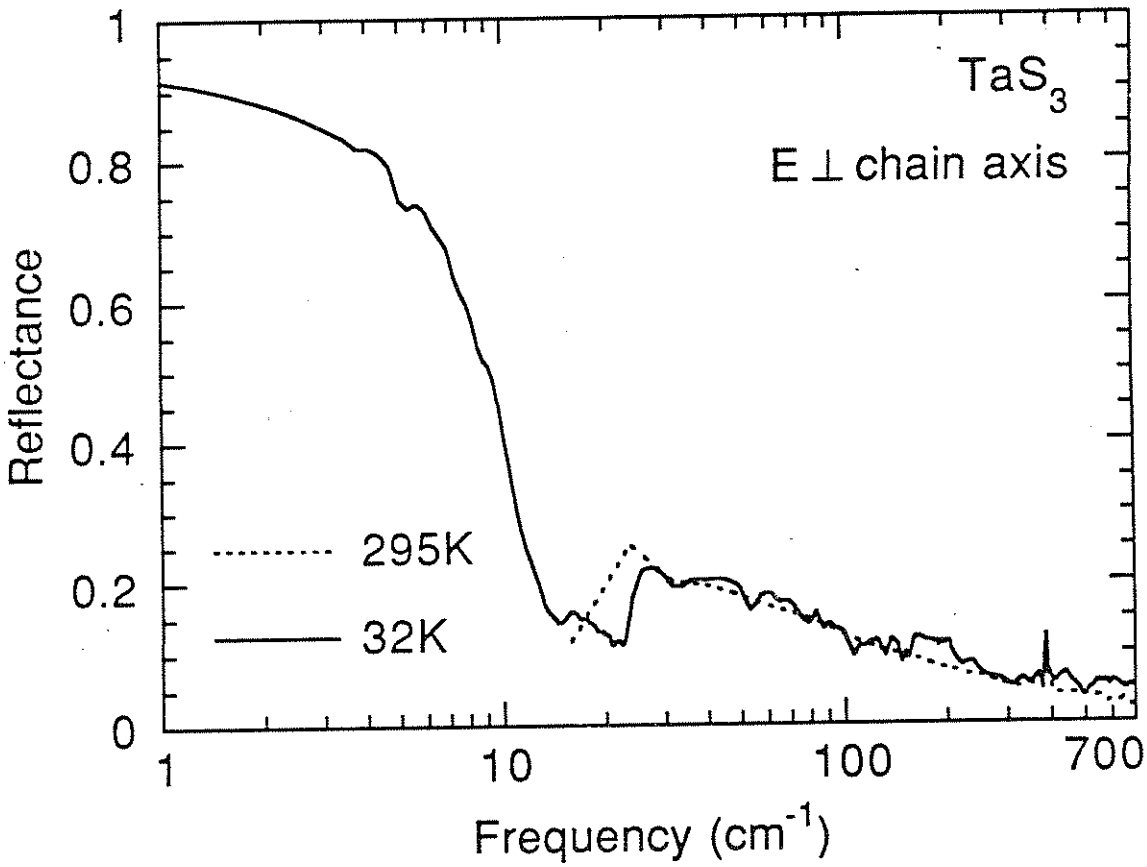
1
0.8
0.6
0.4
0.2
0
Reflectance
TaS3
E ⊥ chain axis
295K
32K
1
10
100
700
Frequency (cm-1)

Fig. 4-4. a) Re ε (dashed line) and Im ε (solid line) deduced by a Kramers-Kronig analysis of the 32K reflectivity data for TaS_3 for light polarized perpendicular to the long axis of the crystals.

b) Multi-oscillator fit to the dielectric function for TaS_3 for perpendicular polarization. Re ε_{fit} is the dashed line, and Im ε_{fit} is the solid line.

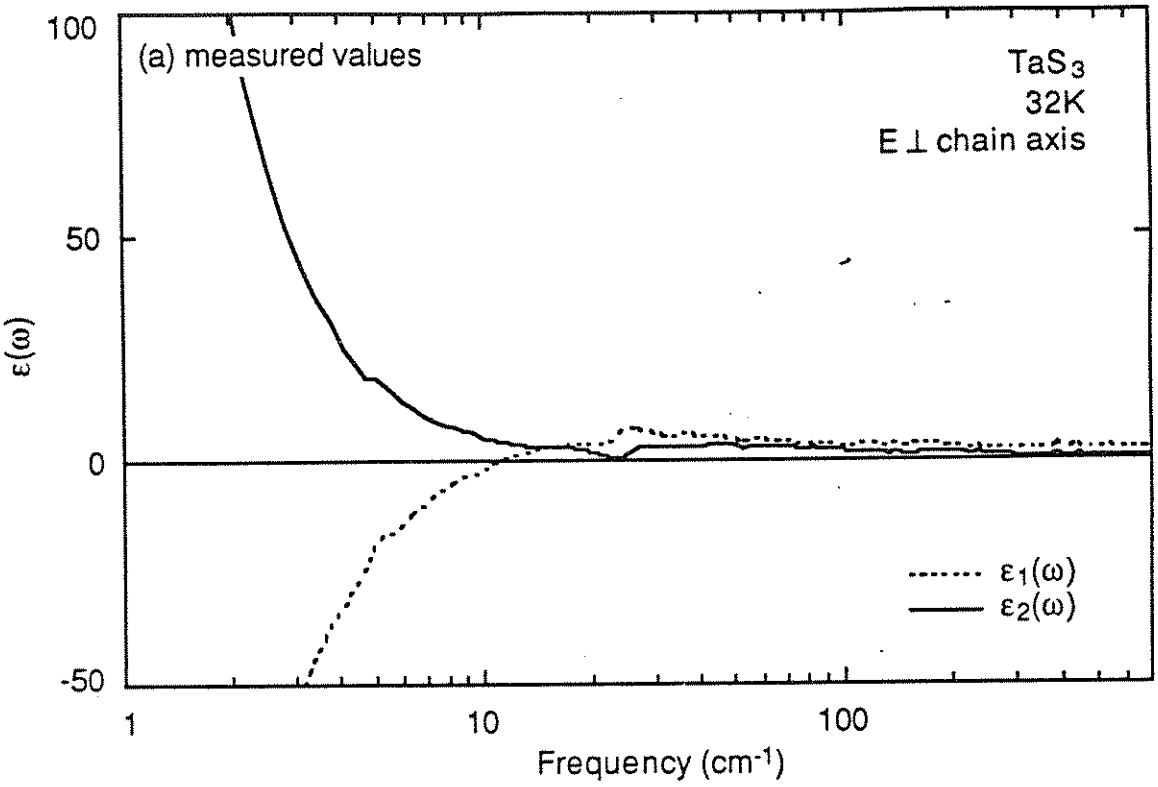
100
50
0
-50
ε(ω)
(a) measured values
TaS3
32K
E ⊥ chain axis
ε1(ω)
ε2(ω)
1
10
100
Frequency (cm-1)

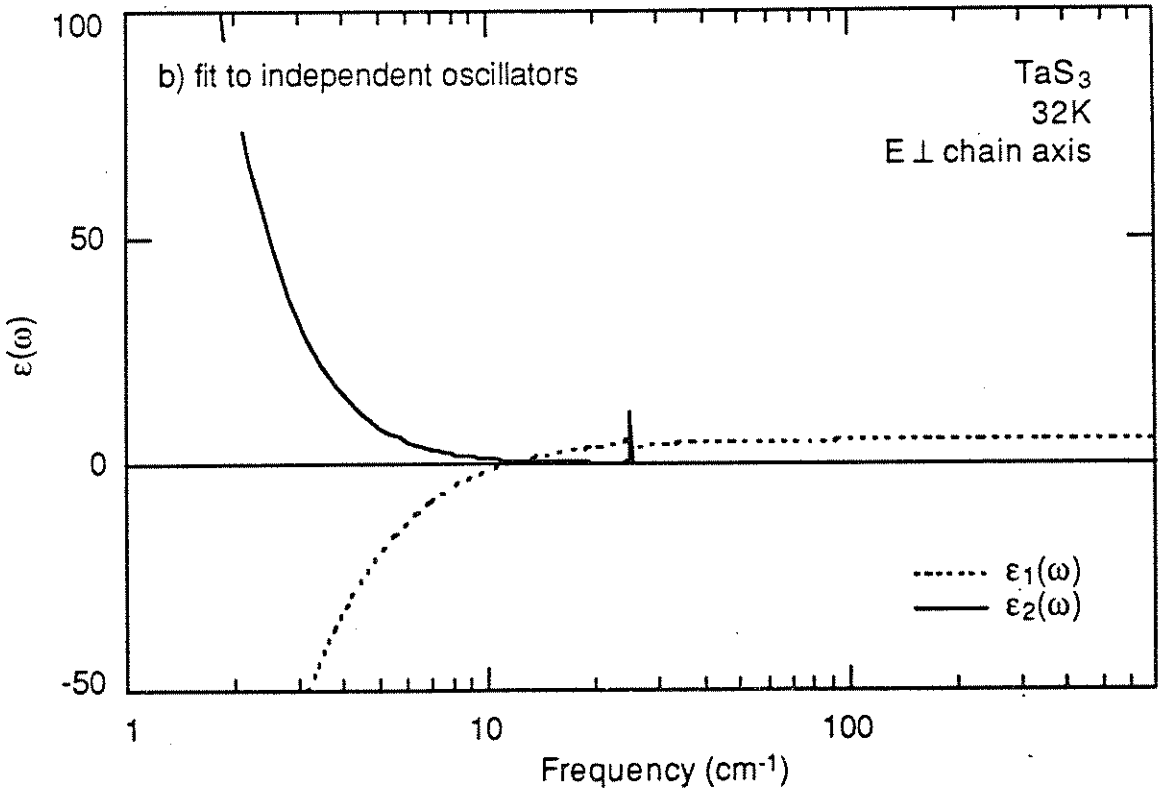
100
50
0
-50
ε(ω)
b) fit to independent oscillators
TaS3
32K
E ⊥ chain axis
ε1(ω)
ε2(ω)
1
10
100
Frequency (cm-1)

The solid lines in the Figure are real part of $\varepsilon(\omega)$ and the dashed lines are the imaginary part. The material is well described at room temperatures as a Drude metal. At low temperatures, the Drude conductivity is supplemented by phonon features that were fit with independent Lorentz oscillators. The parameters for the oscillators and the high temperature Drude fit are given in table 4-I. We note the absence of any strong features associated with the formation of the CDW other than a decrease in carrier density. In particular, there is no strong feature at 500cm^{-1} that might be associated with the feature seen in TaS_3 for this polarization by bolometric absorption techniques.[9]

B: Parallel polarization

Fig. 4-5 shows the measured FIR reflectance of TaS_3 at a variety of temperatures for incident light polarized parallel to the long axis of the crystals. The room temperature reflectance falls slowly and smoothly from near unity at 10cm^{-1} to 25% at 700cm^{-1}. Below 75cm^{-1}, the reflectance for parallel polarization is 4-5 times larger than that for perpendicular polarization. As the sample temperature falls, sharp reflectance features begin to emerge. Fig. 4-6 is a comparison of the reflectance of TaS_3 at room temperature (dashed line) and at 15K, in the CDW state well below T_p (solid line). Neglecting the low frequency Fabry-Perot oscillations due to the measurement apparatus, a substantial drop in the 15K reflectance begins at about 40cm^{-1}, culminating in a sharp fall from about 75% at 60cm^{-1} to about 6% at 76cm^{-1}. This dramatic reflection edge near 70cm^{-1} begins to develop at about 200K, just below T_p, and it sharpens continuously as the temperature is lowered. Beyond the reflectance edge, there is a series of narrow peaks in the reflectance at 83, 89, and 92cm^{-1} followed by a broad maximum centered at 150cm^{-1}. The low temperature reflectance stabilizes to about 9% at 300cm^{-1} and remains featureless and flat out to 700cm^{-1}. Again, we note the absence

Fig. 4-5. Reflectance versus frequency for TaS_3 at room temperatures and a series of temperatures below the Peierls transition Tp. The incident light was polarized parallel to the long axis of the crystals. The curves have been offset for clarity.

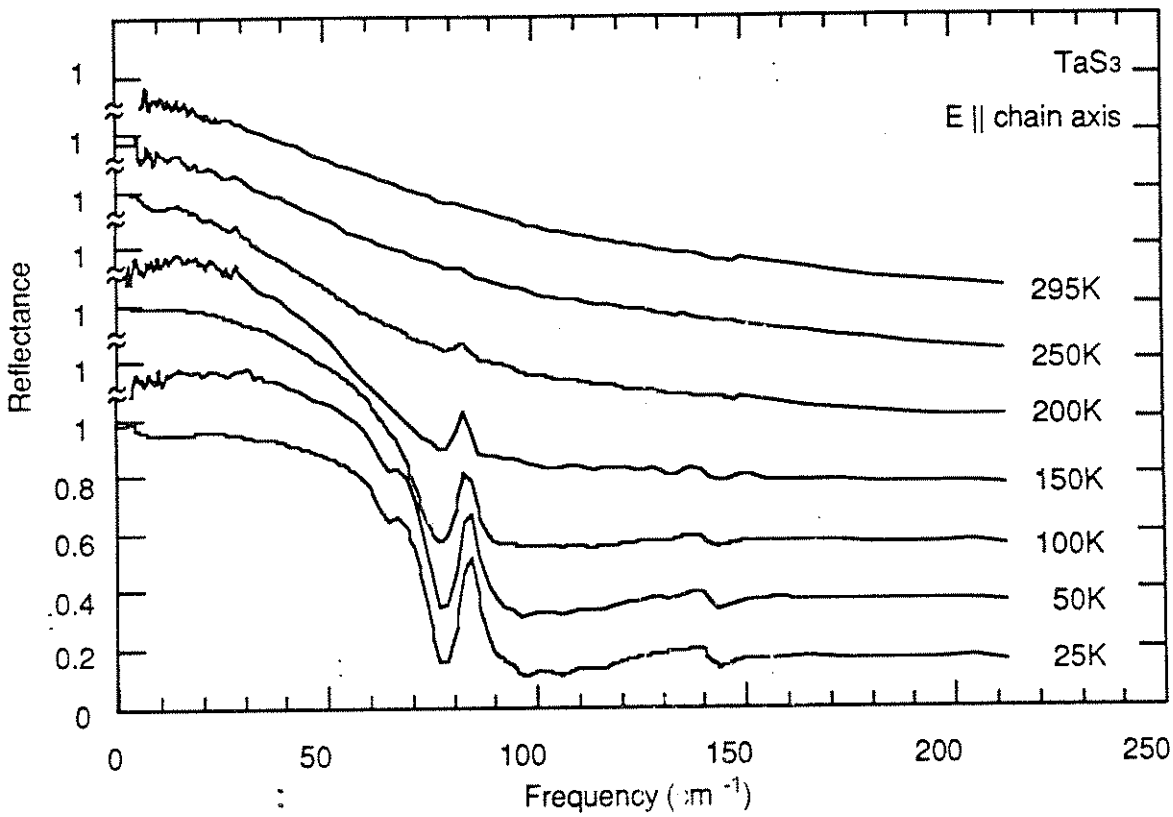
TaS3
E || chain axis
295K
250K
200K
150K
100K
50K
25K
Reflectance
1
0.8
0.6
0.4
0.2
0
0
50
100
150
200
250
Frequency (cm -1)

Fig. 4-6 Reflectance versus frequency for TaS_3 at 15K and 295K. The triangles are reflectances calculated from microwave frequency conductivities measured at 30 K in Reference 5.

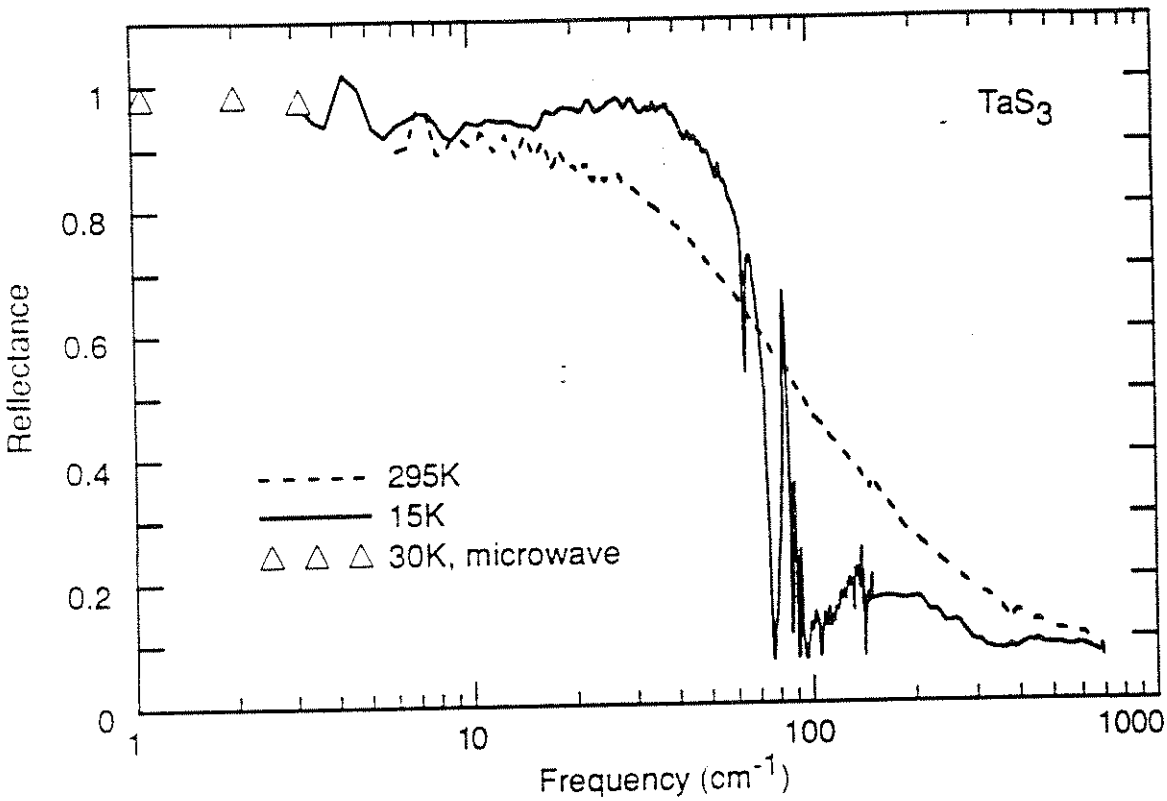
TaS3
295K
15K
30K, microwave
Reflectance
Frequency (cm-1)
0
0.2
0.4
0.6
0.8
1
1
10
100
1000

of any outstanding feature near 500cm^{-1} that might be associated with the 500cm^{-1} anomaly[9] observed in transverse-polarized bolometric absorption spectra of TaS_3.

Repeated efforts were made to determine the reflectance beyond 700cm^{-1}. Absorption measurements using a TaS_3 crystal as a bolometric detector of monochromatic light[8, 9] indicate that gap absorption should begin above 500cm^{-1}. The intensity of the interferometer signal is very low at high frequencies because of absorption lines in the beamsplitters and windows, and the accuracy of the spectra depends crucially on the alignment of the .000125" mylar beamsplitter. Though some of our measurements indicated reflectance features that might be associated with the edge of the Peierls gap, these results could not be repeated consistently enough to firmly establish that conclusion.

Kramers-Kronig analysis: the dielectric function of TaS_3

The complex dielectric function, $\varepsilon(\omega)$, is most directly obtained from the reflectance via a Kramers-Kronig calculation, for which it is desirable to have reflectance data over as wide a frequency range as possible. For this purpose we have generated effective reflectance data for frequencies below our experimental limit of 3cm^{-1} by converting microwave conductivity data previously measured[5] on TaS_3 to reflectance. These microwave data points are shown as triangles in Fig. 1; they agree well with the trend of our measured reflectance at low frequencies.

The Fabry-Perot oscillations in our data between 3 and 11cm^{-1} have been smoothed. These features are due to reflection from the slightly elevated rim of the Eccosorb baffle covering the copper sample holder. The oscillations are nearly independent of temperature and the spacing between reflectance maxima is consistent with the thickness of the baffle. They die

away at higher frequencies as the sample holder becomes effectively a better absorber. Such an artifact cannot be fully removed by the normalization procedure. A line drawn smoothly through the middle of the oscillations should give the true reflectance, and such a line agrees well with the reflectance derived from the microwave conductivity. We used such smoothing in generating the dielectric constant discussed below. Kramers-Kronig transforms performed with and without such smoothing indicate that smoothing the oscillations has no effect on the dielectric constant calculated above 12 cm^{-1}.

The Peierls gap[8] is expected to affect the reflectance above 700cm^{-1}. Modelling of this gap was found to have little effect on the dielectric function calculated at lower frequencies, so the high frequency reflectance was simply continued at its 700cm^{-1} value. The reflectance was smoothly reduced to zero with a ω^{-4} frequency dependence above 10000cm^{-1}.

Fig. 4-7 shows the complex dielectric function $\varepsilon(\omega)$ for TaS_3 calculated from the smoothed and extended 15K reflectance. The vertical scale has been expanded above 50cm^{-1} to show detailed structure at high frequencies. The inset shows the low frequency behavior of $\varepsilon(\omega)$ more clearly. The Figure shows that ε_1 crosses from its large positive value at zero frequency to negative values at about 0.5cm^{-1}, reflecting the pinned acoustic phason mode near this frequency. At higher frequencies, ε_1 then recovers and slowly climbs to another zero crossing that corresponds to the dramatic infrared reflectance edge we observe between 70 and 80cm^{-1}.

Aside from the dominant phason mode observed below 1cm^{-1} in Fig. 4-7, there are several other identifiable modes that modify the gradual rise in ε_1 and affect the location of the zero crossing. To determine the relative

Fig. 4-7 Re ε (dashed line) and Im ε (solid line) deduced by a Kramers-Kronig analysis of the 15K reflectivity data for TaS_3. Above 50 cm^{-1}, the vertical scales are expanded by a factor of 10.

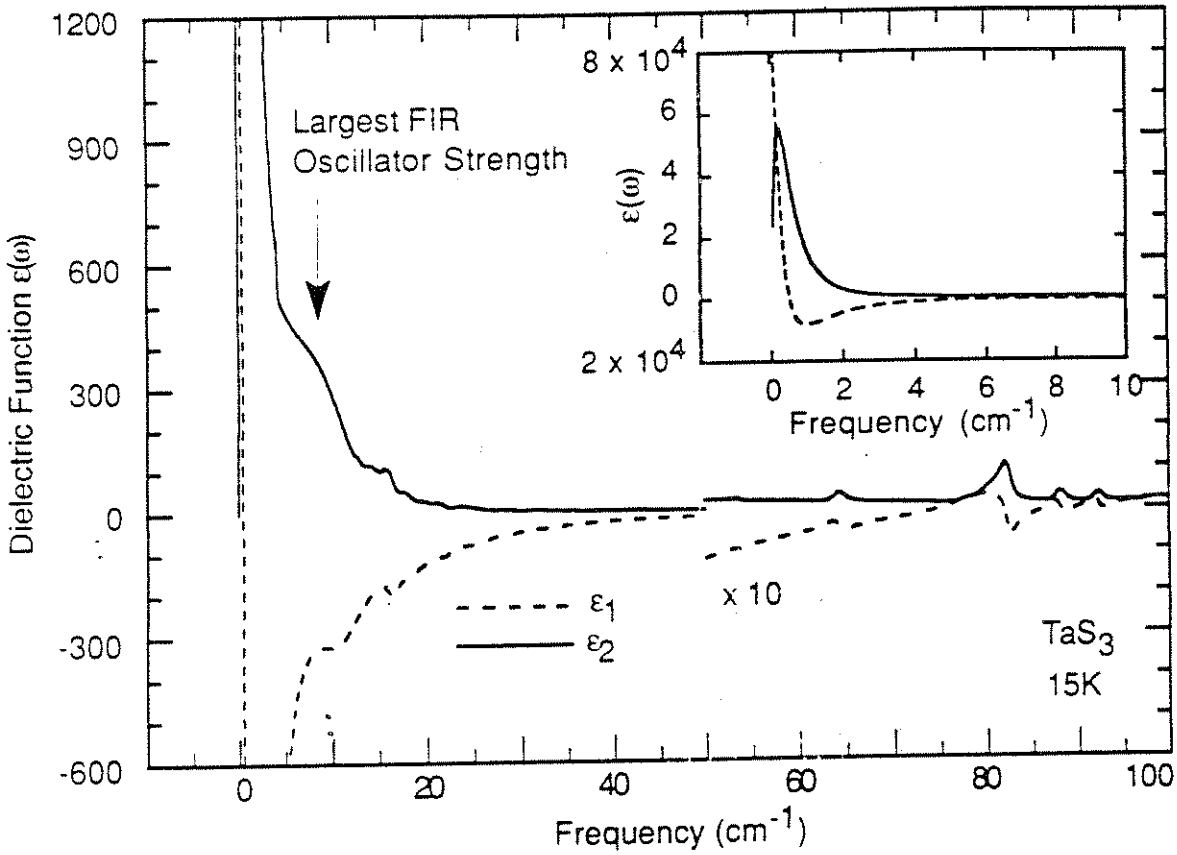
Largest FIR
Oscillator Strength
Dielectric Function ε(ω)
Frequency (cm^{-1})
ε$_1$
ε$_2$
x 10
TaS$_3$
15K
ε(ω)
Frequency (cm^{-1})

strengths of these smaller modes, we fit them to independent Lorentz oscillators and a background dielectric constant ε_∞:

$$\varepsilon_1(f) = \varepsilon_\infty + \sum_i S_i \frac{(1-(\frac{f}{f_i})^2)}{(1-(\frac{f}{f_i})^2)^2 + (\frac{f}{f_i^2\tau_i})^2} \qquad (4\text{-}1)$$

$$\varepsilon_2(f) = \sum_i S_i \frac{\frac{f}{f_i^2\tau_i}}{(1-(\frac{f}{f_i})^2)^2 + (\frac{f}{f_i^2\tau_i})^2} . \qquad (4\text{-}2)$$

The fitting parameters for the ith mode are the mode frequency f_i, damping time τ_i, and static polarizability S_i. The charge density n, mass m*, and charge e* for each mode are related to the oscillator strength Ω_p^2 by the relation:

$$\Omega_p^2 = \frac{4\pi n e^{*2}}{m^*} = (2\pi f_i)^2 S_i . \qquad (4\text{-}3)$$

Table 4-I gives the fitting parameters for all the prominent oscillation modes below 100cm^{-1} that respond to light polarized parallel to the long chain axis. (The table also lists the parameters used to generate the fit to the $\varepsilon(\omega)$ for perpendicular polarization shown in Fig. 4-4.) The strongest mode lies near 8.9cm^{-1} and is marked by an arrow in Fig. 4-7. By considering the uncertainties in the measurement and the smoothing we establish an upper limit $\Omega_p^2 \leq 6.8 \times 10^{26}$ on its oscillator strength, a factor of 40 or more smaller than that of the giant FIR mode[2] in $(TaSe_4)_2I$ at 38cm^{-1}. All the modes at frequencies greater than 60cm^{-1} have oscillator strengths $\Omega_p^2 \leq 9.0 \times 10^{25}$.

TABLE 4-I. Parameters from the fit of Lorentz oscillators to the conductivity of TaS_3

a) E || long axis of crystals

Mode frequency f_i (cm^{-1})	Static Polarizability S_i	Damping time (cm)	Oscillator strength $(2\pi f_i)^2 S_i$ (s^{-2})
.61	73250	.71	9.70×10^{26}
8.88	243.8	.14	6.83×10^{26}
15.4	1.27	.33	1.07×10^{25}
64.3	.16	.35	2.35×10^{25}
81.7	.36	.28	8.53×10^{25}
88.6	.08	.37	2.23×10^{25}
92.6	.05	.63	1.52×10^{25}

b) E ⊥ long axis of crystals

Mode frequency f_i (cm^{-1})	Static Polarizability S_i	Damping time (cm)	Oscillator strength $(2\pi f_i)^2 S_i$ (s^{-2})
0 (Drude)		0.63	2.45×10^{25}
24.9	5.6×10^{-2}	8.18	1.2×10^{24}

Discussion

A: The conductivity of TaS_3 and $(TaSe_4)_2I$

Our FIR measurements on TaS_3 essentially complete the excitation spectrum for this material. In Fig. 4-8, a comparison is made between the real part of the ac conductivity $\sigma(\omega)$ of TaS_3 and that of $(TaSe_4)_2I$ over a wide frequency range. The TaS_3 data in Fig. 4-8a near the Peierls gap are an approximate conversion from the bolometric absorption spectrum published previously by another group.[8] The line below 2×10^{13}Hz is the FIR conductivity determined from this study. It was calculated as described above using a low frequency reflectance based on the 30K microwave data.[5] Other reasonable reflectance extrapolations can shift the frequency of the pinned mode by a factor of 3; in all cases, the conductivity below $3cm^{-1}$ is in qualitative agreement with a low temperature extrapolation of the microwave measurements. Exact agreement is not expected since the pinning frequency varies with impurity concentration and is consequently sample dependent. Dielectric relaxation occurs at frequencies below those shown in the Figure. Fig. 4-8b shows a similar plot of $\sigma(\omega)$ for the related CDW conductor $(TaSe_4)_2I$, obtained from the literature.[2, 17, 18] The intrinsic conductivity modes are identified in the Figure, along with the giant FIR mode at approximately 10^{12}Hz.

A comparison of Figs. 4-8a and 4-8b reveals the dramatic difference between the excitation spectra of these two similar CDW materials. Clearly, no giant FIR mode exists in TaS_3. The reflectance edge is a result of a zero crossing of the real part of the dielectric function, but that zero crossing is primarily a manifestation of the microwave pinned acoustic phason mode rather than any single mode at infrared frequencies. The largest FIR mode in TaS_3 has a relatively small oscillator strength.

Fig. 4-8 a) Re σ for TaS_3. This work is the solid line (intermittently dashed below the measurement limit of 3 cm^{-1}). The dashed line schematically represents the Peierls gap from Ref. 8.

b) Re σ for $(TaSe_4)_2I$ from the literature. The triangles (connected by a line to guide the eye) represent microwave measurements at 50K from Ref. 17, the solid line is calculated from the FIR oscillators reported in Ref. 2, and the dashed line represents the conductivity near the Peierls gap measured at 140 K in Ref. 18.

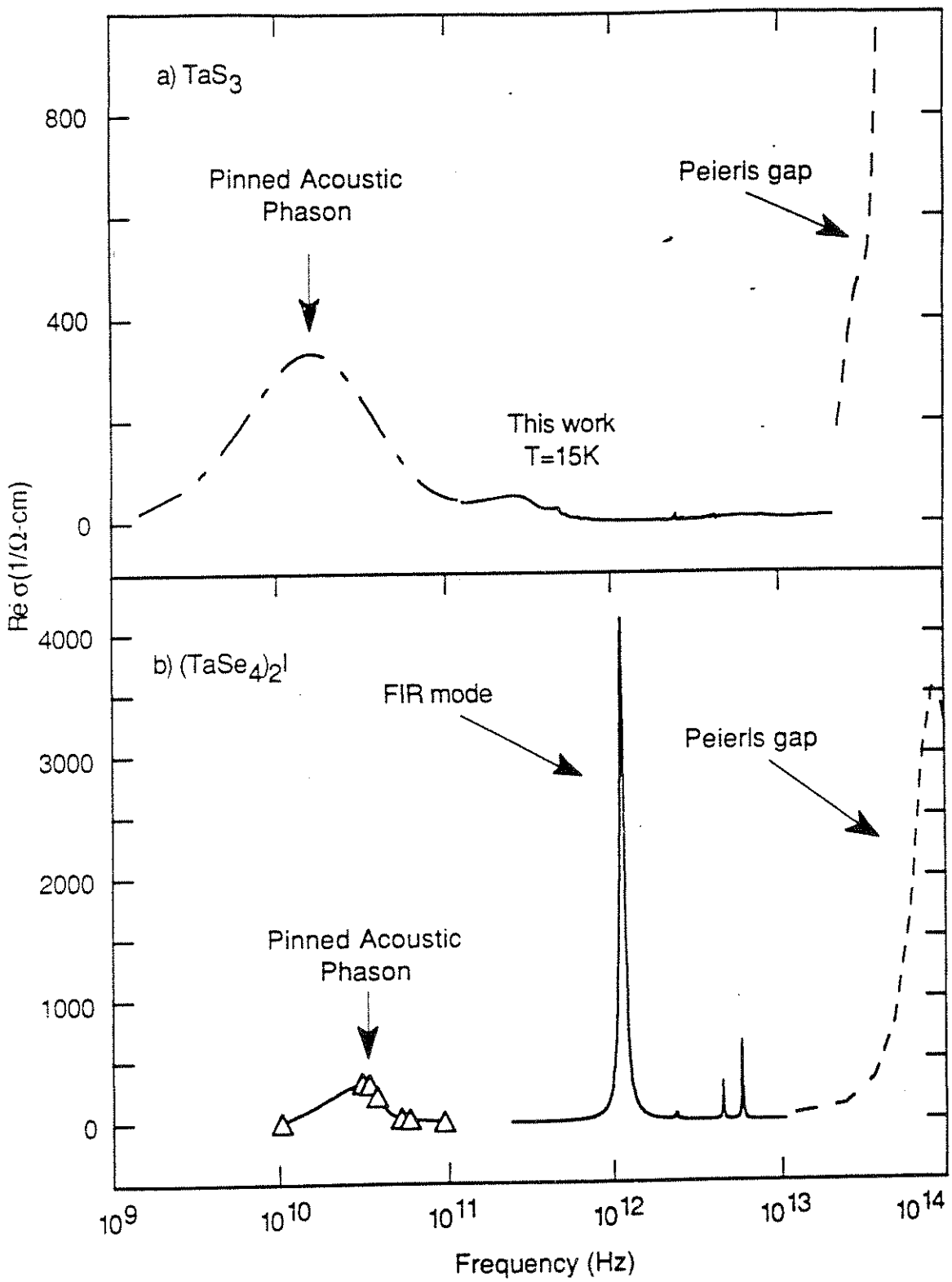
a) TaS3
800
400
0
Pinned Acoustic Phason
Peierls gap
This work
T=15K
Re σ(1/Ω-cm)
4000
3000
2000
1000
0
b) (TaSe4)2I
FIR mode
Peierls gap
Pinned Acoustic Phason
10^9
10^10
10^11
10^12
10^13
10^14
Frequency (Hz)

B: Models of the FIR mode

We now discuss the implications of these results for general models of CDW conduction. None of the existing models fully explains the conductivity of all three materials. The small size and low frequency of the 8.9cm^{-1} mode in TaS_3 place constraints on any theory that describes it as a generic mode of similar origin to the large FIR mode seen in $(TaSe_4)_2I$ and $K_{0.3}MoO_3$. To describe the giant FIR mode, Sherwin *et al.*[2] considered an "optical phason" argument similar to the "first harmonic phason" described earlier by Walker.[19] Lyons and Tucker[4] have attributed the giant FIR mode to coherent oscillations of the CDW phase in tiny regions surrounding impurities. Because each of these models assumes only the presence of a CDW and makes no reference to the crystal structure, each predicts a mode should be present in all CDW materials. The optical phason has a frequency given by[2]

$$f_{OP} = \left(\frac{2}{\pi}\right)\left(\frac{2k_F v_{ph}}{2\pi}\right) \tag{4-4}$$

where k_F is the Fermi wavevector and v_{ph} is the phason velocity. The Lyons-Tucker impurity mode has a frequency[4]

$$f_{LT} = \frac{v_{ph}\xi_{\|}}{4}\left(\frac{A_0}{2\xi_{\perp}^2}\right) \tag{4-5}$$

where $\xi_{\|}$ and $\xi_{\perp}$ are the phase coherence lengths parallel and perpendicular to the CDW wavevector and A_0 is the cross-sectional area per conducting chain. For o-TaS_3, the unit cell of 24 chains has dimensions (38.804Å, 15.173Å, 3.340Å) and the CDW wavevector is $\vec{q}$=(.5, .125, .25).[1] This gives

$k_F = 2.38\times10^7 cm^{-1}$ and $A_0 = 2.45\times10^{-15} cm^2$. The coherence length asymmetry $(\xi_{\|}/\xi_{\perp}) \sim (\sigma_{\|}/\sigma_{\perp})^{1/2} \approx 10$ and the Fröhlich mass $m_{Fr} \approx 1000 m_b$ are given by low frequency transport experiments.[20] Combining these estimates with the Lee-Rice-Anderson[21] expression for the phase velocity $v_{ph} = v_F\sqrt{m_b/m_{Fr}}$, we find the estimated optical phason frequency is $f_{OP} \approx 250 cm^{-1}$ in TaS_3, and the mode described by Lyons and Tucker[4] should appear at about $f_{LT} \approx 85 cm^{-1}$. In addition to predicting a mode frequency far higher than that observed, neither model explains why the oscillator strength of a mode in TaS_3 should be more than an order of magnitude smaller than in the other two materials. Though these mechanisms may possibly account for the small high-frequency features in $\varepsilon(\omega)$, they do not accurately describe the conductivity of TaS_3 and are thus unlikely explanations for the giant mode seen in other CDW materials.

Recently, one additional model has been proposed[22] that predicts a generic FIR mode in CDW conductors. The model predicts a mode at frequencies higher than the pinned acoustic phason frequency as a consequence of interactions between the CDW and impurities. The model will be discussed in the context of our studies of doped $(TaSe_4)_2I$ in Chapter 5.

A different type of model suggests that the giant FIR mode seen in $(TaSe_4)_2I$ and $K_{0.3}MoO_3$ should be entirely absent in TaS_3.[23, 24] This "zone folding mode generation" model is consistent with our results if the small $8.9 cm^{-1}$ mode in TaS_3 is entirely unrelated to the giant FIR mode in the other materials. Mode generation through zone-folding produces the rich phonon spectrum observed by Raman spectroscopy in semiconductor superlattices[25] and the spin wave spectrum expected for magnetic superlattices;[26] it was originally considered by Sugai, Sato, and Kurihara in their studies[23, 24] of the Raman modes in $(TaSe_4)_2I$. In contrast to the magnetic and semiconductor

superlattice systems, which have relatively featureless dispersion curves before the zone folding, CDW materials have a soft Kohn anomaly at $q=2k_F$. In $(TaSe_4)_2I$, a structural distortion expands the unit cell and shrinks the Brillouin zone so that the soft Kohn anomaly phonon is located near the edge of the second Brillouin zone. When the phonon dispersion curve is folded in the reduced zone scheme, the soft mode lies on a transverse optical branch above the transverse acoustic branch. As the temperature is decreased toward T_p, the TO Kohn anomaly begins to soften and triggers the CDW distortion in the usual way, but the interaction between the TO branch and the lower energy TA branch forces the TA branch to $\omega=0$ first. (Additionally, the degenerate modes at $q=\pm 2k_F$ are mixed to yield both a Raman and an infrared active mode for each branch.) In these materials the observed modes are understood as follows: the pinned acoustic phason mode seen at microwave frequencies arises from the TA anomoly, the giant FIR mode from the TO Kohn anomaly, and the two small higher frequency modes from two more TO branches also produced by the folding of the original dispersion curve.

A situation analogous to that just described for $(TaSe_4)_2I$ could occur in any CDW material with $2k_F>\pi/a$ (such as $K_{0.3}MoO_3$) with a FIR mode arising through the interaction of the Kohn anomaly phonon with other phonon branches folded into a common region of the Brillouin zone. No such mode should be present in TaS_3 (or $NbSe_3$), where the chains are uniform and the Kohn anomaly is always on the lowest lying phonon branch.

Though zone-folding mode generation predicts the qualitative difference in $\sigma(\omega)$ between TaS_3 and $(TaSe_4)_2I$ shown in Fig. 4-8, the plausability of the model awaits a mapping by neutron scattering of the phonon dispersion curve in $(TaSe_4)_2I$. In addition, the model requires a separate explanation for the $8.9cm^{-1}$ mode in TaS_3. Initial microwave

measurements[5] indicate that below 60K the CDW is in a glassy state and the conductivity is best described by a broad distribution of pinning energies rather than a single pinning frequency. Within this picture, our measurements suggest that in TaS_3 at low temperatures this distribution is bi-modal, with prominent contributions at 0.5 and 8.9cm^{-1}. The 8.9cm^{-1} mode weakens rapidly as the temperature is raised from 15K and appears to be absent by 100K.

Conclusion

In summary, we have measured the reflectance of TaS_3 and find the FIR conductivity modes to be much smaller than those in two previously measured CDW materials. Though a zone folding mode generation model may be consistent with this qualitative difference between the various materials, several current models that predict a universal FIR mode in CDW conductors are inconsistent with these results.

References

1. L.P. Gor'kov and G. Grüner. *Charge Density Waves in Solids* (North-Holland, Amsterdam, 1989).

2. M.S. Sherwin, A. Zettl and P.L. Richards, Phys. Rev. B **36**, 6708 (1987).

3. S. Donovan, Y. Kim, B. Alavi, L. Degiorgi and G. Grüner, Solid State Comm. **75**, 721 (1990).

4. W.G. Lyons and J.R. Tucker, Phys. Rev. B **40**, 1720 (1989).

5. S. Sridhar, D. Reagor and G. Grüner, Phys. Rev. B **34**, 2223 (1986).

6. Wei-yu Wu, L. Mihály, George Mozurkewich and G. Grüner, Phys. Rev. Lett. **52**, 2382 (1984).

7. S. Sridhar, D. Reagor and G. Grüner, Phys. Rev. B **55**, 1196 (1985).

8. S.L. Herr, G. Minton and J.W. Brill, Phys. Rev. B **33**, 8851 (1986).

9. G. Minton and J.W. Brill, Solid State Comm. **65**, 1069 (1988).

10. Fused quartz tubes, Heraeus Amersil, Inc., Hayward, CA 94545

11. R.E. Thorne, T.L. Adelman, J. McCarten, M. Maher and A. McDowell, Phys. Rev. B **40**, 4205 (1989).

12. Sulfur powder, 99.999% purity, Fluka Chemical Corp., Hauppauge, NY 11778

13. 0.5mm Tantalum wire, m4N7 purity, Alfa Products, Morton Thiokol, Inc., Danvers, MA 01923

14. Castin' Craft clear casting resin, ETI, Fields Landing, CA 95537.

15. Max Born and Emil Wolf, in *Principles of Optics*, ed., (Pergamon Press, Oxford, 1970), p. 631.

16. Permacel black TFE Fluorocarbon electrical tape, Avery International Co., New Brunswick, NJ 08903

17. Tae Wan Kim, D. Reagor, G. Grüner, K. Maki and A. Virosztek, Phys. Rev. B 40, 5372 (1989).

18. H.P. Geserich, G. Scheiber, M. Dürrler, F. Lévy and P. Monceau, Physica B **143**, 198 (1986).

19. M.B. Walker, Can. J. Phys. **56**, 127 (1978).

20. G. Grüner and A. Zettl, Phys. Rep. **119**, 117 (1985).

21. P.A. Lee, T.M. Rice and P.W. Anderson, Solid State Comm. **14**, 703 (1974).

22. L. Degiorgi and G. Grüner, Bull. Am. Phys. Soc. **36**, 608 (1991).

23. S. Sugai, M. Sato and S. Kurihara, Phys. Rev. B **32**, 6809 (1985).

24. Shunji Sugai, Susumu Kurihara and Masotoshi Sato, Physica B **143**, 195 (1986).

25. C. Colvard, R. Merlin, M.V. Klein and A.C. Gossard, Phys. Rev. Lett. **45**, 298 (1980).

26. E.L. Albuquerque, P. Fulco, E.F. Sarmento and D.R. Tilley, Solid State Comm. **58**, 41 (1986).

Chapter 5

Far Infrared Conductivity of $(Ta_{1-x}Nb_xSe_4)_2I$ alloys

Introduction

The previous chapter reports the measurement of the far infrared conductivity of the charge density wave conductor TaS_3. The distinctive features of the conductivity in this material provide key information about the nature of the giant FIR mode previously seen in $(TaSe_4)_2I$ and $K_{0.3}MoO_3$. First, we found that although TaS_3 has a simple Brillouin zone structure along the chain directions and is not expected to have any FIR modes due to folding of the phonon branches to the zone center, a small FIR mode does in fact occur in the material. Second, the size of the mode is remarkable. The appelation "giant" is clearly not descriptive of the FIR mode in TaS_3: the oscillator strength of the mode is only two percent of that for the modes in the other two materials. Finally, the mode in TaS_3 occurs at about $10cm^{-1}$, a lower frequency than the frequency of the large infrared modes in $(TaSe_4)_2I$ and the blue bronze. This low frequency is well above the resonant frequency of the pinned acoustic phason mode, yet well below the characteristic frequencies associated with amplitudons,[1] optical phasons,[2-4] and distortions of the CDW near strong impurity pinning sites.[5] All the theories describing a generic FIR mode in CDW conductors fail to predict the small size and frequency of the mode in TaS_3, and yet the very existence of a small mode makes the zone-folding structural explanation for the mode[5-7] unsatisfying as well.

In this chapter we continue our investigation of the FIR mode by measuring the conductivity of $(Ta_{1-x}Nb_xSe_4)_2I$ alloys. Impurities in CDW materials break the translational invariance of the energy of the condensate and make the Fröhlich "superconductor" into an insulator with a strong

microwave pinning resonance. Intentional doping of the crystals with impurity atoms along the metallic chains can raise the frequency of the pinned acoustic phason mode into the low FIR range. By measuring the FIR reflectance we are able to investigate the interaction of the pinning resonance with the giant FIR mode. In general, we find that the size of the FIR mode is roughly independent of the dopant level, and that its frequency decreases slightly with increasing dopant level. These results are compared with a recent theory of the FIR mode[8, 9] that shows how high frequency oscillator strength associated with polarizable impurities can cause lower frequency resonances. The conductivity of our most highly doped sample can be fit by the new theory. We will evaluate the theory in detail and conclude by discussing the difficulties still presented by the FIR mode in CDW conductors.

Crystal growth and sample characterization

The crystals of $(Ta_{1-x}Nb_xSe_4)_2I$ alloys were grown in a two step process. First, tantalum and niobium powders were sintered to intimately mix them, and the resulting material then served along with added selenium and iodine as starting materials for the growth of the CDW crystals. For the sintering step, we thoroughly mixed high-purity tantalum[10] and niobium[11] powders and sealed the mixture in evacuated 1cmx4cm quartz ampules.[12] These quartz tubes and the larger ones used for crystal growth were new, but not washed with acids or organic solvents. Before the sintering step, the tubes were firepolished, divided into sections, and baked under $1x10^{-6}$ torr vacuum for 24 hours at 850°C to remove the hydrogen, water vapor, and other gases emitted by fresh quartz.[13] The powders were baked in the sealed ampules for 24 hours at 900°C. The sintering produced a hard, granular pellet. We crushed the pellet into small pieces and powder and combined them in

2.5cmx20cm quartz tubes with the proper stoichiometric amount of selenium[14] and half the stoichiometric amount of iodine[15] necessary for the $(TaSe_4)_2I$ crystals. If the full proportion of I_2 is used, it later condenses on the faces of the crystals and on the walls of the tube when they cool, and the iodine fouls the crystals irreparably. We sealed the tubes with a hydrogen-oxygen torch after flushing them with argon five times and evacuating them to 150mtorr.

Each quartz tube was placed in an oven with dual concentric nichrome heating coils wrapped on thick quartz support tubes. The inner coil spanned the entire length of the sample tube. A controller connected to a thermocouple near the empty end of the sample tube regulated the temperature within the coil at 425°C. The shorter outer coil encompassed only the part of the sample tube containing the starting materials. A second temperature controller was set to provide a maximum temperature of 590°C within the short heating coil. In the region where the crystals grew within the sample tube, the temperature gradient was quite sharp, from 580°C to 490°C in 2cm. Large $(TaSe_4)_2I$ crystals grew in this double-wound oven in about 36 hours, whereas substantial crystal growth typically takes 7-10 days in conventional ovens with variably spaced nichrome windings and more gradual temperature gradients. A batch of $(TaSe_4)_2I$ grown from metal powders (rather than metal wires) typically contains many small, tightly intergrown crystals unsuitable for FIR reflectance studies. We avoided this problem by minimizing the number of nucleation sites caused by stray metal powder on the tube walls. This precaution along with the accelerated growth time in the double-wound oven produced large flat crystals relatively free of adjoining crystals. The face of one crystal incorporated in the 1.2% Nb-doped sample was almost 3mmx5mm. At the end of the growth period, the quartz

tubes were removed from the ovens and the hot end of the tube quickly quenched in water to condense the vaporized iodine away from the $(TaSe_4)_2I$ crystals.

Each FIR sample was prepared from crystals grown in a single tube to ensure that the impurity concentration within the sample is as uniform as possible. We prepared two samples of $(Ta_{1-x}Nb_xSe_4)_2I$, one with nominal impurity concentration x=.006 and one with x=.012. The values of x indicate the amount of niobium included in the original metallic sinter. The values of x were chosen to match those of samples whose microwave conductivity had been previously measured.[16] Of course, the amount of Nb introduced to the tube may be widely different from the amount actually incorporated in the $(TaSe_4)_2I$ crystals; we found that if the presintering step is eliminated and Ta and Nb wires are used rather than powders, the crystals contain very little niobium. We characterized the actual impurity level in the crystals by measuring the dc resistivity as a function of temperature. The CDW transition temperature T_P, the sharpness of the transition, and the value of the zero-temperature gap Δ are all affected by the impurity concentration. In particular, the transition temperature of pure samples (T_P = 263K) is reduced as impurities are introduced, with

$$\frac{dT_P}{dx} = -53\text{K/atomic \%} . \qquad (5\text{-}1)$$

This relation was determined by Kim *et al.*[16] in their studies of the microwave conductivity of $(Ta_{1-x}Nb_xSe_4)_2I$ alloys. They measured the actual impurity concentration of their samples using wet chemical methods. The residual impurity level of the nominally pure material could not be determined using their technique, but in other materials it is typically

10^{18} pinning sites/cm^3.[9, 16, 17] These microwave measurements provide the low temperature reflectance extrapolation used in our Kramers-Kronig analysis, and so we will compare our FIR samples with those of Kim *et al.* in some detail.

Part a of Fig. 5-1 shows the normalized resistance of crystals taken from the same preparation batches used in the FIR samples. Part b of the Figure shows the derivitive dln(R(T))/d(1/T) where R(T) is the dc resistance. The resistance was measured every half a degree Kelvin using standard four-probe techniques with sputtered gold contacts. The derivitive at a given temperature is the slope of a straight line fitted to the logarithm of the resistance at that temperature and at neighboring temperatures within 2K. There is a broad maximum in the derivitive for samples of $(Ta_{1-x}Nb_xSe_4)_2I$ with $x = .012$, and a much sharper peak at T = 244K for the more lightly doped $x = .006$ samples. Pure $(TaSe_4)_2I$ is a semiconductor at temperatures well below the Peierls transition, with $\rho \sim \exp(+\Delta/k_BT)$ and $d(\ln\rho)/d(1/T) = \Delta$. The resistance of the impurity-doped samples illustrated in the Figure clearly has a different behavior, with Δ continuing to decrease at temperatures as low as 120K. In this sense, our samples differ from those used in the microwave conductivity measurements of Kim *et al.*[16] For the latter samples, the gap saturates below about 140K, with $\Delta_{x=.006} = 1150$K and $\Delta_{x=.012} = 850$K. On the other hand, both sets of samples show similar behavior at higher temperatures. From Eq. (5-1), the actual impurity concentration within our samples with nominal doping x = .006 and x = .012 is about x = .0035 and x = .0075±.0015 respectively.† Though our samples are somewhat more lightly

† An error in the calibration of the temperature diode used in the R(T) measurement made the derivitive of the resistance unreliable between 214K and 230K. The peak of the broad maximum in the derivitive for the x=.012 sample falls in this range. In Fig. 5-1b, the derivitive values in this temperature range are smoothly interpolated.

Fig. 5-1. a) Resistance vs. temperature for $(Ta_{1-x}Nb_xSe_4)_2I$ crystals with $x = .012$ (solid line) and $x = .006$ (dashed line). The resistance in either case is normalized to the room temperature resistance.

b) $d\ln(R(T))/d(1/T)$ for the same two samples.

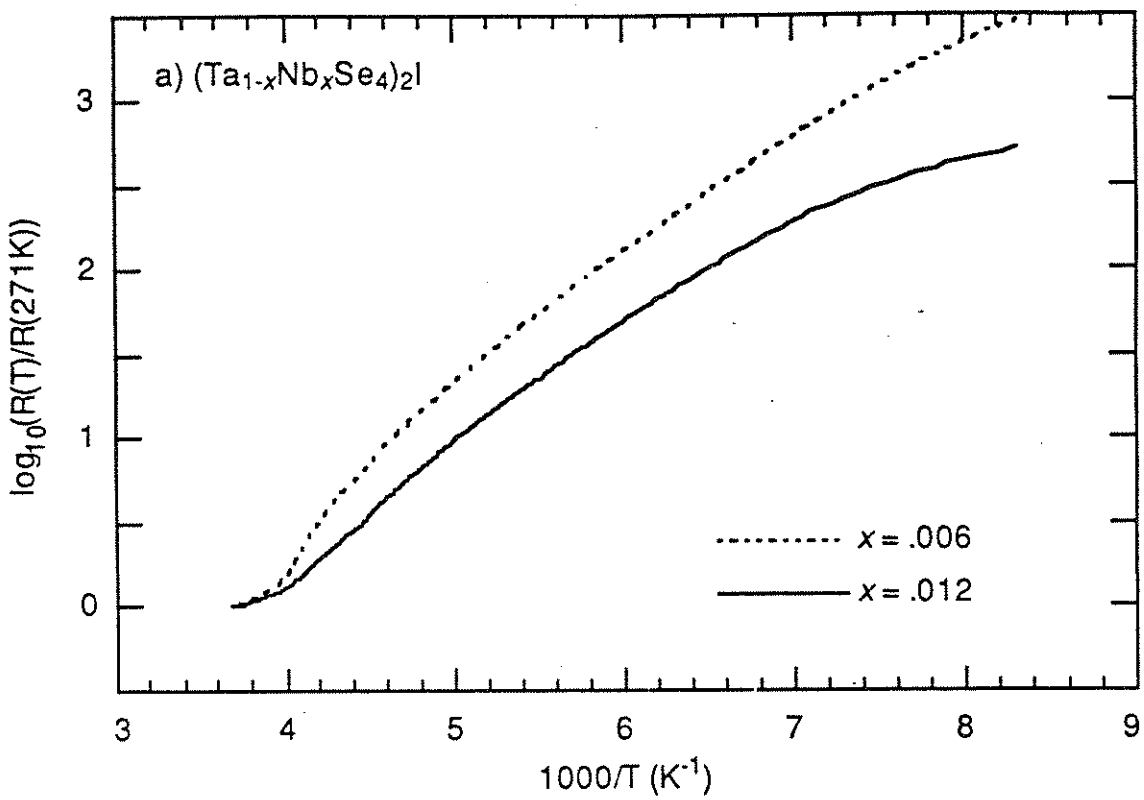
a) $(Ta_{1-x}Nb_xSe_4)_2I$
$\log_{10}(R(T)/R(271K))$
3
2
1
0
3
4
5
6
7
8
9
1000/T (K^{-1})
$x = .006$
$x = .012$

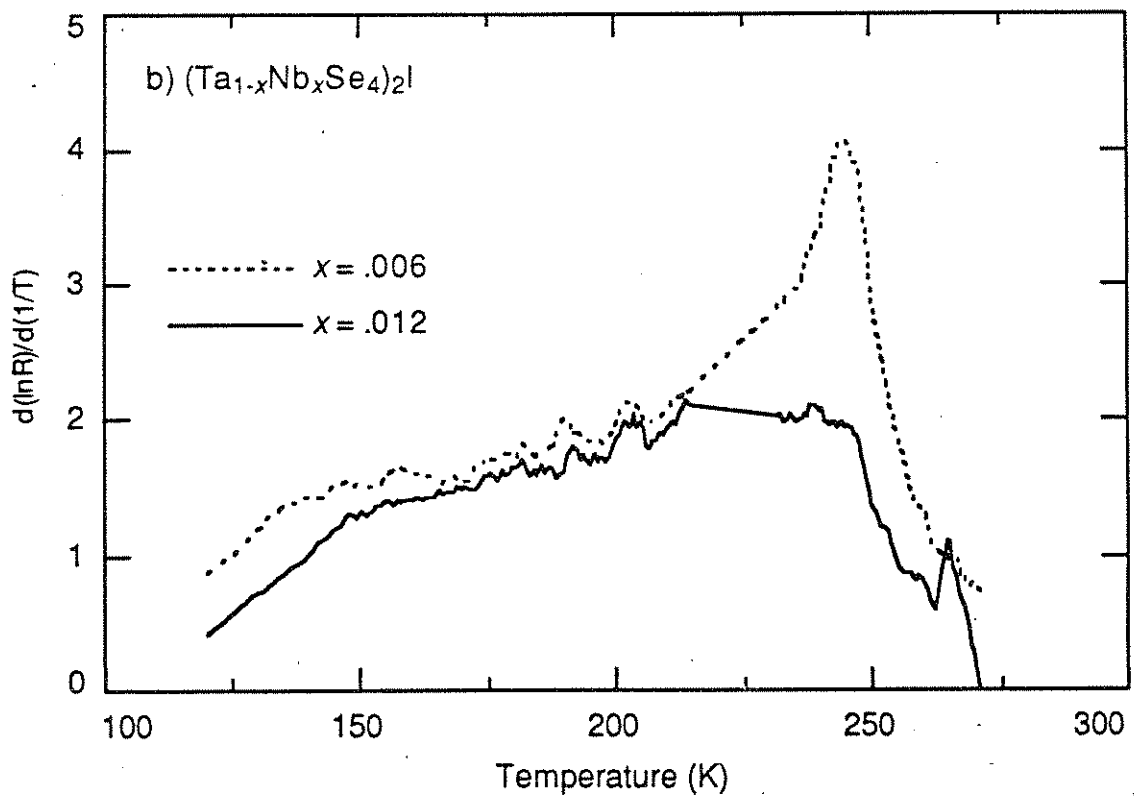
b) $(Ta_{1-x}Nb_xSe_4)_2I$
d(lnR)/d(1/T)
5
4
3
2
1
0
100
150
200
250
300
Temperature (K)
$x = .006$
$x = .012$

doped with impurities than those of Kim *et al.*, we will use their measured conductivities to generate the low temperature reflectance.

Mounting the samples

In Chapter Four we described mounting TaS_3 crystals for FIR reflectance measurements by saturating the many hand-aligned fibers with a plastic resin. In principle, the relatively large, planar faces of $(TaSe_4)_2I$ are better suited for FIR reflectance studies than those of fibrous TaS_3, but they still present many mounting challenges. Only ten to fifteen crystals are required for a typical sample, but the crystals have varying thickness and the front surfaces must be accurately aligned and immobilized in a plane. Because the crystal faces do not fill the entire aperture below the polarizer in the reflectance/transmittance apparatus, the measured reflectance of the samples must be normalized to account for the reduced sample area and the irregular geometry of the crystals. We accomplish this normalization by coating the crystal faces with sputtered gold (and scraping away the gold from the surrounding areas), then remeasuring the reflectance at room temperature. For this normalization to be accurate, the material holding the crystals in place must have extremely low reflectance. In the original FIR investigation of $(TaSe_4)_2I$, Sherwin *et al.*[3] formed a crystal mosaic by pressing warm wax around aligned crystals to immobilize them. They then scraped away part of the wax to expose the rear faces of the crystals and fastened the exposed rear faces with Stycast epoxy. The technique usually works, but it has several problems. Often the crystals shift and their alignment is spoiled as the paraffin is pressed around them. The volatile wax fouls the vacuum chamber when gold is sputtered or evaporated onto the crystals for the normalization measurements. Finally, the wax-over-Stycast combination surrounding the

crystals has a fairly high reflectance, near 10%. In the remainder of this section, we describe a modification of this mounting technique that addresses these problems.

In our modified mounting technique, the $(TaSe_4)_2I$ crystals are potted in a quick-setting plastic binder. The plastic cannot be simply poured around the samples, though; the crystals float, their alignment is ruined, and their faces get covered with plastic. To prevent this problem, we temporarily affix the crystals to a glass slide covered with a thin film of paraffin. A drop of hot paraffin is deposited onto the slide and then quickly wiped across the glass surface with another glass slide. The latter slide is slightly elevated over the first by strips of teflon tape along the edges, and the cold wax film is about .001" thick. $(TaSe_4)_2I$ crystals with large planar faces are removed from a freshly opened quartz tube and aligned face down within a 7/16" circle on a glass slide. After several crystals are in place, the slide is heated from below by the tip of a soldering iron for about 1s. This melts the paraffin locally for a moment, and the crystal faces stick to the slide when the wax resolidifies. Surface tension and gravity draw the flat crystal face tightly against the glass slide when the paraffin is liquid. The displaced wax forms a meniscus around the edge of the crystal that prevents subsequent accumulation of plastic on the crystal face. More crystals are then placed on the slide, and the alignment and local-melting process is repeated until a circular area slightly less than 7/16" diameter is filled with well aligned crystals. We then turn the slide over and examine it under a microscope. We check the meniscus of paraffin surrounding each crystal and ensure that the flat crystal face is entirely surrounded by wax. The orientation of any misaligned crystals can be adjusted, again by local heating of the slide with a soldering iron.

A cylindrical die of aluminum lined with teflon tape is placed over the crystals and fastened tightly to the glass slide. The plastic casting compound[18] is then mixed and poured in around the the crystals. The compound is a dry powder mixed in 2:1 ratio with a solvent, and we let it thicken for about six minutes prior to pouring it over the crystals. The reflectance of the plastic is less than 5% over most of the FIR frequency range, and the material has no strong conductivity modes. The plastic cures at room temperature in about an hour. The glass slide is then released from the crystals by heating it from below with running hot water. We remove traces of residual wax from the crystal surfaces by rinsing them in running 55°C water for about 30s. We found no evidence that such a water wash injures the crystals by intercalation, removal of iodine, or physical damage: the crystals were not visibly changed, the FIR reflectance of the crystals was very similar to that for crystals mounted with the wax/stycast technique, and while elemental iodine has only a small solubility in warm water, $(TaSe_4)_2I$ showed no visible evidence at all of loss of iodine in water.

Each $(TaSe_4)_2I$ sample then, is a 7/16" disk of plastic with an upper surface comprised of aligned crystals. The samples are much sturdier than the fibrous mat samples of TaS_3. They were fastened with set screws into the copper sample slide of the reflectance/transmittance apparatus. The crystal faces were aligned with the top of the first reflectance baffle, rather than with the front plane of the copper sample slide. Such a mounting position should eliminate Fabry-Perot reflectance fringes caused by light reflected from the sample interfering with that reflected from the baffle. The measurement is still susceptible to Fabry-Perot fringes that arise from multiple reflections of light between the sample and the nearby polarizer, from misalignment of the

front faces of the sample and the adjacent brass reference disk, and from other gaps and windows within the system.

Calculation of the normalized reflectance

We measured the reflectance of the $(Ta_{.988}Nb_{.012}Se_4)_2I$ and $(Ta_{.994}Nb_{.006}Se_4)_2I$ samples over a broad range of temperatures from room temperature to 14K. The reflectance of a sample is the ratio of the intensity of light reflected from the sample to that of light reflected from a perfectly reflective sample of the same geometry. We approximate the latter by coating the sample and casting plastic with 2000Å of sputtered gold, then scraping away gold adhering to the plastic. Since the measurement of the reflected intensity from the sample and the gold-coated sample are necessarily widely separated in time, we normalized the raw measured spectrum of each to that of a polished brass disk. Figure 5-2 shows the normalization procedure for $(Ta_{.988}Nb_{.012}Se_4)_2I$ at 14K. The dashed line is the reflectance of the sample (and the surrounding plastic) at 14K and the intermittently dashed line is the reflectance of the gold-coated sample (and the uncoated surrounding plastic) at room temperature. The reflectance of the gold-coated sample falls off approximately logarithmically with increasing frequency. The ratio of the two is the sample reflectance, shown by the solid line.

The gross features of the sample reflectance after normalization are consistent with those usually seen in CDW materials at FIR frequencies: there are a series of resonances with intervening regions where the reflectance is nearly flat, and for the powerful low-frequency resonances the reflectance approaches unity. The details of the normalized reflectance though, are problematic. At low frequencies, the normalized reflectance falls well short of that corresponding to the conductivity measured with microwave techniques.

Fig. 5-2 Normalization procedure for a $(TaSe_4)_2I$ mosaic. The dashed line indicates the reflectance of the bare crystal mosaic and the intermittent dashed line is the reflectance of the gold-coated mosaic. The solid line is the normalized reflectance of the sample.

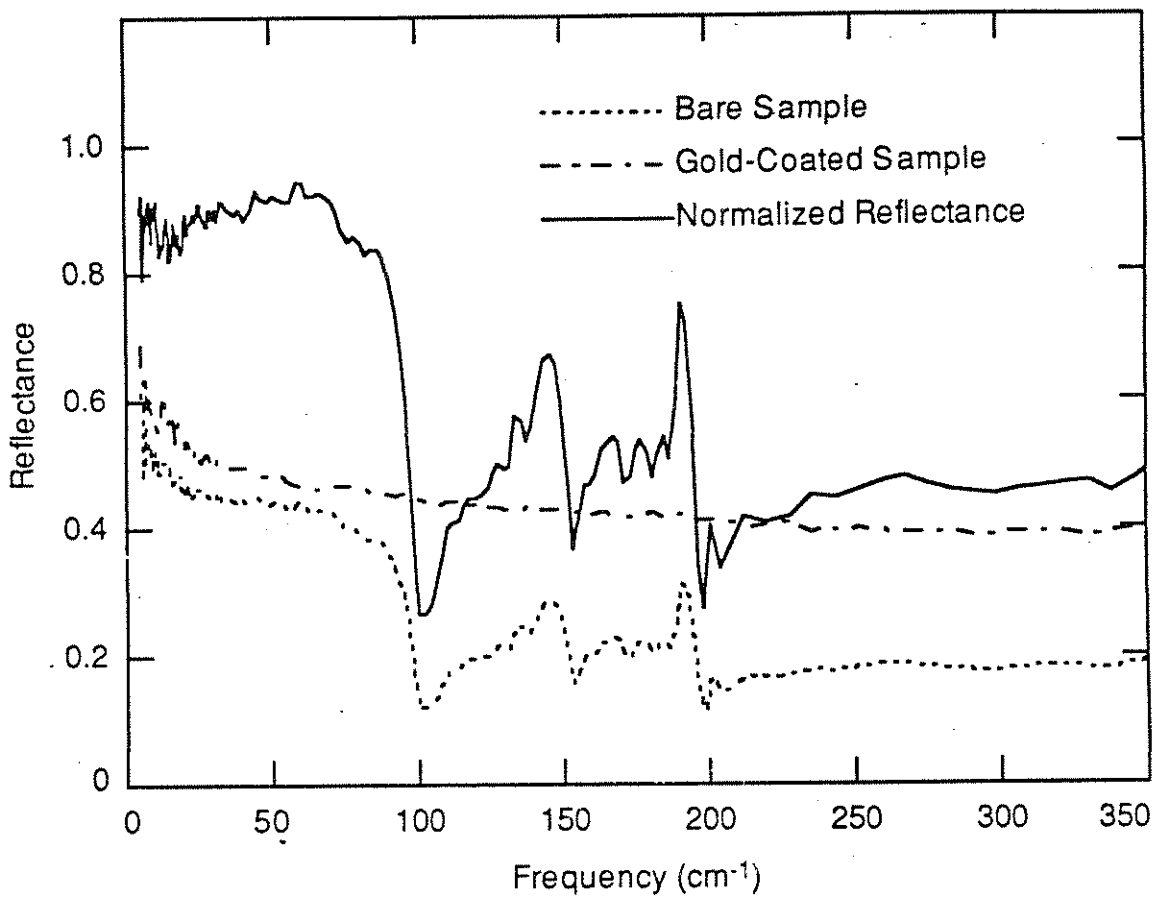
Bare Sample
Gold-Coated Sample
Normalized Reflectance
Reflectance
1.0
0.8
0.6
0.4
0.2
0
0
50
100
150
200
250
300
350
Frequency (cm-1)

This discrepancy may be caused by incomplete removal of the sputtered gold from the plastic matrix (the crystals are extremely fragile and splinter if the scalpel used to remove the gold touches them). If excess gold is left near the crystal edges, the normalized reflectance will be underestimated. A more disturbing feature is the oscillation of the reflectance near and sometimes *above* unity below $30cm^{-1}$. The conductivity calculated by a Kramers-Kronig transform is extremely sensitive to values of the reflectance near unity, and the reflectance oscillations at low frequencies are manifest as a sequence of conductivity resonances that may be spurious. We believe that the normalization procedure is the primary source of uncertainty in our results, and we will thus treat normalization in more detail in the remainder of this section.

In Fig. 5-3 we examine the normalization for frequencies less than $30cm^{-1}$, corresponding to a 10mil mylar beamsplitter in the left part of the Figure and a 3mil mylar beamsplitter in the right part of the Figure. Part a of the Figure shows the raw spectra for the uncoated sample and brass reference, part b shows the raw spectra for the gold-coated sample and brass reference, and part c shows the reflectance corresponding to each pair and the final normalized reflectance. An interference effect somewhere in our apparatus strongly modulates all the raw spectra. Peaks in the detected intensity are separated by about $\Delta f = 2.95cm^{-1}$ for the 3mil beamsplitter, and additional features at about half this frequency separation appear with the 10mil beamsplitter. The peaks in the detected intensity are marked with arrows in part a of the Figure, and identical arrows are placed in parts b and c for comparison. The source of the modulation is not known, but it corresponds to a Fabry-Perot interference with optical path nt=1.7mm.

Fig. 5-3. Details of the normalization scheme for $(Ta_{.988}Nb_{.012}Se_4)_2I$. In all three frames the curves on the left side of the graph correspond to measurements with a 10mil mylar beamsplitter and curves on the right side of the graph correspond to measurements with a 3mil mylar beamsplitter.

a) Raw spectra for the crystal mosaic (solid line) and the brass reference disk (dashed line). The vertical arrows indicate maxima in the modulation of the raw spectra. The set of arrows is reproduced in parts b) and c)

b) Raw spectra for the gold coated crystal mosaic (solid line) and the brass reference disk (dashed line).

c) Nominal reflectance of the bare crystal mosaic (intermittent dashed line), the gold-coated mosaic (dashed line), and the normalized reflectance (solid line), which is the ratio of the previous two quantities.

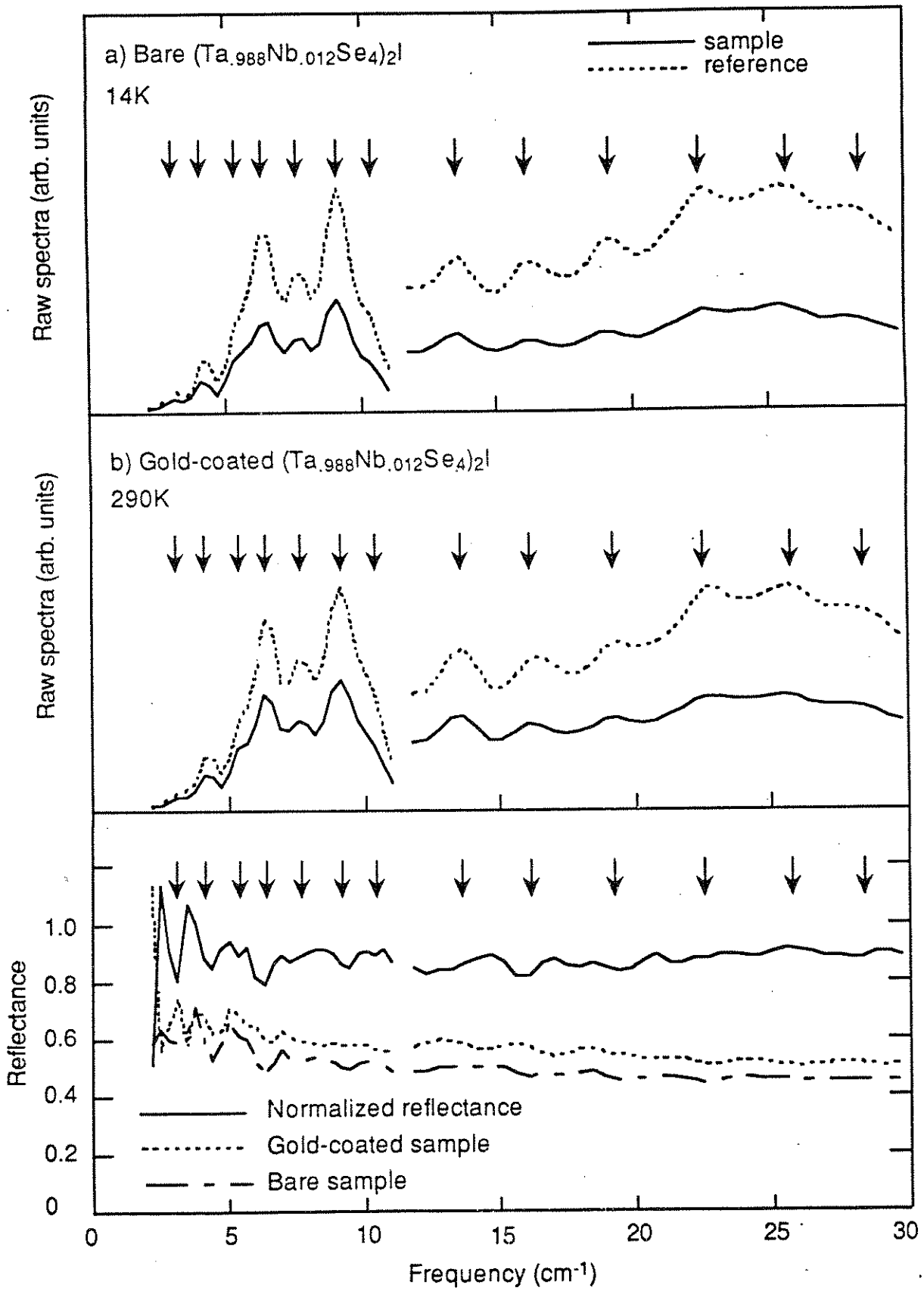
a) Bare $(Ta_{.988}Nb_{.012}Se_4)_2I$
14K
sample
reference
Raw spectra (arb. units)
b) Gold-coated $(Ta_{.988}Nb_{.012}Se_4)_2I$
290K
Raw spectra (arb. units)
Reflectance
1.0
0.8
0.6
0.4
0.2
0
Normalized reflectance
Gold-coated sample
Bare sample
0
5
10
15
20
25
30
Frequency (cm^{-1})

Such modulations should be cancelled in the division of the sample spectrum by the reference spectrum, but Fig. 5-3c clearly shows that the modulations persist in the calculated reflectance of both the bare sample and the gold-coated sample. Even worse, the periodic variations in the measured reflectance are in some cases *enhanced* by the final normalization step, when the sample reflectance is taken to be the ratio of the reflectance of the bare and gold-coated samples. The resultant "sample reflectance" oscillates fairly wildly, especially below $10cm^{-1}$. One of the reasons the modulations of the raw spectra are not fully cancelled is that such modulations correspond to peaks in the interferograms on either side of the large zero-path central peak. The height of the outlying peaks is extremely sensitive to the alignment of the beamsplitter. Any misadjustment or drifting alignment of the beamsplitter causes the interferogram peaks to be slightly asymmetrical and introduces errors in the calculated intensity of the modulations of the spectra. Periodic oscillations within the raw spectra are less significant for the thinner beamsplitters when the resolution of the measurement is necessarily less than the spacing between adjacent modulations. In a later section of this chapter we will discuss the conductivity calculated both from the measured sample reflectance and from a sample reflectance with reduced low frequency resolution.

Temperature dependence of the reflectance

We measured the reflectance of $(Ta_{1-x}Nb_xSe_4)_2I$ alloys with $x = .006$ and $x = .012$ at several temperatures below 263K, the Peierls transition temperature for the pure compound. In general, the overall reflectance of the sample with 1.2% Nb concentration is slightly lower than that that calculated from microwave measurements on similar samples; the overall reflectance of

the heavily doped sample also falls short of the reflectance of the more lightly doped sample. We attribute this low value of the reflectance to incomplete removal of the sputtered gold around the crystals, and consequently have multiplied the reflectance values for the heavily doped crystal by 1.059 to give better agreement with the microwave values.

The reflectance of the two alloys is presented as a function of temperature in Fig. 5-4. Both samples are highly reflective near room temperature, with a sharp reflectance edge developing near 100cm^{-1} and distinct resonances appearing at higher frequencies as the temperature is reduced well below the Peierls transition. The reflectance edge is more precipitous and the resonances more pronounced in $(Ta_{.994}Nb_{.006}Se_4)_2I$ than in $(Ta_{.988}Nb_{.012}Se_4)_2I$. In both samples, the reflectance rises from about 90% at the lowest frequencies to a maximum value near unity on a broad plateau from about 50-80cm^{-1}. The rise in reflectance to a broad plateau indicates the presence of an infrared mode. In the measurements of Sherwin *et al.*[3] on pure $(TaSe_4)_2I$ samples, the reflectance rise corresponding to the giant infrared mode is rather sharp, from 80% to 96% at 38cm^{-1}. Our doped sample with $x = .006$ shows a similar but less distinct feature at about 35cm^{-1}, and and the sample with $x = .012$ shows a broad general increase in the reflectance at slightly lower frequencies. The more gradual onset of enhanced reflectance in the samples with impurities complicates the analysis of the measurements because it precludes accurate fitting of the reflectance to distinct Lorentz oscillators. It does not, however, indicate that the FIR mode is negligible in these samples; the strength of the mode is roughly indicated by the width of the plateau and by the difference in reflectance values at frequencies well above and below the plateau. These two quantities are quite similar for the pure and niobium-doped samples.

Fig. 5-4. a) Reflectance vs. frequency as a function of temperature for $(Ta_{.994}Nb_{.006}Se_4)_2I$.

b) Reflectance vs. frequency as a function of temperature for $(Ta_{.988}Nb_{.012}Se_4)_2I$.

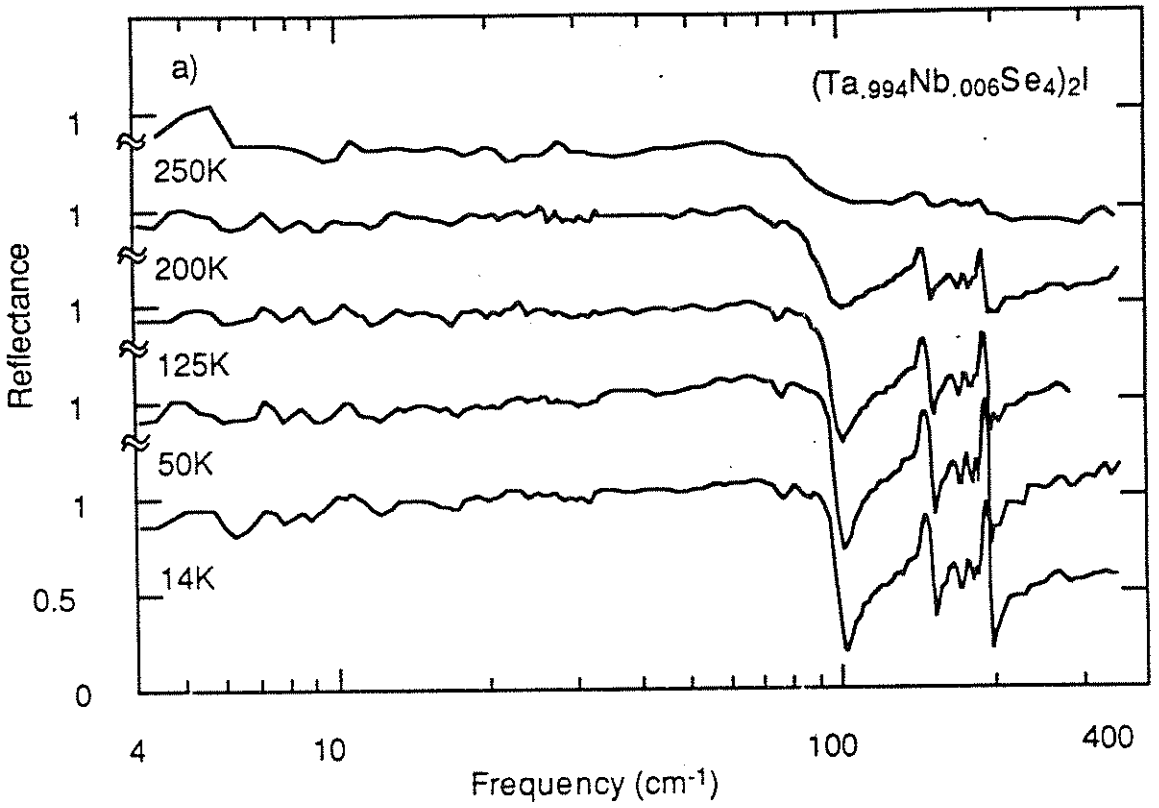
a)
$(Ta_{.994}Nb_{.006}Se_4)_2I$
250K
200K
125K
50K
14K
Reflectance
1
1
1
1
1
0.5
0
4
10
100
400
Frequency (cm^{-1})

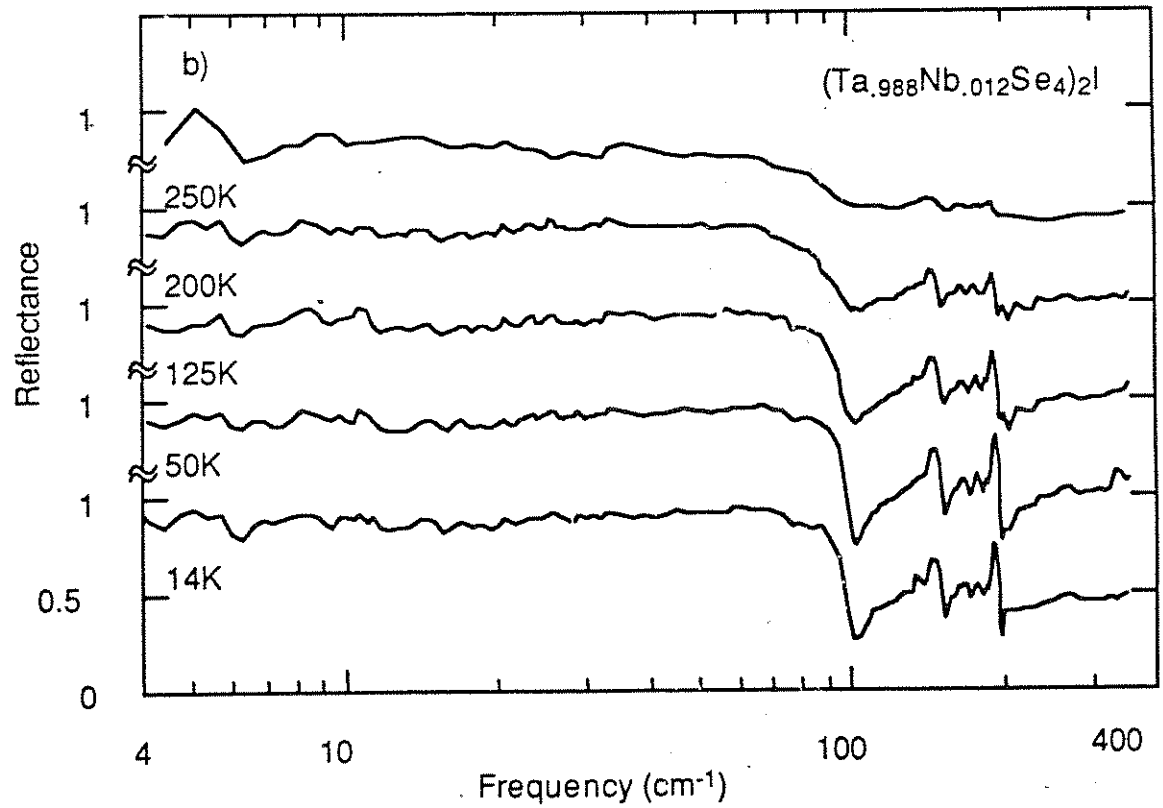
b)
$(Ta_{.988}Nb_{.012}Se_4)_2I$
250K
200K
125K
50K
14K
Reflectance
1
1
1
1
1
0.5
0
4
10
100
400
Frequency (cm^{-1})

Conductivity of $(Ta_{1-x}Nb_xSe_4)_2I$ alloys: a Kramers-Kronig analysis

As described in Chapter 4, the Kramers-Kronig integral relates the reflectance of a sample to the phase shift of the reflected light. The dielectric function and complex ac conductivity are then simple functions of the reflectance and phase shift. We used a Kramers-Kronig analysis to calculate the ac conductivity of the $(Ta_{1-x}Nb_xSe_4)_2I$ samples. Figure 5-5 illustrates the results of the analysis at 14K for the sample with $x = .012$. As a low-frequency extrapolation, we used the microwave conductivity of similar samples measured by Kim *et al.*[16] The reflectance is related to the conductivity $\sigma(\omega) = \sigma_1 + i\sigma_2$ by

$$R(w) = \frac{1 + \frac{4\pi}{\omega}(\sigma_1^2 + \sigma_2^2)^{1/2} - 2\left\{\frac{2\pi}{\omega}[(\sigma_1^2 + \sigma_2^2)^{1/2} + \sigma_2]\right\}^{1/2}}{1 + \frac{4\pi}{\omega}(\sigma_1^2 + \sigma_2^2)^{1/2} + 2\left\{\frac{2\pi}{\omega}[(\sigma_1^2 + \sigma_2^2)^{1/2} + \sigma_2]\right\}^{1/2}} . \tag{5-2}$$

This relation ignores the contribution of ε_∞ to the reflectance; the approximation is valid at microwave frequencies where the dielectric function $\varepsilon(\omega)$ is enormous because of the pinned mode. Our FIR reflectance measurements cover frequencies from 4 to 700cm^{-1}. Between 350cm^{-1} and 700cm^{-1} the reflectance rises very slowly with no prominent features. Within this frequency range, though, a deep minimum in the raw spectra near 360cm^{-1} and a low signal-to-noise ratio introduce errors in the reflectance. To avoid introducting spurious conductivity modes, we used a linear fit to the reflectance in this region rather than the measured values. At frequencies between 700cm^{-1} and 40,000cm^{-1}, we used the reflectance measured by Geserich *et al.*[19] for pure $(TaSe_4)_2I$. Beyond 40,000cm^{-1} we reduced the reflectance exponentially to near zero at the high frequency cutoff of 10^6cm^{-1}.

These measured reflectance along with the low and high frequency extrapolations are shown in Fig. 5-5a. As discussed previously, the oscillations in the reflectance below $30cm^{-1}$ are primarily remnants of an interference effect that modulates the raw spectra. In an attempt to minimize the influence of these oscillations without unduly supressing the trends in reflectance at low frequencies, we smoothed the oscillations by replacing the reflectance at a given frequency by an average of the reflectance at surrounding points within a $3.5cm^{-1}$ window. This smoothed reflectance is also shown in Fig. 5-5a, slightly offset from the measured reflectance. Parts b and c of the Figure show the real part of the conductivity deduced by the Kramers-Kronig technique from the measured and smoothed reflectances. The pinned acoustic phason mode appears at $4.3cm^{-1}$ and a broad FIR mode appears above $20cm^{-1}$. The conductivity is negative below the pinned phason mode; this unphysical result is a consequence of the mismatch between the microwave and FIR reflectances. As expected, the conductivity calculated from the measured reflectance has small, regularly spaced resonances corresponding to the reflectance oscillations. The conductivity corresponding to the smoothed FIR reflectance is much more reminiscent of the giant mode originally fit to the pure material. The smoothing process itself, though, of course introduces uncertainty into the calculated conductivity, because it almost certainly affects the location assigned to the onset of the mode.

In Fig. 5-6 we compare the ac conductivity over a broad frequency range for the two impurity-doped samples and pure $(TaSe_4)_2I$. The conductivity in parts a and b of the Figure is calculated from smoothed reflectances for the $x = .012$ and $x = .006$ samples (part a corresponds to frame c of the previous Figure, plotted on a logarithmic frequency scale). In the $x = .006$ sample, the conductivity of the pinned acoustic phason mode is much larger than

Fig. 5-5. a) Reflectance values for $(Ta_{.988}Nb_{.012}Se_4)_2I$ used as input to the Kramers-Kronig routine. The lower curve represents the measured FIR reflectance and the upper curve is a smoothed version of that reflectance. The low and high frequency extrapolations correspond to measurements in References 16 and 19.

b) Conductivity calculated from a Kramers-Kronig transform of the measured reflectance.

c) Conductivity calculated from a Kramers-Kronig transform of the smoothed reflectance.

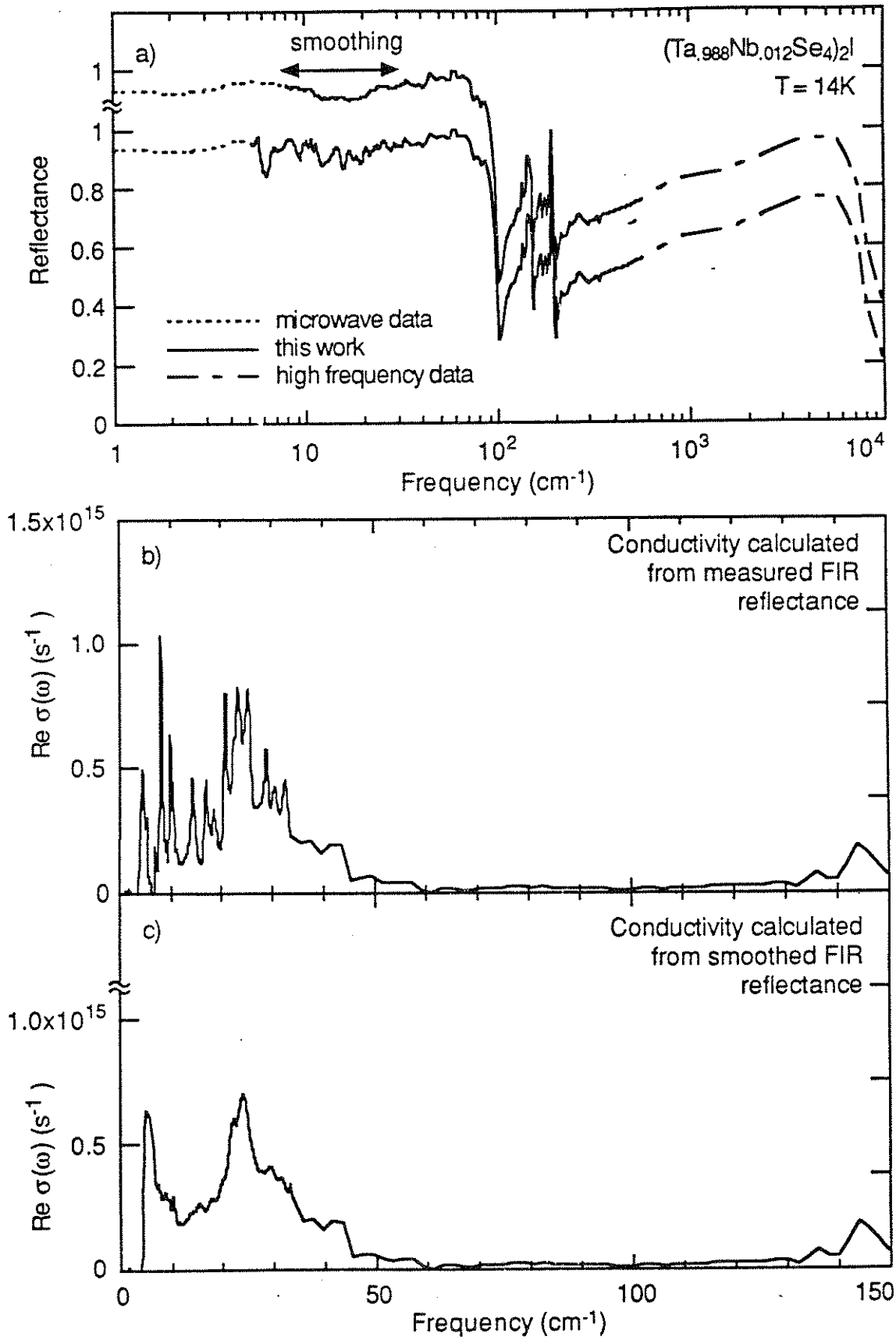
a)
smoothing
$(Ta_{.988}Nb_{.012}Se_4)_2I$
T = 14K
Reflectance
microwave data
this work
high frequency data
Frequency (cm^{-1})
b)
Conductivity calculated from measured FIR reflectance
Re σ(ω) (s^{-1})
c)
Conductivity calculated from smoothed FIR reflectance
Re σ(ω) (s^{-1})
Frequency (cm^{-1})

Fig. 5-6 Conductivity vs. frequency for various $(Ta_{1-x}Nb_xSe_4)_2I$ alloys. The open circles represent microwave measurements from Reference 16.

a) $Re(\sigma(\omega))$ for $(Ta_{.988}Nb_{.012}Se_4)_2I$ calculated from the smoothed reflectance.

b) $Re(\sigma(\omega))$ for $(Ta_{.994}Nb_{.006}Se_4)_2I$ calculated from the smoothed reflectance.

c) $Re(\sigma(\omega))$ for nominally pure $(TaSe_4)_2I$, as reported in Figure 1 of Reference 9.

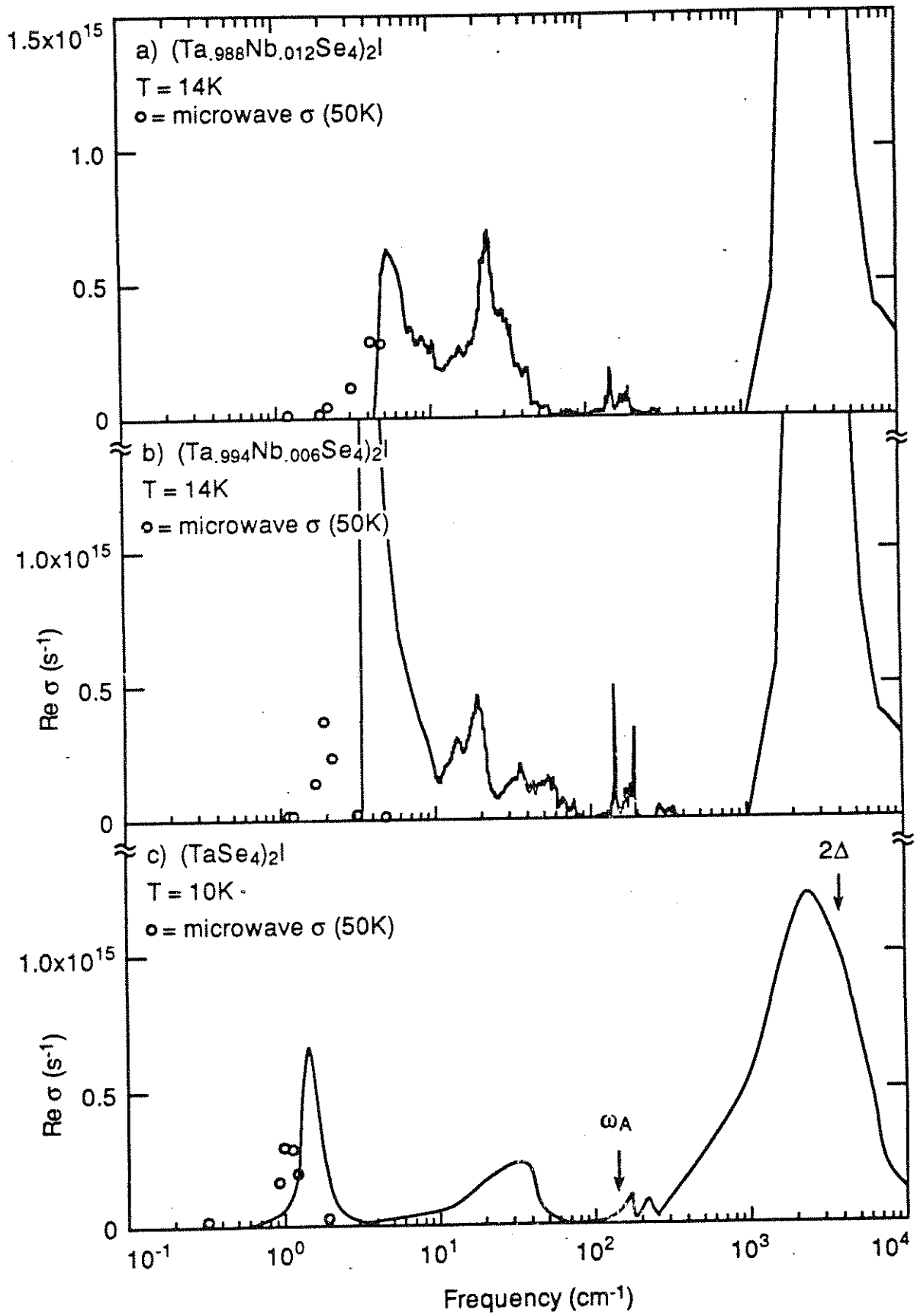
a) (Ta.988Nb.012Se4)2I
T = 14K
o = microwave σ (50K)
b) (Ta.994Nb.006Se4)2I
T = 14K
o = microwave σ (50K)
c) (TaSe4)2I
T = 10K
o = microwave σ (50K)
2Δ
ωA
Re σ (s-1)
Frequency (cm-1)

measured microwave conductivity. This effect is probably due to the mismatch between the microwave and smoothed FIR reflectance at low frequencies. Figure 5-6c is adapted from Figure 1 of Kim *et al.*[16] This is ostensibly the result of a Kramers-Kronig transform of the FIR reflectance of pure $(TaSe_4)_2I$ measured by Sherwin *et al.*,[2, 3] along with rf,[20] microwave,[21] and optical measurements.[19] The FIR reflectance of the pure material, though, has oscillations at low frequencies as severe as those reported here for the impurity doped samples. The preceding discussion makes it clear that Kim *et al.* calculated the extremely smooth conductivity curves of Fig. 5-6c not from the measured FIR reflectance, but from a highly smoothed version of that reflectance. The three frames of Fig. 5-6, then, are illustrations of comparable quantities for the pure and impurity-doped materials. The circles in each frame of the Figure represent the microwave conductivity measured at 50K.

Discussion

A. FIR resonance behavior as a function of doping

Figure 5-6 shows the systematic trends in the conductivity as niobium impurity atoms are introduced into the crystals of $(Ta_{1-x}Nb_xSe_4)_2I$. In accordance with previous microwave measurements,[16] the frequency of the pinned acoustic phason resonance increases monotonically with dopant concentration. The FIR resonance, on the other hand, moves to a slightly lower frequency in the doped materials than in the pure crystals. Similar results were reported[9] for the behavior of the mode in $K_{0.3}MoO_3$ doped with tungsten. From the Kramers-Kronig analysis, the maximum conductivity of the far infrared mode lies at about $19cm^{-1}$ in the $x = .006$ sample and at about $24cm^{-1}$ in the $x = .012$ sample. The magnitude of the peak conductivity of the

FIR resonance may increase slightly as more impurities are introduced. As discussed previously, the accuracy of our determination of the frequency and size of the conductivity peak using the Kramers-Kronig technique is limited by the difficulties in normalization of the raw spectra at low frequencies. The enforced smoothing of the low-frequency data and the slight mismatch between the measured reflectivity and the microwave conductivity (measured at higher temperatures) both cause inaccuracies in the calculated conductivity. It is clear, though, that any shift in the frequency is downward and that it is by a much less dramatic factor than the shift for the pinned resonance. The oscillator strength of the FIR mode, as measured by the integrated conductivity, is approximately constant, independent of the doping level.

B. Bound vibrational modes in polar semiconductors

One of the puzzles that has prevented the identification of the physical mechanism underlying the FIR mode in CDW materials is that that the frequency of the mode lies well above the pinned acoustic phason resonance, yet well below the frequencies characteristic of phonons, optical phasons, excitations of the amplitude of the CDW, and the adjustment of the phase of the CDW near strong pinning sites. Recently, Degiorgi and Gruner proposed a "bound collective mode state" in an effort to explain the FIR resonance.[9] They treat the effects of the polarizability of impurities on the bulk conductivity and show that high frequency oscillator strength localized at impurity sites within a system with a low frequency resonance will cause intermediate frequency modes. Their ideas are an application of the theory originally proposed for localized vibrational modes in polar semiconductors by A.S. Barker.[8] The Barker theory is presented in detail here, together with

its application to charge density wave systems. A subsequent section will make a comparison to the measured data.

A prominent *restrahlung* resonance typically dominates the reflectance of polar semiconductors. A comparison of the room temperature conductivity resonance in pure and impurity-doped samples shows that the resonance broadens and shifts to slightly higher frequencies in the doped material due to the presence of the ionized impurity electrons. At low temperatures, though, an additional resonance emerges for the doped samples (at a frequency above the TO *restrahlung* frequency). The thermally ionized electrons are bound to the impurity sites at low temperatures, and Barker proposed that the polarizable bound electron changes the dielectric function in the vicinity of each impurity .

The combined system has dielectric function $\varepsilon(\omega)$. It consists of pure material embedded with spheres with a different dielectric function. The pure material has dielectric function $\varepsilon_{bulk}(\omega)$, and the material within a radius r_s of an impurity has dielectric function $\varepsilon_s(\omega) = \varepsilon_{bulk}(\omega) + \varepsilon_e(\omega)$, where $\varepsilon_e(\omega)$ is the contribution of the bound electron. The number density of impurities is N_s. When the filling factor $f = N_s\left(\frac{4}{3}\pi r_s^3\right)$ is much less than unity, an effective medium theory can be used to evaluate $\varepsilon(\omega)$. To simplify the algebra, the spheres with $\varepsilon_s(\omega)$ embedded in material with $\varepsilon_m(\omega)$ can be treated as a gas of spheres with relative dielectric function $\varepsilon_{rel}(\omega) = \varepsilon_s(\omega)/\varepsilon_m(\omega)$, surrounded by a vacuum. The dielectric function for the dilute gas is:

$$\varepsilon_{gas} = 1 + \frac{4\pi N_s \alpha}{1 - \frac{4}{3}\pi N_s \alpha}, \qquad (5\text{-}3)$$

where $\alpha = p/E_{loc}$ is the polarizability of the sphere, p is the dipole moment of each sphere, and E_{loc} is the local field at the sphere. The polarization $P = p/(\frac{4}{3}\pi r_s^3)$ is given by:

$$P = \frac{\varepsilon_{rel} - 1}{4\pi}(E_{loc} - \frac{4}{3}\pi P), \tag{5-4}$$

where the second term in the parentheses is the depolarizing field within the sphere. Isolating P in Eq. (5-4) gives:

$$P = \frac{3}{4\pi}\left(\frac{\varepsilon_{rel} - 1}{\varepsilon_{rel} + 2}\right)E_{loc}. \tag{5-5}$$

From the relation between α, p, and P and the definition for the filling factor *f* we have

$$4\pi N_s \alpha = \frac{3f(\varepsilon_{rel}-1)}{(\varepsilon_{rel}+2)}. \tag{5-6}$$

Substitution in Eq. (5-3) gives the dielectric function of the gas of spheres:

$$\varepsilon_{gas}(\omega) = 1 + \frac{3f(\varepsilon_{rel} - 1)}{\varepsilon_{rel} + 2 - f(\varepsilon_{rel} - 1)}. \tag{5-7}$$

Multiplying by $\varepsilon_{bulk}(\omega)$ gives the effective dielectric constant for the impure polar semiconductor material:

$$\varepsilon(\omega) = \varepsilon_{bulk}(\omega) + \frac{3f(\varepsilon_s(\omega) - \varepsilon_{bulk}(\omega))}{\varepsilon_s(\omega) + 2\varepsilon_{bulk}(\omega) - f(\varepsilon_s(\omega) - \varepsilon_{bulk}(\omega))}. \tag{5-8}$$

This function has the expected resonances at frequencies corresponding to the poles of ε_{bulk} and ε_s, but it also diverges when the denominator of the second term goes to zero. This occurs when

$$\varepsilon_{bulk}(\omega) + \frac{1-f}{3}\varepsilon_e(\omega) \rightarrow 0. \qquad (5\text{-}9)$$

Since $f<<1$, this condition is satified when ε_{bulk} and ε_e have opposite sign. For the case when the electronic resonance occurs at a much higher frequency than the bulk mode, then Eq. (5-9) is satisfied just before the zero crossing at ω_{LO} as $\varepsilon_{bulk}(\omega)$ recovers from its deep negative swing on resonance.† Thus, in general there is an additional mode at an intermediate frequency between the electronic and bulk resonances. The location and strength of the mode depend only on the low frequency limit (i.e., the value near ω_{LO}) of the dielectric function associated with the electronic polarizability of the impurities.

Figures 5-7 and 5-8 illustrate the bound phonon mode theory as it was applied in the original doped polar semiconductor case. The two Figures are similar to Figures presented in the original Barker paper.[8] The solid line in part a of Fig. 5-7 shows a model dielectric function for the pure bulk material, using the form:

$$\varepsilon_{bulk}(\omega) = \varepsilon_\infty + \frac{S_0\omega_0^2}{\omega_0^2 - \omega^2 - i\omega\gamma_0}. \qquad (5\text{-}10)$$

The frequency, strength, and damping of the bulk mode have the values $\omega_0 = 367\text{cm}^{-1}$, $S_0 = 1.96$, and $\gamma_0 = 1.96\text{cm}^{-1}$, and $\varepsilon_\infty = 9.1$. This Lorentz oscillator form is identical to the one often used to model the response of the pinned acoustic phason mode in CDW's (see Eqs. (4-1) and (4-2)). The dashed line in Fig. 5-8b shows the dielectric function in the vicinity of the spheres:

---

† Condition (5-9) may be satisfied again just above the electronic resonance if that mode has sufficient oscillator strength. Of course, ε_{bulk} and ε_e are complex quantities and when the real parts of these functions cancel, the mismatch in their imaginary parts causes the pole in $\varepsilon(\omega)$ to have a finite height and width.

Fig. 5-7 a) Real part of the components of the model dielectric function for GaP. The solid line represents the bulk material and the dashed line represents the material near impurity sites. Model parameters are given in the text.

b) Real part of the effective dielectric function for the impurity-doped material. This Figure is based on Figure 4 in Reference 8.

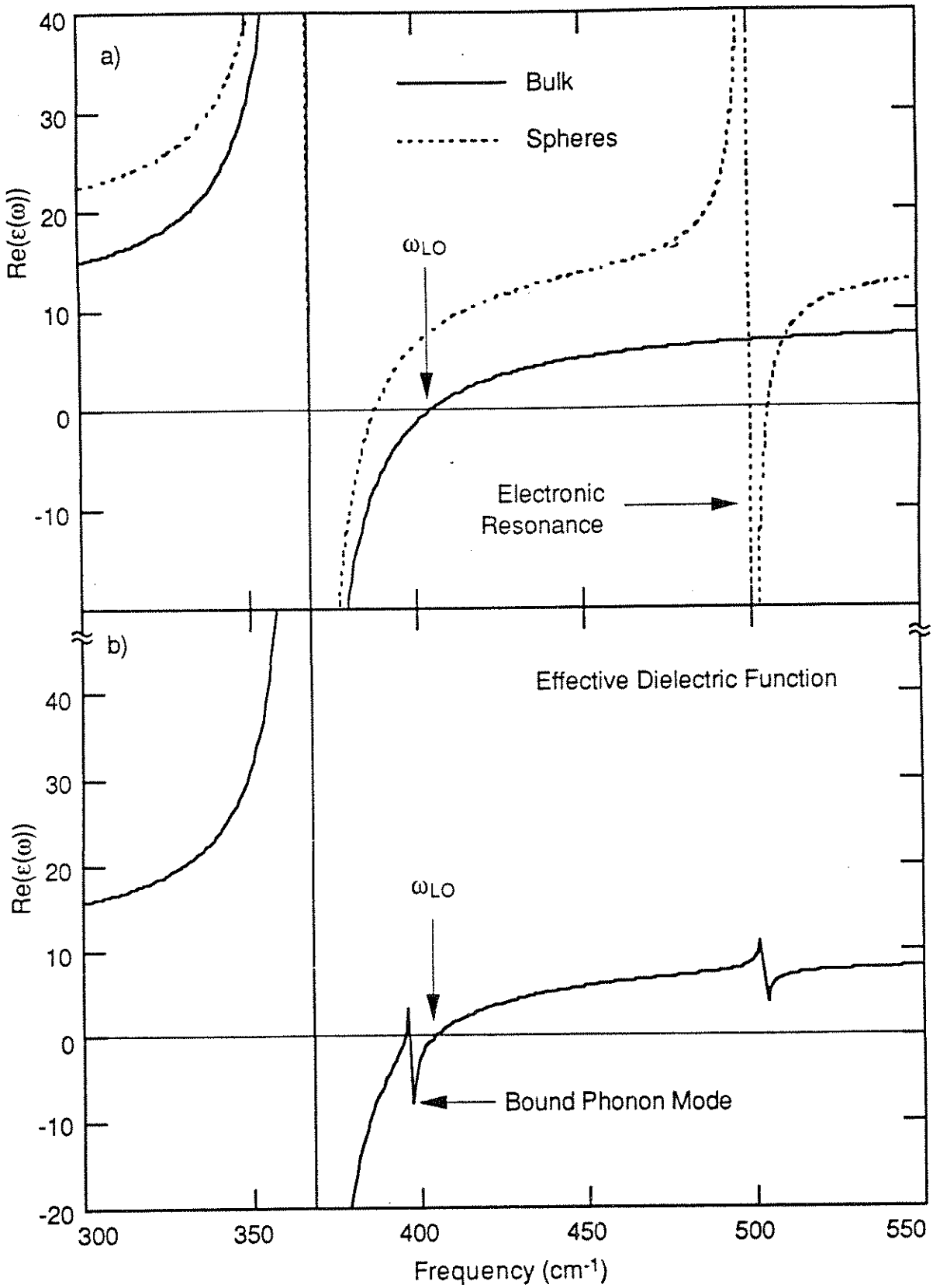
a)
Bulk
Spheres
ω_{LO}
Electronic
Resonance
b)
Effective Dielectric Function
ω_{LO}
Bound Phonon Mode
Re(ε(ω))
Frequency (cm^{-1})
40
30
20
10
0
-10
-20
300
350
400
450
500
550

Fig. 5-8 a) Model reflectance vs. frequency for a bound phonon mode corresponding to GaP doped with Te.

b) $\mathrm{Im}(\varepsilon(\omega))$ for the bound phonon model.

c) $\mathrm{Im}(-1/\varepsilon(\omega))$ for the bound phonon model. Parts b and c of this Figure follow Figure 5 of Reference 8.

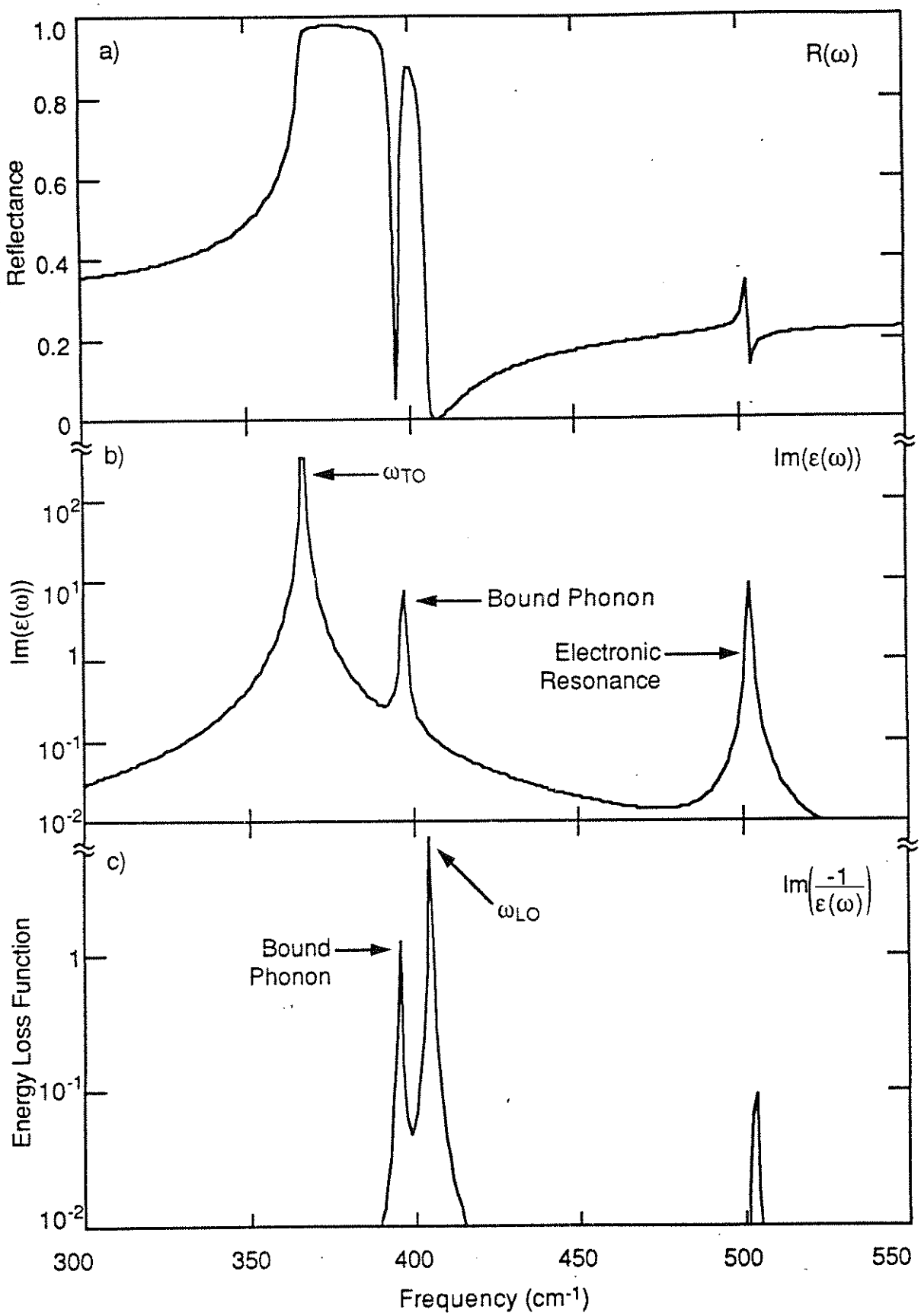
a)
R(ω)
Reflectance
1.0
0.8
0.6
0.4
0.2
0
b)
Im(ε(ω))
ωTO
Bound Phonon
Electronic
Resonance
10^2
10^1
1
10^-1
10^-2
c)
Im(-1/ε(ω))
ωLO
Bound
Phonon
Energy Loss Function
1
10^-1
10^-2
300
350
400
450
500
550
Frequency (cm^-1)

$$\varepsilon_s(\omega) = \varepsilon_{bulk}(\omega) + \varepsilon_0 + \frac{S_1\omega_1^2}{\omega_1^2 - \omega^2 - i\omega\gamma_1}, \qquad (5\text{-}11)$$

with $\omega_1 = 500\text{cm}^{-1}$, $S_1 = 0.3$, $\gamma_1 = 1.0$, and $\varepsilon_0 = 7.0$.

Figure 5-7b shows the effective dielectric function for $f = 0.10$ according to Eq. (5-8). The bound phonon mode lies at 398cm^{-1}, between the electronic and bulk resonances. Fig 5-8a shows the reflectance expected for such a system. Parts b anc c of the Figure highlight the TO and LO features respectively by showing the imaginary part of the dielectric function and the energy loss spectrum $\text{Im}(-1/\varepsilon(\omega))$. The relative strength of the bound phonon mode and the bulk phonon mode can be evaluated by integrating the area under the curve associated with each mode in Fig. 5-8c:

$$A = \frac{\int_{\text{bound mode}} \text{Im}(-1/\varepsilon(\omega))\, dw}{\int_{\text{bulk mode}} \text{Im}(-1/\varepsilon(\omega))\, dw}. \qquad (5\text{-}12)$$

For a model system such as those depicted in Figs. 5-8 and 5-9, the value of A varies linearly with the filling factor f (neither the numerator nor denominator of A varies linearly with f).

C. The bound collective mode in charge density wave materials

Degeorgi and Grüner have applied and adapted the bound mode theory for use with charge density waves materials.[9] They assume that the electronic or other resonance represented by the final term in Eq. (5-11) occurs at a much higher frequency than the pinned acoustic phason mode. The dielectric function of the spheres associated with the pinning sites is then simply

$$\varepsilon_s(\omega) = \varepsilon_{bulk}(\omega) + \varepsilon_0. \qquad (5\text{-}13)$$

The model is fit to the conductivity of TaS_3, $(TaSe_4)_2I$, and $K_{0.3}MoO_3$, and to the conductivity of the impurity-doped blue bronze $K_{0.3}Mo_{.985}W_{.015}O_3$. The fit requires that the dielectric function enhancement ε_0 be 190 for $(TaSe_4)_2I$ and 1000 for the other materials. The filling fraction f is 0.2 or less for the pure materials, and as expected the filling factor is much larger for the doped blue bronze. In general, the fits reproduce the qualitative features of the $\varepsilon(\omega)$ fairly well. The width of the FIR resonance is always underestimated, though, and the peak conductivities of the bound mode and acoustic phason mode are not accurately reproduced. The measured dielectric function and conductivity of TaS_3 and the fit using the bound collective mode model are shown together in Fig. 5-9.

The measurement of the conductivity of $(Ta_{1-x}Nb_xSe_4)_2I$ alloys reported in this chapter allows an evaluation of the theory in greater detail. The conductivity is now known for two values of x, as well as for the pure material with $x = 0$. The dominant pinning mechanism and consequently ε_0 should not vary with x, at least for the impurity-doped samples. The bound collective mode model fit to $\varepsilon(\omega)$ for the sample with, say, $x = .012$ should also fit $\varepsilon(\omega)$ for the more lightly doped sample with only a reduction in the filling factor f. If that conjecture is borne out, a scaling for the bound mode frequency and strength with f can be established. (Barker speculated in his initial paper that the frequency of the bound mode could be used as a measurement of the dopant concentrations in polar semiconductors.[8]) Moreover, if the scaling can be established and extrapolated to the case with $x = 0$, a comparison between the model predictions and the measured $\sigma(\omega)$ for the pure material should indicate whether the residual pinning sites have the same pinning mechanism as the Nb sites in the intentionally doped crystals. Thus, we seek to establish the scaling of the bound mode features with f and

Fig. 5-9 a) Re($\varepsilon(\omega)$) for TaS_3. The solid line is the measured value from Chapter Four, and the dashed line represents the bound collective mode fit using the parameters given in Reference 9.

b) a) Re($\sigma(\omega)$) for TaS_3. The solid line is the measured value from Chapter Four, and the dashed line represents the bound collective mode fit using the parameters given in Reference 9.

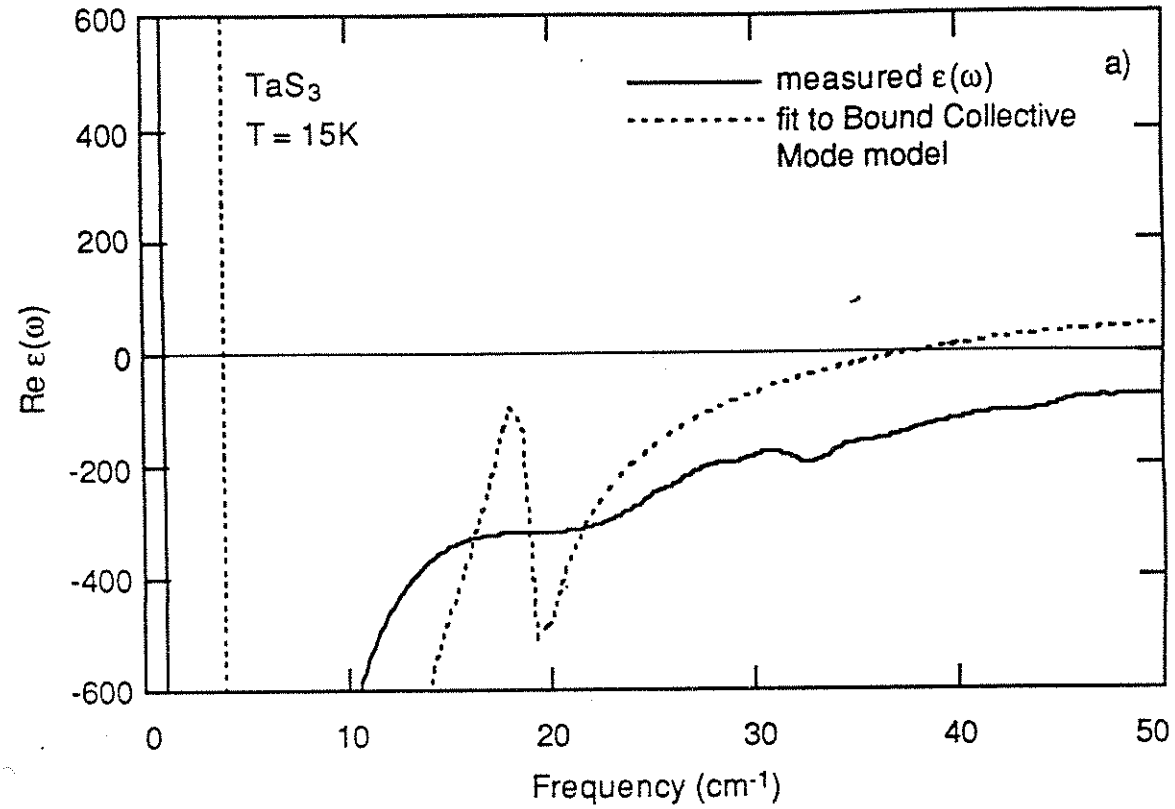
600
400
200
0
-200
-400
-600
Re ε(ω)
TaS3
T = 15K
measured ε(ω)
fit to Bound Collective Mode model
a)
0
10
20
30
40
50
Frequency (cm-1)

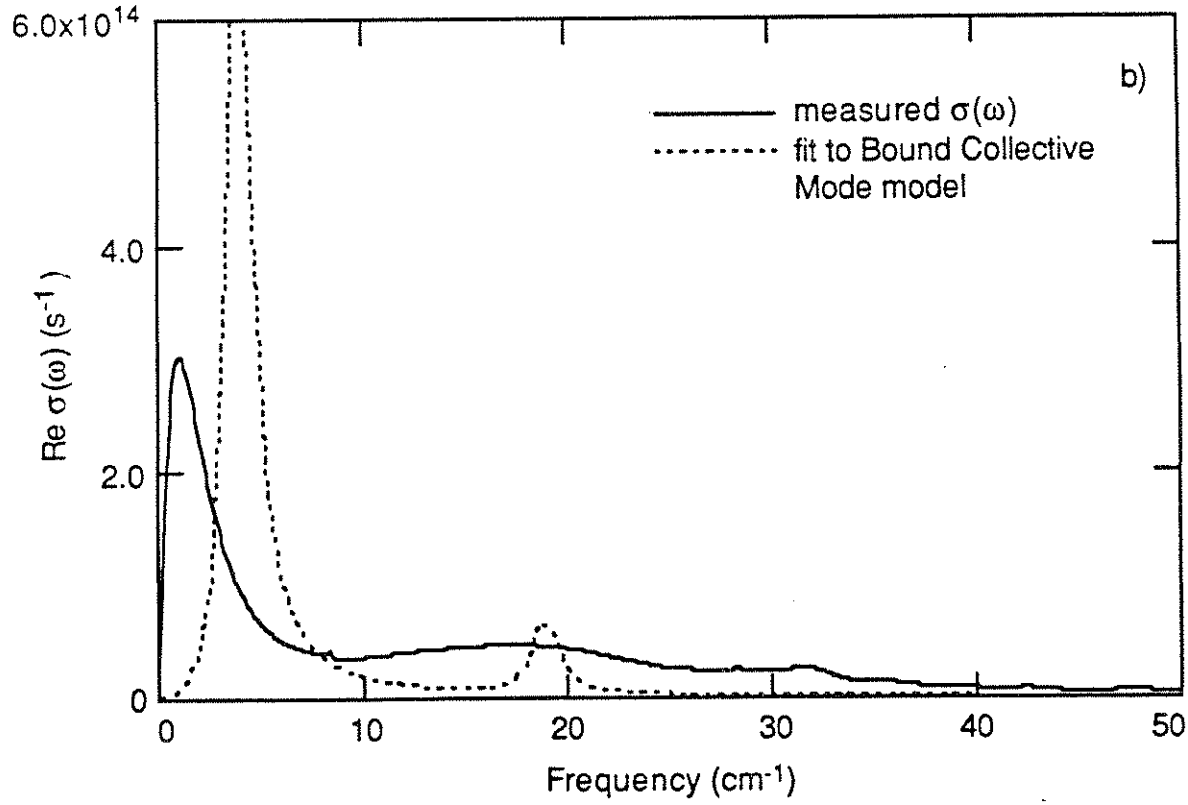
6.0x10^14
4.0
2.0
0
Re σ(ω) (s-1)
measured σ(ω)
fit to Bound Collective Mode model
b)
0
10
20
30
40
50
Frequency (cm-1)

to correlate that scaling with the established scaling of the transition temperature and Peierls gap and N_S.

We find, though, that while the bound collective mode model can independently fit the measured $\varepsilon(\omega)$ for both $x = .012$ and $x = .006$, it cannot fit both with a common ε_0. Fig. 5-10 shows the measured dielectric function and the model fit to it for x=.012. For the pinned acoustic phason we used the parameters of an oscillator fit to the microwave conductivity,[16] and for ε_∞ we used the value at 400cm^{-1}, just below the onset of the reflectance rise due to the gap (this value may underestimate the true ε_∞ if the normalization at high frequencies is inaccurate). We then adjusted f and ε_0 to get the best possible fit to the real part of $\varepsilon(\omega)$. The measured $\varepsilon(\omega)$ is shown as a solid line in Fig. 5-10a, and the best fit to the bound collective mode is shown as a dashed line. The position and size of the bound mode feature can be adjusted over a wide range by varying f and ε_0. In general, increasing ε_0 and decreasing f give approximately equal fits. Thus, in the absense of a definite theory for ε_0, the value of f cannot be considered to be definitely established. Nonetheless, we found that given any ε_0 and the corresponding value of f that fit $\varepsilon(\omega)$ for $x = .012$, we could not fit the dielectric function for $x = .006$ very well using the same ε_0 and a reduced f. One example is shown in Fig. 5-10b. The solid line is the measured dielectric function. The dashed line is the bound collective mode model, using ε_0 from the best fit to the $x = .012$ measurement, parameters for the microwave oscillator appropriate for $x = .006$, and a value for f half way between that for the pure case and the filling fraction determined for the $x = .012$ case. The predicted and measured dielectric functions do not match well, though the qualitative features are again similar.

Fig. 5-10 a) Re($\varepsilon(\omega)$) for $(Ta_{.988}Nb_{.012}Se_4)_2I$. The solid line represents the measured dielectric function. The dashed line represents a fit using the bound collective mode model with parameters $\varepsilon_0 = 350$, $f = 0.65$, $\varepsilon_\infty = 30$, $\omega_0 = 4.2cm^{-1}$, $S_0 = 2180$, $\gamma_0 = 1.8cm^{-1}$.

b) Re($\varepsilon(\omega)$) for $(Ta_{.994}Nb_{.006}Se_4)_2I$. The solid line represents the measured dielectric function. The dashed line represents a fit using the bound collective mode model with parameters $\varepsilon_0 = 350$, $f = 0.3$, and $\varepsilon_\infty = 30$. The pinned mode parameters are $\omega_0 = 2.0cm^{-1}$, $S_0 = 2930$, and $\gamma_0 = .45cm^{-1}$.

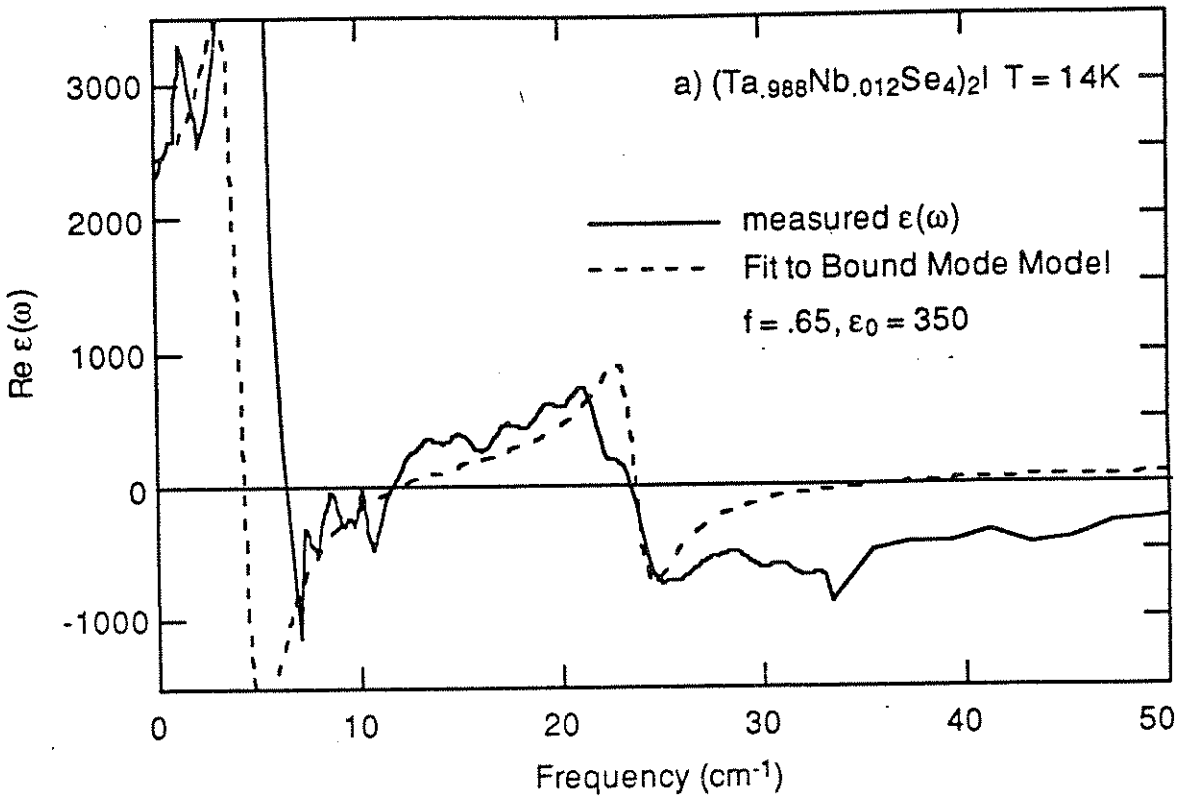
a) $(Ta_{.988}Nb_{.012}Se_4)_2I$ T = 14K
measured ε(ω)
Fit to Bound Mode Model
f = .65, ε_0 = 350
Re ε(ω)
3000
2000
1000
0
-1000
0
10
20
30
40
50
Frequency (cm^{-1})

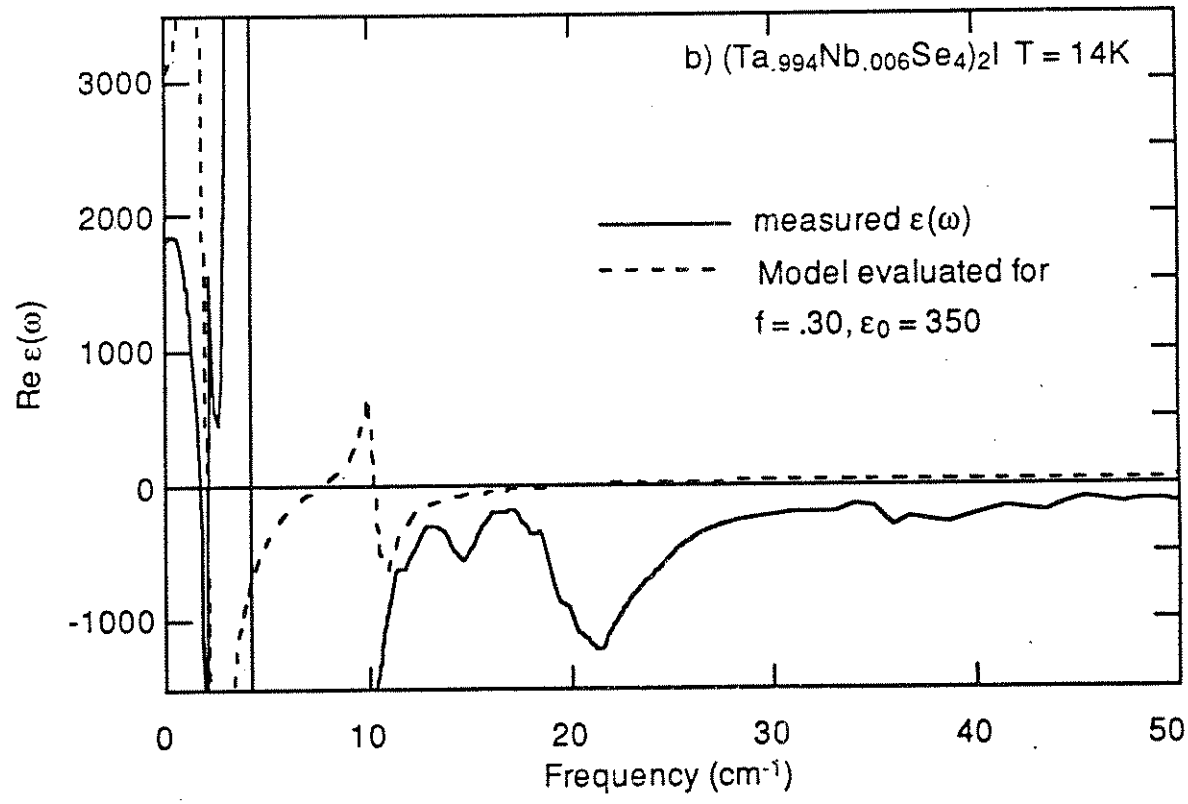
b) $(Ta_{.994}Nb_{.006}Se_4)_2I$ T = 14K
measured ε(ω)
Model evaluated for
f = .30, ε_0 = 350
Re ε(ω)
3000
2000
1000
0
-1000
0
10
20
30
40
50
Frequency (cm^{-1})

Degeorgi and Grüner fit their model to the conductivity of pure $(TaSe_4)_2I$ using appropriate values for the microwave oscillator along with $\varepsilon_0 = 190$, and $f = 0.2$. We were not able to produce a good fit to $\varepsilon(\omega)$ for either alloyed material using $\varepsilon_0 = 190$ given the restriction $f<<1$. This may indicate that the pinning mechanism and sphere radius appropriate for residual pinning sites in the pure material are different from those for the Nb sites in the intentionally doped materials. We attempted to evaluate the dependence of the bound mode strength with impurity concentration using the definition of A given by Eq. (5-12) and the measured values of $Im(-1/\varepsilon(\omega))$, but we could not separate the peak due to the FIR mode from the other background peaks.

In short, the bound collective mode model is capable of independently fitting $\varepsilon(\omega)$ measured for various values of x in $(Ta_{1-x}Nb_xSe_4)_2I$ samples, but we are unable to apply the model consistently for samples with $x = 0$, .006, and .012 by varying onlv the microwave oscillator parameters and the filling factor f. In particular, we cannot establish definite scaling of f with the measured impurity content nor unambiguously compare the character of Nb impurities and residual impurities. These comments do not necessarily imply that the bound collective mode theory fails to describe CDW conductors, especially in light of its success in qualitatively describing the infrared dielectric function of every CDW material measured so far with reasonable model parameters. Indeed, the smoothing of the low frequency reflectance and the mismatch between reflectances from the microwave and FIR measurements may generate errors in $\varepsilon(\omega)$ large enough to account for the fitting difficulties described above. The difficulties do indicate, though, that the bound collective mode theory is not predictive of the infrared features of CDW materials without an accompanying theory that predicts values for ε_0 for various types of impurities. In Barker's original analysis,[8] the Te, Se, S, and

Sn impurities have an extra bound electron with respect to the GaP bulk material. The enhancement ε_0 can be evaluated using a calculation based on the polarizability of a hydrogen atom, adjusted for the background dielectric constant of the semiconductor. In the $(Ta_{1-x}Nb_xSe_4)_2I$ alloys studied here, though, the niobium impurities have the same number of valence electrons as the tantalum atoms they replace. Their polarizability may not sufficiently enhance the bulk dielectric function to account for the FIR mode. The addition of strong impurity pinning atoms such as tungsten into $(TaSe_4)_2I$ or niobium into $K_{0.3}MoO_3$ should substantially change the values found for ε_0. In addition, other mechanisms may give local perturbations of $\varepsilon(\omega)$ bound to impurity sites. In particular, Tütto and Zawadowski have shown that under certain conditions the competition between the Friedel oscillation modulating the amplitude of the CDW near impurities and the undistorded CDW between impurities gives rise to bound states inside and outside the gap.[22]

An additional problem with the bound collective mode model concerns the value of the filling fraction f. Consider $K_{0.3}MoO_3$. For the pure material, the fit to $\varepsilon(\omega)$ yields $f = 0.2$. Given a residual impurity concentration $N_s = 1\times10^{18}/cm^3$, the radius of the spheres is about 36Å.[9] The density of Mo atoms in the crystal is roughly $7\times10^{21}/cm^3$, so the density of W atoms in $K_{0.3}Mo_{.985}W_{.015}O_3$ is about $1\times10^{20}/cm^3$. For the same value of r_s, this gives $f = 20$. This indicates the spheres are highly overlapping and an effective medium theory is inapplicable. The fit of the model for $K_{0.3}Mo_{.985}W_{.015}O_3$ requires $f = 0.8$. Clearly, either r_s for the tungsten impurities is much smaller than r_s for the residual impurities, or only a tiny fraction of the incorporated tungsten serves as a local mode site, or the theory is inappropriate for the high doping level, or perhaps all three. Once again, it proves difficult to

evaluate the validity of the bound collective mode theory unless it is coupled to a theory predicting a value for ε_0, and the importance of the task of identifying specific pinning mechanisms for various types of impurities is emphasized.

Conclusion

In this chapter, we have described the measurement of the FIR reflectance and the associated dielectric function for $(Ta_{1-x}Nb_xSe_4)_2I$ alloys. We described the measurement of the reflectance, the correction of the measured values for systematic errors associated with the normalization procedure, and the use of Kramers-Kronig procedures to evaluate the conductivity. These measurements confirm the shift of the pinned acoustic phason mode to low FIR frequencies when the CDW crystals are highly doped. They establish that the frequency of the FIR mode in $(TaSe_4)_2I$ decreases slightly with increasing doping, and that the strength of the mode does not depend strongly on the density of impurities.

We compared these results with the predictions of a new "bound collective mode" model proposed by Degeorgi and Grüner[9] and based on a theory of FIR modes in polar semiconductors by A.S. Barker.[8] The theory has reproduced the qualitative features of the FIR conductivity in other materials. We found that, with reasonable parameters, the theory can fit $\varepsilon(\omega)$ for the $(Ta_{1-x}Nb_xSe_4)_2I$ alloys. On the other hand, we could not fit the theory to the data for both the $x = .006$ and $x = .012$ alloys by varying only the parameters that should depend on the concentration of impurities. This difficulty may be due to errors in our measured dielectric function caused by the problematic normalization procedure, or it may indicate a fundamental shortcoming in the theory. In either case, a microscopic theory of ε_0 is needed to fully

evaluate the applicability of the the bound collective mode theory for charge density wave systems. In addition, the interpretation of reflectance measurements on samples with a variety of dopant concentrations will require accurate determinations of the number of incorporated impurities; other types of experiments will be necessary to characterize the various types of pinning at chemical impurities, grain boundaries, and crystal imperfections.

In the absence of these necessary supplements to the bound collective mode theory and the refinements of the experimental approach to reflectance measurements on doped CDW systems, we conclude that the bound collective mode theory qualitatively reproduces most of the accumulated data, but it has very little predictive power. A very different type of experiment, though, can evaluate the bound collective mode theory without reference to varying dopant levels, normalization difficulties, or problematic Kramers-Kronig transforms. The CDW dynamics can be probed not by varying the characteristics of the FIR mode, but be fundamentally altering the underlying pinned acoustic phason mode. Such an experiment will be described in Chapter 6, which will conclude the first portion of this dissertation.

References

1. P.A. Lee, T.M. Rice and P.W. Anderson, Solid State Comm. **14**, 703 (1974).

2. M.S. Sherwin, Doctoral Thesis, University of California at Berkeley (1988).

3. M.S. Sherwin, A. Zettl and P.L. Richards, Phys. Rev. B **36**, 6708 (1987).

4. M.B. Walker, Can. J. Phys. **56**, 127 (1978).

5. W.G. Lyons and J.R. Tucker, Phys. Rev. B **40**, 1720 (1989).

6. S. Sugai, M. Sato and S. Kurihara, Phys. Rev. B **32**, 6809 (1985).

7. Shunji Sugai, Susumu Kurihara and Masotoshi Sato, Physica B **143**, 195 (1986).

8. A.S. Barker, Phys. Rev. B **7**, 2507 (1973).

9. L. Degiorgi and G. Grüner, (in press).

10. Tantalum powder, 99.99% purity, Leico Industries, Inc., New York, NY 10107.

11. Niobium powder, 99.99% purity, Leico Industries, Inc., New York, NY 10107.

12. Fused quartz tubes, Heraeus Amersil, Inc., Hayward, CA 94545.

13. R.E. Thorne, T.L. Adelman, J. McCarten, M. Maher and A. McDowell, Phys. Rev. B **40**, 4205 (1989).

14. Selenium shot, m5N+;t4N purity, Alfa Products, Morton Thiokol, Inc., Danvers, MA 01923.

15. Crystalline Iodine, 99.999% purity, Aldrich Chemical Company, Milwaukee, WI 53201.

16. Tae Wan Kim, S. Donovan, G. Grüner and A. Philipp, Phys. Rev. B **43**, 6315 (1991).

17. D. Reagor and G. Grüner, Phys. Rev. B **39**, 7626 (1989).

18. Buehler Plastic Set, Buehler, Ltd., Lake Bluff, IL 60044.

19. H.P. Geserich, G. Scheiber, M. Dürrler, F. Lévy and P. Monceau, Physica B **143**, 198 (1986).

20. R.J. Cava, P. Littlewood, R.M. Fleming, R.G. Dunn and E.A. Rietman, Phys. Rev. B **33**, 2439 (1986).

21. D. Reagor, S. Sridhar, M. Maki and G. Grüner, Phys. Rev. B **32**, 8445 (1985).

22. I. Tütto and A. Zawadowski, Phys. Rev. B **32**, 2449 (1985).

Chapter 6

Optical Properties of $K_{0.3}MoO_3$ with Pinned and Sliding Charge Density Waves

Introduction

Charge density waves are historically important because they provided an intriguing early model for superconductivity: in principle, a perfectly rigid, freely sliding density wave would carry current with zero resistance because its energy would be translationally invariant.[1] The model is wrong, of course. Real charge density waves do not slide freely. Instead, impurities and crystal imperfections immobilize them and they resonate at a pinning frequency proportional to the impurity concentration. Moreover, charge density waves are not rigid, and the internal excitations of the condensate are revealed by dielectric relaxation at radio frequencies and other phenomena. Neither are they undamped: the finite width of the pinning resonance is one manifestation of the damping of charge density waves. Normal electrons in the crystals flow to compensate for regions of internal polarization of the CDW and the condensate also interacts with thermal excitations. Charge density waves slide, but only when sufficient force is applied, and only with dissipation.

The amount of dissipation varies with the number of normal electrons that are present in the material. At low temperatures, the number of uncondensed electrons becomes exponentially small in materials where the Fermi surface is fully gapped by the CDW lattice distortion. Recent experiments[2-5] in $K_{0.3}MoO_3$, and later[6] in TaS_3 and $(TaSe_4)_2I$ show that at very low temperatures, ideal Fröhlich conductivity may in fact occur when the charge density waves break free from the impurity potential. The

materials are true insulators with virtually no free electrons at helium temperatures ($R > 10^{12}\Omega$), but current-voltage measurements show that the differential conductivity increases dramatically if the bias voltage exceeds a well-defined threshhold field E_T. Above the depinning threshold, the current may increase by many orders of magnitude without a measureable change in the bias voltage. We will call the phenomena "ideal differential conductivity" or "ideal Fröhlich conductivity" to emphasize the fact that it only occurs above a threshhold field and not at zero field as in true superconductivity.

In this chapter we will present a model of the far infrared properties of materials with ideal Fröhlich differential conductivity and the results of an attempt to measure the optical properties of $K_{0.3}MoO_3$ in its insulating and ideally conducting states. The work has fundamental importance for several reasons. First, it recalls the classic experiment of Glover and Tinkham[7] in which the oscillator strength within the superconducting gap was shown to be distributed above the gap and in the conductivity delta function at dc associated with superconductivity. A similar effect is expected in Fröhlich conductivity: the oscillator strength in the pinned mode is removed from the gap at T_p, and a further shift from the microwave pinned mode to zero frequency must occur when the highly insulating CDW state suddenly develops dc conductivity. Second, the experiment constitutes the first investigation of the far infrared conductivity mode not based on reflectance measurements. The reflectance measurements all use Kramers-Kronig transforms to calculate $\varepsilon(\omega)$. The previous chapters have shown that such techniques give problematic results if the measurements in different frequency ranges are made on different samples, or at different temperatures, or if the measurement apparatus introduces systematic errors. Though the

transmittance can only interpreted by reference to particular models of $\varepsilon(\omega)$ (if Kramers-Kronig transforms are not used), the signatures of the infrared and pinned modes and the shift in oscillator strength to dc are strong, and the results can be interpreted in qualitative terms. Finally, the measurement of the transmittance of a CDW compound in pinned and sliding states is a sensitive test for the bound collective mode theory.[8, 9] When the CDW slides, it perturbs the bulk dielectric function, and the bound collective mode develops a distinctive transmittance signature independent of the parameters used in the model.

The arguments supporting these three points will be expanded in the sections to follow. We will first present a history of experiments that suggest the existence of the ideal Fröhlich differential conductivity, then discuss our model for the conductivity of CDW in the pinned and sliding CDW states. We will calculate the simulated transmittance for crystals with pinned and sliding states in the presence of an infrared mode. We will then present similar calculations for crystals with a bound collective infrared mode rather than a true dissipative mechanism. The results of the two simulations are quite different. They suggest transmittance features associated with the movement of oscillator strength to dc, and an additional transmittance signature indicative of the presence of a bound mode. We will present the experimental details of a measurement of the transmittance of $K_{0.3}MoO_3$ and compare the measured $T(\omega)$ to the predicted $T(\omega)$. Though the changes in the measured transmittance when the CDW depins are much less prominent than those predicted by the models, they do suggest that the anticipated shift in oscillator strength does in fact occur in one sample. We will close the chapter and the first part of this dissertation with a discussion of the

implications of this attempt and offer suggestions for improved and related experiments.

Evidence for ideal Fröhlich differential conductivity in $K_{0.3}MoO_3$

Nonlinear conductivity caused by the depinning of the CDW in $NbSe_3$ was first reported by Monceau[10] in 1980, and the phenomena was later reported in all the other quasi-1D CDW crystals by many other authors. The conductivity is ohmic below the threshhold field because the current is carried by the normal electrons. The slope of the current-voltage curve increases above the threshold voltage as the charge density wave breaks free of the impurities. The threshold field decreases below the transition temperature and then increases again at lower temperatures. The first evidence for ideal Frohlich differential conductivity came in a series of papers by Mihály, Beauchêne, *et al.*[2-4, 6] They showed that two threshhold fields are actually present in $K_{0.3}MoO_3$. The lower threshold field is the one described by Monceau. It corresponds to the depinning and subsequent *damped* motion of the charge density wave. Below 48K, the extra conductivity at the first threshold field disappears. A second threshold voltage of about 2V corresponds to the depinning and subsequent *free sliding* motion of the charge density wave. At very low temperatures, the CDW current can increase at the threshold field by nine orders of magnitude with no discernable increase in bias voltage. The differential conductivity in the ideal Fröhlich sliding state exceeds $10^4\Omega^{-1}cm^{-1}$, though one study indicates that the differential resistance may be non-zero above 1.25K.[5]

Similar sharp current-voltage characteristics are present at low tempertures[6] in TaS_3 and $(TaSe_4)_2I$. The onset of the conducting state occurs within 10^{-8}s of the application of the bias voltage. The parameters of the

pinned acoustic phason mode determine the dc dielectric constant. They are related to the threshold field by $\varepsilon(\omega = 0)E_T/en_\perp \sim$ const in all the materials ($n_\perp$ is the number of conducting chains per unit cross section).[6] There have been no studies of the ac conductivity in the sliding state.

Optical properties of crystals with pinned and sliding charge density waves

A. Measured and model conductivities of $K_{0.3}MoO_3$

The optical properties of the pinned charge density wave in $K_{0.3}MoO_3$ have been measured over a wide frequency range at several temperatures below the Peierls transition.[11-13] The acoustic phason mode dominates the spectrum at microwave and low FIR frequencies. Above 15cm^{-1}, the powerful infrared mode discussed in Chapters Four and Five is prominent. There are additional infrared resonances near 72cm^{-1} and 84cm^{-1}. The measured conductivity of $K_{0.3}MoO_3$ is presented in Fig. 6-1 along with two model conductivities for the pinned and infrared modes.

The open circles in Fig. 6-1a are the microwave conductivity at 6K.[8] The giant infrared conductivity resonance is shown as a dashed line with a peak at about 15cm^{-1}, as initially reported by Travaglini and Wachter for crystals at 5K.[13] Other groups[11, 12] subsequently reported the center of the mode at 22cm^{-1} and 35cm^{-1}, with a peak conductivity within 15% of that shown here. The samples in our experiment are immersed in superfluid helium with $T \leq 2K$. We chose to put the peak of our model conductivity at 22cm^{-1} in accordance with the data of Ng *et al.*, also measured at 2K. The solid line in Fig. 6-1a is a fit to the measured conductivity using separate microwave and infrared resonances. The dielectric function is given by:

Fig. 6-1. a) Conductivity of $K_{0.3}MoO_3$ at low temperature. Open circles are the microwave conductivity at 2K of the pinned acoustic phason mode, from Figure 3 of Reference 8; the dashed line represents the conductivity of the FIR mode at 5K, from Reference 13. The solid line is $\sigma(\omega)$ for a model using two independent resonances, with parameters given in Table I.

b) Conductivity for a model using a microwave resonance and a bound collective infrared mode.

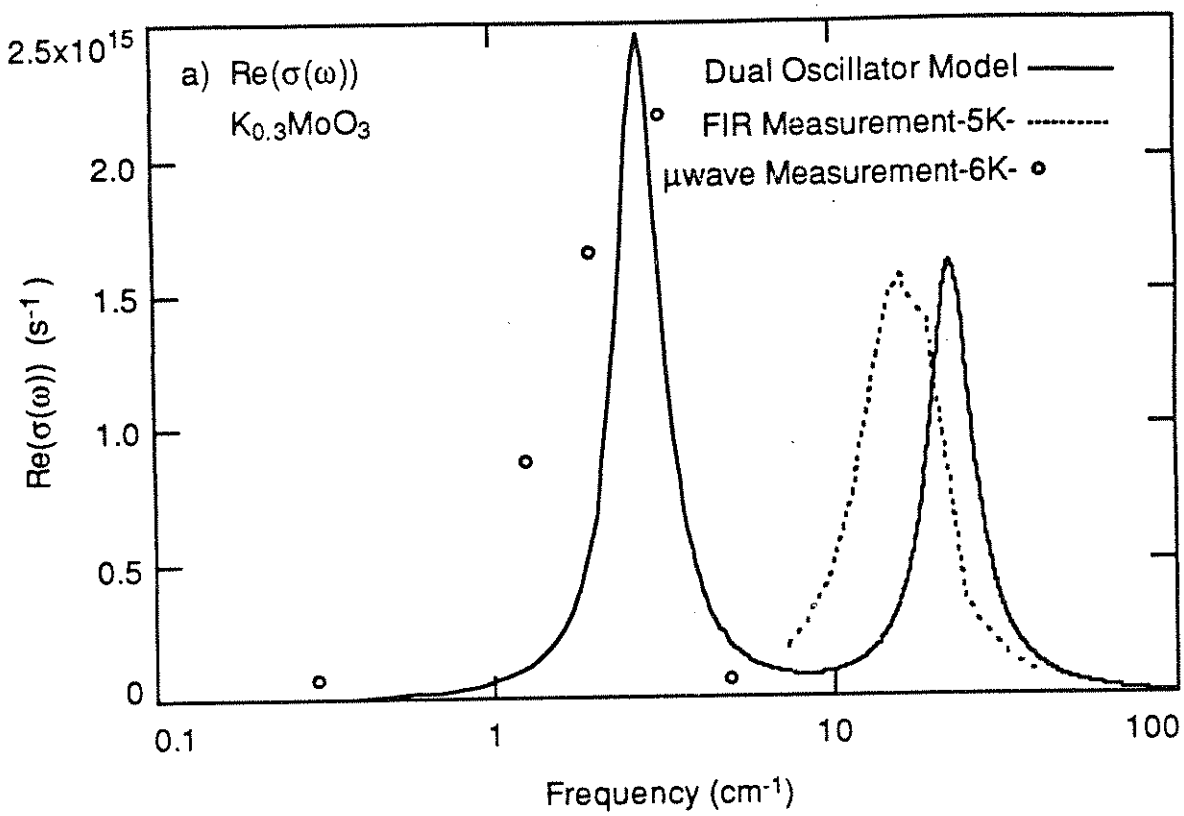
a) Re(σ(ω))
$K_{0.3}MoO_3$
Dual Oscillator Model
FIR Measurement-5K-
μwave Measurement-6K-
2.5x10^15
2.0
1.5
1.0
0.5
0
Re(σ(ω)) (s^-1)
0.1
1
10
100
Frequency (cm^-1)

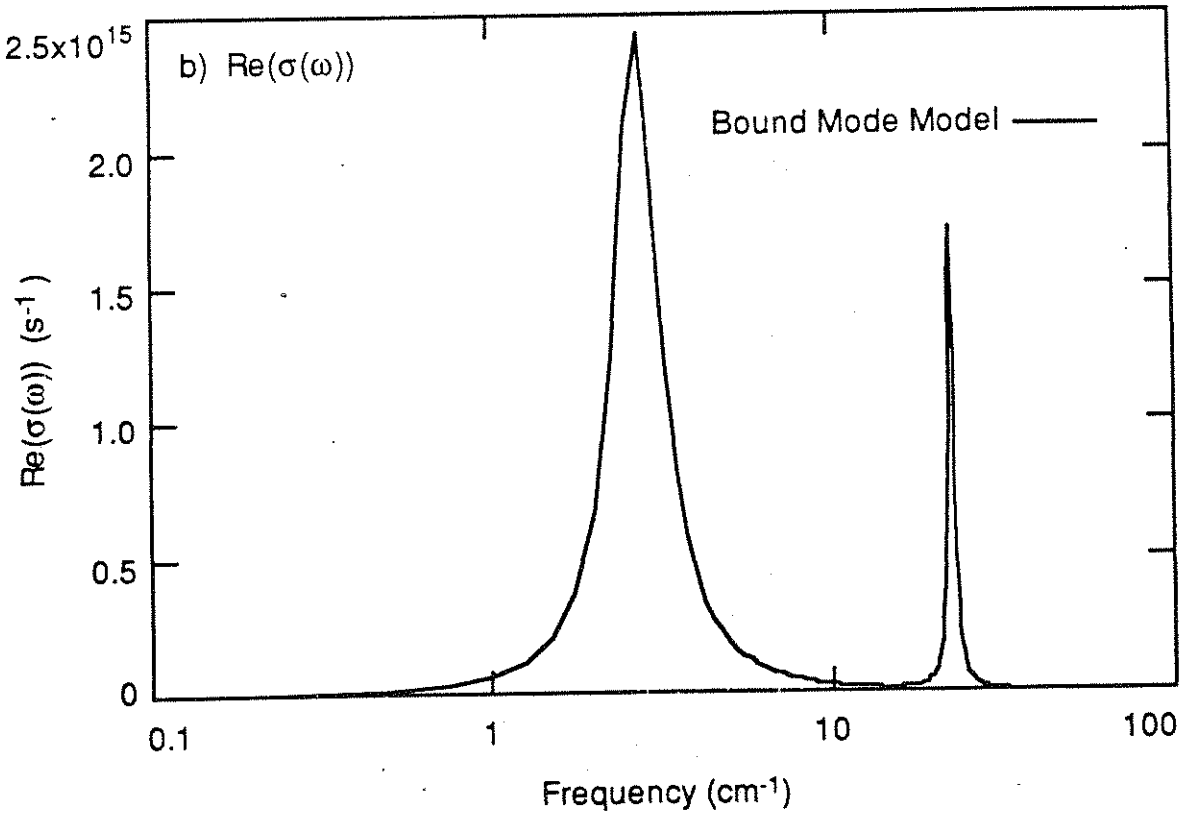
b) Re(σ(ω))
Bound Mode Model
2.5x10^15
2.0
1.5
1.0
0.5
0
Re(σ(ω)) (s^-1)
0.1
1
10
100
Frequency (cm^-1)

$$\varepsilon(\omega) = \varepsilon_\infty + \sum_{j=0}^{1} \frac{S_j \omega_j^2}{\omega_j^2 - \omega^2 - i\frac{\omega}{\tau_j}}. \qquad (6\text{-}1)$$

The resonant frequencies, strengths, and damping times of the two modes are given in Table 6-I. In the remainder of this chapter, we will refer to this conductivity fit as the "dual oscillator model".

The conductivity for a second model of the infrared mode is depicted in Fig. 6-1b. This model is the bound collective infrared mode introduced by Degiorgi and Grüner.[8] It describes the bulk dielectric function for pure $K_{0.3}MoO_3$ with the same microwave resonance used in the dual oscillator model. The effective dielectric function for the crystal is then:

$$\varepsilon(\omega) = \varepsilon_{bulk}(\omega) + \frac{3f\,(\varepsilon_s(\omega) - \varepsilon_{bulk}(\omega))}{\varepsilon_s(\omega) + 2\varepsilon_{bulk}(\omega) - f\,(\varepsilon_s(\omega) - \varepsilon_{bulk}(\omega))}. \qquad (6\text{-}2)$$

where $\varepsilon_s(\omega)=\varepsilon_{bulk}(\omega)+\varepsilon_0$. Parameters for the filling fraction f and the impurity enhancement ε_0 of the dielectric function are given in Table 6-I. The frequency and peak conductivity of the infrared mode match those of the dual oscillator model, but the bound collective mode is quite narrow. The narrowness of the infrared resonance is typical for fits using the bound mode model for all the charge density wave materials. The model predicts a lower frequency for the zero crossing of $\varepsilon_1(\omega)$ and the infrared reflectance edge than those observed. In addition, we note that while the bound collective mode model can often reproduce the qualitative $\sigma(\omega)$ if the infrared mode is smaller than the microwave mode, the initial reports[12-14] of the infrared modes in both $K_{0.3}MoO_3$ and $(TaSe_4)_2I$ show the peak conductivity of the infrared mode to be much larger than that of the pinned acoustic phason mode. In our experience, the bound mode collective model cannot reproduce such

Table 6-I

Parameters used in model fits to the conductivity of $K_{0.3}MoO_3$ at 2K

Dual Oscillator Model

Infrared Mode:	$\omega_1 = 22cm^{-1}$	$S_1 = 1763$	$\tau_1 = .125cm$
Acoustic phason mode: pinned CDW	$\omega_0 = 2.7cm^{-1}$	$S_0 = 22500$	$\tau_0 = 1.0cm$
Acoustic phason mode: sliding CDW	$\frac{\omega_p^2}{4\pi} = 1.32x10^{30}$	$m^* = 10000$	$\Delta = 1600cm^{-1}$

$\varepsilon_\infty = 100.$

Bound Collective Mode Model

Infrared Mode:	$\varepsilon_0 = 1050$	$f = 0.32$	
Acoustic phason mode: pinned CDW	$\omega_0 = 2.7cm^{-1}$	$S_0 = 22500$	$\tau_0 = 1.0cm$
Acoustic phason mode: sliding CDW	$\frac{\omega_p^2}{4\pi} = 1.32x10^{30}$	$m^* = 10000$	$\Delta = 1600cm^{-1}$

$\varepsilon_\infty = 100.$

features. For the remainder of this chapter, the conductivity depicted in Fig. 6-1b will be called the "bound collective mode model".

Neither of these models has any oscillator strength at $\omega = 0$; the sample is an insulator. When a voltage in excess of the threshold voltage is applied across the sample, the CDW depins and the sample becomes an ideal Fröhlich conductor. The conductivity above threshold is a manifestation of a shift of oscillator strength to dc from some other portion of the conductivity spectrum. The dielectric function of the portions of a sample that become conducting should be strongly affected when the charge density wave depins. The conductivity of an ideal Fröhlich charge density wave conductor was calculated by Lee, Rice, and Anderson (LRA).[15] The salient features of the theory were summarized in Chapter Two, and the LRA conductivity is given by Eqs (2-5)-(2-7). The parameters used for the plasma frequency ω_p, the gap Δ, and the CDW effective mass m^* that characterize the LRA mode are given in Table 6-I. The values were taken from the infrared reflectance experiments.[12, 13] In the next section we will compare the dielectric functions and transmittances expected within the dual oscillator model for thin samples of $K_{0.3}MoO_3$ with pinned and sliding CDWs. The subsequent section will make the same comparison using the bound collective mode model.

B. Pinned and sliding CDWs interacting with an intrinsic infrared mode

The real parts $\varepsilon_1(\omega)$ and $\sigma_1(\omega)$ of the dielectric function and conductivity for the dual oscillator model are shown as dashed lines in Fig. 6-2. When the microwave mode is replaced by the Lee-Rice-Anderson conductivity, the solid lines in the Figure are the result. When the CDW depins, the conductivity in the pinned mode shifts to a delta function at $\omega = 0$. The dielectric function for the sliding CDW no longer has the large positive static dielectric constant

Fig. 6-2 a) Real part of the simulated dielectric function for a sliding CDW (solid line, Lee-Rice-Anderson conductivity) and a pinned CDW (dashed line, pinned microwave mode). The infrared mode is modeled as an independent resonance.

b) Real part of the simulated ac conductivity for the models in a).

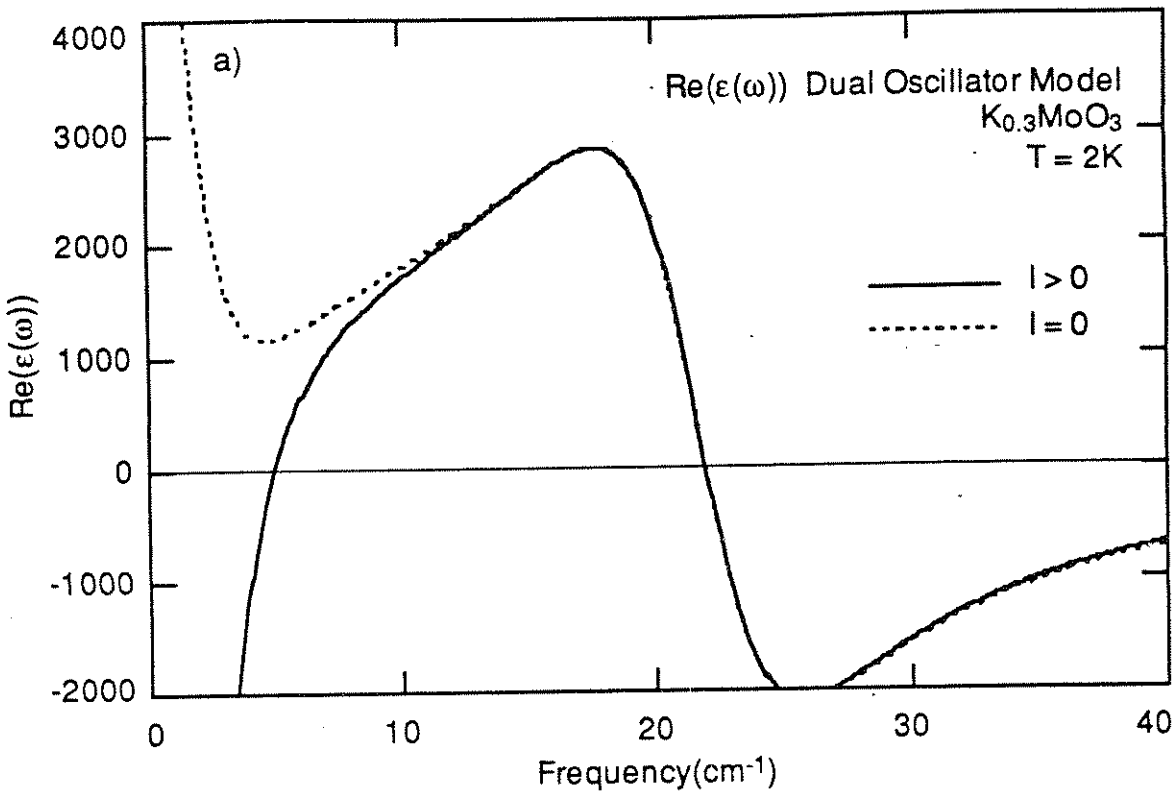
a)
Re(ε(ω)) Dual Oscillator Model
$K_{0.3}MoO_3$
T = 2K
I > 0
I = 0
Re(ε(ω))
4000
3000
2000
1000
0
-1000
-2000
0
10
20
30
40
Frequency(cm^{-1})

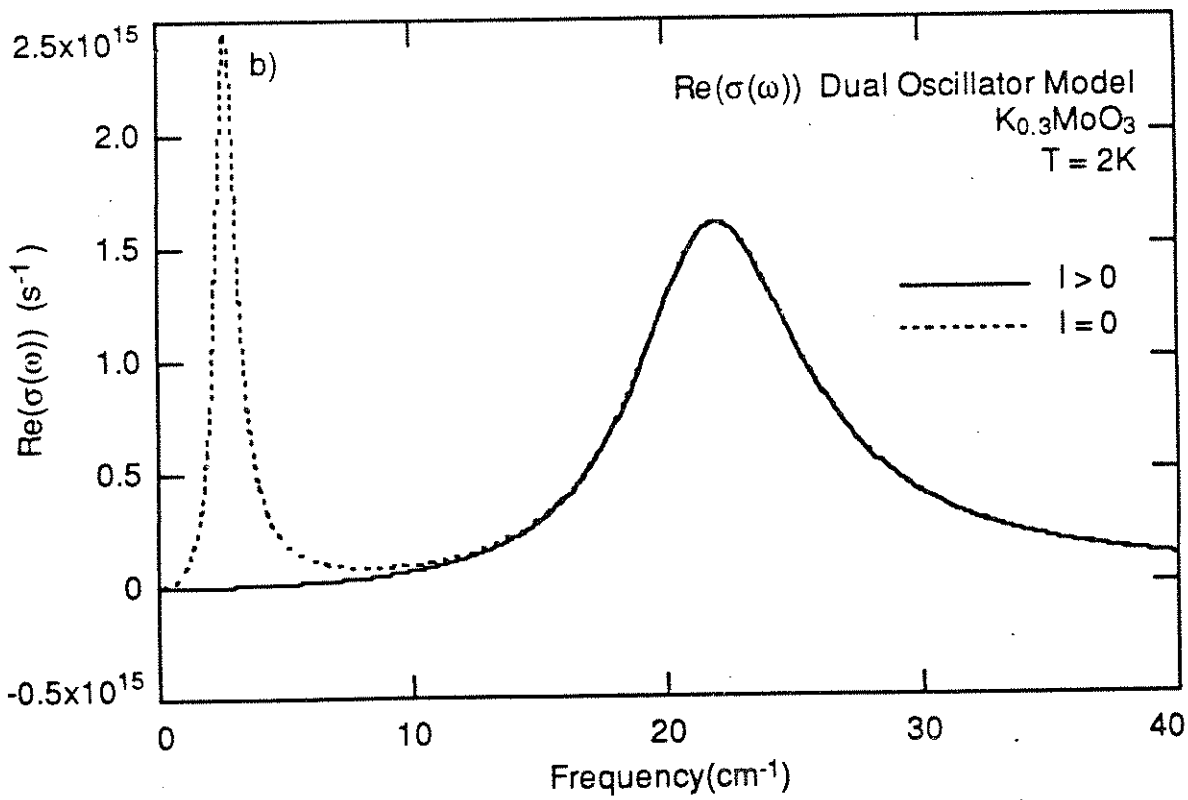
b)
Re(σ(ω)) Dual Oscillator Model
$K_{0.3}MoO_3$
T = 2K
I > 0
I = 0
Re(σ(ω)) (s^{-1})
$2.5x10^{15}$
2.0
1.5
1.0
0.5
0
$-0.5x10^{15}$
0
10
20
30
40
Frequency(cm^{-1})

characteristic of the highly polarizable static CDW. Instead, $\varepsilon_1(\omega)$ is negative and diverging at dc. For conducting material with complex index of refraction $\hat{n}(\omega) = \sqrt{\varepsilon(\omega)} = n + iK$, then transmittance of thin samples in vacuum is given by[16]

$$T = \frac{\tau_{12}^2 \tau_{23}^2 e^{-2K\eta}}{1 + \rho^4 e^{-4K\eta} - 2\rho^2 e^{-2K\eta}\cos(2\Theta+2n\eta)} . \qquad (6\text{-}3)$$

In this expression, $\eta = 2\pi h/\lambda$, where h is the sample thickness and λ is the wavelength of the incident light. The formulae for the reflection coefficient ρ, the phase shift Θ, and the transmission coefficients τ_{12} and τ_{23} are given in the Appendix. Equation (6-3) must be modified when edge effects are important, that is, when the lateral sample dimension and λ are comparable. The cosine term in the denominator modulates the transmittance with the familiar Fabry-Perot pattern. The exponential prefactor to the oscillatory term damps the interference fringes when the optical thickness of the sample exceeds the wavelength of the light. The same exponential term in the numerator strongly suppresses the transmittance for materials with negative or complex $\varepsilon(\omega)$.

We simulated $T(\omega)$ for thin crystals with pinned and sliding charge density waves using Eq. (6-3) and the dielectric functions shown in Fig. 6-2. The result is shown in Fig. 6-3, with a dashed line for the pinned charge density wave and a solid line for the sliding CDW. The magnitude of the transmittance varies exponentially with the imaginary part of the index of refraction. Since our models only approximate that value for $K_{0.3}MoO_3$ crystals, we have plotted $T(\omega)$ on a logarithmic scale to emphasize the large-scale features. The sample thickness in this simulation is 20μm, equivalent to the thickness of the thinnest free standing crystal we were able to make.

Fig. 6-3. a) Simulated transmittance for a thin crystal with a sliding CDW condensate (solid line) and a stationary CDW condensate (dashed line). The sliding state is modelled using a Lee-Rice-Anderson conductivity and the stationary state uses a pinned microwave resonance. The infrared mode is an independent resonance. Fig. 6-2 shows $\varepsilon(\omega)$ and $\sigma(\omega)$ corresponding to these transmittances.

b) Relative transmittance of the sliding and pinned CDW states with an independent infrared resonance.

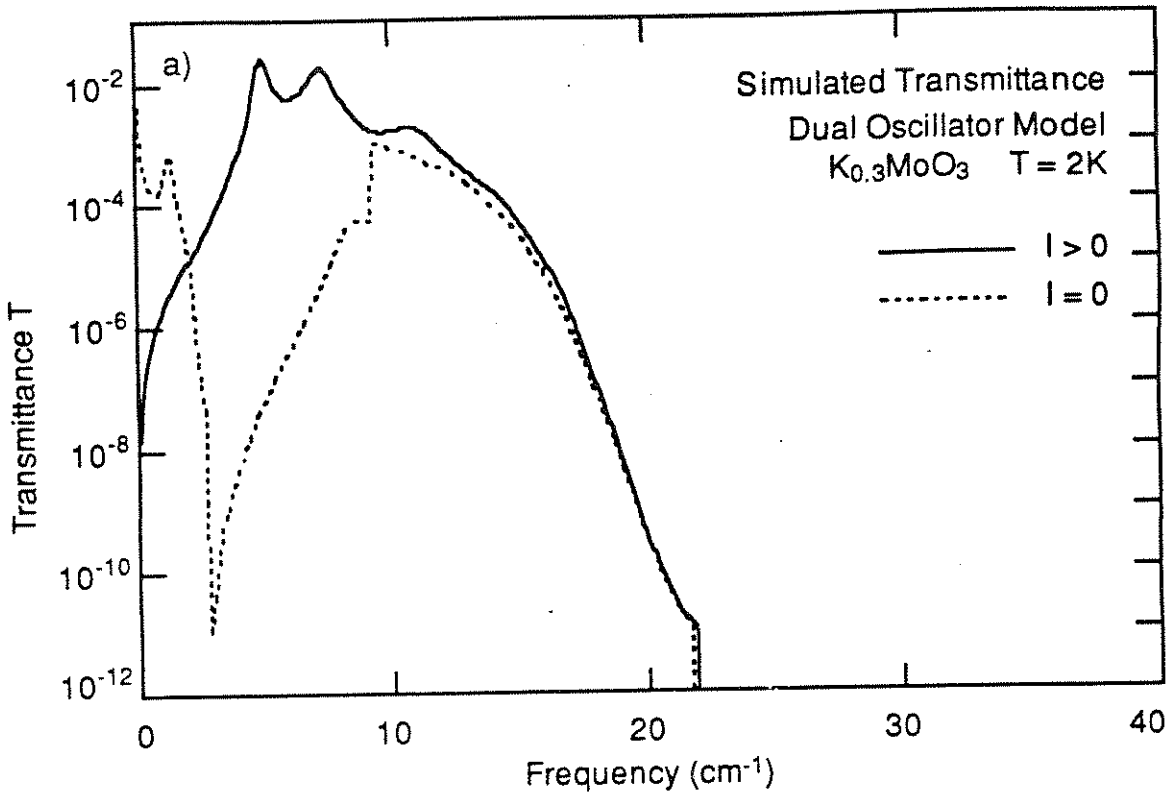
a)
Simulated Transmittance
Dual Oscillator Model
$K_{0.3}MoO_3$ T = 2K
I > 0
I = 0
Transmittance T
10^{-2}
10^{-4}
10^{-6}
10^{-8}
10^{-10}
10^{-12}
0
10
20
30
40
Frequency (cm^{-1})

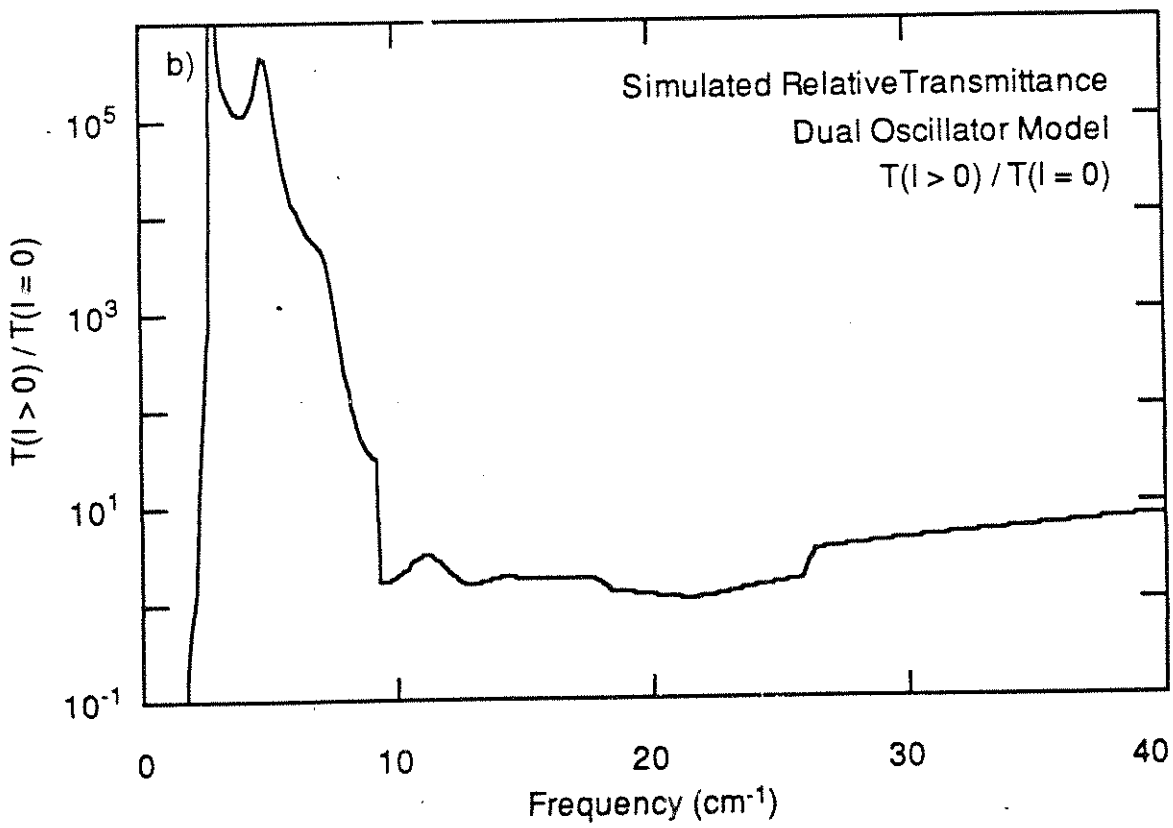
b)
Simulated RelativeTransmittance
Dual Oscillator Model
T(I > 0) / T(I = 0)
T(I > 0) / T(I = 0)
10^{5}
10^{3}
10^{1}
10^{-1}
0
10
20
30
40
Frequency (cm^{-1})

Above 10 cm^{-1}, the transmittances for the pinned and sliding CDWs are approximately equal because in either case the infrared resonance dominates the optical properties of the sample. The transmittances of the samples decrease as the ratio of the sample thickness to the light wavelength increases, and they plummet sharply at 22cm^{-1} when $\varepsilon_1(\omega)$ becomes negative. Below 10cm^{-1}, the transmittances of the pinned and sliding CDWs are quite different. At the lowest frequencies, the crystal with the pinned CDW has a very large, real, positive dielectric function. The associated reflection coefficient is near unity, so the absolute value of the transmittance is only about 1%. The first interference peak in $T(\omega)$ occurs at about 2cm^{-1}, but the transmittance quickly falls at higher frequencies due to the increasing conductivity of the pinned mode. From 3 to 10cm^{-1} the transmittance slowly recovers as the pinned mode conductivity decreases, only to fall again above 10cm^{-1} as the infrared mode begins absorbing energy. No Fabry-Perot fringes are present above 3cm^{-1}. The crystal remains in the thick-sample limit well beyond 40cm^{-1} because of the finite conductivity of the microwave and infrared modes.

The sample with a sliding CDW has very different optical characteristics. At zero frequency the delta function in the conductivity has an associated negative divergence of the real part of $\varepsilon(\omega)$, and $T(\omega)$ is essentially zero. The transmittance remains strongly suppressed until $\varepsilon_1(\omega)$ crosses zero at about 5cm^{-1}. From 6 to 10cm^{-1}, $\varepsilon_1 > 0$ and $\sigma_1 \approx 0$. Strong interference peaks develop. The peaks gradually die away at higher frequencies as the conductivity associated with the infrared mode grows.

The relative transmittance T(I>0)/T(I=0) for the crystal is plotted in Fig. 6-3b. A signature indicating the presence of the LRA sliding mode is clear: at frequencies below the pinning frequency the transmittance for the

crystal with a sliding CDW should fall well short of that for a crystal with a stationary CDW, and at frequencies near and above the pinning frequency the relative transmittance will be greatly enhanced. Moreover, oscillations should develop in the relative transmittance due to prominant Fabry-Perot interference peaks in the transmittance of the sliding mode and the suppression of similar peaks by the pinned mode. These oscillations in $T(I > 0)/T(I = 0)$ may persist to $10cm^{-1}$ and beyond.

C. Pinned and sliding CDWs interacting with a bound collective infrared mode

The infrared transmittance of crystals with pinned and sliding charge density waves also holds clues about the physical mechanism associated with the giant infrared mode. In the previous section we described the transmittance of CDW crystals with a true dissipative mechanism at a particular infrared frequency. Here we examine the transmittance of crystals with a bound collective infrared mode arising from a perturbation of the dielectric function near the impurity sites. In Figure 6-4a, the dashed line is the dielectric function calculated from Eqs. (6-1) and (6-2) for a pinned acoustic phason mode and a bound collective infrared mode. The solid line represents the altered $\varepsilon_1(\omega)$ when the pinned mode is replaced by a LRA mode. The infrared mode shifts to a sharply lower frequency when the charge density wave begins to slide. The frequency of the infrared mode in this model is set not by the energy of any physical mechanism, but by the frequency at which the denominator of Eq. (6-2) is minimized. When the bulk dielectric function changes, the location of the bound mode shifts.† The

† If the bound collective mode theory proves to be the explanation for the infrared mode, a similar effect may account for the shift in the infrared resonance from sample to sample and with varying dopant concentrations and temperatures.

Fig. 6-4. a) Real part of the simulated dielectric function for a sliding CDW (solid line, Lee-Rice-Anderson conductivity) and a pinned CDW (dashed line, pinned microwave mode). The infrared mode is modeled as a bound collective mode.

b) Real part of the simulated ac conductivity for the models in a).

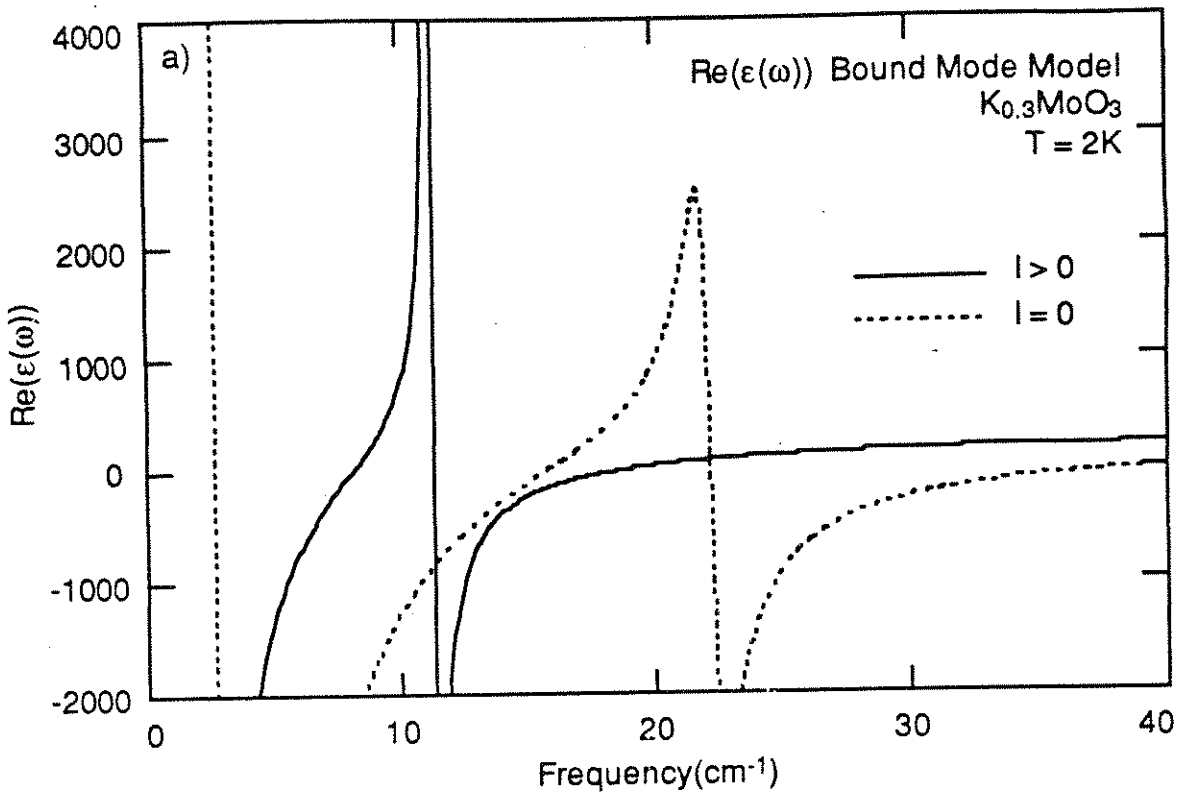
a)
Re(ε(ω)) Bound Mode Model
$K_{0.3}MoO_3$
T = 2K
I > 0
I = 0
Re(ε(ω))
4000
3000
2000
1000
0
-1000
-2000
0
10
20
30
40
Frequency(cm^{-1})

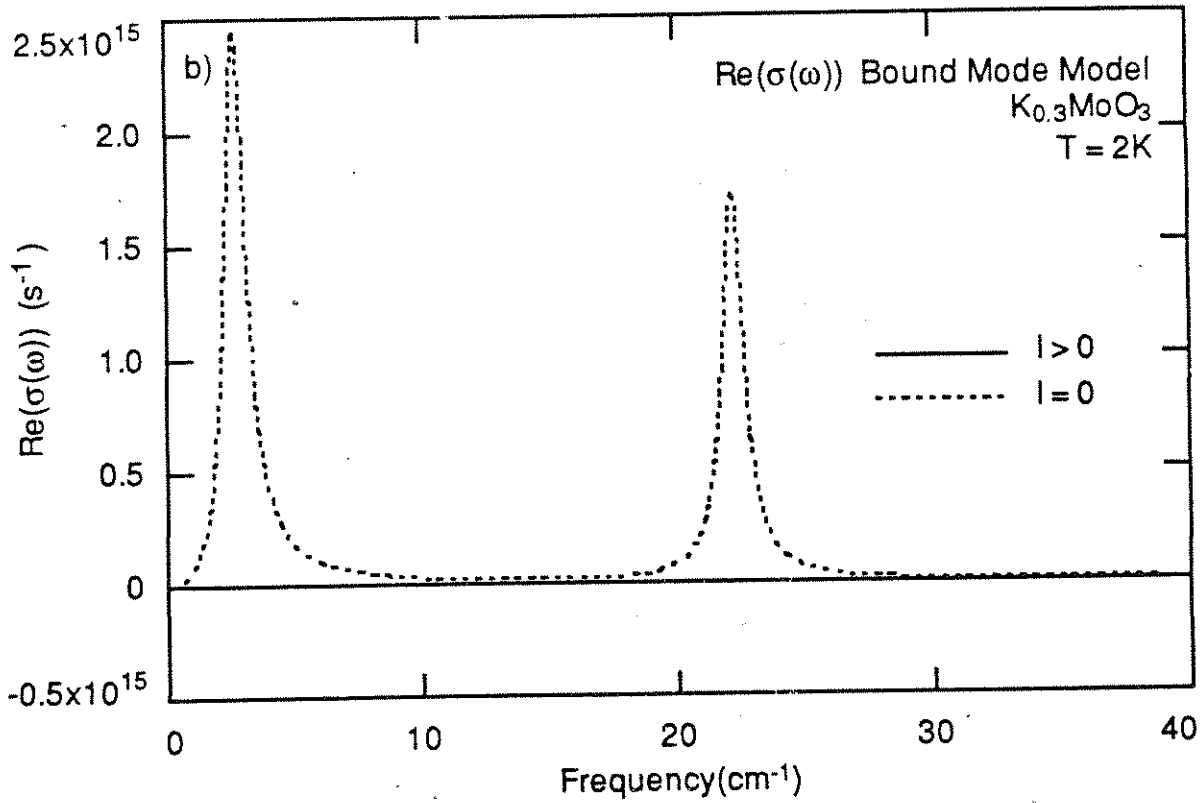
b)
Re(σ(ω)) Bound Mode Model
$K_{0.3}MoO_3$
T = 2K
I > 0
I = 0
Re(σ(ω)) (s^{-1})
2.5x10^{15}
2.0
1.5
1.0
0.5
0
-0.5x10^{15}
0
10
20
30
40
Frequency(cm^{-1})

magnitude of the frequency shift of the infrared mode depends on the slope of the bulk dielectric function in the vicinity of the mode, and as the Figure shows, the shift may be quite pronounced. In applying the bound collective mode model to the experiment on $(Ta_{1-x}Nb_xSe_4)_2I$ alloys in Chapter Five, we altered the size and frequency of the infrared mode to fit the observed $\varepsilon(\omega)$ by changing ε_0 and f. Here, ε_0 and f remain the same for a crystal as the charge density wave depins, and the size and frequency of the infrared mode vary as $\varepsilon_{bulk}(\omega)$ changes.

A more surprising consequence of the bound collective mode model is shown in Fig. 6-4b: the real part of the conductivity for the bound mode model is identically zero in the presence of a sliding CDW described by a LRA theory. This striking feature follows from Eq.(6-2). The conductivity of the Lee-Rice-Anderson model is zero inside the gap, so the dielectric function is real. At frequencies well below the resonance associated with the electronic polarization of the impurity atoms, the sphere dielectric functions are real as well, and hence all the terms in Eq. (6-2) are real. Thus, within the bound mode model, the infrared mode still exists in the dielectric function, but there is no associated conductivity. The onset of ideal Fröhlich differential conductivity not only destroys the dissipation associated with the pinned mode, but it also destroys the dissipation associated with the giant infrared mode. This profoundly affects the transmittance at frequencies in the vicinity of the infrared mode.

We calculated simulated transmittances for the pinned and sliding cases with the infrared mode modelled as a bound collective mode. The results are shown in Fig. 6-5a as dashed and solid lines, respectively. The transmittance of the crystal with a pinned CDW and a bound mode is very similar to the transmittance for a crystal with a pinned CDW and an intrinsic

Fig. 6-5. a) Simulated transmittance for a thin crystal with a sliding CDW condensate (solid line) and a stationary CDW condensate (dashed line). The sliding state is modelled using a Lee-Rice-Anderson conductivity and the stationary state uses a pinned microwave resonance. The infrared mode is modelled as bound collective mode localized on impurities in the system. Fig. 6-4 shows $\varepsilon(\omega)$ and $\sigma(\omega)$ corresponding to these transmittances.

b) Relative transmittance of the sliding and pinned CDW states with an bound collective infrared mode.

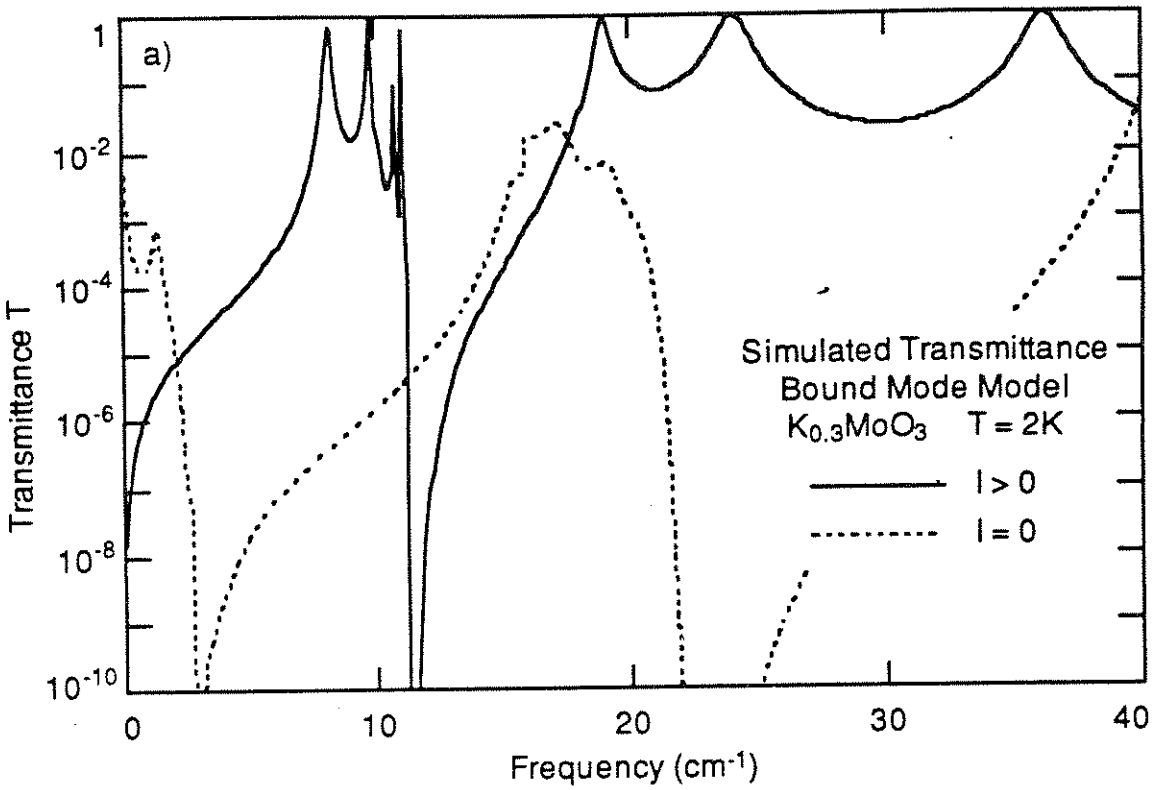
a)
Transmittance T
1
10^{-2}
10^{-4}
10^{-6}
10^{-8}
10^{-10}
0
10
20
30
40
Frequency (cm^{-1})
Simulated Transmittance
Bound Mode Model
$K_{0.3}MoO_3$ T = 2K
I > 0
I = 0

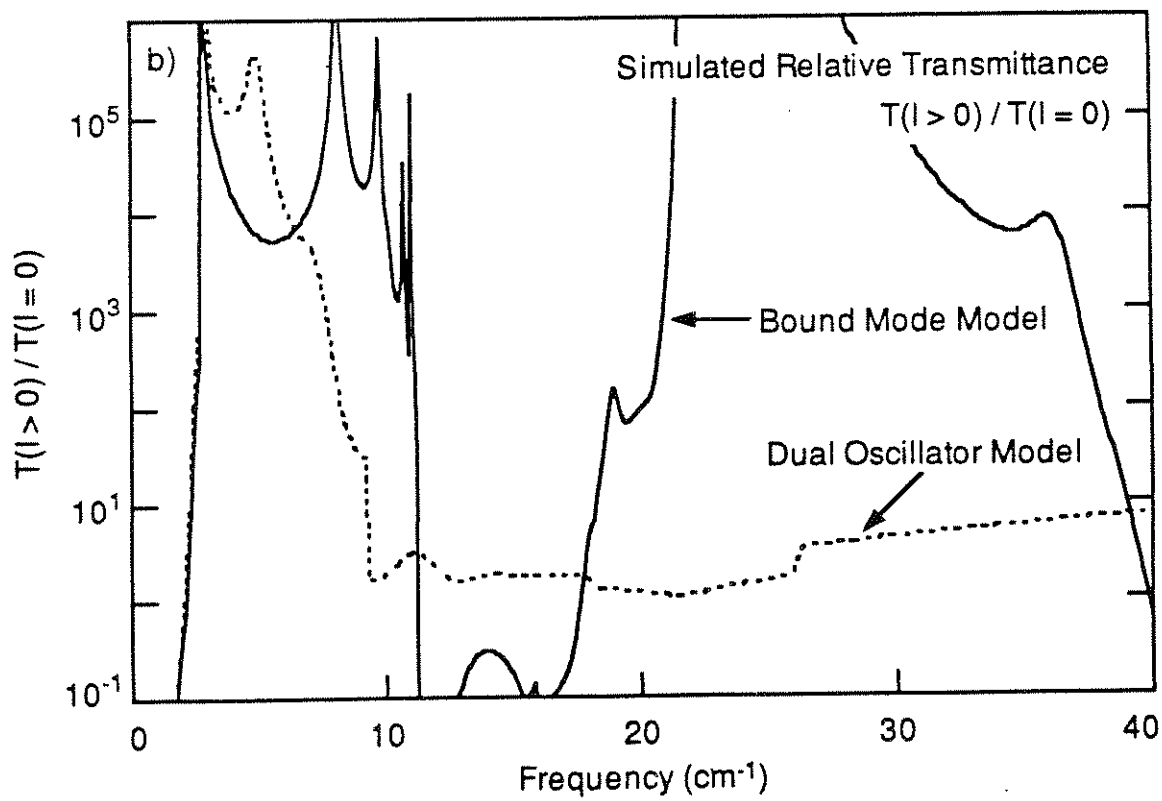
b)
T(I > 0) / T(I = 0)
10^{5}
10^{3}
10^{1}
10^{-1}
0
10
20
30
40
Frequency (cm^{-1})
Simulated Relative Transmittance
T(I > 0) / T(I = 0)
Bound Mode Model
Dual Oscillator Model

infrared mode. At high frequencies, $T(\omega)$ recovers more rapidly for the bound mode case. This is primarily due to the reduced width of the bound mode in comparison to the measured infrared resonance. When the CDW slides, the low frequency features of T(w) are reminiscent of those for the sliding case with intrinsic infrared mode. The transmittance is small near dc when $\varepsilon_1 < 0$, but strong Fabry-Perot transmittance peaks develop at frequencies below the infrared mode. The divergent dielectric function strongly suppresses the transmittance near the frequency of the shifted infrared mode, but $T(\omega)$ quickly recovers at higher frequencies and approaches unity. Above the infrared mode, there is no dissipation and ε_1 is small. Regular interference peaks occur out to the onset of midgap states or phonons. The transmittance maxima approach unity, and the minima should exceed 10%. This enhancement of $T(\omega)$ occurs in the same frequency range where the bound collective infrared mode suppresses the transmittance when the charge density wave is pinned.

The relative transmittance of the sliding and pinned CDW states for the bound mode infrared theory are shown as the solid line in Fig. 6-5b. At low frequencies, $T(I > 0)/T(I = 0)$ is enhanced for the crystal with a sliding mode, and prominent oscillations associated with Fabry-Perot peaks for the sliding state should be present. The situation is qualitatively similar to that for the dual oscillator model, shown for comparison as a dashed line in the Figure. At frequencies above about $20cm^{-1}$, the two models give different predictions: for a dual oscillator model the relative transmittance should remain constant, while in the bound mode model the relative transmittance should be greatly enhanced and contain strong oscillations due to undamped Fabry-Perot interference. We now turn to an experiment designed to test these predictions.

Measurement of the transmittance of thin samples of $K_{0.3}MoO_3$

A. Preparation of blue bronze crystals.

Many quasi-one dimensional charge density wave materials are fibrous or fragile, but the sturdy crystals of $K_{0.3}MoO_3$ and $Rb_{0.3}MoO_3$ are well suited for transmittance studies. Single crystals of the blue bronzes often grow in cubes as large as 1/2cm on a side, and they can easily be cleaved or shaped by abrasion into thin slabs. We grew large crystals of $K_{0.3}MoO_3$ by electrolytically reducing a melt of K_2MoO_4 and MoO_3.[17] The starting materials[18] were intimately mixed in a crucible and then tightly packed into a 10ml pyrex beaker with platinum electrodes crimped along the sides. Nichrome wires connected the electrodes through the walls of a box furnace to a current source. With the current souce off, we slowly heated the beakers in air to 620°C. The powders melt to a brown liquid at about 560°C. After letting the melted powders mingle for ten minutes, we lowered the temperature about 1°C/min to 558°C, just above the recrystallization temperature. We turned the current source on and adjusted it for 40mA current through the beaker. The chemical reaction caused violent bubbling in the melt. As the reaction proceeded, the flux gradually solidified and the current became erratic. After twenty four hours we turned the current source and the oven off and let the crystals cool slowly to room temperature.

The crystals have a beautiful deep blue-black sheen; they are encased in a clear yellow flux. After removing the beakers from the oven, we cracked them and then further cracked the flux surrounding the crystals with a hammer. This technique often preserved more intact crystals than gradually removing the tough crystallized flux with a scalpel or dentist's drill. We prepared thin samples for the transmittance measurements by mechanically

polishing them with a Buehler Minimet oscillatory polishing machine. First, we cleaved a large crystal to expose a clean flat face and mounted it face down with hard sealing wax onto the steel sample holder of the polishing machine. Most of the bulk of the sample was abraded away by 600grit emery cloth lubricated with water. The final 50μm were removed by a using a 0.05μm Al_2O_3 polishing emulsion mixed with distilled water on a soft fabric base. We carefully monitored the thickness of the sample to avoid breaking it. Our thinnest samples were 20μm thick and the samples used in the measurements reported here are 72μm thick. We removed the sample from the steel slug by dissolving the wax with warm methanol.

We chemically polished the freestanding samples in a solution of NH_4OH and attached contacts to either end. The best contacts to the blue bronzes are typically made by depositing electroplated copper from a saturated copper sulfate solution. Our thin crystal slabs, though, were extremely fragile. The handling involved in the electroplating process precluded the use of such contacts. Instead, we covered the middle section of the samples with thin aluminum foil and evaporated 2000Å of indium onto the exposed ends of the samples. We tilted the crystal during the evaporation to ensure full coverage of the end surfaces. Gold lead wires were then attached to the indium pads using silver paint.

The samples, bolometric detector, and filters were all mounted on an insert within a double glass dewar. The experiment was performed at 1.5-2K with the samples immersed in superfluid helium to ensure uniform temperature throughout the crystals. They sat in a rotating brass wheel at the end of a light pipe connected to the Michelson Fourier transform interferometer. We attached each sample with rubber cement to a brass disk covered with insulating mylar tape. An aperture through the disk and the

tape admitted light to the sample. The gold wires from the sample contacts were connected to solder pads on the brass disk, and from there via manganin wires to the electronics external to the dewar. The disk and a companion reference disk with the same aperture were mounted in adjacent positions on the sample wheel. A polarizer similar to those in the reflectance/transmittance apparatus was mounted on the end of the light pipe above the samples. The electric field was polarized along the conducting axis of the crystals. A second brass rotator wheel with infrared low-pass filters sat between the samples and the mylar window that sealed the chamber containing the bolometer.

We measured the transmittance of two different samples that were fragments from a single initial polished crystal. The larger sample A was mounted atop a 1.5mm square aperture, and the smaller sample B covered a circular aperture with 0.052" diameter. Sample A had a longitudinal crack partway through the sample that may have enhanced its apparent transmittance by leaking some light. The crack certainly impeded a uniform current distribution in the sample.

We placed a current-limiting resistor in series with the sample outside the dewar and connected a HP6234A voltage source across the combination. We measured the applied voltage with a Keithley 177 DVM and monitored the current with a chart recorder connected to PAR113 amplifier connected across the current-limiting resistor. For measurements in the sliding CDW case, we slowly increased the bias voltage until the sharp CDW threshhold voltage, then increased the voltage drop across the limiting resistor to maintain the desired current.

B. Results

Figure 6-6 shows the transmittance of $K_{0.3}MoO_3$ for sample A. The quantity shown is a ratio of the detected spectra for light transmitted through the sample and through the reference aperture. The sample transmittance is quite low, so the optical loading on the bolometer is reduced when the sample replaces the reference aperture. The bolometer is colder and more sensitive for the sample spectrum than for the reference spectrum. The displayed value of the transmittance has not been corrected for the differences in bolometer responsivity and it overestimates the actual transmittance by a factor of about 2. The transmittance decreases with increasing frequency and it is modulated with periodic interference maxima. The peaks are suppressed somewhat near $40cm^{-1}$ and more closely spaced above $50cm^{-1}$. These two features may signal the dissipation associated with the infrared mode. The interference peaks are suppressed again at 70 and $80cm^{-1}$ near the locations of small modes at 72 and $84cm^{-1}$ in the infrared reflectance spectrum. In general, the transmittance of sample A is greater than expected from the simulations portrayed in Figs. 6-3 and 6-5. The Fabry-Perot modulation is also more prominent than expected. These features may indicate that the pinned and infrared modes in $K_{0.3}MoO_3$ have lower peak conductivities and larger damping times than assumed in our model.

The threshold voltage of Sample A was 18.1V. We depinned the CDW and set the current at 8 mA. The relative transmittance shown in Fig. 6-6b is the spectrum of light transmitted by the sample with the sliding CDW normalized by the spectrum of light transmitted by the sample with the CDW pinned. The relative transmittance is 95% from about $20cm^{-1}$ out to $250cm^{-1}$. The value falls short of unity, probably because heat dissipated at the sample contacts warms the helium bath and makes the bolometer less responsive.

Fig. 6-6 a) Measured transmittance for a $K_{0.3}MoO_3$ sample with a stationary CDW. The sample is 72μm thick. Heavy optical loading reduces the bolometer sensitivity during measurements of the reference spectrum, and hence the true transmittance is less than that shown here.

b) Relative transmittance $\mathcal{T}(I = 8ma)/\mathcal{T}(I = 0)$ for the sample when the CDW is sliding and pinned.

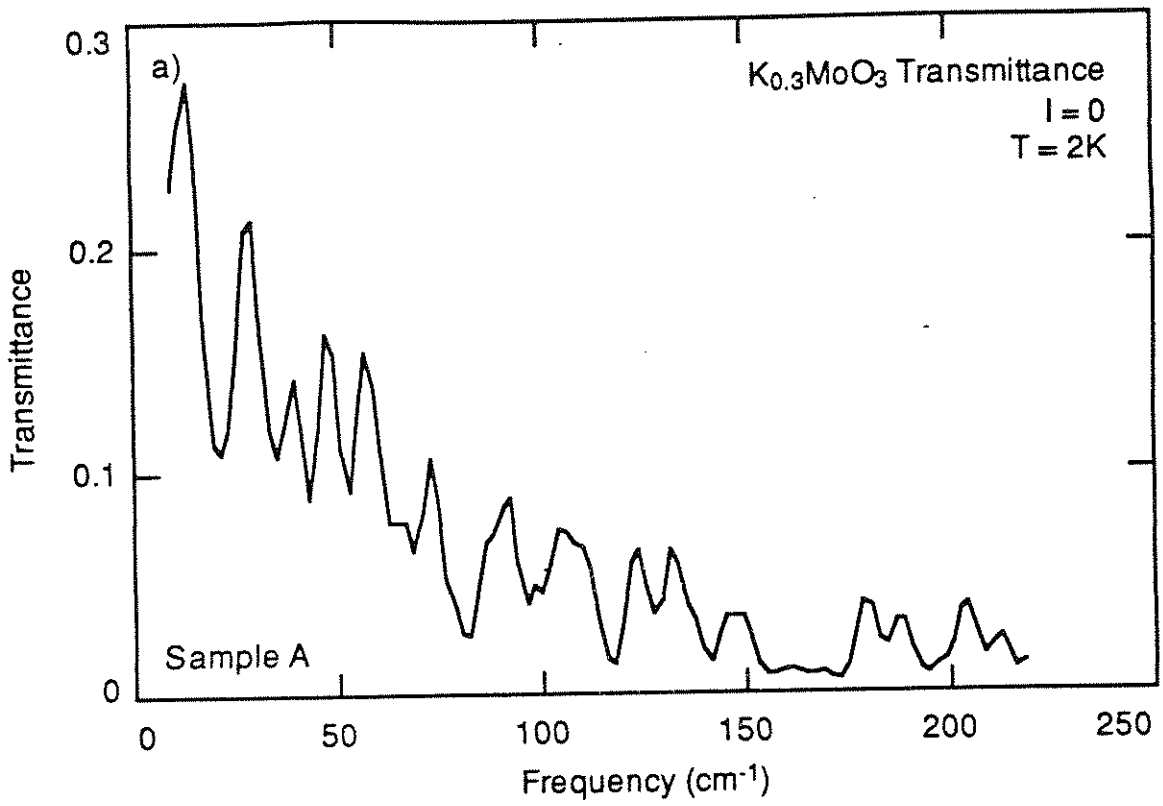
a)
$K_{0.3}MoO_3$ Transmittance
I = 0
T = 2K
Sample A
Transmittance
0.3
0.2
0.1
0
0
50
100
150
200
250
Frequency (cm^{-1})

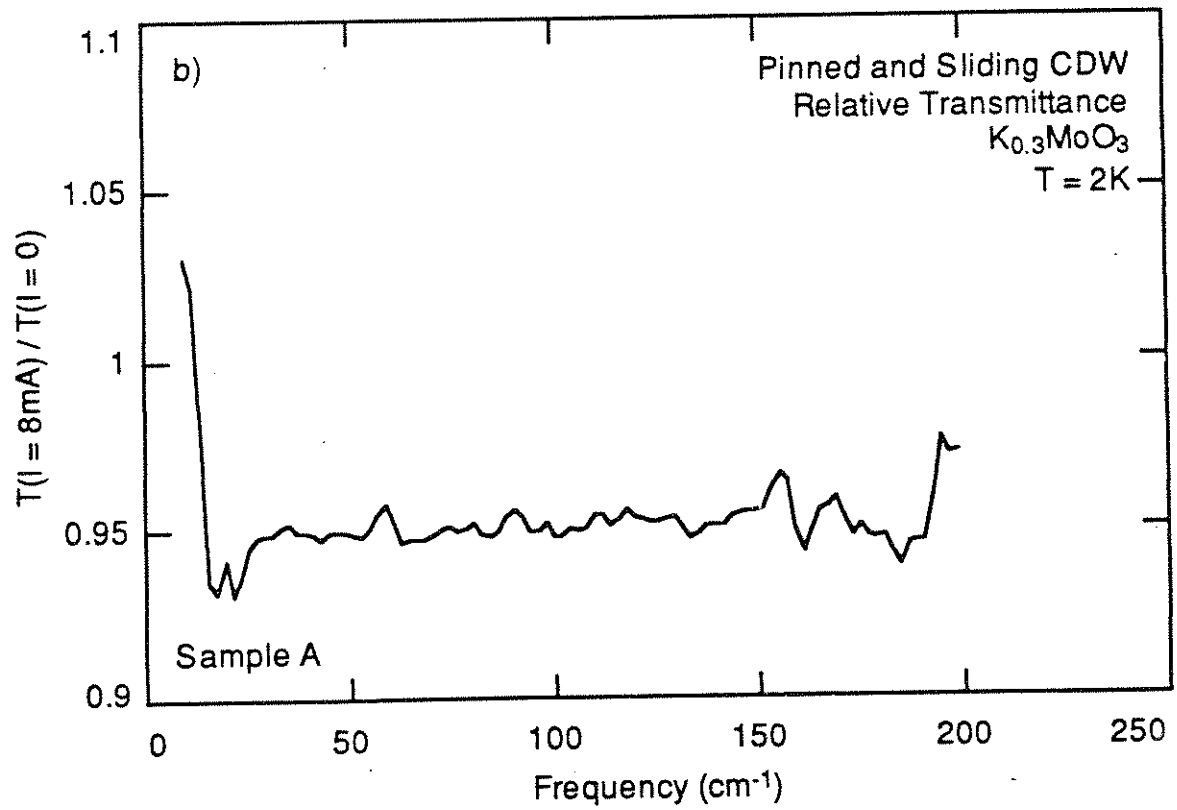
b)
Pinned and Sliding CDW
Relative Transmittance
$K_{0.3}MoO_3$
T = 2K
Sample A
T(I = 8mA) / T(I = 0)
1.1
1.05
1
0.95
0.9
0
50
100
150
200
250
Frequency (cm^{-1})

The transmittance drops slightly at low frequencies and shows evidence of a more pronounced interference peak, and below $15cm^{-1}$ the relative transmittance is enhanced. Both these features are reminiscent of the transmittance signature for the presence of the LRA mode in the dual oscillator mode model.

We repeated the measurements on the smaller sample B in an effort to more fully characterize $T(\omega)$ at frequencies below $25cm^{-1}$. The current was limited to $85\mu A$ to avoid heating the helium bath. The dc voltage across the bolometer (a measure of its temperature) remained constant when the CDW depinned. Fig. 6-7 shows the relative transmittance below $40cm^{-1}$. The solid line represents measurements for a .010" mylar beamsplitter and the dashed line represents measurements with a mylar beamsplitter .003" thick. The signal for these measurements was much lower than that for the measurements on Sample A because of the reduced size of the aperture and the reduced passband of the infrared filters. We partially compensated for the reduced signal to noise ratio by alternating measurements with and without current. The displayed transmittance is the average of ten such pairs of spectra. At the very lowest frequencies, the relative transmittance again diverges (the divergence may well be caused by slow drifts in the interferograms rather than by changes in $T(\omega)$ in the sample). Between 20 and $25cm^{-1}$ the interference oscillations are suppressed, perhaps by the presence of the FIR mode. The oscillations reform at higher frequencies.

Discussion

Some of the features of the measured transmittances are reminiscent of the features expected from our modelling of LRA conductivity in CDW conductors. In particular, the measurements on sample A indicate an

Fig. 6-7 Relative transmittance $\mathcal{T}(I = 85\mu a)/\mathcal{T}(I = 0)$ for a sample of $K_{0.3}MoO_3$ when the CDW is sliding and pinned. The solid line represents measurements from 2-10cm^{-1} using a 10mil mylar beamsplitter, and the dashed line represents measurements from 8-40cm^{-1} using a 3 mil mylar beamsplitter. Each line is an average of ten spectra.

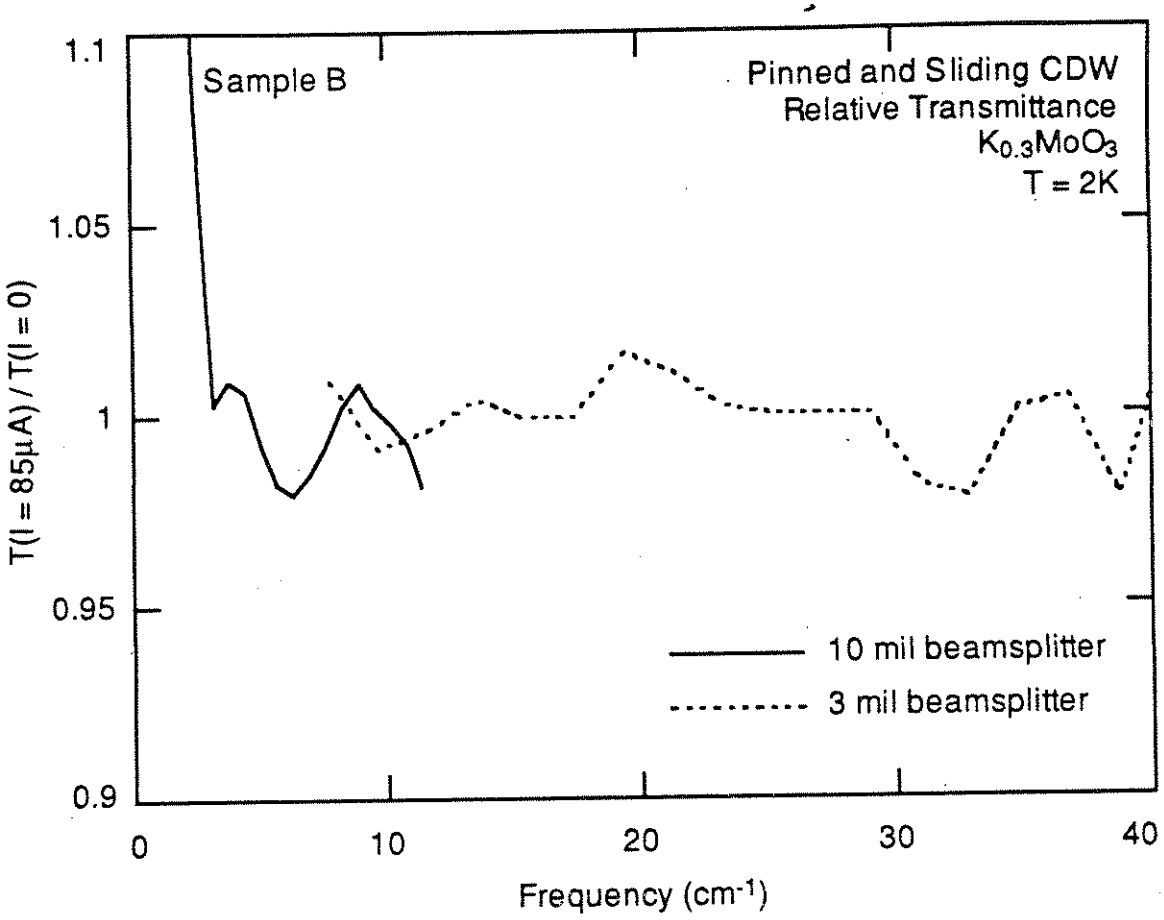
Sample B
Pinned and Sliding CDW
Relative Transmittance
$K_{0.3}MoO_3$
T = 2K
10 mil beamsplitter
3 mil beamsplitter
T(I = 85μA) / T(I = 0)
Frequency (cm^{-1})
1.1
1.05
1
0.95
0.9
0
10
20
30
40

enhanced low frequency transmittance and enhanced Fabry-Perot interference peaks in the conducting state above $10cm^{-1}$. The spectra for Sample A were extremely quiet and reproducible, and we believe the effects are real. We do not see a concurrent enhancement of the transmittance in the region of the infrared mode. To the extent that the results on sample A reveal the existence of a LRA mode, they also indicate that the infrared mode is not a bound collective mode. On the other hand, the observations could not be repeated on sample B. The measurements on sample B are less reliable, and the oscillatory features in the relative transmittance are comparable in size to the variations between nominally identical spectra.

In both samples the effects of the presence of a sliding CDW on the transmittance are quite small, on the order of a few percent. The dual oscillator and bound collective mode models in the initial part of this chapter predict a much larger perturbation of T(w). One problem is that the models assume a change in the dielectric constant throughout the sample. The differential conductivity of the sliding charge density wave, though, is zero. Once the CDW in one part of the sample depins, it shunts all the current and prevents a subsequent voltage rise in other parts of the sample. If various sections of the crystal have slightly different threshold voltages, only the first filament that conducts will have an altered dielectric constant. Estimates of the fraction of the crystal volume occupied by the sliding CDW range from 1% to more than 50%, but all authors agree that once the conduction begins, there is no substantial increase in the conducting area once the current exceeds 1mA.[3, 12] We could perhaps raise the volume of the sample under the influence of the current by providing multiple current paths through the sample, or more simply by requiring the current to trace a sinuous path through the sample.

Conclusion

In this chapter we have presented a simulation of the change in the optical properties of $K_{0.3}MoO_3$ when the CDW breaks free from the impurity potential and slides freely. The acoustic phason mode was modelled as a microwave oscillator and with the Lee-Rice-Anderson conductivity. The giant infrared resonance was modelled as an intrinsic physical oscillator and with the bound collective mode model. We found that the signature of the shift in oscillator strength is an enhancement of the transmittance in the vicinity of the pinned mode, and a suppression of the transmittance near dc, below the frequency of our FIR measurements. In addition, we found that if the LRA mode accurately models the shift in oscillator strength, then the nature of the infrared mode is also revealed. The bound mode model gives a surprising result for depinned charge density waves: the infrared mode strongly affects the real part of the dielectric function, but there is no associated conductivity. The transmittance of the crystal should approach unity, with sharp Fabry-Perot fringes, in the vicinity of the infrared mode. We have presented measurements of the transmittance of $K_{0.3}MoO_3$ with the charge density wave in the pinned and sliding states for two different samples. In the larger sample, the transmittance is enhanced below $15cm^{-1}$. The rise is in general agreement with the models of $T(\omega)$ when oscillator strength shifts from the pinned mode to dc. We do not see the concurrent rise in the transmittance in the vicinity of the infrared mode that would be characteristic of a bound infrared mode associated with additional electronic polarization near the impurity sites. The observations could not be repeated for a second sample. The quality of the spectra for the latter sample was compromised by the small sample size, the low signal-to-noise ratio at low

frequencies, and possibly by the small current through the sample. Though our measurements on the larger sample are suggestive of a shift in oscillator strength, we cannot claim the that the shift has been unambiguously demonstrated. The changes in the transmittance of these samples are at the very limits of our experimental sensitivity. The transmittance experiments could be improved by using larger samples or a brighter infrared light source. The influence of the moving CDW on the optical properties may be enhanced by applying multiple contacts to the sample and depinning separate sections of the crystal simultaneously.

References

1. H. Fröhlich, Proc. R. Soc. London Ser. A **223**, 296 (1954).

2. G. Mihály and P. Beauchêne, Solid State Comm. **63**, 911 (1987).

3. G. Mihály, P. Beauchêne and J. Marcus, Solid State Comm. **66**, 149 (1988).

4. G. Mihály, P. Beauchêne Ting Chen, L. Mihály and G. Grüner, Phys. Rev. B **37**, 6536 (1988).

5. S. Martin, R.M. Fleming and L.F. Schneemeyer, Phys. Rev. B **38**, 5733 (1988).

6. G. Mihály, T. Chen, T.W. Kim and G. Grüner, Phys. Rev. B **38**, 3602 (1988).

7. R.E. Glover III and M. Tinkham, Phys. Rev. **108**, 243 (1957).

8. L. Degiorgi and G. Grüner, (in press).

9. A.S. Barker, Phys. Rev. B **7**, 2507 (1973).

10. P. Monceau, J. Richard and M. Renard, Phys. Rev. Lett. **45**, 43 (1980).

11. S. Donovan, Y. Kim, B. Alavi, L. Degiorgi and G. Grüner, Solid State Comm. **75**, 721 (1990).

12. H.K. Ng, G.A. Thomas and L.F. Schneemeyer, Phys. Rev. B **33**, 8755 (1986).

13. G. Travaglini and P. Wachter, Phys. Rev. B **30**, 1971 (1984).

14. M.S. Sherwin, A. Zettl and P.L. Richards, Phys. Rev. B **36**, 6708 (1987).

15. P.A. Lee, T.M. Rice and P.W. Anderson, Solid State Comm. **14**, 703 (1974).

16. Max Born and Emil Wolf, in *Principles of Optics*, (Pergamon Press, Oxford, 1970), p. 631.

17. A. Wold, W. Kunnmann, R.J. Arnott and A. Ferreti, Inorg. Chem. **3**, 545 (1964).

18. K_2MoO_4, 98% purity, and MoO_3, 99.5% purity, in a 1:3.35 molar ratio. Fluka Chemical Corp., Hauppauge, NY 11778.

Part II: Oxygen Isotope Effect in High-Tc Superconductors

Chapter 7

Introduction to the Isotope Effect

Variation of transition temperature with isotopic mass

The spectacularly high transition temperatures of the newly discovered classes of oxide superconductors[1-3] have resulted in suggestions that the superconductivity in these materials may be fundamentally very different from that of "conventional" superconductors. The Bardeen Cooper Schrieffer (BCS)[4, 5] theory of phonon-mediated electron pairing may not be adequate to explain superconductivity within these new materials. Shapiro step experiments[6] on $La_{1.85}Sr_{0.15}CuO_4$ and $YBa_2Cu_3O_7$, which exploit intrinsic ac Josephson effects within polycrystalline specimens, have clearly indicated that a fundamental charge $q = 2e$ is associated with the superconducting state. Although most researchers believe that this result demonstrates that electron pairing does occur, the specific pairing mechanism (phonon or non-phonon) is generally considered to be an open question.

In Chapter 8 we will present details of a careful measurement of the oxygen isotope effect in $YBa_2Cu_3O_{7-\delta}$. The measurement gives information about the contribution of phonons in the formation of Cooper pairs; this chapter serves as an introduction to this experiment. We will discuss the historical role of isotope effect experiments in superconductivity research and then give an extensive overview of previous measurements of the isotope coefficient α in the oxide superconductors. Previous experiments have given contradictory results and have been plagued by systematic errors. The experiment to be discussed in Chapter 8 was designed to greatly reduce such errors, and our results set the tightest error limits on α reported for any oxide superconductor.

The dependence of the superconducting transition temperature T_c on isotopic mass M in the host lattice has been one of the most revealing tests for phonon-mediated pairing. The original isotope effect experiments[7, 8] in elemental mercury showed that $T_c \sim M^{-\alpha}$, with $\alpha = 0.5$. This discovery provided one of the important clues which resulted in the BCS theory of superconductivity. According to the simple BCS model, T_c is given by

$$k_B T_c = 1.13\, \hbar\omega_D\, e^{-\frac{1}{N(0)V}} \qquad (7\text{-}1)$$

where N(0) is the (constant) density of states at the Fermi level, V is the strength of the attractive interaction between members of the Cooper pair, and ω_D is the Debye frequency, an upper cutoff energy for the phonons that mediate the interaction. T_c is directly proportional to ω_D, which in turn varies as $M^{-0.5}$ in an ideal harmonic solid. When the electron-phonon interaction λ and the renormalized interelectron Coulomb repulsion μ^* are treated separately in a two-square-well model[9] within BCS theory, α takes the form

$$\alpha = \frac{1}{2}\left[1 - \left(\frac{\mu^*}{\lambda - \mu^*}\right)^2\right]. \qquad (7\text{-}2)$$

It may be reduced from 0.5 and assume negative values. However, within this model α cannot be greater than +0.5.[10] Indeed, isotope studies in conventional superconductors find α ranging from 0.5 (mercury) to -2.2 (α-uranium).[11] Interestingly, for zirconium and ruthenium, $\alpha \equiv 0$. This value is consistent with phonon-mediated electron pairing in the two square well model using values of μ^* and λ calculated from the normal state and superconducting properties of the individual materials.

Background of high-T_c isotope studies

The first isotope studies on high-T_c oxide superconductors were oxygen isotope substitution experiments performed on the $YBa_2Cu_3O_7$ structure. Batlogg *et al.*[12, 13] substituted ^{18}O isotopes in $YBa_2Cu_3O_7$ and in $EuBa_2Cu_3O_7$ by heating samples to 550° C in vacuum, removing approximately 10% of the oxygen, and heating again in an $^{18}O_2$ atmosphere. After 3 cycles, 74%±7% of the ^{16}O had been substituted with ^{18}O, as determined by Rutherford backscattering spectroscopy. They observed resistive shifts of -0.3K to -0.4K in T_c, but observed no shifts in the magnetization data and therefore set a limit on the isotope shift of $\alpha = 0.0 \pm .02$. A Raman line at 500 cm^{-1} that was assigned[14] to the O(1) site which bridges the inequivalent Cu atoms gave isotope shifts of about 4% demonstrating that at least some of the phonon modes were isotope shifted. Bourne *et al.*[15] substituted ^{18}O for ^{16}O in $YBa_2Cu_3O_7$ by heating a sample at 950°C in an ^{18}O atmosphere. An identical heat treatment was performed in ^{16}O on another sample derived from the same parent pellet. The oxygen isotope content was measured with temperature-programmed-desorption and with 50% (random) removal of the total oxygen content, 90% of the desorbed oxygen was found to be ^{18}O. Within an experimental uncertainty of ±0.3K, no isotope effect was observed in both magnetization and resistivity measurements, yielding $\alpha = 0.0 \pm 0.027$.

Leary *et al.*[16] reported a finite oxygen isotope shift in $YBa_2Cu_3O_7$. Using a gas exchange technique similar to that of Bourne *et al.*, they obtained ^{18}O enrichments of 73% to 90% (determined by thermally programmed desorption), and identified shifts in T_c of -0.3K to -0.5K from magnetization data. The shifts in T_c were reversed in one sample and partially reversed in a second sample by re-substituting ^{16}O for the ^{18}O. The same group later

reported magnetization data[16] suggestive of ^{18}O isotope shifts of -0.5K to -0.9K for 67% ^{18}O enrichment, yielding $\alpha = 0.07$ to 0.12. The isotope shifts determined by this group lie outside the original error limits set by Batlogg *et al.* and Bourne *et al.*

Morris *et al.*[17] attempted to reduce the error limits of the oxygen isotope effect in $YBa_2Cu_3O_7$. Since an applied magnetic field was found to substantially increase the measured transition width, they used applied field values of only 3 Oe during the magnetization measurement. A high temperature gas exchange technique was again used to substitute ^{18}O for ^{16}O. After measuring the T_c's, the isotope species of the two samples were reversed with another high temperature gas exchange treatment and the T_c's were again determined. With ^{18}O isotope enrichments of approximately 88% (estimated from sample weight changes), α was found to be 0.019 ± 0.005. The error limits were estimated from variations in ΔT_c at different points in the susceptibility vs. temperature curves and from variations between the two annealing runs.

Lopdrup *et al.*[18] also performed gas phase oxygen isotope exchange studies on $YBa_2Cu_3O_7$. Samples containing up to 95% ^{18}O enrichment (determined by thermally programmed desorption measurements) were initially reported[18] to have T_c's as much as 1K lower than the corresponding ^{16}O samples, but subsequent work[19, 20] revised these shifts to about -0.2K, again giving $\alpha \approx 0.02$. One sample prepared with 98% enriched $^{18}O_2$ gas was found to have 97% ^{18}O enrichment.

Reports have also emerged of extremely large oxygen isotope shifts in $YBa_2Cu_3O_7$. Ott *et al*[21] prepared oxygen isotope enriched $YBa_2Cu_3O_7$ samples by dissolving Y, Cu, and $BaC^{16}O_3$ in ^{18}O or ^{17}O enriched HNO_3. The resistive midpoint transition temperatures were 93K for the ^{16}O samples, 77K

for samples with ^{17}O, and 59K for samples with 95% ^{18}O. The sample quality decreased dramatically with decreasing T_c's, with magnetic susceptibility measurements showing transition widths of 40K or more for the lower T_c's. A brief heat treatment in ^{16}O increased T_c from 59K to 77K for an ^{18}O sample and from 77K to 90K for an ^{17}O sample. The large T_c shifts reported by Ott *et al.* correspond to $\alpha \approx 3.5$.

In $YBa_2Cu_3O_7$, isotope experiments have also been performed on the other atomic sites. In general these experiments are less easily controlled since it is not possible to reversibly exchange isotopes on the Y, Ba, or Cu sites for a given sample. A new sample must be prepared for each isotopic species. Bourne *et al.*[22] prepared $YBa_2Cu_3O_7$ with different Ba and Cu isotopes through a solid-state reaction process using Y_2O_3, $BaCO_3$, and CuO. HNO_3 was used to dissolve and mix the precalcined powder to yield sharp transitions. CuO with 99.6% ^{65}Cu and CuO with 99.7% ^{63}Cu were used for one pair of samples; $BaCO_3$ with 78.8% ^{135}Ba and $BaCO_3$ with 99.7% ^{138}Ba were used for another pair of samples. Through resistivity measurements the isotope shift was determined to be less than 0.2K for Cu ($\alpha = 0.0 \pm .07$) and less than 0.1K for Ba ($\alpha = 0.0 \pm .1$). Quan *et al.*[23] placed similar bounds on the isotope shift for Cu ($\Delta T_c = 0.0 \pm 0.2K$) using both a.c. susceptibility and resistivity to characterize the transition, and the value has also been confirmed by Vasiliev *et al.*[24, 25] Hidaka *et al.*[26] studied the effects of ^{134}Ba (85% pure) substitution for naturally occurring Ba (70% ^{138}Ba). With an inductive technique, they determined that there was no isotope shift within 0.15K.

Although no experiments have been reported for different Y isotopes in $YBa_2Cu_3O_7$, the Y site has been substituted by a host of other rare earth elements with very different masses.[27] Some T_c dependence on rare earth

species is observed, but there is no correlation between T_c and the ion mass. Hence no obvious isotope effect is observed.

Isotope studies in other high-T_c superconductors

Oxygen isotope studies have also been performed on several high-T_c oxides distinct from the $YBa_2Cu_3O_7$ structure. For $La_{1.85}Sr_{0.15}CuO_4$, Cohen *et al.*,[28] Batlogg *et al.*,[29] Faltens *et al.*,[30] zur Loye *et al.*,[31] and Bourne *et al.*[32] have reported significant shifts for 70%-80% ^{18}O enrichment corresponding to α between 0.1 and 0.2. For $La_{1.85}Ca_{0.15}CuO_4$, zur Loye *et al.* report shifts of -1.3K to -1.6K with 75% ^{18}O enrichment, yielding $\alpha = 0.73$ to 0.90; the same group has reported oxygen isotope shifts corresponding to similar large values of α for $BaPb_{0.75}Bi_{0.25}O_3$. Values of α greater than 0.5 have never before been observed for any superconductor, and such values are inexplicable within conventional BCS theory, regardless of the value of T_c. Batlogg *et al.*,[33] on the other hand, report $\alpha = 0.22 \pm .03$ for oxygen isotope substitution in $BaPb_{0.75}Bi_{0.25}O_3$.

Recent studies of oxygen isotope substitution in Bi-Sr-Ca-Cu-O indicate $\alpha = 0.026$ and 0.048 for the $T_c = 110K$ and $T_c = 85K$ phases, respectively.[34] In the copper-free perovskite system $(Ba,K)BiO_3$, $Tc \approx 30K$ and $\alpha = .35$-$.41$.[35, 36] This relatively large value of the isotope shift indicates that the pairing is mediated by phonons in this material.

Conclusion

Despite much work, the determination of more precise estimates of the magnitude of the isotope effect in most high-T_c oxide superconductors is still an important area of research. Part of the difficulty in achieving this goal is in producing sufficiently well-characterized samples with sharp and

reproducible transitions. Some ambiguity may even arise from the interpretation of the data. For example, in deducing the finite oxygen isotope shift of -0.5K in $YBa_2Cu_3O_7$, Leary *et al.*[16] compare magnetization curves which differ by the quoted amount near the transition onset, but cross near the transition midpoint (suggestive of a zero isotope effect with large error bars).

Reliable determination of α with small error limits necessitates careful control of sample preparation, measurement, and data interpretation. In the following chapter, we present a study of the oxygen isotope effect in $YBa_2Cu_3O_7$ in which we have attempted to lower the error limits for each of these contributions.

References

1. J.G. Bednorz and K.A. Müller, Z. Phys. B **64**, 189 (1986).

2. H. Maeda, Y. Tanaka, M. Fukuton and T. Asano, Jpn. J. Appl. Phys. Lett. **27**, L207 (1988).

3. M.K. Wu, J.R. Ashburn, C.J. Torng, P.H. Hor, R.L. Meng, L. Gao, Z.J. Huang, Y.Q. Wang and C.W. Chu, Phys. Rev. Lett. **58**, 908 (1987).

4. J. Bardeen, L.N. Cooper and J.R. Schrieffer, Phys. Rev. **106**, 162 (1957).

5. J. Bardeen, L.N. Cooper and J.R. Schrieffer, Phys. Rev. **108**, 1175 (1957).

6. D. Estève, J.M. Martinis, C. Urbina, M.H. Devoret, G. Collin, P. Monod and A. Revcolevschi, Europhys. Lett. **3**, 1237 (1987).

7. E. Maxwell, Phys. Rev. **78**, 477 (1950).

8. C.A. Reynolds, B. Serin, W.H. Wright and L.B. Nesbitt, Phys. Rev. **78**, 487 (1950).

9. N.N. Bogoliubov, V.V. Tolmachev and D.V. Shirkov, in *A New Method in the Theory of Superconductivity*, (Consultants Bureau, New York, 1959), Sec. 6.3.

10. C. Swihart, Phys. Rev. **116**, 45 (1959).

11. R. Meservey and B.B. Schwartz, in *Superconductivity*, R.D. Parks ed., (Marcel Dekker, New York, 1969), p. 126.

12. B. Batlogg, C.J. Cava, A. Jayaraman, R.B. van Dover, G.A. Kouraouklis, S. Sunshine, D.W. Murphy, L.W. Rupp, H.S. Chen, A. White, K.R. Short, A.M. Mujsce and E.A. Rietman, Phys. Rev. Lett. **60**, 754 (1988).

13. B. Batlogg, C.J. Cava, A. Jayaraman, R.B. van Dover, G.A. Kouraouklis, S. Sunshine, D.W. Murphy, L.W. Rupp, H.S. Chen, A. White, K.R. Short, A.M. Mujsce and E.A. Rietman, Phys. Rev. Lett. **58**, 2333 (1987).

14. G.A. Kourouklis, A. Jayaraman, B. Batlogg, R.J. Cava, M. Stavola, D.M. Krol, E.A. Rietman and L.F. Schneemeyer, Phys. Rev. B **36**, 8320 (1987).

15. L.C. Bourne, M.F. Crommie, A. Zettl, Hans-Conrad zur Loye, S.W. Keller, K.L. Leary, Angelica M. Stacy and Don Morris, Phys. Rev. Lett. **58**, 2337 (1987).

16. Kevin J. Leary, Hans-Conrad zur Loye, Steven W. Keller, Tanya A. Faltens, William K. Ham, James N. Michaels and Angelica M. Stacy, Phys. Rev. Lett. **59**, 1236 (1987).

17. Donald E. Morris, Randy M. Kuroda, Andrea G. Markelz, Janice H. Nickel and John Y.T. Wei, Phys. Rev. B **37**, 5936 (1988).

18. E. Lopdrup, M. Crawford, W.E. Farneth, R.K. Bordia, E.M. McCarron and S.J. Poon, Bull. Am. Phys. Soc. **33**, 558 (1988).

19. E.L. Benitez, J.J. Lin, S.J. Poon, W.E. Farneth, M.K. Crawford and E.M. McCaron, Phys. Rev. B **38**, 5025 (1988).

20. E. Lopdrup (personal communication).

21. K.C. Ott, R.M. Aikin, L. Bernardez, A. Connor, M.J. Fluss, E. Garcia, M. Goldblatt, W.B. Hutchinson, G.H. Kwei, C.J. Maggiore, J.A. Martin, R. Meisenheimer, M. Nastasi, Eric J. Peterson, Eugene J. Peterson, C.B. Pierce, R.B. Schwarz, J.F. Smith, J.L. Smith, J.R. Tesmer, T.E. Walker, J.O. Willis and P.J. Yvon, Phys. Rev. B **39**, 4285 (1989).

22. L.C. Bourne, A. Zettl, T.W. Barbee III and Marvin L. Cohen, Phys. Rev. B **36**, 3990 (1987).

23. Lin Quan (C. Lin), Wei Yu-rian, Yan Qi-wei, Chen Geng-hua, Zhang-sin, Ning Tai-gang, Ni Yong-ming, Yang Qian-sheng, Liu Chao-xin, Ning Tai-shang, Zhao Jin-Kue, Shao You-yu, Han Shun-hui and Li Jing-yuan, Solid State Comm. **65**, 869 (1988).

24. B.V. Vasiliev and V.I. Lushcikov, Physica C **153-155**, 261 (1988).

25. B.V. Vasiliev, V.I. Lushcikov and V.V. Sikolenko, Zh. Eksp. Teor. Fiz. **48**, 276 (1988) [JETP Lett. **48**, 252 (1988)].

26. Takehiko Hidaka, Toshimi Matsui and Yoshihiko Nakagawa, Jpn. J. Appl. Phys. Lett. **27**, L553 (1988).

27. Z. Fisk, J.D. Thompson, E. Zirngiebl, J.L. Smith and S.-W. Cheong, Solid State Comm. **62**, 743 (1987).

28. M.L. Cohen, D.E. Morris, A. Stacy and A. Zettl, in *Novel Superconductivity*, V. Kresin and S. Wolf eds., (Plenum, New York, 1987), p. 733.

29. B. Batlogg, G. Kourouklis, W. Weber, R.J. Cava, A. Jayaraman, A.E. White, K.T. Short, L.W. Rupp and E.A. Rietman, Phys. Rev. Lett. **59**, 912 (1987).

30. Tanya A. Faltens, William K. Ham, Steven W. Keller, Kevin J. Leary, James N. Michaels, Angelica M. Stacy, Hans-Conrad zur Loye, Donald E. Morris, T.W. Barbee III, L.C. Bourne, Marvin L. Cohen, S. Hoen and A. Zettl, Phys. Rev. Lett. **59**, 915 (1987).

31. Hans-Conrad zur Loye, Kevin J. Leary, Steven W. Keller, William K. Ham, Tanya A. Faltens, James N. Michaels and Angelica M. Stacy, Science **238**, 1558 (1987).

32. L.C. Bourne, S. Hoen, M.F. Crommie, W.N. Creager, A. Zettl, M.L. Cohen, L. Bernardez, J. Kinney and D.E. Morris, Solid State Comm. **67**, 707 (1988).

33. B. Batlogg, R.J. Cava and M. Stavalo, Phys. Rev. B **60**, 754 (1988).

34. H. Katayama-Yoshida, T. Hirooka, A. Oyamada, Y. Okabe, T. Takahashi, T. Sasaki, A. Ochiai, T. Suzuki, A.J. Mascarenhas, J.I. Pankove, T.F. Ciszek, S.K. Deb, R.B. Goldfard and Youngkang Li, Physica C **156**, 481 (1988).

35. S. Kondoh, M. Sera, Y. Ando and M. Sato, Physica C **157**, 469 (1989).

36. D.G. Hinks, D.R. Richards, B. Dabrowski, D.T. Marx and A.W. Mitchell, Nature **333**, 836 (1988).

Chapter 8

Measurement of Finite Filamentary and Bulk Isotope Effects in $YBa_2Cu_3O_7$

Introduction

Recently, several studies have examined isotope effects in oxide superconductors. The first experiments[1-3] involved oxygen isotope substitution in $YBa_2Cu_3O_7$, and found no or very little shift, with $\alpha \equiv 0.0 \pm .03$. This small value of α is not easily explained within the standard two square well model if $T_c \sim 90K$, and is thus suggestive of a non-phonon pairing mechanism. Later studies,[4-6] on the other hand, indicated that for oxygen isotope substitution in $YBa_2Cu_3O_7$, α might be as large as 0.12, or even greater than 3.5. Hence, the findings to date are contradictory. Since different pairing mechanisms yield different values of α, it is important to establish the magnitude of the isotope shift.

In this chapter, we report on a detailed study of the oxygen isotope effect in $YBa_2Cu_3O_7$, where up to 94% of the ^{16}O in the sample was replaced by ^{18}O.[7] Multiple cross-exchanges of oxygen isotopes were performed in high quality sample/control pairs to eliminate T_c shifts not associated with isotopic mass. Time dependent effects were also s udied by monitoring transition temperatures for various isotopically substituted samples over a period of five months.

We find that a small but finite oxygen isotope effect occurs in $YBa_2Cu_3O_7$. Magnetic measurements indicate that for the bulk material $\alpha_{bulk} \equiv 0.019 \pm .004$. Resistivity measurements in freshly prepared samples show evidence for filamentary superconductivity occuring one to two Kelvin above the bulk superconducting transition temperature. The isotope shift associated with the filamentary superconductivity is similar to but slightly

larger than the bulk shift: $\alpha_{fil} \equiv 0.028 \pm .003$. The transition temperature for filamentary superconductivity is not stable, but decays smoothly toward the bulk transition temperature over a period of several months. Our observed values of α are within the error limits of several previous $YBa_2Cu_3O_7$ oxygen isotope studies,[1-3, 8, 9] but are inconsistent with other findings.[4-6] We show that our values of α cannot be explained within a standard three dimensional phonon-mediated pairing model, and we examine other possible mechanisms.

Experiment

A.Sample preparation

Polycrystalline samples of $YBa_2Cu_3O_7$ were produced by the solid state reaction of high purity (99.999%) powders of Y_2O_3, $BaCO_3$, and CuO. All grinding was done in an agate mortar in a nitrogen filled glove box to maintain high purity and to reduce the deleterious effects of water vapor. The precalcining and subsequent sintering heat treatments used gold foil as a substrate to minimize contamination. The mixed powders were heated to 850°C, held for 15 hours, then cooled over 8 hours to room temperature. The resulting blackened powder was reground and calcined at 930°C for 15 hours then cooled to room temperature over 9 hours. This powder was reground, pelletized, and sintered at 930°C for 15 hours then cooled over 9 hours. After the final heat cycle the pellets were stored with a desiccant, P_2O_5, in vials and the vials were kept in an evacuated desiccator.

Samples of $YBa_2Cu_3O_7$ produced by the above procedure were characterized by magnetic susceptibility and dc resistivity measurements. T_c's were typically near 92K with sharp transitions. Full magnetic transition widths were 2-3K, with 50% Meissner signals.

B. Isotope exchange and measurement technique

The isotope exchange was achieved with a high-temperature gas diffusion technique and after each exchange the samples were characterized magnetically and resistively. To reduce the effects of any existing sample inhomogeneities in the initial samples or differences (unrelated to isotopic species) introduced during the high temperature exchange process, we designed an experimental procedure which averaged out such deviations. As outlined in Fig. 8-1, four $YBa_2Cu_3O_7$ pellets (two pairs) of near identical weights were chosen and each pellet underwent several oxygen isotope exchanges. Within each pair, one sample was designated primarily for resistive tests (R_a or R_b) and one sample was designated primarily for magnetic tests (M_a or M_b).

During the isotopic exchange, the samples were placed on platinum boats in identical quartz tubes. The quartz tubes were placed side-by-side and equidistant from the coils of a small tube furnace. The quartz tubes were coupled to similar static gas reservoirs containing 99.99% pure ^{16}O and 95% (occasionally 98%) enriched ^{18}O, respectively. At room temperature the pressures in the two reservoirs were 740 torr and during the exchange, they would rise to 750 torr. In each of the first three exchanges, the samples were heated to 950°C over 2 hours, held for 10 hours, cooled to 300°C over 9 hours, then cooled in the oven to room temperature. In one test, the ^{16}O and ^{18}O gases were switched between reservoirs to ensure that no asymmetries existed in the isotope exchange apparatus; none were found.

After each exchange, a small chip was removed from each of the two samples designated for resistance measurements (R_a and R_b). The chips were mounted in the standard four probe resistance measurement configuration

Fig. 8-1. Schematic of ^{16}O and ^{18}O isotope exchange. R and M refer to samples used for resistive and magnetic tests, respectively. Subscripts differentiate between different samples and superscripts refer to the last exchange that the sample has undergone. The numbers in parentheses refer to the associated curves in Figs. 8-2 and 8-3.

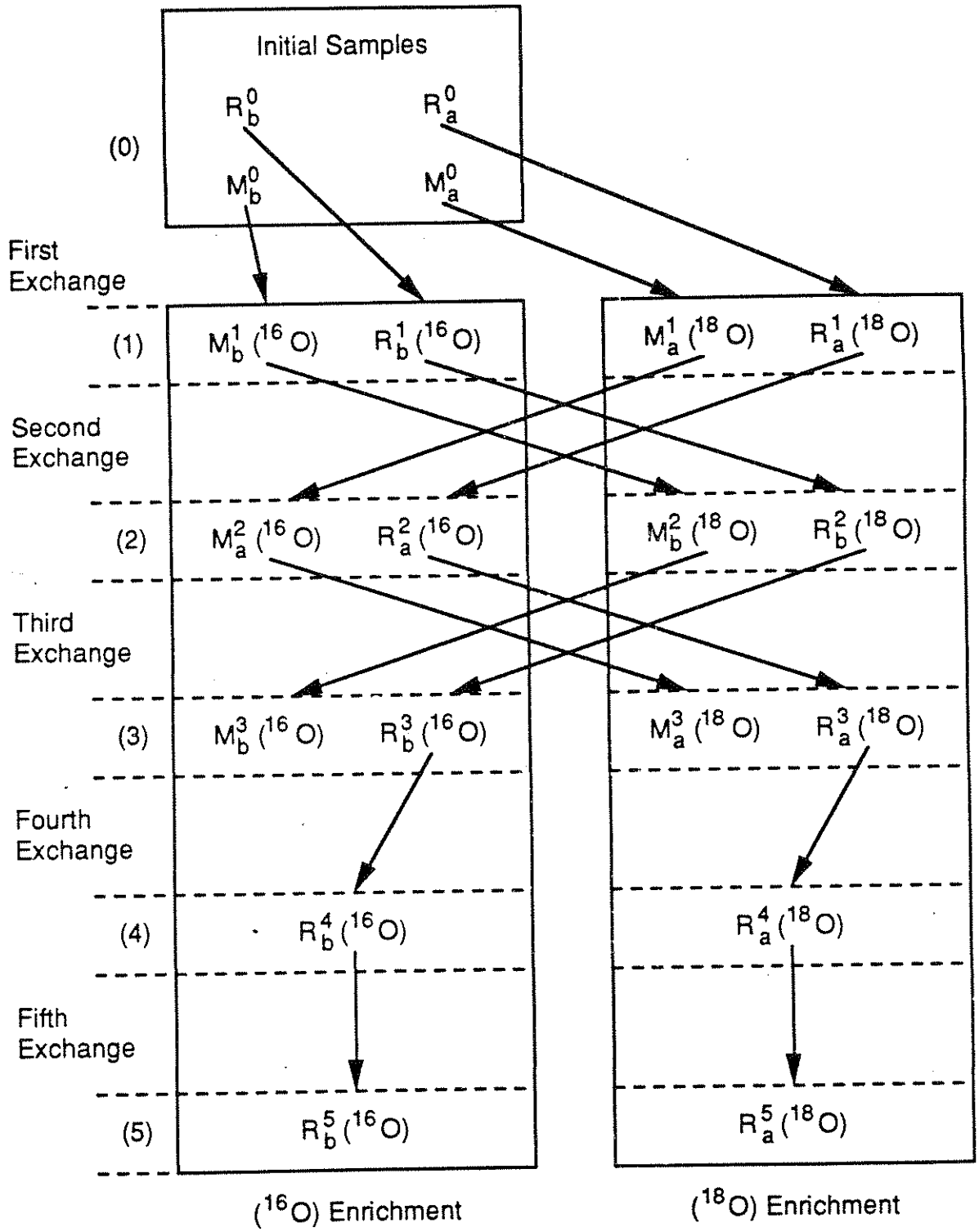
Initial Samples
R_b^0
R_a^0
(0)
M_b^0
M_a^0
First Exchange
(1)
M_b^1 (^{16}O)
R_b^1 (^{16}O)
M_a^1 (^{18}O)
R_a^1 (^{18}O)
Second Exchange
(2)
M_a^2 (^{16}O)
R_a^2 (^{16}O)
M_b^2 (^{18}O)
R_b^2 (^{18}O)
Third Exchange
(3)
M_b^3 (^{16}O)
R_b^3 (^{16}O)
M_a^3 (^{18}O)
R_a^3 (^{18}O)
Fourth Exchange
(4)
R_b^4 (^{16}O)
R_a^4 (^{18}O)
Fifth Exchange
(5)
R_b^5 (^{16}O)
R_a^5 (^{18}O)
(^{16}O) Enrichment
(^{18}O) Enrichment

with silver paint contacts, and placed side-by-side on a solid copper probe in close proximity to a calibrated diode thermometer. The samples were cooled with a helium gas flow system. The resistance versus temperature curve for each sample did not change when the sample positions on the copper probe were interchanged, indicating negligible thermal gradients across the copper probe. Each resistance measurement at a given temperature was performed with forward and then reversed dc current (typically 1mA) to ensure freedom from thermal EMF's.

We measured the magnetic susceptibility (usually of samples M_a and M_b) using a modified S.H.E. model VTS-805 SQUID magnetometer. In its unmodified form, the instrument measures the magnetic moment of a sample by passing it slowly through a pair of coils coupled to the SQUID, a process that takes about 25 seconds. For a given measurement, a proportional controller stabilizes the temperature of a flowing exchange gas and then a computer averages the moment measured during five such cycles of the sample through the coils. Though the gas temperature remains within a threshold range of the target temperature set by the operator, the temperature does drift and may oscillate by as much as 0.5K during the several minutes of data accumulation. The modifications in the magnetometer allowed the sample temperature to be regulated with greater precision and determined with greater accuracy than possible with the standard magnetometer configuration. To remove temperature gradients within the sample tube, we stabilized the system at a temperature slightly above the transition for thirty minutes. A computer controlled the slow downward temperature drift (0.01K/min.) for the samples in the magnetometer and recorded their magnetization typically 12 times per .1 degree. Subsequent tests have verified that the temperature of the samples was accurate to 0.05K and repeatable

between runs to 0.03K. The magnetic field was typically 2-3 Oe and was calibrated before each run by measuring the magnetization of a small superconducting tin sphere. The susceptibility of a given sample at $T \equiv 40K$, well below the transition, varied by as much as 10% between repeated magnetization measurements due to flux-trapping effects, but the susceptibility curves for any given sample at higher temperatures near T_c were found to be repeatable. Samples M_a and M_b were kept intact throughout the series of isotopic exchanges and magnetic measurements to avoid errors from changing the geometrical demagnetization factors for the samples.

We determined the isotopic content of the samples both by measuring the weight change caused by the exchange and by the more accurate method of Laser-Assisted Ion Mass Analysis (LIMA). In the LIMA technique, a 4eV laser vaporizes and ionizes a small portion of the sample. Constituents of the resulting plasma are driven through a time of flight spectrometer, thus determining (within approximately 1 or 2% accuracy) relative isotopic content of the sample. The samples were examined at different locations across their surface, and as a function of depth into the bulk. No evidence for inhomogeneous isotopic enhancement was found. For analysis purposes, we shall use the LIMA results for the isotopic enrichment, which agree to within ~10% with those determined by sample weight changes.

Results

Fig. 8-2 shows the results of resistive and magnetic measurements for the pure and isotopically exchanged $YBa_2Cu_3O_7$ samples. Within the Figure, Graphs (0) show R(T) and $\chi(T)$ for the samples as initially prepared. Graphs (1)-(3) show resistive and magnetic data for the sample sets following the first, second, and third exchanges, respectively (see Fig. 8-1). Ideally, the sample

Fig. 8-2. Resistance vs. temperature for samples R_a and R_b, and magnetization vs. temperature for samples M_a and M_b: (0) immediately after initial preparation of the samples; (1) after the first isotopic exchange; (2) after the second exchange; (3) after the third exchange.

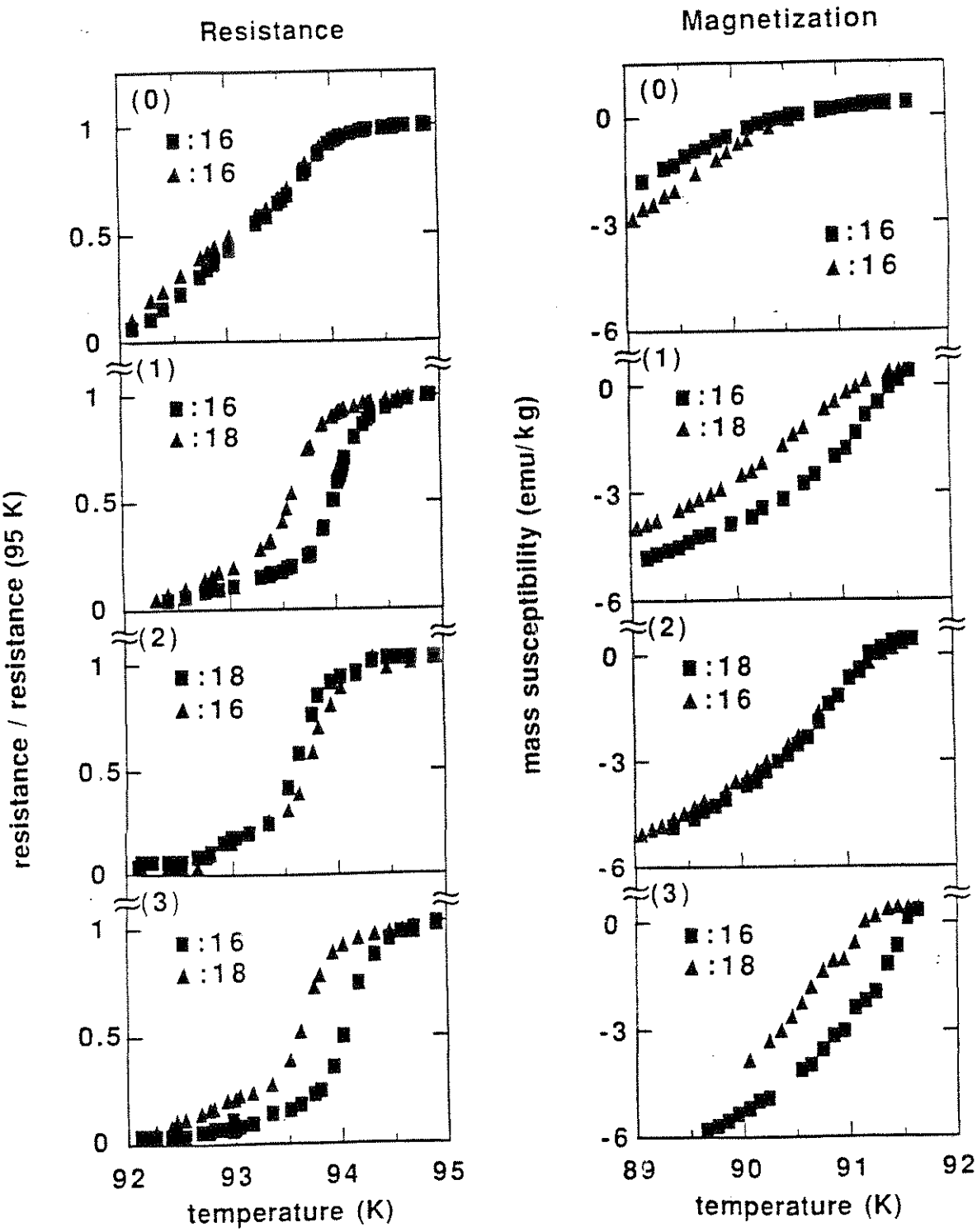
Resistance
Magnetization
(0)
■:16
▲:16
(1)
■:16
▲:18
(2)
■:18
▲:16
(3)
■:16
▲:18
resistance / resistance (95 K)
mass susceptibility (emu/kg)
temperature (K)
temperature (K)
92
93
94
95
89
90
91
92
1
0.5
0
-3
-6

data plotted together should be identical in (0), and the curves for ^{16}O and ^{18}O enriched pellets in (1) should reflect directly any oxygen isotope shift. The curve for a given sample would then be expected to switch between the ^{16}O and ^{18}O positions in subsequent frames after each isotope exchange step. This ideal situation is not realized in Fig. 8-2 because the initial samples already show slightly different T_c's. Nevertheless, for each sample, both resistive and magnetic measurements exhibit a clear pattern of oscillation between a higher value of T_c for ^{16}O enrichment and a lower value of T_c for ^{18}O enrichment as one progresses from graphs (0) to (3).

Tables 8-I and 8-II summarize the isotope shift information drawn from the data illustrated in Fig. 8-2. For resistance samples R_a and R_b, the transition temperature was taken to be the temperature midway between the temperatures where the sample resistance was 90% and 50% of the normal state resistance at 95.05K. For magnetization samples M_a and M_b measured after the second or third exchange, the transition temperature was taken to be the temperature midway between the temperatures where the sample magnetization was 10% and 50% of the superconducting state magnetization at 89.55K. The onset temperature of the transition for the magnetization samples after only one exchange is about a degree lower than the onset after the samples had further exchanges; the transition temperatures after the first exchange were accordingly normalized to 88.45K for the magnetization samples. We chose not to normalize the magnetization measurements to the values of the magnetic moment at lower temperatures because flux trapping was found to contaminate the measurements well below the transition temperature. Using these definitions of T_c, Table 8-I gives the change in transition temperature for each sample after each isotopic exchange relative to its transition temperature before the exchange. The change in transition

TABLE 8-I. Isotope shift information for resistance samples.

	R_a			R_b			Relative T_c shift (K)
	ΔT_c (K)	Spread (K)	% Isotope enrichment	ΔT_c (K)	R_b Spread (K)	% Isotope enrichment	
After first exchange	+0.303	0.205	75.3 (^{18}O)	+0.601	0.183	100 (^{16}O)	+0.298
After second exchange	+0.150	0.003	84.6 (^{16}O)	−0.379	0.007	73.3 (^{18}O)	+0.265
After third exchange	−0.017	0.084	84.3 (^{18}O)	+0.440	0.010	88.9 (^{16}O)	+0.229

TABLE 8-II. Isotope shift information for magnetization samples.

	Ma		Mb		Relative
	ΔT_c (K)	Spread (K)	ΔT_c (K)	Spread (K)	T_c shift (K)
After first exchange	+0.285	0.065	+0.640	0.210	+0.355
After second exchange	+0.030	0.010	−0.255	0.015	+0.143
After third exchange	−0.095	0.045	+0.295	0.005	+0.195

temperature could in principle be due to both an isotope effect and the annealing cycle; by subtracting the change in transition temperature for the ^{18}O sample from the change for the ^{16}O sample the effects of the annealing cycle are canceled. The relative T_c shift must be divided by two for the second and third exchanges to obtain the net shift since these are cross exchanges. The spread is the variation of the relative T_c shift over half the transition width according to the above definitions. (A small spread corresponds to the two R(T) or M(T) curves for the samples being virtually parallel over most of the width of the transition.) The results of the LIMA measurements of isotopic enrichment are also shown in the table.

The resistive and magnetic data taken after the second and third exchanges are most appropriate for extracting a net isotope shift. The exchanges are both cross-exchanges, and the data reveal sharp transitions and consistent ^{18}O isotope enrichments of approximately 80%. From Table 8-I we determine from resistance measurements a net oxygen isotope shift in $YBa_2Cu_3O_7$ of -0.25±.02K, and from magnetization measurements a net shift of -0.17±.03K. In the discussion section below, we extrapolate these shifts to full oxygen isotope substitution and determine corresponding values of α.

After the three isotope exchanges discussed above, two additional exchanges were performed to increase the relative ^{18}O content of a particular specimen (sample R_a) as much as possible. The additional exchange sequences are also shown in Fig. 8-1. In the fourth exchange, the ~95% enriched ^{18}O from the third exchange experiment was reused in the ^{18}O arm of the exchange apparatus, and the samples were held at 950°C for 25 hours and cooled to 300°C over 9 hours. In the fifth exchange, the samples were held at 950°C for 40 hours before cooling to 300°C over 9 hours, and the purity of the ^{18}O exchange gas was increased to 98% enrichment.The results of the

fourth and fifth exchanges are shown in Fig. 8-3, together with the results of the third exchange. The third exchange data, Fig. 8-3, graph (3), correspond to 84% enrichment of the ^{18}O sample. The isotopic enrichment for the ^{18}O sample after the fourth exchange was increased to 91%, and to 94% after the fifth exchange. Fig. 8-3 shows a similar isotope shift between ^{16}O and ^{18}O samples following the fourth and fifth exchanges as was observed following the third exchange. This suggests that the few ^{16}O atoms which remain in the $YBa_2Cu_3O_7$ lattice in a typical ^{18}O substitution experiment do not by some unusual mechanism mask a large intrinsic isotope shift.

The data of Figs. 8-2 and 8-3 also illustrate interesting time dependent phenomena. Although the isotope exchanges and measurements of Fig. 8-2 were all performed within several weeks of the initial sample synthesis, the measurements described in Fig. 8-3 span a period of five months. In Fig. 8-3, the data in graph (3) were recorded on fresh samples, two weeks after initial synthesis. The data of graphs (4) and (5) were recorded six weeks and five months after initial synthesis, respectively.

Fig. 8-2 shows that the superconducting transition temperature determined resistively is consistently between one and two Kelvin higher than that determined magnetically for the corresponding sample. We identify the magnetic transition temperature as representing T_c for the bulk material. The higher resistive transitions are taken as evidence for filamentary superconductivity above $T_{c(bulk)}$. Fig. 8-3 shows that the bulk superconducting transition temperature is relatively time independent: the magnetization graphs (3) and (5) have nearly identical onset temperatures for a given isotope, even though the measurements were taken 5 months apart. On the other hand, the resistance data of Fig. 8-3 show a steady decrease in T_c with time. For example, the ^{16}O sample has a T_c near 94K in graph (3), and a

Fig. 8-3. Resistive and magnetic transitions of oxygen exchanged samples: (3) after third exchange, one week after initial production of the samples; (4) after fourth exchange, one month later; (5) after fifth exchange, five months after initial production. The magnetization measurement (3) was performed on samples M_a^3 and M_b^3 while (5) was performed on samples R_a^5 and R_b^5.

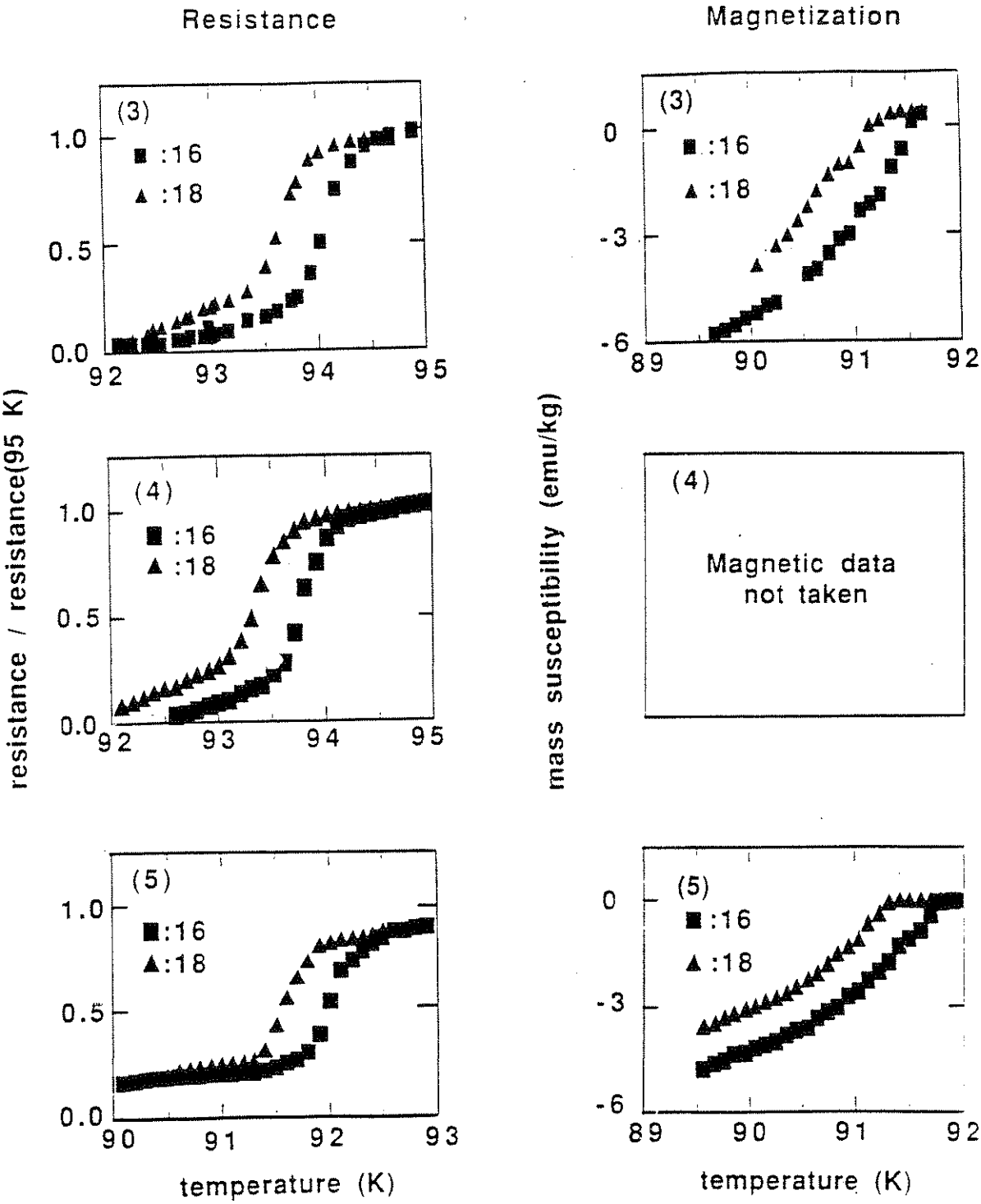
Resistance
Magnetization
(3)
■ :16
▲ :18
1.0
0.5
0.0
92
93
94
95
0
-3
-6
89
90
91
92
(4)
Magnetic data
not taken
(5)
resistance / resistance(95 K)
mass susceptibility (emu/kg)
temperature (K)

T_c near 92K in graph (5). The later T_c corresponds to that determined magnetically for the same specimen. This indicates that the filamentary superconductivity is time dependent and disappears after several months. The resistive and magnetic transition temperatures coincide thereafter.

Apparently resistive measurements near T_c test a small portion of the material (estimated from our magnetic data to be less than 0.3% volume fraction of the specimen) which is compositionally different from the bulk and undergoes "degradation" faster than the bulk. Over the span of 5 months, the bulk properties remained constant while the resistive transition shifted steadily downward. It seems likely that the filamentary superconductivity is restricted to regions of high oxygen or impurity mobility such as those between grains or within a small distance of the grain boundaries. Figs. 8-2 and 8-3 and Table 8-I show, however, that the filamentary superconductivity experiences an oxygen isotope shift similar to that of the bulk $YBa_2Cu_3O_7$ and that the relative shift remains constant in time.

Discussion

A. Calculation of α

The results of our oxygen isotope cross-exchange experiments described in Fig. 8-2 and Table 8-I unequivocally demonstrate a small but finite superconducting transition temperature shift between ^{16}O and ^{18}O samples of $YBa_2Cu_3O_7$. The calculation of the appropriate α for full oxygen substitution from the observed T_c shifts is not immediately obvious for two reasons. First, our experiments did not achieve 100% ^{18}O replacement for ^{16}O, and second, oxygen constitutes only 54% of the total number of atomic sites in $YBa_2Cu_3O_7$. The first problem can be corrected by extrapolating our measured T_c shifts to

100% oxygen isotope replacement. The second complication must be addressed when comparison is made between our measured α and that predicted by various models.

Of the four inequivalent oxygen sites within the $YBa_2Cu_3O_7$ unit cell, one (O(1)) is singly occupied and three (O(2), O(3), and O(4)) are doubly occupied. It is desired to extrapolate the measured T_c shift to an effective shift (and α) which would occur with complete substitution at each of the four sites. For each site, there will be a different shift of the transition temperature with complete ^{16}O to ^{18}O exchange. If there were non-uniform substitution of oxygen atoms, then a site on which T_c were particularly dependent could be left unsubstituted. For the chain site(O1) to be left unsubstituted, the sample must contain less than 86% ^{18}O, and for any other site, no more than 72% could be exchanged. With our 91% and 94% exchange achieved in the fourth and fifth exchanges, at least half of any particular site must have been substituted. From the constancy of the relative shifts, we deduce that incomplete substitution is not a serious concern in our isotope shift determination.

At least two methods can be used to extrapolate the measured T_c shifts to 100% isotopic substitution. In one method one assumes that the mass that enters into $T_c \propto M^{-\alpha}$ is in fact an average over all similar sites; thus, for 75% ^{18}O substitution, a mass of 17.5 is used. Alternatively, one can divide the shift by the isotopic ratio, (# of ^{18}O atoms)/(Total # of oxygen atoms), to normalize the shift to 100% substitution. In practice, these two methods differ in the calculated value of α by only a few percent, less than the typical experimental error. Here, we use the latter method.

To determine α for the bulk material, we use the averaged shift obtained from magnetic measurements at approximately 80% ^{18}O

enrichment: $\Delta T_c \equiv -0.17 \pm .03K$, with $T_c \equiv 92K$. This leads to an effective $YBa_2Cu_3O_7$ oxygen isotope exponent of $\alpha_{bulk} \equiv 0.019 \pm .004$. The resistive data for similar ^{18}O enrichment yield an oxygen isotope effect relevant to the filamentary superconductivity in $YBa_2Cu_3O_7$. From $\Delta T_c \equiv -0.25 \pm .02K$ and $T_c \equiv 94K$, we find $\alpha_{fil} \equiv 0.028 \pm .003$. Hence the isotope effect for the bulk material and that for the filamentary regions are very similar, and this suggests that the bulk and filamentary regions are structurally similar. Our value of α_{bulk} lies within the original error limits set by Batlogg *et al.*[1, 2] and Bourne *et al.*[3] for oxygen isotope substitution in bulk $YBa_2Cu_3O_7$. Fig. 8-4 gives a graphic summary of oxygen isotope effects reported for $YBa_2Cu_3O_7$ prior to the completion of this experiment.

Interpretation of the isotope shift is less straightforward for compounds than for elemental solids. Anharmonic and zero point motion effects can cause anomalous changes in T_c upon isotopic substitution. In PdH, for example, substitution of D or T for H results in a substantial increase in T_c and a large negative value for α.[10-12] Even in the absence of these effects, the meaning of α in the relationship $T_c \propto M^{-\alpha}$ is not obvious. In superconducting compounds, α is conventionally expressed as $\alpha \equiv \Sigma\alpha_i$ and $T_c \propto \Pi M_i^{-\alpha i}$ where M_i is the mass of the atom in the i^{th} position within the unit cell. Since different lattice positions contribute to the phonon spectrum in different ways, the various α_i are unlikely to be equal. To perform a theoretical calculation of α_i, it would be necessary to know how each lattice site affects each portion of the phonon spectrum and which phonons are active in binding the electrons. More simply, an effective α' can be calculated by assuming an equal scaling of all atomic masses M_i by a factor γ: $M_i' \equiv \gamma M_i$. The phonon spectrum will then scale in frequency as $\omega' \equiv \omega/\gamma^{1/2}$, and the resulting shift in T_c can be used to define $\alpha' \equiv -\Delta \ln T_c / \Delta \ln M \equiv -\Delta \ln T_c / \ln \gamma$. The

Fig. 8-4. Graphical plot of the reported values of the oxygen isotope exponent α in $YBa_2Cu_3O_7$. The appropriate reference is noted alongside the first author of a particular experiment.

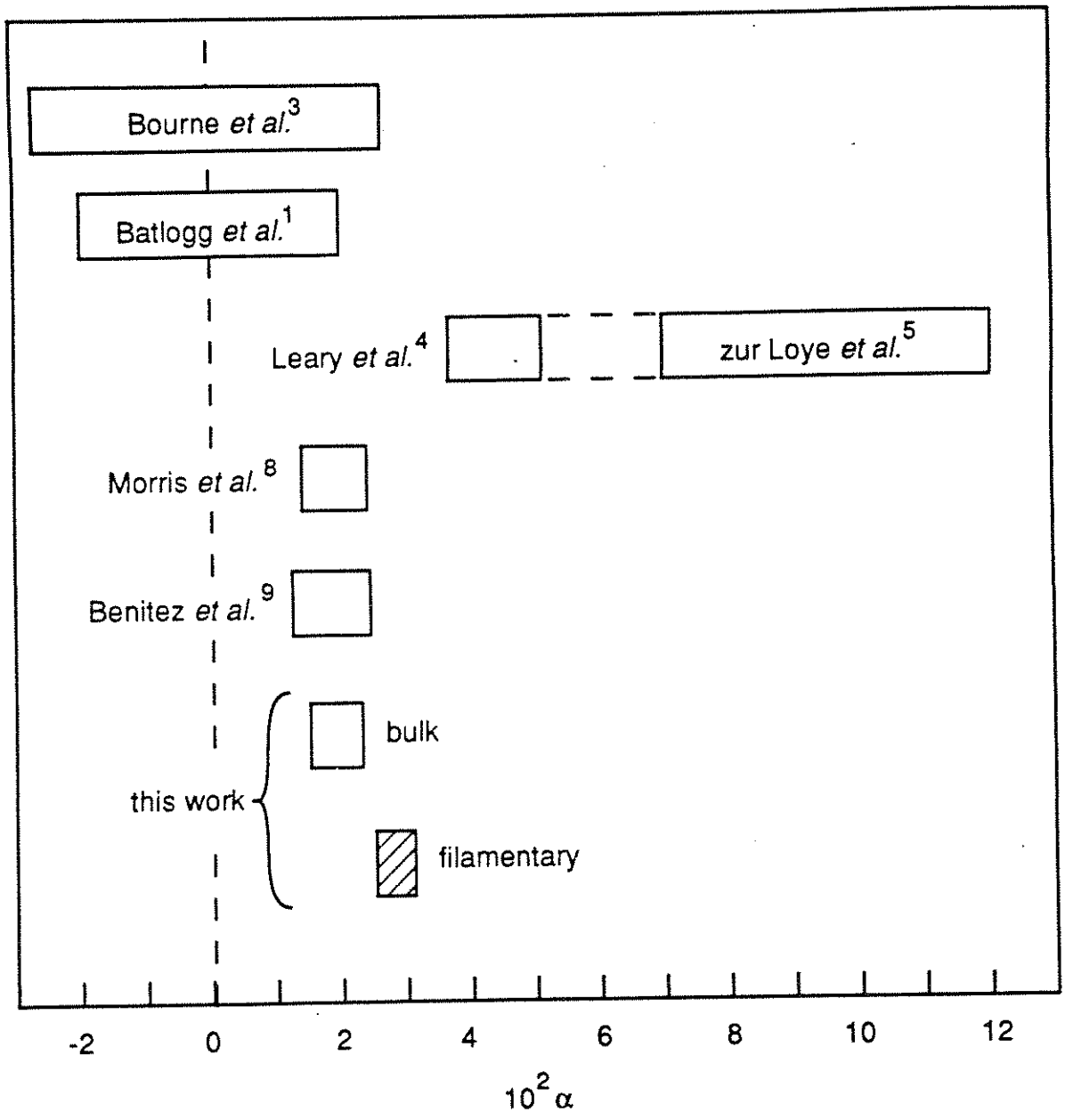
Bourne et al.[3]
Batlogg et al.[1]
Leary et al.[4]
zur Loye et al.[5]
Morris et al.[8]
Benitez et al.[9]
this work
bulk
filamentary
-2
0
2
4
6
8
10
12
$10^2\alpha$

above definition of α_i ensures that in the limit of infinitesimal mass changes, $\alpha' \equiv \Sigma\alpha_i$.

In the particular case of oxygen substitution at the four inequivalent sites in $YBa_2Cu_3O_7$, we expect the resulting oxygen isotope exponent $\alpha_O \equiv \alpha_{O1} + \alpha_{O2} + \alpha_{O3} + \alpha_{O4}$ to be nearly equal to the theoretically derived α' since oxygen is much lighter than the other elements. A one-square-well BCS model will not describe this compound since experiments with Ba,[13, 14] Cu[13, 15] and rare earths[16] have shown that $\alpha' \equiv \alpha_Y + \alpha_{Ba} + \alpha_{Cu} + \alpha_O < 0.5$.

The small observed value of α and the high T_c~90K suggest the possibility that the electron pairing mechanism in $YBa_2Cu_3O_7$ differs from that of low transition temperature superconductors. We next examine the consequences of the observed isotope shift for three dimensional BCS phonon-mediated pairing.

B. BCS theory

To test the applicability of the standard isotropic three-dimensional phonon-mediated model of superconductivity to $YBa_2Cu_3O_7$, we calculate transition temperatures and isotope shifts from the electron-phonon interaction spectrum $\alpha^2F(\omega)$ and the Coulomb repulsion parameter μ^* using the Matsubara representation[17] of the Eliashberg theory.[18] The isotope effect exponent α is not related to the electron-phonon matrix element which is also represented by an α in $\alpha^2F(\omega)$. We consider several different models of the electron-phonon interaction spectrum $\alpha^2F(\omega)$ to test the dependence of the isotope shift α on $\alpha^2F(\omega)$.

We consider a simple model of oxygen isotope substitution in which various parts of the $\alpha^2F(\omega)$ spectrum are shifted, and assume that the repulsive Coulomb interaction μ is independent of isotopic mass. Hence, the

calculated isotope effects are obtained by simulating the change in the frequency of the phonons arising from the substitution of one isotope for another.

Since shifting the entire $\alpha^2F(\omega)$ spectrum would be appropriate only for calculating the isotope effect in the case of an elemental superconductor, we have also calculated the shifts resulting from shifting only the high-frequency half of $\alpha^2F(\omega)$ as a simple approximation for oxygen substitution. Fig. 8-5 shows the calculated isotope effects for shifting the entire $\alpha^2F(\omega)$ spectrum. We find that the calculated values of the isotope effect are independent of the shape of $\alpha^2F(\omega)$ for small values of μ^* and exhibit only a small amount of scatter for extremely large values of μ^*, where μ^* is the renormalized Coulomb interaction evaluated at the root-mean-square phonon frequency. Therefore, we expect that small differences between our model spectra and the actual $\alpha^2F(\omega)$ in $YBa_2Cu_3O_7$ will not affect the calculated values of the isotope shifts significantly.

Using electron-phonon spectra similar to those presented in experimental data, we have calculated the isotope effect in $YBa_2Cu_3O_7$ with the goal of determining whether a standard phonon-mediated pairing in three dimensions can be responsible for superconductivity in the ceramic oxides. From the results presented above, we assume the following values for $YBa_2Cu_3O_7$: $\alpha \equiv 0.023 \pm 0.008$ and $T_c \approx 93K$.

For $YBa_2Cu_3O_7$, the experimental results appear to exclude a solely harmonic phonon-mediated isotropic three-dimensional model. Fig. 8-6 shows the results for $YBa_2Cu_3O_7$, with the $T_c \equiv 93K$ isotherm and the lines of constant $\alpha \approx 0.023 \pm 0.008$. When the entire spectrum is shifted, no values of the parameters λ and μ^* will yield the necessary values of α and T_c. When we consider a simulated oxygen substitution by shifting only the high-frequency

Fig. 8-5. Values of α calculated for $\lambda = 1$ (open symbols) and $\lambda = 7$ (filled symbols) using an Einstein phonon spectrum (squares) and a model $La_{1.85}Sr_{0.15}CuO_4$ spectrum (triangles). At constant λ, the values of α are nearly independent of the shape of the phonon spectrum.

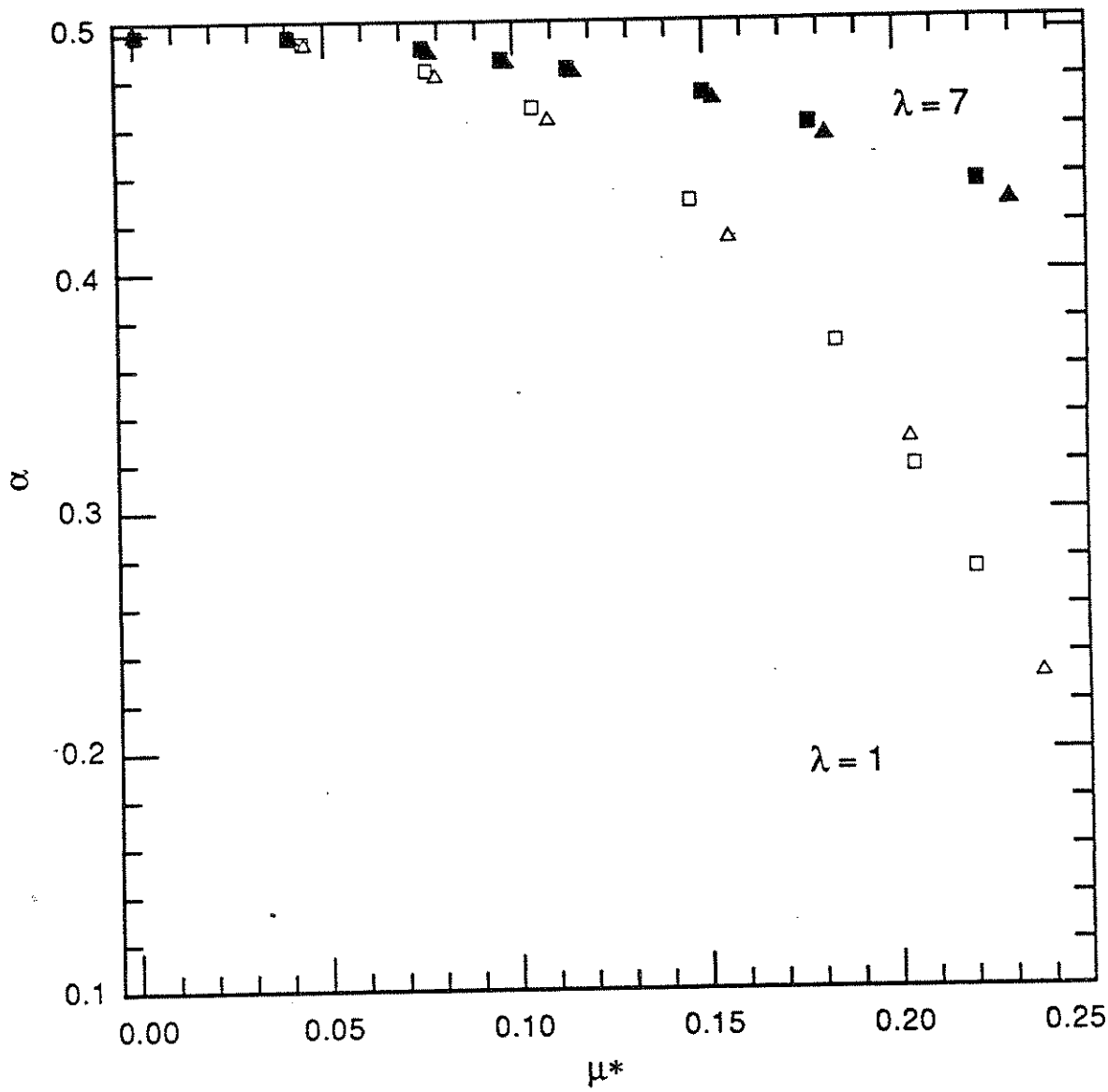
0.5
0.4
0.3
0.2
0.1
α
0.00
0.05
0.10
0.15
0.20
0.25
μ*
λ = 7
λ = 1

Fig. 8-6. Values of λ and μ^* for which $T_c = 93K$ from numerical calculations (dashed curve). The shaded area represents solutions with $\alpha = 0.023 \pm 0.008$ found numerically by shifting only the phonon spectrum peaks corresponding to oxygen vibrations. An intersection of the solid curve with the shaded area would indicate values of λ and μ^* consistent with phonon-mediated superconductivity in $YBa_2Cu_3O_7$.

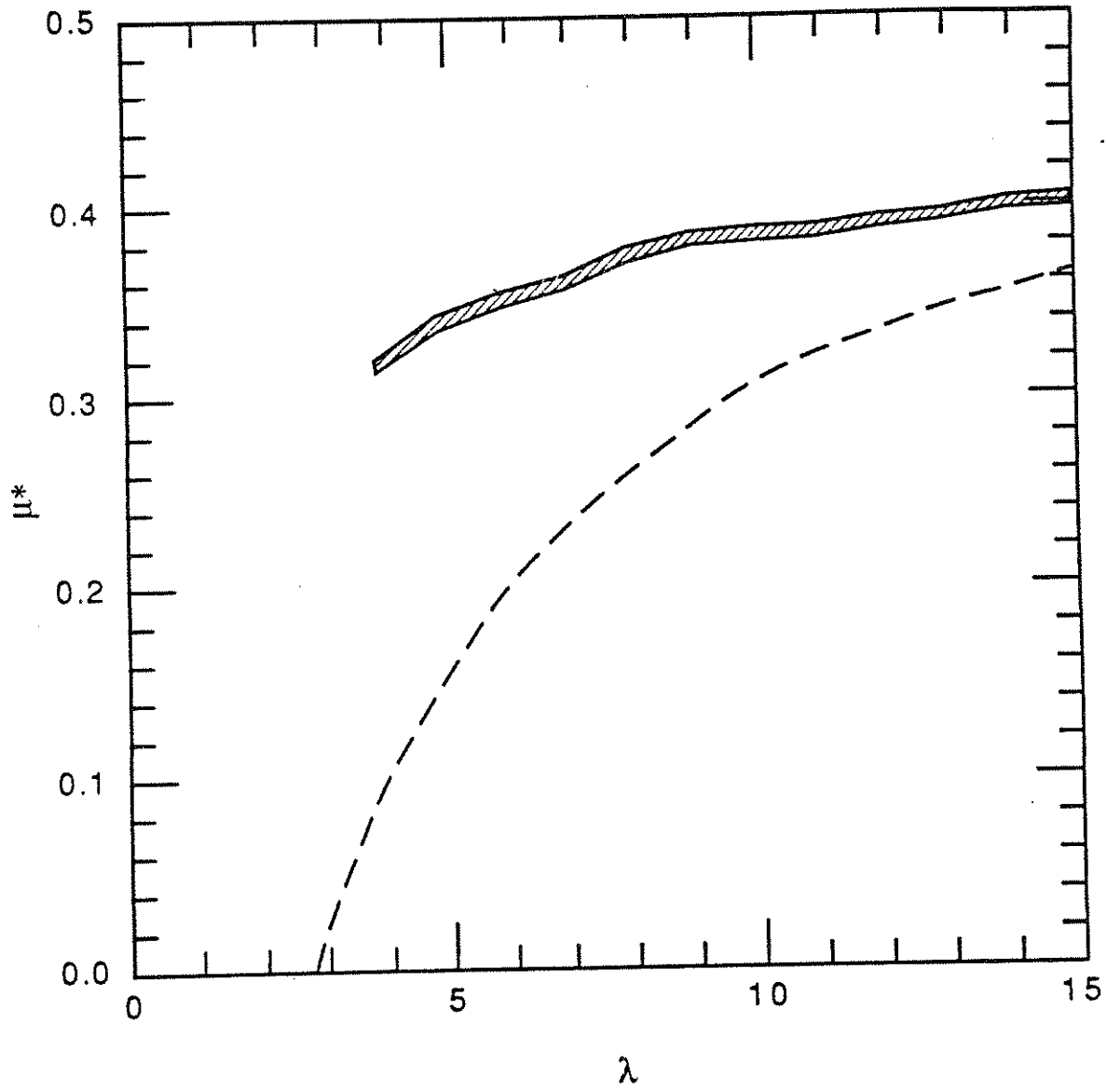
0.5
0.4
0.3
0.2
0.1
0.0
μ*
0
5
10
15
λ

phonon modes, we find that the intersection of the T_c isotherm and the constant-α line occurs for unphysically large $\lambda > 30$. We therefore conclude that our standard three-dimensional harmonic phonon-mediated model is incapable of describing superconductivity in $YBa_2Cu_3O_7$.

Discussion of the results of other investigations

A. Further isotope effect experiments

Since the completion of the experiment reported here, other workers have performed various types of isotope effect experiments. One such set of experiments was motivated by the concern[19] that the inequivalent oxygen sites in $YBa_2Cu_3O_7$ may have different binding energies so that a gas-exchange experiment may reflect preferential occupation of sites with low binding energies and anomalous isotope effects. These experiments typically involve preparation of the superconducting compound with incorporation of ^{18}O from the outset. Franck *et al.* prepared $BaC^{18}O_3$ and $Cu^{18}O$ (but not $Y_2{}^{18}O_3$) and made sintered samples from these starting materials.[20] They found magnetic isotope shifts of -1.7K. Yvon *et al.* prepared metallic YBa_2Cu_3 by mechanically alloying BaCu and CuY intermetallics that had been cleansed of oxygen impurities with a hot zirconium getter.[21] The alloy was then oxidized in a differential scanning calorimeter in flowing ^{18}O or ^{16}O. The samples showed isotope shifts of $-.4 \pm .1$K.

Though these experimenters have obviously eliminated some of the problems[6] inherent in the technique, the isotope shifts they report may not reflect intrinsic effects. In our experience, the transition temperature of freshly prepared samples is extremely sensitive to the preparation conditions. In the latter experiment, the temperature rise of the samples is not strictly controlled during the exothermic oxidation of the samples; in the former, the

oxides incorporating different isotopes were prepared by a commercial company under conditions that may not have been identical. Even under more carefully monitored preparation conditions, samples can have initially different transition temperatures, as shown in Graph (0) of Fig. 8-2. We note the results of Garcia *et al.* in which samples prepared from isotopically enriched starting materials showed transition temperature shifts of no more than 0.2K.[22]

A different set of experiments has determined the oxygen isotope shift as a function of carrier concentration. Crawford *et al.*[23, 24] measured T_c and α as a function of x in $La_{2-x}Sr_xCuO_4$ and $La_{2-x}Ba_xCuO_4$. In both compounds, α increases with x for $0<x<0.12$, and the value of a is *greater than* 0.5, the upper limit set by standard BCS theory. As x exceeds 0.12, α plummets, reaching a minima at $x=0.15$, the doping concentration that gives the highest T_c. The sharp drop in α at $x=0.12$ is coincident with a structural distortion identified as a tilting of the apical oxygens in the CuO_6 octahedra and with a small drop in T_c. The orthorhombicity of the structure is unaffected by isotopic content though, so the structural distortion is not directly caused by the isotope exchange. In a related experiment, the hole concentration in $YBa_2Cu_3O_{7-\delta}$ was varied by substituting Pr for some of the Y atoms. With increasing Pr content, α rises from near zero to 0.4 as T_c falls smoothly from 90K to 40K.[25]

B. Variations on electron-phonon coupling

Equation (7-1) shows that the transition temperature can be enhanced and the isotope effect modified in several ways. A non-phonon mechanism for coupling the members of the Cooper pair can change the magnitude and mass dependence of the cutoff frequency. Anharmonicity in the ionic potential can change the dependence of the phonon frequency on ionic mass

and consequently change the form of α. A non-constant density of states near the Fermi surface changes not only the exponential factor in T_c, but also the cutoff frequency and isotope effect. These and other theoretical approaches to the concomitant existence of high transition temperatures and weak isotope effects in the oxide superconductors will be discussed in the next two sections of this chapter.

Several attempts have been made to explain the experimental results by changing features of the standard isotropic three-dimensional model. The idea of reduced dimensionality, based on the one-dimensional chains or two-dimensional planes occuring in high-T_c superconductors, could possibly explain both the high T_c and small α seen. Labbe and Bok[26, 27] have proposed a two-dimensional model where the Fermi energy occurs near a logarithmic divergence (van Hove singularity) in the electronic density of states, resulting in a large λ and a small α, since the relevant energy scale is the width of the peak in the density of states rather than ω_D. Tsuei *et al.*[28] calculate T_c for such a diverging density of states using the BCS gap equation and find that $T_c \approx 100K$ can be consistent with $\lambda < 4$. Even with weaker divergences, α can be reduced when the Fermi level coincides with the singularity; α can also exceed 0.5 under certain conditions. By varying the Fermi level about the divergence, the authors reproduce curves of T_c and α vs. dopant concentration reminiscent of the experimental measurements of Crawford *et al.*[23, 24] Another approach modifies $N(E_F)$ with a Lorentzian function rather than a divergence.[29] A simple BCS calculation and an Eliashberg extension of it both show that α can be enhanced beyond 0.5 for material parameters appropriate for Nb_3Sn. Seki *et al.* consider modifications to the density of states arising from asymmetric potentials at various oxygen sites in the *a-b* plane and find that the modifications can enhance or depress α.[30]

A second variation on the standard model is the consideration of anharmonic effects, perhaps due to defects or zero-point motion. Hardy and Flocken[31] calculate that λ may be increased dramatically if the oxygen atoms vibrate within a double well potential, but such a mechanism should not suppress the isotope shift α. Phillips[32, 33] considers a model based on ordered oxygen defects where the defects move so as to optimize T_c. Near a maximum of T_c, the isotope shift should be nearly zero as seen in $YBa_2Cu_3O_7$. Fisher[34] has commented that the effect of the change in zero point motion on the Cu-O hopping parameter due to isotopic substitution could itself account for the observed shift in T_c in the oxide superconductors. Bussmann-Holder *et al.*[35] consider the relation between displacive structural transitions in ferroelectric materials and the anharmonic potentials in superconducting oxides.

Enz and Galasiewicz[36] calculate the renormalization of phonon frequencies for two specific anharmonic potentials. They find the effects of anharmonicity to be small for the high transition temperatures in the oxide superconductors. Müller[37] reviews the published isotope effect results for all the oxide compounds and notes that α decreases roughly in proportion to the ratio of apical oxygens to the total number of oxygen ions in each compound. He speculates that the oxygen ions in these highly anharmonic sites may dominate the observed isotope effect.

Several authors[38-41] have performed calculations similar to the Eliashberg calculation discussed earlier in this chapter. Akis and Carbotte[40, 41] claim that if the electron-coupling is confined to very high energy phonons, then $Tc \approx 100K$ and α near zero can be achieved for $\lambda \approx 5$ and $\mu^* \approx .5$.

C .Non-phonon mechanisms

Many proposed explanations of high-T_c superconductivity[42-49] explain the experimental results by considering an additional non-phonon-mediated coupling between electrons. These new coupling mechanisms are mediated by electronic excitations (such as plasmons, excitons, etc.) which are independent of isotopic mass and of much higher energy than phonons; therefore, the combination of high T_c and small α can be satisfied easily within these models. Daemon and Overhauser[50] consider a generalized two square-well model at high critical temperatures, and Cohen *et al.*[43] examine a three square-well model with renormalization and calculate T_c and α. With the inclusion of higher-energy non-phonon interactions, they find possible agreement with the observed values of T_c and α for $La_{1.85}Sr_{.15}CuO_4$ and $YBa_2Cu_3O_7$ and speculate that the differences between the materials could be explained solely by changing the strength of the non-phonon interaction. A recent measurement[51] of $\alpha \equiv 0.22 \pm .03$ for Pb-Bi-Ba-O is nearly in agreement with the predictions of Cohen et al.[43]

Conclusion

Our results conclusively show that there exists a small but finite oxygen isotope shift in $YBa_2Cu_3O_7$. In samples with ^{18}O substituted for ^{16}O at approximately 80% of the atomic sites, magnetic measurements indicate a shift $\Delta T_c(\text{bulk}) \equiv -.17 \pm .03$K. dc resistance measurements on similar samples show a transition temperature 1-2K higher than the bulk transition temperature, suggesting that filaments of a distinct material are present in the samples. The isotope shift for these filaments is $\Delta T_c \equiv -.24 \pm .02$K. After adjusting these values for full oxygen substitution, we find respectively for the bulk and filamentary superconductivity $\alpha_{bulk} \equiv 0.019 \pm .004$ and $\alpha_{fil} \equiv 0.028 \pm .003$, where $T_c \propto M^{-\alpha}$. These results are within the error limits of

several previous $YBa_2Cu_3O_7$ oxygen isotope studies,[1-3, 8, 9] but are inconsistent with other reports.[4-6]

We find that the small values of α and high-T_c reported here can only be explained within the standard three-dimensional phonon-mediated BCS theory if an unphysically large electron-phonon coupling constant λ is used. It appears that additional features (such as anisotropy, anharmonicity, or an additional non-phonon interaction) will be necessary to explain superconductivity in $YBa_2Cu_3O_7$.

References

1. B. Batlogg, C.J. Cava, A. Jayaraman, R.B. van Dover, G.A. Kouraouklis, S. Sunshine, D.W. Murphy, L.W. Rupp, H.S. Chen, A. White, K.R. Short, A.M. Mujsce and E.A. Rietman, Phys. Rev. Lett. **58**, 2333 (1987).

2. B. Batlogg, C.J. Cava, A. Jayaraman, R.B. van Dover, G.A. Kouraouklis, S. Sunshine, D.W. Murphy, L.W. Rupp, H.S. Chen, A. White, K.R. Short, A.M. Mujsce and E.A. Rietman, Phys. Rev. Lett. **60**, 754 (1988).

3. L.C. Bourne, M.F. Crommie, A. Zettl, Hans-Conrad zur Loye, S.W. Keller, K.L. Leary, Angelica M. Stacy and Don Morris, Phys. Rev. Lett. **58**, 2337 (1987).

4. Kevin J. Leary, Hans-Conrad zur Loye, Steven W. Keller, Tanya A. Faltens, William K. Ham, James N. Michaels and Angelica M. Stacy, Phys. Rev. Lett. **59**, 1236 (1987).

5. Hans-Conrad zur Loye, Kevin J. Leary, Steven W. Keller, William K. Ham, Tanya A. Faltens, James N. Michaels and Angelica M. Stacy, Science **238**, 1558 (1987).

6. K.C. Ott, R.M. Aikin, L. Bernardez, A. Connor, M.J. Fluss, E. Garcia, M. Goldblatt, V.B. Hutchinson, G.H. Kwei, C.J. Maggiore, J.A. Martin, R. Meisenheimer, M. Nastasi, Eric J. Peterson, Eugene J. Peterson, C.B. Pierce, R.B. Schwarz, J.F. Smith, J.L. Smith, J.R. Tesmer, T.E. Walker, J.O. Willis and P.J. Yvon, Phys. Rev. B **39**, 4285 (1989).

7. S. Hoen, W.N. Creager, L.C. Bourne, M.F. Crommie, T.W. Barbee III, M.L. Cohen, A. Zettl, L. Bernardez and J. Kinney, Phys. Rev. B **39**, 2269 (1989).

8. Donald E. Morris, Randy M. Kuroda, Andrea G. Markelz, Janice H. Nickel and John Y.T. Wei, Phys. Rev. B **37**, 5936 (1988).

9. E.L. Benitez, J.J. Lin, S.J. Poon, W.E. Farneth, M.K. Crawford and E.M. McCaron, Phys. Rev. B **38**, 5025 (1988).

10. T. Stoskiewisc, Phys. Status Solidi A **11**, K123 (1972).

11. B. Stratzker and W. Buckel, Z. Phys. **257**, 1 (1972).

12. J.E. Schirber, J.M. Mintz and W. Wall, Solid State Comm. **52**, 837 (1984).

13. L.C. Bourne, A. Zettl, T.W. Barbee III and Marvin L. Cohen, Phys. Rev. B **36**, 3990 (1987).

14. Takehiko Hidaka, Toshimi Matsui and Yoshihiko Nakagawa, Jpn. J. Appl. Phys. Lett. **27**, L553 (1988).

15. Lin Quan (C. Lin), Wei Yu-nian, Yan Qi-wei, Chen Geng-hua, Zhang-sin, Ning Tai-gang, Ni Yong-ming, Yang Qian-sheng, Liu Chao-xin, Ning Tai-shang, Zhao Jin-Kue, Shao You-yu, Han Shun-hui and Li Jing-yuan, Solid State Comm. **65**, 869 (1988).

16. Z. Fisk, J.D. Thompson, E. Zirngiebl, J.L. Smith and S.-W. Cheong, Solid State Comm. **62**, 743 (1987).

17. G. Bergmann and D. Rainer, Z. Phys. **263**, 59 (1973).

18. G.M. Eliashberg, Zh. Eksp. Teor. Fiz. **38**, 966 (1960) [Sov. Phys. JETP **11**, 696 (1960)].

19. M. Grimsditch, T.O. Brun, R. Bhadra, B. Dabrowski, D.G. Hinks, J.D. Jorgensen, M.A. Beno, J.Z. Liu, H.B. Schüttler, C.U. Segre, L. Soderholm, B.W. Veal and Ivan K. Schuller, Phys. Rev. Lett. **60**, 752 (1988).

20. J.P. Franck, J. Jung, G. Salomons, W.A. Miner, M.A.-K. Mohemed, J. Chrzanowski, S. Gygax, J.C. Irwin, D.F. Mitchell and G.I. Sproule, Physica C **172**, 90 (1990).

21. Pascal J. Yvon, R.B. Schwarz, C.B. Pierce, L. Bernardez, A. Conners and R. Meisenheimer, Phys. Rev. B **39**, 6690 (1989).

22. E. Garcia, R.R. Ryan, N.N. Sauer, Z. Fisk, B. Pierce, M. Fluss and L. Bernardez, Phys. Rev. B **38**, 2900 (1988).

23. M.K. Crawford, M.N. Kunchur, W.E. Farneth, E.M. McCarron III and S.J. Poon, Phys. Rev. B **41**, 282 (1990).

24. M.K. Crawford, W.E. Farneth, E.M. McCarron III, R.L. Harlow and A.H. Moudden, Science **250**, 1390 (1990).

25. J.P. Franck, J. Jung, M.A.-K. Mohamed, S. Gygax and I. Sproule, submitted to *Proc. XIX International Conference on Low Temperature Physics* (Brighton, 1990).

26. J. Labbe and J. Bok, Europhys. Lett. **3**, 1225 (1987).

27. J. Labbe and J. Friedel, J. Phys. (Paris) **27**, 303 (1966).

28. C.C. Tsuei, D.M. Newns, C.C. Chi and P.C. Pattnaik, Phys. Rev. Lett. **65**, 2724 (1990).

29. E. Schachinger, M.G. Greeson and J.P. Carbotte, Phys. Rev. B **42**, 406 (1990).

30. Seiichi Seki and Kosai Tanabe, Prog. Theor. Phys. **83**, 455 (1990).

31. J.R. Hardy and J.W. Flocken, Phys. Rev. Lett. **60**, 2191 (1988).

32. J.C. Phillips, Phys. Rev. Lett. **59**, 1856 (1987).

33. J.C. Phillips, Phys. Rev. B **43**, 6257 (1991).

34. Daniel S. Fisher, A.J. Millis, B. Shraiman and R.N. Bhatt, Phys. Rev. Lett. **61**, 482 (1988).

35. A. Bussmann-Holder, H. Büttner and A. Simon, Ferroelec. **105**, 21 (1990).

36. C.P. Enz and Z.M. Galasiewicz, Physica C **166**, 49 (1990).

37. K. Alex Müller, Z. Phys. B **80**, 193 (1990).

38. Fu-sui Liu, Yechorn Chen (Hua Chen) and Wan-feng Chen, Phys. Lett. A **144**, 397 (1990).

39. Chen Hua and Liu Fusui, Chin. J. Low Temp. Phys. **11**, 333 (1990) [Chin. Phys. **10**, 268 (1990)].

40. R. Akis and J.P. Carbotte, Physica B **165&166**, 1069 (1990).

41. R. Akis and J.P. Carbotte, Phys. Rev. B **41**, 11661 (1990).

42. B. Ashauer, W. Lee, D. Rainer and J. Rammer, Physica B **148**, 243 (1987).

43. R.W. Cohen, M.H. Cohen and M.L. Cohen, (unpublished).

44. F. Marsiglio, R. Akis and J.P. Carbotte, Solid State Comm. **64**, 905 (1987).

45. Xi-yu Su, Jiang Shen and Li-yuan Zhang, Phys. Lett. A **143**, 489 (1990).

46. Shijie Xiong, Phys. Lett. A **145**, 461 (1990).

47. P.C.W. Fung and W.Y. Kwok, Solid State Comm. **72**, 365 (1989).

48. J. Kasperczyk and H. Büttner, Solid State Comm. **75**, 105 (1990).

49. M. Tachiki and S. Takahashi, Phys. Rev. B **39**, 293 (1989).

50. L.L. Daemen and A.W. Overhauser, Phys. Rev. B **41**, 7182 (1990).

51. B. Batlogg, R.J. Cava and M. Stavalo, Phys. Rev. B **60**, 754 (1988).

Appendix

The Determination of the Dielectric Function from Far Infrared Optical Measurements

Introduction

The dielectric function $\varepsilon(\omega)$ characterizes the charge density wave, electron, and phonon dynamics in the quasi-one dimensional materials considered in the first part of this dissertation. The function $\varepsilon(\omega)$ cannot be measured directly at far infrared frequencies; rather, it is calculated from the measured optical properties of the materials. This appendix includes a detailed explanation of the techniques used to derive $\varepsilon(\omega)$ from the reflectance and transmittance. We will first consider the relationship of $\varepsilon(\omega)$ to the optical properties for various sample geometries, then discuss derivation of phase shift information from Kramers-Kronig calculations. Finally, we will list an extensive library of computer applications we developed for manipulation of the data from our optical measurements.

The relation of $\varepsilon(\omega)$ to the reflectance and transmittance

A conducting sample with dielectric function $\varepsilon(\omega)=\varepsilon_1 + i\varepsilon_2$ has a complex index of refraction $\hat{n}(\omega) = \sqrt{\varepsilon(\omega)} = n + iK$ where

$$\varepsilon_1(\omega) = n^2 - K^2 \tag{A-1}$$

and

$$\varepsilon_2(\omega) = 2nK \tag{A-2}$$

The reflectance $R(\omega)$ of the sample is the ratio of the intensity of light reflected from the sample to the intensity of light incident on it.† The complex

† In textbooks and experiments treating the optical properties of monochromatic light, this quantity if often called the "reflectivity". To make matters even more confusing, some authors call the ratio of the reflected and incident *fields* the "reflectivity coefficient".[1] Throughout this thesis we have used the radiometric terms "reflectance" and "transmittance" to refer to

reflection coefficient $r(\omega)$ is the ratio of the electric fields in the reflected and incident light, and $R(\omega) = |r(\omega)|^2$. The reflection coefficient $r(\omega) = \rho(\omega)e^{i\theta(\omega)}$ includes both an amplitude change $\rho(\omega)$ and a phase shift $\theta(\omega)$ for the light. The transmittance $T(\omega)$ and transmission coefficient $t(\omega)$ have similar definitions.

If the sample is a slab of thickness h embedded between two dielectrics with (real) indices of refraction n_1 and n_2, the reflectance and transmittance of the sample for light incident from material 1 are given by[2]

$$R = \frac{\rho_1^2 e^{2v\eta} + \rho_2^2 e^{-2v\eta} + 2\rho_1\rho_2\cos(\Theta_1 - \Theta_2 + 2u\eta)}{e^{2v\eta} + \rho_1^2\rho_2^2 e^{-2v\eta} + 2\rho_1\rho_2\cos(\Theta_1 + \Theta_2 + 2u\eta)} \qquad \text{(A-3)}$$

$$T = \frac{n_2\cos\phi_2}{n_1\cos\phi_1}\,\frac{\tau_1^2\tau_2^2 e^{-2v\eta}}{1 + \rho_1^2\rho_2^2 e^{-4v\eta} + 2\rho_1\rho_2 e^{-2v\eta}\cos(\Theta_1 + \Theta_2 + 2u\eta)} \qquad \text{(A-4)}$$

where ϕ_1 and ϕ_2 are the angles of incidence and refraction, ρ and Θ are the amplitude and phase change upon reflection at either boundary, and τ is the amplitude change on transmission at either boundary. The quantity $\eta = (2\pi h/\lambda)$ is a function of the sample thickness and the wavelength of the incident light, and u and v are defined by

$$u^2 - v^2 = n^2 - K^2 - n_1^2\sin^2\phi_1 \qquad \text{(A-5)}$$

$$uv = nK \qquad \text{(A-6)}$$

---

the ratio of the reflected or transmitted flux to the incident flux. We retain this terminology even in reference to a single frequency component of the measured quantity to emphasize that the bolometer detects a broad range of optical frequencies; the individual frequency components are sorted by the Fourier transform of the interferogram.

The quantities ρ, τ, and Θ are different for incident TE and TM waves. Eqs. (A-3) and (A-4) are simplified when the sample is suspended in a vacuum and the angle of incidence is zero:

$$R = \frac{\rho^2 e^{2K\eta} + \rho^2 e^{-2K\eta} + 2\rho^2\cos(2n\eta)}{e^{2K\eta} + \rho^4 e^{-2K\eta} + 2\rho^2\cos(2\Theta - 2n\eta)} \tag{A-7}$$

$$T = \frac{\tau_1^2 t_2^2 e^{-2K\eta}}{1 + \rho^4 e^{-4K\eta} + 2\rho^2 e^{-2K\eta}\cos(2\Theta - 2n\eta)} \tag{A-8}$$

with

$$\rho^2 = \frac{(1-n)^2 + K^2}{(1+n)^2 + K^2} \tag{A-9}$$

$$\tau_1^2 = \frac{4}{(1+n)^2 + K^2} \tag{A-10}$$

$$\tau_2^2 = \tau_1^2 (n^2 + K^2) \tag{A-11}$$

$$\Theta = \tan^{-1}\left(\frac{2K}{n^2 + K^2 - 1}\right) \tag{A-12}$$

For a very thick sample, Eqs. (A-7) and (A-8) simplify further to

$$R \approx \left|\frac{n + iK - 1}{n + iK + 1}\right|^2 \tag{A-13}$$

$$T = \tau^4 e^{-2\nu\eta} \tag{A-14}$$

For the samples of TaS_3 and $(TaSe_4)_2I$ considered in Chapters 4 and 5, the exponential factor in Eq. (A-14) is less than 1×10^{-5} for the frequencies near the strongest FIR modes and the measurements are in the semi-infinite sample

limit. For the transmittance measurements on $K_{0.3}MoO_3$ in Chapter 6 and the reflectance and transmittance measurements on the plastic binding resin in Chapter 4, the more general equations Eqs (A-7) and (A-8) connecting $\varepsilon(\omega)$ with $R(\omega)$ and $T(\omega)$ must be used.

When both transmittance and reflectance measurements are available, the equations above can in principle be fit to the measured values to give the dielectric function of a material. If only $R(\omega)$ or $T(\omega)$ have been measured, and no phase shift information is available, one approach is to assume a form for $\varepsilon(\omega)$ (for instance, a sum of independent Lorentz oscillators and a background dielectric constant) and then use the equations above to generate a reflectance or transmittance that can be compared to the measured value. (A program **Oscil** that generates $\varepsilon(\omega)$ and $R(\omega)$ for any number of superimposed oscillators is included later in this appendix.) Another more general approach exploits the relation between the real and imaginary parts of the response function for a linear passive system given by the Kramers-Kronig relations.[1] The reflection coefficient $r(\omega)$ is the response function linking the incident and reflected electric fields, and the Kramers-Kronig relations applied to $r(\omega)$ give

$$\theta(\omega) = -\frac{\omega}{\pi} P \int_0^\infty \frac{\ln R(s)}{s^2 - \omega^2} ds \ . \qquad \text{(A-15)}$$

The dielectric function is then given by $\sqrt{\varepsilon(\omega)} = n + iK$ utilizing the inverse of Eq. (A-12),

$$n + iK = \frac{1 + \sqrt{R(\omega)}\, e^{i\theta(\omega)}}{1 - \sqrt{R(\omega)}\, e^{i\theta(\omega)}} . \qquad \text{(A-16)}$$

In Fourier Transform Infrared spectroscopy, the measured reflectance is sampled at discrete intervals within a limited frequency range, so any

calculation of $\theta(\omega)$ using Eq. (A-15) is an approximation at best. Moreover, any inaccuracies in the measured value of $R(\omega)$ are accentuated by the divergence of the integrand at $s=\omega$. The methods we used to minimize the various potential errors in the calculation of $\theta(\omega)$ are discussed in the sections to follow.

Overview of the calculation scheme

Fig. A-1 is a block diagram of the various steps in processing of the optical measurements. The **FIRMS** spectroscopy software used for data collection stores the reflectance information in a file with a header containing the file name, the amplifier sensitivities, the resolution, and various other parameters and comments pertinent to the particular measurement. Data from measurements with different beamsplitters (or at different temperatures) reside in separate files. We convert the files from an IBM to a Macintosh-compatible format, then read them one-by-one with the **Preprocess** application.

All of our reflectance measurements have unusable noisy sections at the upper and lower limiting frequencies where the intensity of the light falls to zero and the signal to noise ratio is small. The user deletes these noisy points in **Preprocess** and can elect to extend the edited spectra to a broader frequency range. When the beamsplitter alignment is poor or the sample or detector temperature drifts, the reflectance measured at the same frequency at different times with different beamsplitters may not agree precisely. If two such spectra are concatenated, the resulting sharp reflectance discontinuity will appear in $\varepsilon(\omega)$ as a small mode. To avoid such spurious modes, the user can distort or shift a reflectance spectrum by specifying the parameters a, b, and c in

Fig. A-1. Block diagram of the series of computer programs used to calculate $\varepsilon(\omega)$ by processing the raw reflectance files generated by the **FIRMS** spectroscopy software.

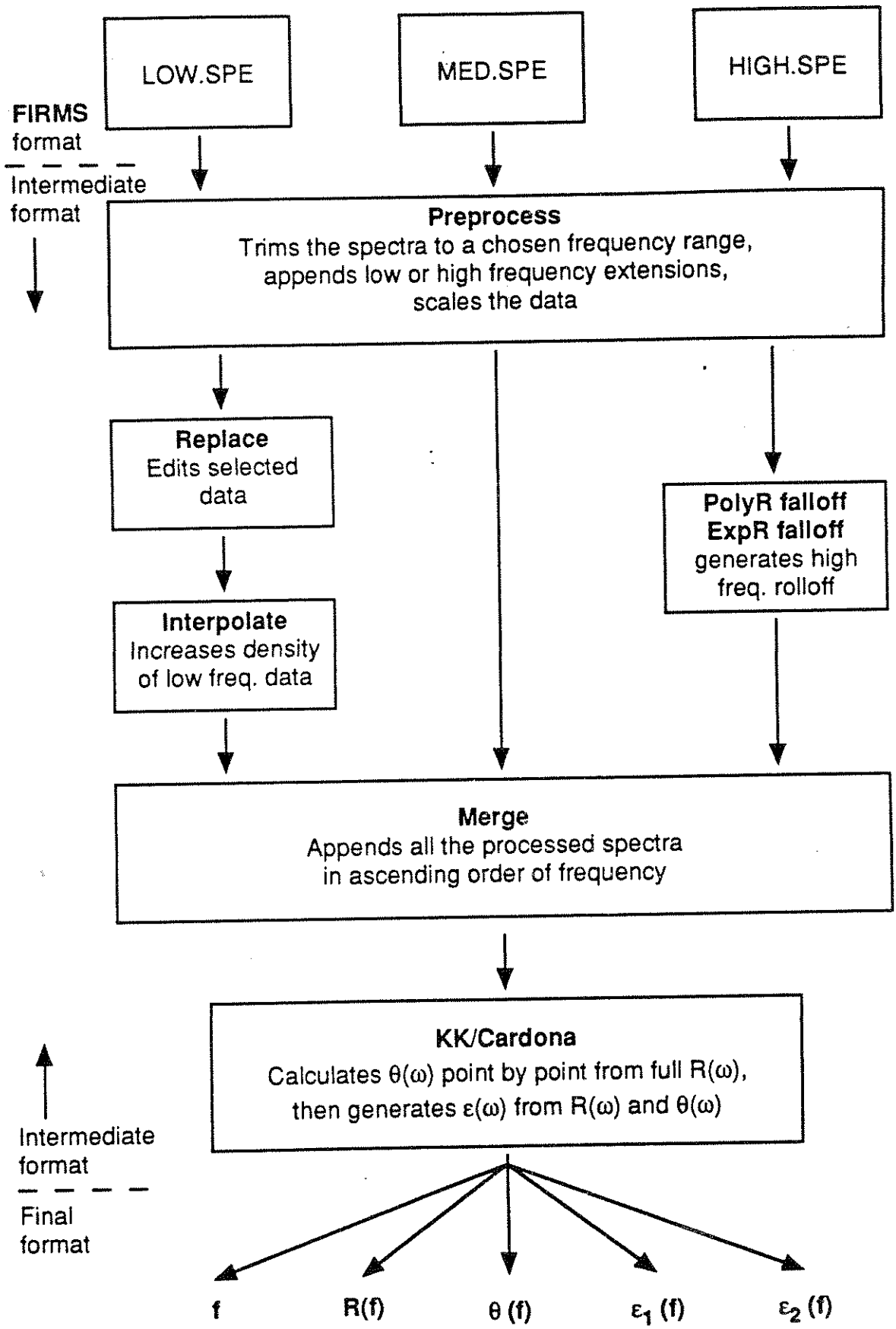
LOW.SPE
MED.SPE
HIGH.SPE
FIRMS format
Intermediate format
Preprocess
Trims the spectra to a chosen frequency range, appends low or high frequency extensions, scales the data
Replace
Edits selected data
Interpolate
Increases density of low freq. data
PolyR falloff
ExpR falloff
generates high freq. rolloff
Merge
Appends all the processed spectra in ascending order of frequency
KK/Cardona
Calculates θ(ω) point by point from full R(ω), then generates ε(ω) from R(ω) and θ(ω)
Intermediate format
Final format
f
R(f)
θ (f)
ε1 (f)
ε2 (f)

$$R(\omega) \rightarrow R(\omega) + a + bR(\omega) + c\omega \qquad \text{(A-17)}$$

We emphasize that no such intentional distortions of the reflectance were performed on any of the optical measurements presented in this dissertation; the feature is only used for preliminary analysis of non-ideal measurements. The **Preprocess** program and all subsequent programs shown in the middle section of Fig. A-1 store the results in "intermediate form" (i.e., as a sequence of pairs of frequency-reflectance values).

Occasionally, the reflectance values in a certain frequency range are inaccurate (one example is the Fabry-Perot fringes due to the sample holder in the measured TaS_3 reflectance). The **Replace** program allows editing of such defects. The calculation of $\theta(\omega)$ from Eq. (A-15) can be inaccurate if the reflectance is sampled sparsely in frequency regions where the reflectance is quickly changing. The program **Interpolate** alleviates some of this problem by generating additional reflectance values between the measured ones using linear interpolation. The programs **PolyR Falloff** and **ExpR Falloff** generate an extension of the measured reflectance beyond the experimental limit of $700cm^{-1}$ to more closely approximate the upper limit of the Kramers-Kronig integration. The **Merge** program connects the processed reflectance files from the various beamsplitters into one large file that covers a very broad frequency range. Finally, the **Kramers-Kronig** routine generates $\theta(\omega)$ and $\varepsilon(\omega)$ by integrating Eq. (A-15) and writes the result to a file that can be read by various graphing programs.

Computer code library: I. Programs

In this section we list the code for the various routines shown in Fig. A-1. In a subsequent section, we will list the code for several libraries of

utility routines that implement mathematical functions for complex numbers and facilitate handling of file input/output, allocation of memory, and interaction with the user. All the code is in C and was designed for use on the Apple Macintosh computer. However, the programs do not implement any specific features of the Apple desktop or file handling systems, and as such they should compile and run properly on other computers with C compilers. The files that serve as input to these routines should reside in the same folder or directory as the programs themselves. The programs invoke the Motorola 68881 mathematics coprocessor and should be linked to the ANSI-881 C library of mathematical functions.

In the lists of code to follow, we give the name of the program, followed by a list of the utility libraries to which it must be linked after compiling. A general description of the program function precedes the program listing. One of the first tasks of most of the routines is displaying on the monitor a description of the program. Since this display is redundant with the general description preceding the listing, we have replaced it with the word *description* (in italics) in the code.

A. Preprocess (link to Fileroutines, Menu, NRutil, Optical, and Complex)

This program preprocesses a reflectance SPE file generated by the FIRMS program. It reads in the reflectance values, assigns proper frequencies to each value, allows the user to specify cutoff frequencies at either end of the data to eliminate noisy points, and appends user-specified values to either end of the frequency range. It then applies a user-specified corrections to the data corresponding to Eq. (A-17), and writes the data to a file in intermediate form.

Preprocess

```
#include <stdio.h>
#include <math.h>
#include <complex881.h>
#include <nrutil881.h>
#include <wncutil881.h>

main()
{
        long numpoints,i,first,last,numout,lowpad,highpad,restart;
        double freq_range,low,high,a,b,c,freq_skip,freqmax;
        double *frequency;
        magphase *reflec,*processed_reflec;
        char filename[20];
        restart=1;

        printf("preprocess 68881 (uses the coprocessor):\n\n\n");
        printf("description\n");

        while (restart==1) {                    /*Read the file header, allocate memory for     */
                                                /*arrays, and read the data from the file.      */
                numpoints=read_file_header_spe(&freq_range,filename);
                reflec=magphase_vector(0,numpoints-1);
                read_file_data_spe(filename,reflec);

                                                /*Ask the user to define the good parts of the  */
                                                /*data and find the range of array indices for  */
                                                /*the good data.                                */
                printf("\nThe frequency range covered is 0->%f cm-1\n",freq_range);
                printf("You should choose the frequency range over which the data is reliable.\n");
                printf("Enter lower frequency limit (>=0., include decimal point): >");
                scanf("%lf",&low);
                printf("Enter upper frequency limit (<=%f ): >",freq_range);
                scanf("%lf",&high);
                first=last=-1;
                freq_skip=freq_range/(numpoints-1);
                for(i=0;last== -1;i++){
                        if(((i*freq_skip)>=low)&&(first== -1)) first=i;
                        if(((i*freq_skip)>high)&&(last== -1)) last=i-1;
                }
                                                /*If the user wants to, replace the noisy data  */
                                                /*at high and low frequencies with the value of */
                                                /*the last good data point.                     */
                if(low!=0.) {
                        printf("\nPADDING:\nDo you want padding from w=0 to w=%12.4f cm-1",low);
                        printf("\nwith the reflectance value %12.4f (from w=%12.4f cm-1)? :",
                                                reflec[first].mg,(float)first*freq_skip);
                        lowpad=menu_response(2,"","No","Yes")-1;
                }
                else {
                        lowpad=0;
                }
                printf("\nDo you want padding at frequencies beyond w=%12.4f cm-1",high);
                printf("\nwith the reflectance value %12.4f (from w=%12.4f cm-1)? :",
                                                reflec[last].mg,(float)last*freq_skip);
                highpad=menu_response(2,"","No","Yes")-1;
                if(highpad) {
```

```
        printf("\nEnter the maximum frequency for padding: ");
        scanf("%lf",&freqmax);
}

if(highpad) {
        if(lowpad)numout=freqmax/freq_skip+1;
        elsenumout=freqmax/freq_skip-first+1;
}
else{
        if(lowpad) numout=last+1;
        lse numout=last-first+1;
}
                                        /*Alocate arrays for the processed spectrum    */
                                        /*and load them with the quiet, extended       */
                                        /*spectrum that was just prepared.             */
frequency=dvector(0,numout-1);
processed_reflec=magphase_vector(0,numout-1);
if (lowpad) {
        for(i=0;i<=last;i++) {
                frequency[i]=i*freq_skip;
                if(i<first) processed_reflec[i]=reflec[first];
                else processed_reflec[i]=reflec[i];
        }
}
else {
        for(i=first;i<=last;i++) {
                frequency[i-first]=i*freq_skip;
                processed_reflec[i-first]=reflec[i];
        }
}
if(highpad) {
        if(lowpad) {
                for(i=last+1;i<numout;i++) {
                        frequency[i]=i*freq_skip;
                        processed_reflec[i]=reflec[last];
                }
        }
else {
        for(i=last-first+1;i<numout;i++) {
                frequency[i]=(i+first)*freq_skip;
                processed_reflec[i]=reflec[last];
                }
        }
}
                                        /*Scale and shift the data as the user specifies. */
printf("DATA PROCESSING: The reflectance values will now be processed now:
                                \n\n");
printf("R(w)--->R(w) + a + (b*R(w)) + (c*w)\n");
printf("Enter a [don't forget decimal]: ");
scanf("%lf",&a);
printf("Enter b : ");
scanf("%lf",&b);
printf("Enter c : ");
scanf("%lf",&c);

for(i=0;i<numout;i++)
        processed_reflec[i].mg += a +(b*processed_reflec[i].mg) + (c*frequency[i]);
```

```
                                        /*Save the file in intermediate form, free all   */
                                        /*the memory from various arrays, and exit       */
                                        /*gracefully.                                    */
            save_file_int(numout,frequency,processed_reflec);

            free_dvector(frequency,0,numout-1);/*free memory used by arrays*/
            free_magphase_vector(reflec,0,numpoints-1);
            free_magphase_vector(processed_reflec,0,numout-1);

            printf("\nDo you want to process another file?");
            restart=menu_response(2,"","No","Yes")-1;
        }

        printf("PROGRAM FINISHED: Press <<return>> to exit to Macintosh Environment.");
        exit(1);
}
```

B. Replace (link to Fileroutines and NRutil)

This program facilitates replacement of noisy or erroneous reflectance values in a certain frequency range with a curve that approximates the true reflectance values. The curve parameters should be chosen to match $R(\omega)$ and $dR(\omega)/d\omega$ on either side of the frequency interval. The program reads in a file in intermediate form, replaces the spurious data with a fourth order polynomial, then saves the file in the same form.

Replace

```
#include <stdio.h>
#include <math.h>
#include <complex881.h>
#include <nrutil881.h>
#include <wncutil881.h>

main()
{
        long num,i;
        long first,last;
        double low,high,m0,m1,m2,m3,m4,freq2,freq3,freq4;
        double *frequency;
        magphase *reflec;
        char filename[20];

        printf("replace 68881 (uses the coprocessor):\n\n\n");
        printf("description\n");
                                        /*Read the file header, allocate memory for the */
                                        /*input array, and load it.                     */
        printf("input FILE:\n");
        num=read_file_header_int(filename);

        frequency=dvector(0,num-1);
```

```
    reflec=magphase_vector(0,num-1);
    read_file_data_int(filename,frequency,reflec);
                                        /*Ask the user to define the bad parts of the   */
                                        /*data and find the range of array indices for  */
                                        /*the bad data.                                 */
    printf("The data extends from %10.4f to %10.4f cm-1.\n",frequency[0],frequency[num-1]);
    printf("You should choose the frequency range for data replacement.\n");
    printf("Enter lower frequency limit (>=0., include decimal point): ");
    scanf("%lf",&low);
    printf("Enter upper frequency limit: ");
    scanf("%lf",&high);
    first=last=-1;
    for (i=0;i<num;i++)       {
          if((frequency[i]>=low)&&(first== -1)) first=i;
          if((frequency[i]>high)&&(last== -1)) last=i-1;
    }
    if (first== -1) first=0;
    if (last== -1) last=num-1;

                                        /*Get the parameters for the fourth order       */
                                        /*polynomial.                                   */
    printf("Enter m0 at low frequency limit:\n");
    scanf("%lf",&m0);
    printf("Enter m1 at low frequency limit:\n");
    scanf("%lf",&m1);
    printf("Enter m2 at low frequency limit:\n");
    scanf("%lf",&m2);
    printf("Enter m3 at low frequency limit:\n");
    scanf("%lf",&m3);
    printf("Enter m4 at low frequency limit:\n");
    scanf("%lf",&m4);
                                        /*Replace the designated values                 */

    for(i=first;i<=last;i++) {
          freq2=frequency[i]*frequency[i];
          freq3=freq2*frequency[i];
          freq4=freq3*frequency[i];
          reflec[i].mg = m0+(m1*frequency[i])+(m2*freq2)+
                                    (m3*freq3)+(m4*freq4);

    }
                                        /*Free the memory occupied by the input array, */
                                        /*save the output file, and exit gracefully.    */

    free_dvector(frequency,0,num-1);
    free_magphase_vector(reflec,0,num-1);
    save_file_int(num,frequency,reflec);
    free_dvector(frequency,0,num-1);
    free_magphase_vector(reflec,0,num-1);

    printf("PROGRAM FINISHED: Press <<return>> to exit to Macintosh Environment.");
    exit(1);
}
```

C. Interpolate (link to Fileroutines and NRutil)

This program reads in a file in intermediate form. It uses linear interpolation to generate a user-specified number of data points between each

pair of existing data points, then saves the interpolated data set in the same form.

Interpolate

```
#include <stdio.h>
#include <math.h>
#include <complex881.h>
#include <nrutil881.h>
#include <wncutil881.h>

main()
{
        long numin,numout,i,j,interpfactor;
        double *frequencyout,*frequencyin,slope,interval;
        magphase *reflecout,*reflecin;
        char filenameout[20],filenamein[20];

        printf("merge 68881 (uses the coprocessor):\n\n\n");
        printf("description\n");
                                                /*Read the input file header, ask the user      */
                                                /*to specify the number of intercalated         */
                                                /*points, allocate memory for the various       */
                                                /*arrays, and load the input file.              */
        printf("INPUT FILE:\n");
        numin=read_file_header_int(filenamein);
        printf("What interpolation factor do you want (integer)?:\n");
        scanf("%li",&interpfactor);
        numout=1+(numin-1)*(interpfactor+1);
        frequencyin=dvector(0,numin-1);
        reflecin=magphase_vector(0,numin-1);
        frequencyout=dvector(0,numout-1);
        reflecout=magphase_vector(0,numout-1);
        read_file_data_int(filenamein,frequencyin,reflecin);

                                                /*Fit a line to adjacent R(w) points.  Interpolate */
                                                /*to generate the new data points, and load     */
                                                /*the output arrays                             */
        for(i=0;i<numin-1;i++) {
                slope=(reflecin[i+1].mg-reflecin[i].mg)/
                (frequencyin[i+1]-frequencyin[i]);
                interval=(frequencyin[i+1]-frequencyin[i])/(interpfactor+1);
                for(j=0;j <= interpfactor; j++) {
                        frequencyout[j+i*(interpfactor+1)] = frequencyin[i] + (j*interval);
                        reflecout[j+i*(interpfactor+1)].mg = reflecin[i].mg + (j*interval*slope);
                }
        }
        frequencyout[(numin-1)*(interpfactor+1)]=frequencyin[numin-1];
        reflecout[(numin-1)*(interpfactor+1)].mg=reflecin[numin-1].mg;

                                                /Free the memory used by the input and        */
                                                /output arrays, save the output file, and exit */
                                                /*gracefully.                                   */
        free_dvector(frequencyin,0,numin-1);
        free_magphase_vector(reflecin,0,numin-1);
```

```
    save_file_int(numout,frequencyout,reflecout);
    free_dvector(frequencyout,0,numout-1);
    free_magphase_vector(reflecout,0,numout-1);

    printf("PROGRAM FINISHED: Press <<return>> to exit to Macintosh Environment.");
    exit(1);
}
```

D. PolyR falloff and ExpR falloff (link to Fileroutines, Menu, NRutil, Optical, and Complex)

These programs generate a file in intermediate form containing widely spaced high frequency reflectance values that gradually fall to zero. Such a rolloff of the high frequency R(ω) prevents divergence of the Kramers-Kronig integrals. **PolyR falloff** (which will be listed first) generates a polynomial falloff in the reflectance over a frequency range $\omega_{lower} \le \omega \le \omega_{upper}$ using:

$$R(\omega) = \begin{cases} R_{lower}\left(\frac{\omega_{lower}}{\omega}\right)^{s} & \text{for } \omega_{lower} \le \omega \le \omega_{middle} \\ R_{middle}\left(\frac{\omega_{middle}}{\omega}\right)^{4} & \text{for } \omega_{middle} \le \omega \le \omega_{upper} \end{cases} \qquad \text{(A-18)}$$

where ω_{lower} and R_{lower} are the frequency and reflectance of the highest frequency measured data, $s=-(dR/d\omega)/(R/\omega)$ is the normalized slope at ω_{lower}, ω_{upper} is the frequency where $R \to 0$, and ω_{middle} is some intermediate frequency. **ExpR falloff** (the second listing) generates an exponential falloff in the reflectance:

$$R(\omega) = R_{lower} \exp(a(\omega_{lower} - \omega)) \qquad \text{(A-19)}$$

where $a=-(dR/d\omega)/R$ at ω_{lower}. The output file from either falloff program should be appended to the measured reflectance values using the **Merge** program. Proper choices for the parameters R_{lower}, s, and a ensure that the measured reflectance will join the generated falloff reflectance smoothly.

PolyR falloff

```
#include <stdio.h>
#include <math.h>
#include <stdlib.h>
#include <complex881.h>
#include <nrutil881.h>
#include <wncutil881.h>
#include <wncoptical881.h>

main()
{
        double *frequency;
        magphase *reflec;
        double wupper,wmiddle,wlower,s,rlower;
        int response;
        long numpoints,morepoints,i;

        printf("PolyR falloff68881 (uses the coprocessor):\n\n\n");
        printf("description\n");
                                        /*Get the output frequency range from the      */
                                        /*user                                         */
        printf("Enter lower frequency limit for output:\n");
        scanf("%lf",&wlower);
        printf("Enter middle frequency limit for output:\n");
        scanf("%lf",&wmiddle);
        printf("How many frequencies should I output between these limits (integer)?:\n");
        scanf("%li",&numpoints);
        printf("Enter upper frequency limit for output:\n");
        scanf("%lf",&wupper);
        printf("How many more frequencies should I output before this limits (integer)?:\n");
        scanf("%li",&morepoints);
                                        /*Get the parameters characterizing the        */
                                        /*highest frequency measured reflectance       */
                                        /*from the user.                               */
        printf("Enter R at low frequency limit:\n");
        scanf("%lf",&rlower);

        printf("Enter s=-(dR/dw)/(R/w) evaluated at low freq limit:\n");
        scanf("%lf",&s);

                                        /*Alloca e memory for the output arrays.       */
        frequency=dvector(0,numpoints+morepoints-1);
        reflec=magphase_vector(0,numpoints+morepoints-1);

                                        /*Calculate the frequencies and reflectance.   *//

        for(i=0;i<numpoints;i++) {
                frequency[i]=wlower+(i*(wmiddle-wlower)/(numpoints-1));
                reflec[i].mg=rlower*pow((wlower/frequency[i]),s);
        }
        for(i=numpoints;i<numpoints+morepoints;i++) {
                frequency[i]=frequency[numpoints-1]
                                        +((i-numpoints+1)*(wupper-wmiddle)/(morepoints));
                reflec[i].mg=rlower*pow((wmiddle/frequency[i]),4)*
                pow((wlower/wmiddle),s);
        }
                                        /*Free the memory used for the various arrays  */
                                        /*and exit gracefully.                         */
        save_file_int(numpoints+morepoints,frequency,reflec);
```

```
        free_dvector(frequency,0,numpoints+morepoints-1);
        free_magphase_vector(reflec,0,numpoints+morepoints-1);

        printf("PROGRAM FINISHED: Press <<return>> to exit to Macintosh Environment.");
        exit(1);
}
```

ExpR falloff

```
#include <stdio.h>
#include <math.h>
#include <stdlib.h>
#include <complex881.h>
#include <nrutil881.h>
#include <wncutil881.h>
#include <wncoptical881.h>

main()
{
        double *frequency;
        magphase *reflec;
        double wupper,wlower,a,rlower;
        int response;
        long numpoints,i;

        printf("PolyR falloff68881 (uses the coprocessor):\n\n\n");
        printf("description\n");
                                                /*Get the output frequency range from the      */
                                                /*user                                         */
        printf("Enter lower frequency limit for output:\n");
        scanf("%lf",&wlower);
        printf("Enter upper frequency limit for output:\n");
        scanf("%lf",&wupper);
        printf("How many frequencies should I output between these limits (integer)?:\n");
        scanf("%li",&numpoints);
                                                /*Get the parameters characterizing the        */
                                                /*highest frequency measured reflectance       */
                                                /*from the user.                               */
        printf("Enter R at low frequency limit:\n");
        scanf("%lf",&rlower);
        printf("Enter a=-(dR/dw)/R evaluated at low freq limit:\n");
        scanf("%lf",&a);
                                                /*Allocate memory for the output arrays.       */
        frequency=dvector(0,numpoints-1);
        reflec=magphase_vector(0,numpoints-1);
                                                /*Calculate the frequencies and reflectance.   *//

        for(i=0;i<numpoints;i++) {
                frequency[i]=wlower+(i*(wupper-wlower)/(numpoints-1));
                reflec[i].mg=rlower*exp(a*(wlower-frequency[i]));
        }
                                                /*Free the memory used for the various arrays  */
                                                /*and exit gracefully.                         */
        save_file_int(numpoints,frequency,reflec);
        free_dvector(frequency,0,numpoints-1);
        free_magphase_vector(reflec,0,numpoints-1);

        printf("PROGRAM FINISHED: Press <<return>> to exit to Macintosh Environment.");
        exit(1);
}
```

E. Merge (link to Fileroutines, Menu, and NRutil)

This program reads in two files, each in intermediate form. It appends the second file to the first and saves the result in the same form. It then gives the user the option to repeat the process. To merge a set of several files, the user sorts them by ascending frequency ranges, merges the first two files into a temporary file, then merges the temporary file with the third file, and so on.

Merge

```
#include <stdio.h>
#include <math.h>
#include <complex881.h>
#include <nrutil881.h>
#include <wncutil881.h>

main()
{
      long num1,num2,numout,i,restart;
      double *frequency,*frequency1,*frequency2;
      magphase *reflec,*reflec1,*reflec2;
      char filename1[20],filename2[20];
      restart=1;

      printf("merge 68881 (uses the coprocessor):\n\n\n");
      printf("description\n");

      while (restart==1) {
                                          /*Read the file headers, allocate memory for the*/
                                          /*input arrays, and load them.                  */
            printf("FILE #1:\n");
            num1=read_file_header_int(filename1);
            printf("FILE #2:\n");
            num2=read_file_header_int(filename2);
            numout=num1+num2;
            frequency1=dvector(0,num1-1);
            reflec1=magphase_vector(0,num1-1);
            frequency2=dvector(0,num2-1);
            reflec2=magphase_vector(0,num2-1);
            read_file_data_int(filename1,frequency1,reflec1);
            read_file_data_int(filename2,frequency2,reflec2);
                                          /*Allocate memory for the output arrays and     */
                                          /*them                                          */
            frequency=dvector(0,numout-1);
            reflec=magphase_vector(0,numout-1);
            for(i=0;i<numout;i++) {
                  if(i<num1) {
                        frequency[i]=frequency1[i];
                        reflec[i].mg=reflec1[i].mg;
                  }
                  else {
                        frequency[i]=frequency2[i-num1];
```

```
                reflec[i].mg=reflec2[i-num1].mg;
            }
        }
                                    /*Free the memory used by the various arrays,  */
                                    /*save the output file, and exit gracefully.   */
        free_dvector(frequency1,0,num1-1);
        free_dvector(frequency2,0,num2-1);
        free_magphase_vector(reflec1,0,num1-1);
        free_magphase_vector(reflec2,0,num2-1);

        save_file_int(numout,frequency,reflec);
        free_dvector(frequency,0,numout-1);
        free_magphase_vector(reflec,0,numout-1);
        printf("\nDo you want to process another set of files?");
        restart=menu_response(2,"","No","Yes")-1;
    }

    printf("PROGRAM FINISHED: Press <<return>> to exit to Macintosh Environment.");
    exit(1);
}
```

F. Kramers-Kronig (link to Fileroutines, Menu, NRutil, Optical, and Complex)

This routine reads in a file in intermediate form prepared by the **Preprocess** and **Merge** routines. The file should contain R(ω) over a very wide range of frequencies. This program calculates the phase as a function of frequency by using the variation of the standard Kramers-Kronig integral suggested by Cardona and Greenaway[3]:

$$\theta(\omega) = -\frac{\omega}{\pi} \mathbf{P} \int_0^{\infty} \frac{\ln R(s) - \ln R(\omega)}{s^2 - \omega^2} ds \ . \qquad \text{(A-20)}$$

The second term in the numerator integrates to zero; the advantage of its inclusion is that the numerator now goes to zero more quickly than the denominator as s approaches ω and the divergence of the integrand is avoided. This integrand is calculated and summed using a trapezoidal integration rule for all frequencies except s=ω. Though the integrand does not formally diverge at s=ω, its numerator and denominator separately go to zero

and calculation of the integrand at that point gives unexpected results. The program calculates instead the integrand suggested by L'Hospital's rule:

$$\left.\frac{\frac{\partial}{\partial s}\ln R(s)}{2s}\right|_{s=\omega} \tag{A-21}$$

or, for s=0:

$$\left.\frac{\frac{\partial^2}{\partial s^2}\ln R(s)}{2}\right|_{s=0} \tag{A-22}$$

The program calculates the partial derivatives in Eqs. (A-21) and (A-22) by fitting ln(R(s)) to a parabola near s=ω:

$$\ln(R(s)) = a + b(s-\omega) + c(s-\omega)^2 \tag{A-23}$$

For a discretely (but perhaps irregularly) sampled reflectance R(s),

$$\left.\frac{\partial \ln R(s)}{\partial s}\right|_{s=\omega} = b = \frac{(s_+-s)^2(\ln R(s)-\ln R(s_-)) + (s_--s)^2(\ln R(s_+)-\ln R(s))}{(s_--s)^2(s_+-s)-(s_+-s)^2(s_--s)} \tag{A-24}$$

and

$$\left.\frac{\partial^2 \ln R(s)}{\partial s^2}\right|_{s=0} = 2c = 2\,\frac{s_+(\ln R(0) - \ln R(s_{++})) + s_{++}(\ln R(s_+) - \ln R(0))}{s_+ s_{++}(s_+ - s_{++})} \tag{A-25}$$

where s_- is the next frequency lower than s, and s_+ and s_{++} are the next two frequencies higher than s.

The calculated phase $\theta(\omega)$ and measured reflectance $R(\omega)$ are converted to a complex dielectric function $\varepsilon(\omega)$ using equation (A-16). The results are written to a file in five columns: ω, $R(\omega)$, $\theta(\omega)$, $\varepsilon_1(\omega)$, and $\varepsilon_2(\omega)$.

Kramers-Kronig

```
#include <stdio.h>
#include <math.h>
#include <complex881.h>
#include <nrutil881.h>
#include <wncutil881.h>
#include <wncoptical881.h>
#define PI 3.141592653589793

main()
{
        long numpoints,target,i,first,last;
        double freq_range,percent,low,high,*integrand;
        double lnri,lnrj,lnrk,lnrh,h,j,k,denom;
        double *frequency,cardona,interval,total1,factor;
        magphase *reflec;
        fcomplex *epsilon; /*, *sigma;*/
        fcomplex rcoeff,n;
        char filename[20];

        printf("description\n");
                                                /*Read the file header, allocate memory for     */
                                                /*the input and output arrays, then load the    */
                                                /*input arrays
        numpoints=read_file_header_int(filename);
        frequency=dvector(0,numpoints-1);
        reflec=magphase_vector(0,numpoints-1);
        epsilon=complex_vector(0,numpoints-1);
        integrand=dvector(0,numpoints-1);
        read_file_data_int(filename,frequency,reflec);
                                                /*Ask the user to define the frequencies for    */
                                                /*which θ(ω) and ε(ω) should be calculated.     */
                                                /*Determine which indices in the arrays         */
                                                /*correspond to the desired frequency range.    */
        printf("The data extends from %10.4g to %10.4g cm-1.\n",
                                        frequency[0],frequency[numpoints-1]);
        printf("You should choose the frequency range for the Kramers-Kronig analysis.\n");
        printf("Enter lower frequency limit (>=0., include decimal point): ");
        scanf("%lf",&low);
        printf("Enter upper frequency limit: ");
        scanf("%lf",&high);
        first=last=-1;
        for (i=0;i<numpoints;i++)       {
                if((frequency[i]>=low)&&(first== -1)) first=i;
                if((frequency[i]>high)&&(last== -1)) last=i-1;
        }
        if (first== -1) first=0;
        if (last== -1) last=numpoints-1;

                                                /*Begin the calculation                         */
```

```
printf("Point#          ");
for(target=first;target<=last;target++)       {
      printf("\b\b\b\b\b\b\b\b\b\b\b\b\b%5ld of %5ld",target-first,last-first);
      cardona=log(reflec[target].mg);
      total1=0.;
      for(i=0;i<numpoints;i++)  {
            if (target==i) {
                                          /*If s=w and w=0, evaluate the integrand using */
                                          /*Eq. (A-25).                                  */
                  if (frequency[target] == 0.) {
                        lnri=log(reflec[target].mg);
                        lnrj=log(reflec[target+1].mg);
                        lnrk=log(reflec[target+2].mg);
                        j=frequency[target+1]-frequency[target];
                        k=frequency[target+2]-frequency[target];
                        integrand[i]=(((j-k)*lnri)+(k*lnrj)-(j*lnrk))/(j*k*(j-k));
                  }
                                          /*If s=w and w≠0, evaluate the integrandusing  */
                                          /*Eq. (A-24).                                  */
                  else  {
                        lnrh=log(reflec[target-1].mg);
                        lnri=log(reflec[target].mg);
                        lnrj=log(reflec[target+1].mg);
                        h=frequency[target-1]-frequency[target];
                        j=frequency[target+1]-frequency[target];
                        integrand[i]= -(lnrh*pow(j,2));
                        integrand[i] -= lnri*pow(h,2);
                        integrand[i] += lnri*pow(j,2);
                        integrand[i] += lnrj*pow(h,2);
                        denom=j*pow(h,2) - h*pow(j,2);
                        denom=denom*2.*frequency[target];
                        integrand[i] = integrand[i]/denom;
                  }
            }
                                          /*If s≠w, evaluate the integrand using         */
                                          /*Eq. (A-20).                                  */
            else  {
                  integrand[i]=log(reflec[i].mg)-cardona;
                  integrand[i]=integrand[i]/(pow(frequency[i],2)-pow(frequency[target],2));
            }
      }
                                          /*Sum the integral.                            */
      for (i=0;i<numpoints-1;i++)  {
            interval=(frequency[i+1]-frequency[i])/2.;
            total1 += interval*(integrand[i]+integrand[i+1]);
      }
                                          /*Constrain the phase to be -π/2 < θ < +π/2    */
      reflec[target].ph= -(total1*frequency[target])/PI;
      while (reflec[target].ph > (PI/2.))
            reflec[target].ph -= PI;
      while (reflec[target].ph < -(PI/2.))
            reflec[target].ph += PI;
                                          /*Calculate the dielectric function            */
      epsilon[target]=calc_dielectric_const(reflec[target]);
}
printf("\n");
                                          /*Save the output file, free the memory        */
                                          /*allocated for arrays, and exit gracefully.   */
```

```
    save_file_final(last-first+1,&frequency[first],&epsilon[first],&reflec[first]);
    free_dvector(frequency,0,numpoints-1);
    free_dvector(integrand,0,numpoints-1);
    free_complex_vector(epsilon,0,numpoints-1);
    free_magphase_vector(reflec,0,numpoints-1);

    printf("PROGRAM FINISHED: Press <<return>> to exit to Macintosh Environment.");
    exit(1);
}
```

G. Oscil (Compile with Complex, NRutil, Optical, Menu, and Fileroutines)

This program generates the complex dielectric constant for a set of harmonic oscillators given their frequencies, static polarizabilities, and decay times. The file it generates has the same form as the files constructed by **Kramers-Kronig**.

Oscil

```
#include <stdio.h>
#include <math.h>
#include <stdlib.h>
#include <complex881.h>
#include <nrutil881.h>
#include <wncutil881.h>
#include <wncoptical881.h>

main()
{
    double *frequency;                          /*pointers to frequency array                */
    fcomplex *epsilon;                          /*dielectric constant                        */
    magphase *reflec;                           /*reflectance and phase shift                */
    double wupper,wlower,a,b,c,s,t,wosc,e00;    /*upper and lower frequency limits,          */
                                                /*oscillator parameters                      */
    int response;
    long numpoints,i;

                                                /*Get the frequency range, number of points  */
                                                /*to be calculated, and background dielectric*/
                                                /*contant from the user.                     */

    printf("Enter lower frequency limit for output:\n");
    scanf("%lf",&wlower);
    printf("Enter upper frequency limit for output:\n");
    scanf("%lf",&wupper);
    printf("How many frequencies should I output between these limits (integer)?:\n");
    scanf("%li",&numpoints);
    printf("Enter the background dielectric constant e00 you want to use:\n");
    scanf("%lf",&e00);
                                                /*Allocate memory for the necessary arrays.  */
```

```
        frequency=dvector(0,numpoints-1);
        epsilon=complex_vector(0,numpoints-1);
        reflec=magphase_vector(0,numpoints-1);

                                                /*Calculate the frequencies, put in ε∞,        */
                                                /*initialize reflec                            */
        for(i=0;i<numpoints;i++) {
              frequency[i]=wlower+(i*(wupper-wlower)/(numpoints-1));
              epsilon[i].re=e00;
              epsilon[i].im=0.;
              reflec[i]=ref_and_phase(epsilon[i]);
        }
                                                /*Shall we superimpose another oscillator?     */
        while((response=menu_response(3,"Would you like to:","Add an oscillator","Save the
                                        information","Quit"))!=3) {
              switch(response){
                    case 1:
                          printf("Enter oscillator frequency:\n");
                          scanf("%lf",&wosc);
                          printf("Enter oscillator strength S:\n");
                          scanf("%lf",&s);
                          printf("Enter lifetime t:\n");
                          scanf("%lf",&t);
                          for(i=0;i<numpoints;i++) {
                                a=1.-pow((frequency[i]/wosc),2);
                                b=frequency[i]/(wosc*wosc*t);
                                c=pow(a,2)+pow(b,2);
                                epsilon[i].re+=s*a/c;
                                epsilon[i].im+=s*b/c;
                                reflec[i]=ref_and_phase(epsilon[i]);
                                /*sigma[i]=calc_conductivity(epsilon[i],frequency[i]);*/
                                }
                          break;
                    case 2:
                                                /*save the file in final form.                 */
                          save_file_final(numpoints,frequency,epsilon,reflec);
                          break;
                    default:
                          break;
              }
        }
                                                /*Free the allocated memory and exit gracefully*/
        free_dvector(frequency,0,numpoints-1);
        free_complex_vector(epsilon,0,numpoints-1);
        free_magphase_vector(reflec,0,numpoints-1);

        printf("PROGRAM FINISHED: Press <<return>> to exit to Macintosh Environment.");
        exit(1);

}
```

Computer code library II: Utility routines

A. Complex

These programs use an extended version of the complex number manipulation library in Appendix E of *Numerical Recipes in C*[4]. The code for that library should be included with the following exceptions: (1) All "float" variables should be declared as "double", all "int" variables declared as "long". This change is required by the C compiler[5] used with the Macintosh computer; (2) The *Numerical Recipes* library couples the real and imaginary part of a complex number as the structure "fcomplex", so that for a complex number z, Re(z) is labelled z.r and Im(z) is labelled z.i. We have added a similar structure "magphase" for complex numbers in polar form. For the number z, |z| is labelled z.mg and Arg(z) is labelled z.ph. In addition, we have changed the appellations z.r and z.i to z.re and z.im throughout the code so that "i" can be retained as an array index without confusion; (3) The following routines have been added to the library. They facilitate conversion between the various types of complex numbers:

Complex

```
#include <complex881.h>

double Creal(z)                          /*Creal: return the real part of a complex    */
fcomplex z;                              /*number in x+iy form                         */

{
      return z.re;
}

double Cimag(z)                          /*Cimag: return the imaginary part of a       */
fcomplex z;                              /*complex number in x+iy form                 */

{
      return z.im;
}

double Cphase(z)                         /*Cphase: returns the phase of a complex      */
fcomplexz;                               /*number initially in x+iy form               */

{
      return atan(z.im/z.re);
}
```

```
magphase Cpolar(z)                          /*Cpolar: given a complex number in          */
fcomplex z;                                 /*rectangular form, return its magnitude and */
                                            /*phase form                                 */
{
      magphase c;
      c.mg=sqrt(pow(z.re,2)+pow(z.im,2));
      c.ph=atan(z.im/z.re);
      return c;
}

fcomplex Crect(n)                           /*Crect: given a complex number in polar form */
magphase n;                                 /*return its rectangular form                */
{
      fcomplex c;
      c.re=(n.mg)*cos(n.ph);
      c.im=(n.mg)*sin(n.ph);
      return c;
}
```

B. NRutil

This collection of routines allocates memory to vectors and matrices. It is identical to the standard utility library found in Appendix D of *Numerical Recipes in C*,[4] (again, with the exception that "float" variables are declared as "double", and "int" variables are declared as "long"). In addition, the first line of *Numerical Recipes* code should be deleted, and the following additional code should be included:

```
NRUtil
#include <stdlib.h>
#include <complex881.h>

fcomplex *complex_vector(nl,nh)
long nl,nh;                                 /* Allocates a vector of complex numbers in */
                                            /*in x+iy form with range [nl...nh]        */
{
      fcomplex *v;

      v=(fcomplex *)malloc((unsigned) (nh-nl+1)*sizeof(fcomplex));
      if (!v) nrerror("allocation failure in complex_vector()");
      return v-nl;
}

magphase *magphase_vector(nl,nh)
long nl,nh;                                 /* Allocates a vectorof complex numbers in  */
                                            /*magnitude-phase form with range [nl...nh] */
{
      magphase *v;
```

```
    v=(magphase *)malloc((unsigned) (nh-nl+1)*sizeof(magphase));
    if (!v) nrerror("allocation failure in magphase_vector()");
    return v-nl;
}

void free_complex_vector(v,nl,nh)
fcomplex *v;
long nl,nh;
                                        /*Frees a complex x+iy vector allocated by    */
                                        /*complex_vector().                           */
{
    free((char*) (v+nl));
}

void free_magphase_vector(v,nl,nh)
magphase *v;
long nl,nh;
                                        /*Frees a complex magnitude-phase vector      */
                                        /*allocated by magphase_vector().             */
{
    free((char*) (v+nl));
}
```

C. Optical

This set of routines calculates dielectric functions given a reflectance and phase shift (and vice versa) by implementing Eqs. (A-1), (A-2), (A-12), and (A-16).

Optical

```
#include <math.h>
#include <complex881.h>
#include <wncutil881.h>
#include <wncoptical881.h>
#define PI 3.141592653589793

fcomplex calc_dielectric_const(magphase reflec)
                                        /*calc_dielectric_const: a function that returns */
                                        /*a fcomplex structure containing the dielectric */
                                        /*function given a pointer to a magphase         */
                                        /*structure containing the reflectance and       */
                                        /*phase shift.                                   */
{
    fcomplex n,rcoeff;

    rcoeff=Complex(sqrt(reflec.mg) * cos(reflec.ph),sqrt(reflec.mg) * sin(reflec.ph));
    n=Cdiv(Cadd(Complex(1.,0.),rcoeff),Csub(Complex(1.,0.),rcoeff));
    return Cmul(n,n);

}

magphase ref_and_phase(fcomplex epsilon)    /*ref_and_phase:a function that returns a    */
                                            /*magphase structure containing the          */
                                            /*reflectance and phase given a pointer to a */
```

```
                                        /*complex structure containing the dielectric  */
                                        /*function                                     */
{
        fcomplex n,rcoeff;
        magphase temp;

        n=Csqrt(epsilon);
        rcoeff=Cdiv((Csub(n,Complex(1.,0.))),(Cadd(n,Complex(1.,0.))));
        temp.mg=Cabs(rcoeff)*Cabs(rcoeff);
        temp.ph=Cphase(rcoeff);
        return temp;
}
```

D. Menu

This utility routine prints a menu of choices on the monitor and returns the user's response to the menu.

Menu

```
#include <stdio.h>
#include <complex881.h>
#include <wncutil881.h>
#include <stdarg.h>
#include <string.h>
int menu_response(int i,char *query,...)
{
        va_list ap;
        char *sval;
        int j,is_int,response,length;

        length=strlen(query);
        va_start(ap,query);
        printf(query);
        for(j=1;j<=i;j++) {
                printf("\n%*s%i-",length," ",j);
                for(sval=va_arg(ap,char*);*sval;sval++)
                        putchar(*sval);
        }
        va_end(ap);
        printf("\n%*s>?",length," ");
        get_response(&response);
        while ((response<1)||(response>i))          {
                printf("Invalid response--try again!\n\t\t>?");
                get_response(&response);
        }

        printf("\n");
        return response;
}
void get_response(int *response)
{
        int is_int;
        is_int=scanf("%i",response);
        if (is_int != 1) {
```

```
            do {
                printf("Invalid format--try again!\n\t\t>?");
                fflush(stdin);
                is_int=scanf("%i",response);
            } while (is_int != 1);
        }
        return;
}
```

E. Fileroutines

This set of routines fetches and saves files and file headers in various formats.

Fileroutines

```
#include <stdio.h>
#include <complex881.h>
#include <nrutil881.h>
#include <wncutil881.h>

                                                /* save_file_final: this routine saves a file in final*/
                                                /*form: 'numpoints' sets of frequency, R, θ,      */
                                                /*Re(ε), and Im(ε).                               */
void save_file_final(long numpoints, double *frequency, fcomplex *epsilon,magphase *reflec)

{
        FILE *fp;
        FILE *fopen(char *name, char *mode);
        long i;
        char filename[20];
                                                /*Get the filename from the user                  */
        printf("Please enter your filename (<=20 characters):");
        scanf("%20s",filename);
                                                /*Open the file and write the labels over the     */
                                                /*columns.                                        */
        if((fp=fopen(filename,"w"))==NULL)
                nrerror("Can't open file");
        if((fprintf(fp,"%15s%15s%15s%15s%15s\n"," Frequency","Reflectance",
                                "Phase","eps_re","eps_im"))<0)
                nrerror("Error in write file header");

        for(i=0;i<numpoints;i++) {              /*write the data to the file                      */

        if((fprintf(fp,"%15.6lg%15.6lg%15.6lg%15.6lg%15.6lg\n",frequency[i],reflec[i].mg,reflec[i]
.ph                                     ,epsilon[i].re,epsilon[i].im))<0)
                nrerror("Error in writing file data");
        }
        fclose(fp);
        return;
}

                                                /*save_file_int: this routine saves data in       */
                                                /*intermediate form: 'numpoints' sets of ω and    */
                                                /*R, after saving the number 'numpoints' itself.  */
void save_file_int(long numpoints, double *frequency,magphase *reflec)

{
```

```
        FILE *fp;
        FILE *fopen(char *name, char *mode);
        long i;
        char filename[20];

                                                /*get the filename from the user                */
        printf("Please enter filename for output file (<=20 characters):");
        scanf("%20s",filename);

        if((fp=fopen(filename,"w"))==NULL)      /*open the file and write the number of points  */
                nrerror("Can't open file");
        if((fprintf(fp,"%5ld\n",numpoints))<0)
                nrerror("Error in writing number of points");

        for(i=0;i<numpoints;i++) {                      /*write the data to the file            */
                if((fprintf(fp,"%27.16e%20.6e\n",frequency[i],reflec[i].mg))<0)
                        nrerror("Error in writing file data");
        }
        fclose(fp);
        return;
}

                                                /*read_file_header_int: this routine reads the  */
                                                /*header of an intermediate form file.  It returns */
                                                /*the number of points in the file and stores the*/
                                                /*filename in an address pointed to by          */
                                                /**filename.  The routine should be followed by*/
                                                /*a call to read_file_data_int to actually retrieve */
                                                /*the R(ω) data stored in the file              */
long read_file_header_int(char *filename)
{
        FILE *fp;
        FILE *fopen(char *name, char *mode);
        long numpoints;

                                                /*get the filename from the user*/
        printf("Please enter filename for input file (<=20 characters):");
        scanf("%20s",filename);

        if((fp=fopen(filename,"r"))==NULL)      /*open the file and read the number of points   */
                nrerror("Can't open file");
        if((fscanf(fp,"%ld",&numpoints))<0)
                nrerror("Error in reading number of points");

        fclose(fp);
        return numpoints;
}

                                                /*read_file_data_int: this routine reads data   */
                                                /*a file in intermediate form.  It reads 'numpoints'*/
                                                /*but ignores other information in the header,  */
                                                /*then stores 'numpoints' sets of R and w in the*/
                                                /*arrays pointed to by 'frequency' and the      */
                                                /*the magnitude part of 'reflec'                */
long read_file_data_int(char *filename,double *frequency,magphase *reflec)
```

```
{
        FILE *fp;
        FILE *fopen(char *name, char *mode);
        long i,numpoints;
        int dummy;
        double fdummy,reflectance,freq;

        if((fp=fopen(filename,"r"))==NULL)          /*open the file, read the number of points      */
                nrerror("Can't open file");
        if((fscanf(fp,"%ld",&numpoints))<0)
                nrerror("Error in reading number of points header");

        for(i=0;i<numpoints;i++) {                  /*read the remaining data from the file         */
                if((fscanf(fp,"%le%le",&freq,&reflectance))<0)
                        nrerror("Error in reading file data");
                reflec[i].mg=(double) reflectance;
                frequency[i]=(double) freq;
        }

        fclose(fp);
        return;
}                                                   /*Reads the header from an SPE file             */
long read_file_header_spe(double *freq_range_ptr,char *filename)

{
        FILE *fp;
        FILE *fopen(char *name, char *mode);
        long i,numpoints;
        int dummy;
        double fdummy;


        /*get the filename from the user*/
        printf("Please enter filename for input file (<=20 characters):");
        scanf("%20s",filename);

                                                    /*open the file and read the FIRMS filetype,    */
                                                    /*the number of points, the number of coadded*/
                                                    /*numerators then denominators, the             */
                                                    /*resolution, and the upper frequency limit.    */
        if((fp=fopen(filename,"r"))==NULL)
                nrerror("Can't open file");
        if((fscanf(fp,"%i%li%i%i%lf%lf",&dummy,&numpoints,&dummy,&dummy,&fdummy,
                                        freq_range_ptr))<0)
                nrerror("Error1 in reading SPE header");

        fclose(fp);
        return numpoints;
}
                                                    /* read_file_data_spe: this routine reads the   */
                                                    /*data in a file originally saved in the SPE form  */
                                                    /*by the FIRMS program on the IBM.  It ignores  */
                                                    /*the header, then stores 'numpoints' values of*/
                                                    /*R in the magnitude part of the array pointed to*/
                                                    /*by 'reflec'.                                  */
```

```
long read_file_data_spe(char *filename,magphase *reflec)

{
        FILE *fp;
        FILE *fopen(char *name, char *mode);
        long i,numpoints;
        int dummy;
        double fdummy,reflectance;
                                                /*open the file, read and ignore the FIRMS      */
                                                /*header                                        */
        if((fp=fopen(filename,"r"))==NULL)
                nrerror("Can't open file");
        if((fscanf(fp,"%i%ld%i%i%lf%lf",&dummy,&numpoints,&dummy,&dummy,&fdummy,
                                        &fdummy))<0)
                nrerror("Error1 in reading SPE header");

        for(i=0;i<numpoints;i++) {              /*read the remaining data from the file         */
                if((fscanf(fp,"%le",&reflectance))<0)
                        nrerror("Error in reading file data");
                reflec[i].mg=(double) reflectance;
        }

        fclose(fp);
        return;
}
```

F. Headers

These brief sections of code are included at the beginning of many of the C routines listed in this appendix. They declare the various functions and specify the variable types each function receives and returns.

complex881.h

```
typedef struct FCOMPLEX {double re,im;} fcomplex;
                                                /*complex number in x+iy format                 */
typedef struct MAGPHASE {double mg,ph;} magphase;
                                                /*complex number in Ae^iθ format                */

fcomplex Complex(double, double);
double Creal(fcomplex);
double Cimag(fcomplex);
double Cabs(fcomplex);
double Cphase(fcomplex);
fcomplex Cadd(fcomplex ,fcomplex);
fcomplex Csub(fcomplex,fcomplex);
fcomplex Conjg(fcomplex);
magphase Cpolar(fcomplex);
fcomplex Crect(magphase);
fcomplex Cmul(fcomplex,fcomplex);
fcomplex Cdiv(fcomplex,fcomplex);
fcomplex Csqrt(fcomplex);
fcomplex RCmul(double,fcomplex);
```

nrutil881.h

```
void nrerror(char[]);
float *vector(long,long);
int *ivector(long,long);
```

```
double *dvector(long,long);
fcomplex *complex_vector(long,long);
magphase *magphase_vector(long,long);
float **matrix(long,long,long,long);
double **dmatrix(long,long,long,long);
int **imatrix(long,long,long,long);
float **submatrix(float **,long,long,long,long,long,long);
void free_vector(float *,long,long);
void free_ivector(int *,long,long);
void free_dvector(double *,long,long);
void free_complex_vector(fcomplex *,long,long);
void free_magphase_vector(magphase *,long,long);
void free_matrix(float **,long,long,long,long);
void free_dmatrix(double **,long,long,long,long);
void free_imatrix(int **,long,long,long,long);
void free_submatrix(float **,long,long,long,long);
float **convert_matrix(float *,long,long,long,long);
void free_convert_matrix(float **,long,long,long,long);
```

wncoptical881.h

```
fcomplex calc_dielectric_const(magphase reflec);
magphase ref_and_phase(fcomplex epsilon);
```

wncutil881.h

```
int menu_response(int,char *,...);
void get_response(int *);
void save_file_final(long , double *, fcomplex *,magphase *);
void save_file_int(long , double *,magphase *);
long read_file_header_spe(double *,char *);
long read_file_data_spe(char *,magphase *);
long read_file_header_int(char *);
long read_file_data_int(char *,double *,magphase *);
```

References

1. See, for instance, Charles Kittel, *Introduction to Solid State Physics*, 5th ed., (John Wiley & Sons, New York, 1976), p. 324.

2. Max Born and Emil Wolf, *Principles of Optics*, 4th ed., (Pergamon Press, Oxford, 1970), p. 627ff.

3. Manual Cardona and D.L. Greenaway, Phys. Rev. **133** , A1685 (1964).

4. William H. Press, Brian P. Flannery, Saul A. Teukolsky, and William T. Vetterling, *Numerical Recipes in C*, (Cambridge University Press, Cambridge, 1988).

5. **Think C** Version 4.0, Symantec Corporation, Cupertino, CA 95014.